Springer ThesesRecognizing Outstanding Ph.D. Research

Umberto Celano

Metrology and Physical Mechanisms in New Generation Ionic Devices

EXTRAS ONLINE



Springer Theses

Recognizing Outstanding Ph.D. Research

Aims and Scope

The series "Springer Theses" brings together a selection of the very best Ph.D. theses from around the world and across the physical sciences. Nominated and endorsed by two recognized specialists, each published volume has been selected for its scientific excellence and the high impact of its contents for the pertinent field of research. For greater accessibility to non-specialists, the published versions include an extended introduction, as well as a foreword by the student's supervisor explaining the special relevance of the work for the field. As a whole, the series will provide a valuable resource both for newcomers to the research fields described, and for other scientists seeking detailed background information on special questions. Finally, it provides an accredited documentation of the valuable contributions made by today's younger generation of scientists.

Theses are accepted into the series by invited nomination only and must fulfill all of the following criteria

- They must be written in good English.
- The topic should fall within the confines of Chemistry, Physics, Earth Sciences, Engineering and related interdisciplinary fields such as Materials, Nanoscience, Chemical Engineering, Complex Systems and Biophysics.
- The work reported in the thesis must represent a significant scientific advance.
- If the thesis includes previously published material, permission to reproduce this must be gained from the respective copyright holder.
- They must have been examined and passed during the 12 months prior to nomination.
- Each thesis should include a foreword by the supervisor outlining the significance of its content.
- The theses should have a clearly defined structure including an introduction accessible to scientists not expert in that particular field.

More information about this series at http://www.springer.com/series/8790

Umberto Celano

Metrology and Physical Mechanisms in New Generation Ionic Devices

Doctoral Thesis accepted by the KU Leuven and IMEC, Belgium



Author

Dr. Umberto Celano

Material and Component Analysis

IMEC

Leuven Belgium Supervisor

Prof. Wilfried Vandervorst

Material and Component Analysis

IMEC

Leuven

Belgium

ISSN 2190-5053 Springer Theses ISBN 978-3-319-39530-2 DOI 10.1007/978-3-319-39531-9 ISSN 2190-5061 (electronic)

ISBN 978-3-319-39531-9 (eBook)

Library of Congress Control Number: 2016940821

© Springer International Publishing Switzerland 2016

This work is subject to copyright. All rights are reserved by the Publisher, whether the whole or part of the material is concerned, specifically the rights of translation, reprinting, reuse of illustrations, recitation, broadcasting, reproduction on microfilms or in any other physical way, and transmission or information storage and retrieval, electronic adaptation, computer software, or by similar or dissimilar methodology now known or hereafter developed.

The use of general descriptive names, registered names, trademarks, service marks, etc. in this publication does not imply, even in the absence of a specific statement, that such names are exempt from the relevant protective laws and regulations and therefore free for general use.

The publisher, the authors and the editors are safe to assume that the advice and information in this book are believed to be true and accurate at the date of publication. Neither the publisher nor the authors or the editors give a warranty, express or implied, with respect to the material contained herein or for any errors or omissions that may have been made.

Printed on acid-free paper

This Springer imprint is published by Springer Nature
The registered company is Springer International Publishing AG Switzerland

But nevertheless, we now have a much more humble point of view of our physical laws—everything can be wrong!

Richard Feynman, Lectures on Physics



Supervisor's Foreword

Modern life would not be the same without the ubiquitous presence of electronic devices connecting us to society, actuators, and sensors facilitating our life and available at our fingertips for complex operations and calculations. Driven by the dynamics of Moore's law, continuous downscaling of nano-electronic components and systems is pursued leading to an ever-increasing complexity of micro-electronics devices and systems. At the heart of every system resides a storage system ("memory") which is subjected to the same scaling laws in terms of reduced dimensionality and increased complexity. Although in this field, various requirements such as speed, power, size, etc., co-exist, modern society has become extremely dependent on non-volatile data storage for consumer (music, photo, data) and professional applications (data storage, encryption, access codes). Hence, research in advancing the state of the art in (non-volatile) memories and the exploration of novel concepts, which can be scaled further than present technologies, has drawn considerable academic and industrial attention. The required technological developments are extremely challenging and can only be reached if supported with profound physical insight and understanding. As such, paraphrasing Henry Marks (1829–1898, "Science is measurement"), metrology apt to deal with such novel developments is essential to pave the way to success.

Within this thesis U. Celano has focused on establishing metrology towards unraveling the physical and electrical properties of the emerging resistive memory devices. Resistive memory devices are based on the creation/dissolution of nanoscale filaments (1–2 nm) which are induced by atom (or vacancy) migration under the influence of an electric field. Fundamental insight in their operational principle (formation and dissolution of the filament, conduction within the filament) was linked to the nanoscale observation of the filament shape, conductivity, structure, dimensionality, and evolution depending on material systems and electrical probing and resetting sequences. The whole switching process is based on solid-state electrochemical reactions occurring in very confined volumes.

The important contribution of Umberto Celano is the development of a novel scanning probe microscopy concept termed SPM tomography or Scalpel SPM.

Through this development the first direct observations of the 3D shape, size, and electrical properties of the nanoscale filaments have been obtained. These nanoscale observations created insight in the entire filament formation mechanisms and the balance between field-induced atom migration and neutralization enabling to link apparently controversial observations of filament shapes from the literature into one consistent theory. Moreover, a close correlation was established between the physical phenomena of filament formation and the dissolution with device characteristics (low resistive state, high resistive state, switching mechanisms, and reliability).

In addition, Umberto investigated the ultimate scaling prospects of such devices by exploiting the SPM-tip as a nanoscale electrode enabling to create, observe, and manipulate these filaments. Based on his observations, U. Celano could demonstrate that the scaling of RRAM devices can be achieved well below the sub-10 nm regime.

In summary, U. Celano has devoted his work and dissertation in the unraveling of physical and electrical properties of emerging resistive memory devices with an emphasis on the fundamental insight on the operational principles on the nanoscopic scale and the link to the fabrication processes. As the research lingers at the borderline of fundamental physics (studying field-induced atom migration and the impact on electrical conduction of solid-state ionic) and engineering (creating new device concepts and novel 3D metrology concepts), it represents a cornerstone for future developments in this field as represented already by many invited papers and presentations of U. Celano. The scalpel metrology is an important step forward in 3D metrology with already demonstrated applications in other areas such as logic devices, interconnect, etc.

Leuven, Belgium March 2016 Prof. Wilfried Vandervorst

Abstract

The ionic movement in thin films can induce structural changes involving the local conductivity of the material. Filamentary-based resistive switching cells represent an intriguing emerging class of electronic devices, using ion migration to create or dissolve nanoscale conductive filaments in insulating materials. The change in the resistance state of such materials can be used to store a logical bit or to compute nonconventional logic in ultra-scaled devices.

However, tuning the non-volatile internal state of a sub-20 nm device by displacing ions in the space can turn into a difficult task. In such conditions, the transport of ions lies at the boundary between classical physics and quantum mechanics. The whole switching mechanism is based on solid-state electrochemical reactions happening in confined volumes (tens of nm³). This has created a gap between physical understating and devices experimental results.

This Ph.D. work targets to relate resistive switching with the related nanoscopic fundamental mechanisms. Establishing a correlation between the device and the observed physical effects is the first step toward the understanding and the engineering of new devices. By using scanning probe microscopy (SPM) methods we create, observe, and manipulate conductive filaments (CFs). We characterize the fundamental switching mechanisms at nanoscale for cation- and anion-based resistive switching memory devices. We leverage the probe-sample interaction in order to investigate the RS phenomena in the sub-10 nm regime. The generated fundamental understanding on the filament formation and rupture is transferred to the integrated memory cells that we characterize in three dimensions under real operative conditions. This is enabled by an AFM-based tomographic technique named scalpel SPM, which is developed for the characterization of ultra-confined volumes. The extreme high resolution and the precise force control of the AFM is combined to a sub-nm material removal method. The technique has a spatial resolution below 5 nm for the electrical characterization of ultra-confined volume $(\approx 100 \text{ nm}^3)$.

Acknowledgments

The experimental work contained in this book as well as my human and professional growth of the past 4 years would not be the same without a long list of persons that I would like to acknowledge here.

I am very grateful to my promoter Prof. Wilfried Vandervorst for the opportunity to carry out my research in his group during my master thesis first and my Ph.D. afterward. I thank him for the freedom and support received during the past 5 years in the endless quest for "more physics." His critical evaluation and genuine curiosity have guided me in the achievement of my research objectives and certainly they have shaped me as a scholar. I thank also the members of my thesis committee for their insightful advice that improved the quality of this manuscript. I am indebted to the Agency for Innovation by Science and Technology for my Ph.D. fellowship in the period 2012–2015.

Special thanks go to Prof. J. Yang (University of Massachusetts, Amherst) and Dr. A. Volodine (Laboratory of Solid-State Physics and Magnetism, KU Leuven) to enrich the quality of this dissertation by reviewing the Chaps. 2 and 3, respectively. I want to acknowledge all the colleagues of the material and component analysis (MCA) group for the fruitful discussions and continuous support. In particular, Thierry Conard and Thomas Hantschel for their support from the time of my master thesis. Alain Moussa for introducing me to the intriguing world of SPM and for all the laughs in the lab. Danielle Vanhaeren to fix the impossible in the AFM lab and to contribute to this book with the Dutch version of the abstract. And Ilse, Inge, Chris, Alexis, Bastian, Mustafa, Janusz, Kristof, Pierre, Hugo, Olivier, Paola thanks for sharing your knowledge with me during these years. For the daily amusement a special recognition goes to my office mates, Annelies and Ravi, also to Manuel, Grazia, Felix, Supriya, Andreas, and Aftab for our chats and coffee breaks.

As my research has crossed the material analysis to arrive at the memory devices, I wish to thank the whole RRAM team of imec without whom this dissertation would certainly be worse. In particular, Jurczak Malgorzata for integrating

xiv Acknowledgments

me with the team from the beginning. Ludovic Goux for the numerous discussions and for his constant technical support, I don't think to exaggerate when I say that he has been an unofficial daily supervisor in these years. Andrea Fantini, Robin Degraeve, Yangyin Chen, Attilio Belmonte, and Karl Opsmer for their availability and for sharing their knowledge (and data) with me. Together with them I acknowledge Sergiu, Bogdan, Augusto, Micheal, Sruti, Subhali, and Leqi for making the undiscussed leadership of the RRAM team.

A lot of my experiments, especially the unconventional ones, would never have been possible without Frank Gijbels, I thank him for being always supportive when I pop up in the "elektronische werkplaats" with some strange requests. Rita Rooyackers for her availability with chemical etching and Mihaela Popovici and Judit Lisoni for the numerous material deposition.

I am in debt to Jo De Boeck and the SANKEN program for the support during my visiting period in Japan at Osaka University, and I wish to acknowledge here Profs. Takeshi Yanagida and Kazuki Nagashima for guiding me and hosting me in their group in the summer 2013.

I am grateful to the students that I had the privilege and duty to supervise these years: Martina Iapichino, Guido Giammaria, Luigi Mirabelli, Yi Hou, Kentaro Soma, and Ahmed Youssef. I wish this experience was enriching for you at least a fraction of what it was for me.

From the very beginning of my arrival at Belgium, I would like to thank many of the former Ph.D. students and all the old friends; in particular, Marco Facchini, Massimo Mastrangeli, Antonio Arreghini, Claudia Santini, and Emanuele Cornagliotti (for our nice Cali-trip). Last but not least, Jacopo Franco for his friendship, to be my favorite conference fellow and for all our guitar jam. You all have been a guide and inspiration already before starting.

I am proud to say that the list of friends that I have made in the last years in Leuven is too long to fit in here. I am especially grateful to Federica and Giuseppe for our long friendship and for their endless support. A big hug goes to my former flatmates, Rocco and Franky, for the years spent living together, for bearing me, for the laughs, and all the Ballaró at our place. For the great fun had in those years in Oude Markt, special thanks go to Ashesh, il Cecchi, Paolo, and Casini. I thank the large Italian community in imec, KU Leuven and Cafe Belge: Stefano, Serena, Francesca, Antonio, Lisa, Oreste, Ivan, Vito, Nino, Elisabetta, Gabriele, Davide, Elena, and Luca; also Emidio, Carla, Giovanna, and Alessandra. You always represented a piece of home here in Belgium. Then I want to acknowledge my Spanish friends, who made me reconsider the meaning of the verb "to party." Elia, Manu, Daniel, Sofie, Julio, and in particular Marta and Lucia for welcoming/bearing me in their place during the last period. This list could not be closed without an acknowledgment to my lifelong friends, Lorenzo, Fabio, Andrea, Andres, Sascha, and Giorgio, thank you for your ability to stop the time.

Acknowledgments xv

Finally, I would like to thank my family for their love and endless support. My parents for the values that I try to preserve, my mother Rosanna for being a consistent example of life, and Giulia for making me feel like home never changes. Special thanks go to Amira whose love, strength, and beauty inspire me everyday, thanks for being by my side unconditionally in all the important moments.

Leuven, Belgium December 2015 Umberto Celano

Contents

| 1 | Intr | oductio | on | 1 | |
|---|------------|--|---|----|--|
| | 1.1 | Nonvo | platile Memory for Sub-15 nm Node | 2 | |
| | 1.2 | New A | Applications, New Needs and Old Problems | 4 | |
| | 1.3 | | ive Switching: Bits Made of Filaments | 5 | |
| | 1.4 | Object | tives and Outline of the Dissertation | 6 | |
| | Refe | erences | | 8 | |
| 2 | Fila | mentar | y-Based Resistive Switching | 11 | |
| | 2.1 | Basic | Operating Principles | 11 | |
| | 2.2 | Condu | active Bridge Resistive Memory | 14 | |
| | | 2.2.1 | The Electrochemistry in CBRAM | 15 | |
| | | 2.2.2 | The Rate-Limiting Process | 17 | |
| | | 2.2.3 | CBRAM Device Operation | 18 | |
| | | 2.2.4 | Device Optimization | 21 | |
| | 2.3 | Oxide- | -Based Valence Change Memory | 24 | |
| | | 2.3.1 | VCM Device Operation | 25 | |
| | | 2.3.2 | Switching Mechanism and Electron Transport in VCM | 27 | |
| | | 2.3.3 | The Filament as a Quantum Point Contact | 28 | |
| | | 2.3.4 | VCM Device Optimization | 30 | |
| | 2.4 | 4 Review of Conductive Filaments Observation | | 31 | |
| | | 2.4.1 | Filament Observation in CBRAM | 32 | |
| | | 2.4.2 | Filament Observation in VCM | 36 | |
| | 2.5 | Summ | nary of the Chapter | 39 | |
| | References | | | | |
| 3 | Nan | oscaled | Electrical Characterization | 47 | |
| | 3.1 | Overv | iew | 47 | |
| | 3.2 | Condu | active Atomic Force Microscopy | 50 | |
| | | 3.2.1 | Conductive Tips | 52 | |
| | | 3.2.2 | Contact Forces | 54 | |
| | | 3.2.3 | Artifacts in C-AFM | 56 | |
| | | 3.2.4 | Electrical Lateral Resolution | 60 | |

xviii Contents

| | | 3.2.5 Effective Emission Area Evaluation | 61 |
|---|------|---|-----|
| | | 3.2.6 Extending C-AFM Current Range | 66 |
| | 3.3 | Peak Force: Intermittent Contact Mode | 67 |
| | | 3.3.1 Peak Force TUNA Case Studies | 70 |
| | | 3.3.2 Electrical Tip-Contact: Dragged Versus Intermittent | 73 |
| | 3.4 | Three-Dimensional SPM Tomography | 75 |
| | | 3.4.1 Overview of 3D Tomography | 76 |
| | | 3.4.2 SPM Tomography | 78 |
| | 3.5 | Summary of the Chapter | 82 |
| | Refe | erences | 83 |
| 4 | Con | ductive Filaments: Formation, Observation | |
| | and | Manipulation | 87 |
| | 4.1 | Tip-Induced Filament Formation and Observation | 87 |
| | | 4.1.1 Areal Switching | 88 |
| | | 4.1.2 Ultra-Scaled Device Sizes with C-AFM | 89 |
| | | 4.1.3 The Role of the Tip | 91 |
| | | 4.1.4 Resistive Switching C-AFM Versus Devices | 93 |
| | | 4.1.5 Filament Observation | 96 |
| | 4.2 | C-AFM Probing the Reset State | 100 |
| | | 4.2.1 Gap Formation in Cu Filaments | 100 |
| | | 4.2.2 Low-Defects Assisted Quantum-Point-Contact | 103 |
| | 4.3 | Device De-Process: Filament Observation | 107 |
| | 4.4 | Summary of the Chapter | 111 |
| | Refe | erences | 111 |
| 5 | Thr | ee-Dimensional Filament Observation | 115 |
| | 5.1 | Scalpel SPM for Filament Observation | 115 |
| | 5.2 | Tomographic Observation of Cu-Based Filaments | 116 |
| | | 5.2.1 CBRAM: Low-Resistive-State Observation | 117 |
| | | 5.2.2 CBRAM: High-Resistive-State Observation | 119 |
| | | 5.2.3 Cu-Filament Growth Model in Low-Mobility Media | 120 |
| | | 5.2.4 Filament Volume Modulation and Multibit Capability | 122 |
| | 5.3 | On the Dual Nature of Cu Filament Dissolution | 124 |
| | | 5.3.1 A Model for Broken and Nonbroken HRS Filaments | 127 |
| | | 5.3.2 A Ruptured Filament Is Not a Conventional Tunnel | |
| | | Junction | 129 |
| | | 5.3.3 Hourglass Shaped Cu Filament | 130 |
| | 5.4 | Tomographic Filament Observation in VCM | 132 |
| | | 5.4.1 Filament Size Modulation in VCM | 136 |
| | 5.5 | Summary of the Chapter | 139 |
| | Refe | prences | 140 |
| 6 | Reli | ability Threats in CBRAM | 143 |
| | 6.1 | Reliability Threats of Cu Filaments | 143 |
| | 6.2 | Filament Multiplicity as Source of State Instability | 144 |

Contents xix

| | 6.4 | Stuck in LRS: A Cu Filament Degeneracy | 149 | | | | | |
|------------------|------|---|-----|--|--|--|--|--|
| 7 | Con | clusions and Outlook | 151 | | | | | |
| | 7.1 | Filaments Formation and Dissolution | | | | | | |
| | | 7.1.1 Challenges with Tip-Induced Analysis | 153 | | | | | |
| | 7.2 | Filaments 3D Observation | 154 | | | | | |
| | | 7.2.1 Challenges in the Three-Dimensional Observation | 156 | | | | | |
| | 7.3 | Outlook | 157 | | | | | |
| | | 7.3.1 Improving Scalpel SPM | 159 | | | | | |
| Ap | pend | lix A: Cellulose Nanopaper Memory | 161 | | | | | |
| Curriculum Vitae | | | | | | | | |

Abbreviations

1T1R One-Transistor-One-Resistor

3D Three-Dimensional

AFM Atomic Force Microscopy
ALD Atomic Layer Deposition
BRAD Buried Recessed Access Device

C-AFM Conductive Atomic Force Microscopy

CBRAM Conductive Bridge Random-Access Memory

CFs Conductive Filaments
CPU Central Processing Unit
CVD Chemical Vapor Deposition

DRAM Dynamic Random-Access Memory

DT Direct Tunneling e-beam Electron Beam

EBIC Electron Beam-Induced Current
ECM Electrochemical Metalization Cell
EELS Electron Energy Loss Spectroscopy
eNVM Embedded Non-Volatile Memory

FDT Full Diamond Tip

FNT Fowler–Nordheim Tunneling HAADF High-Angle Annular Dark-Field

HFCVD Hot-Filament Chemical Vapor Deposition

HRS High Resistance State

KPFM Kelvin Probe Force Microscopy

LRS Low Resistance State

MFM Magnetic Force Microscopy

MIM Metal-Insulator-Metal

MOSFET Metal-Oxide-Semiconductor Field Effect Transistor

PCM Phase Change Memory

PE-ALD Plasma-Enhanced Atomic Layer Deposition

PFTUNA Peak Force TUNA sensor

PMC Programmable Metalization Cells

xxii Abbreviations

PMCM Pressure-Modulated Conductance Microscopy

PVD Physical Vapor Deposition QPC Quantum Point Contact RAM Random-Access Memory

RMS Root Mean Square

RRAM Resistive Random-Access Memory

RS Resistive Switching SCM Storage Class Memory

SEM Scanning Electron Microscopy

SoC System on Chip

SPM Scanning Probe Microscopy SRAM Static Random-Access Memory

SSD Solid-State Drive

SSRM Scanning Spreading Resistance Microscopy

STM Scanning Tunneling Microscopy

STT-MRAM Spin-Transfer-Torque Magnetic Random-Access Memory

TB Terabyte

TEM Transmission Electron Microscopy

TMA Trimethyl Aluminum
TSV Through Silicon Vias
TUNA Tunneling Current AFM
VCM Valence Change Memory

VMCO Vacancy-Modulated Conductive Oxide

Symbols

| HfO_2 | Hafnium Oxide |
|-------------------------------|---|
| Al_2O_3 | Aluminum Oxide |
| TiN | Titanium Nitride |
| O_2 | Oxygen |
| $\overline{\mathrm{Cu}}^{n+}$ | Copper Cation |
| e | Elementary Charge |
| i_0 | Exchange Current (A) |
| α | Charge Transfer Coefficient |
| k_B | Boltzmann Constant (J K ⁻¹) |
| T | Temperature (K) |
| V | Voltage, Electrochemical Overpotential (V) |
| c | Ions Concentration (kg m ⁻³) |
| k_0 | Reaction Rate Constant (mol $L^{-1} s^{-1}$) |
| \boldsymbol{A} | Area (m ²) |
| \mathbf{E}_{A} | Reaction Energy Barrier (eV) |
| a | Hopping Distance (nm) |
| E | Electric Field (V m ⁻¹) |
| d | Oxide Thickness (nm) |
| ν | Attempt Frequency Factor (Hz) |
| $\Delta E_{\mathrm{hop,0}}$ | Ion hopping Activation Energy at equilibrium (eV) |
| t_n | Nucleation Time (s) |
| t_0 | Nucleation Time Prefactor (s) |
| N_C | Number of Atoms for Critical Nucleus Formation |
| I_{cc} | Current Compliance (A) |
| SiO_2 | Silicon Oxide |
| Ta_2O_5 | Tantalum Oxide |
| Ag_2S | Silver Sulfide |
| $GeSe_2$ | Germanium Diselenide |
| CuTe | Copper Telluride |
| TaN | Tantalum Nitride |
| WN | Tungsten Nitride |
| | |

xxiv Symbols

Ru Ruthenium

 $\begin{array}{lll} {\rm TiW} & {\rm Titanium\ Tungsten} \\ {\rm F} & {\rm Feature\ Size\ (nm)} \\ {\rm HfCl_4} & {\rm Hafnium\ Tetrachloride} \\ {\it V_{\ddot{O}}} & {\rm Oxygen\ Vacancy} \end{array}$

 E_F Fermi Energy Level (eV)

 E_V Valence Band Energy Level (eV) E_C Conduction Band Energy Level (eV)

 E_t Trap Energy Barrier (eV) ω_x Length Constriction Factor (Hz) ω_v Width Constriction Factor (Hz)

ZrO₂ Zirconium Oxide

CuGeTe Copper Germanium Telluride

 Γ Oxidation (Reduction) Rate (nm s⁻¹)

TiO₂ Titanium Oxide SrTiO₃ Strontium Titanate

EYoung's Modulus (N m $^{-2}$)hCantilever Thickness (nm)wCantilever Width (nm)lCantilever Length (nm)kSpring Constant (N m $^{-1}$)

InGa Indium Gallium

Chapter 1 Introduction

Filamentary-based resistive switching cells have a unique characteristic: their electrical resistance can be altered by applying an electrical voltage. This process is reversible and can be repeated millions of times. In other words, they have an ON and OFF state. This enables digital information to be stored e.g. a distinguishable "1" and "0". Resistive switching (RS) devices can be switched rapidly, consume little energy and maintain their state event after long periods of time with no external power. Most of the remarkable properties aforementioned, relay on mobile ions. Similarly to a battery, ions move back and forth between two electrodes in a solid electrolyte (e.g. a metal oxide) only few nanometers thick. This poses severe limitations to the existing observation techniques, and thus to the fundamental comprehension and exploitation of the phenomena. For long time, although a strong theoretical framework has described the resistive switching operations, the direct observation of the ionic filaments was impossible, creating gap between physical understanding and device experimental results.

This dissertation focuses on the creation, observation and manipulation of nanosized conductive channels; whose tunable conductivity is at the foundation of RS memory and logic applications. Confined in few hundreds of nanometers cubic, these conductive filaments (CFs) are the result of ion migration and nanoscaled redox reactions in solid electrolytes. The resistance modulation, i.e. resistive switching, induced by the presence/absence of a CF in the solid electrolyte is used to encode the bit of information. The results of this PhD thesis embrace the fundamental physics and the practical applications of RS. Experimental methodologies based on electrical scanning probe microscopies (SPM) are used to form, characterize and manipulate CFs at the nanoscale. The possibility to relate the macroscopic resistive switching with the nanoscopic fundamental mechanisms is the main goal of this study. This is achieved by two- and three-dimensional electrical characterization of confined volumes with nanometer spatial resolution, leading to two major outcomes. First, enhanced understanding on the filament growth dynamics for the filament formation and dissolution. Second, application of the generated insights on the optimization of high performance devices for logic and memory application.

1

2 1 Introduction

1.1 Nonvolatile Memory for Sub-15 nm Node

At the time this is book is written, memory devices store information in the charge state of a capacitor [1]. The presence or absence of charges represents logic "1" or "0". Today's computing hierarchy is based on volatile and nonvolatile data storage devices, providing an optimal trade-off between cost and performances [1]. A memory is said volatile when its storage mechanism does not retain the data if the power supply is disconnected. In contrast, nonvolatile are those memories capable of retaining data in absence of continuous power supply. Traditionally, the region of memory closest to the processor core is accessed frequently, and therefore it requires the fastest operation speed possible. This is achieved by static random access memory (SRAM) which uses the state of a logic circuit (e.g. a latch element) to store the data. One SRAM cell is made of six transistors which implies large chip area and therefore high costs [1, 2]. Other levels in the memory hierarchy are optimized for storage capacity and speed (Fig. 1.1). The random access memory (RAM) and the nonvolatile flash NAND for storage are located in a separated chip far away from the processor and they are cheaper slower and denser. Dynamic random access memory (DRAM) is composed of a single capacitor with one plate grounded and the other connected to the source of a pass-gate transistor. The main advantage is the higher density achievable due to the use of only one transistor, but it is also volatile. The charge pushed into the capacitor decreases over time (normally $\ll 1$ s) leaking away drained from the off-current of the transistor and needs to be periodically refreshed. Finally, flash memory stores the information in an array of cells made of floatinggate-transistors [3]. The threshold voltage shift induced by the charges trapped in the floating gate enables the storage of 2 even 3 bits per cell. NAND flash cell is a nonvolatile memory, it is slower than SRAM and DRAM but provides the smallest usage of chip area. For over 30 years SRAM, DRAM and flash NAND have been the workhorses of the memory hierarchy [1, 3]. With continuous downscaling today

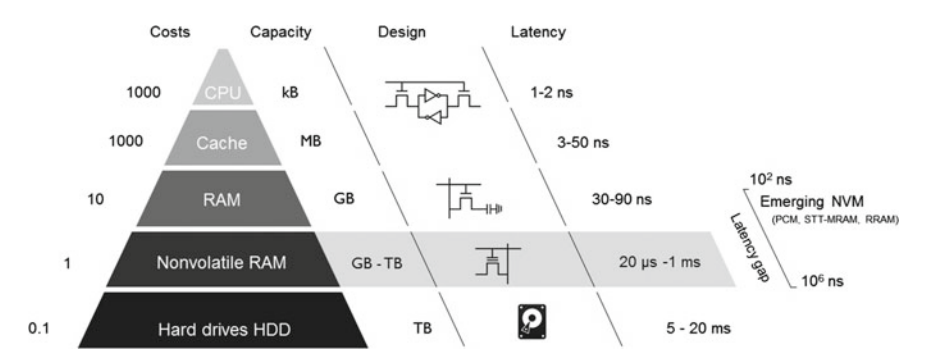


Fig. 1.1 *Memory hierarchy.* Illustration of the current memory hierarchy, comparing costs, design and latency for different memory devices. The remarkable latency gap of nonvolatile memory is shown (*gray shadow*), as most of the emerging memory concepts are targeting to high density and high speed

DRAM chips are available up to 8 Gb densities in a 25 nm technology node while Flash has reached 16 nm half pitch dimension, yielding 128 Gb on a single chip with 2 or even 3 bits per cell. Both types of memory are facing scaling issues and it would not be possible to scale them down below the 15 nm technology node [4].

In the meantime three-dimensional (3D) architectures like FinFETs have been successfully introduced in logic to overcome the scaling limitation of classical metal-oxide-semiconductor field-effect transistor (MOSFET) [5]. Thus 3D architectures and stackable alternatives have been proposed also for memory [6]. For DRAM a viable solution is a 3D stacking, where different DRAM dies are stacked and connected using through-Si vias (TSV). This concept referred as hybrid memory cube is an interesting way to scale on performance and power and introduces the possibility of logic functions directly on the memory chip. In the case of Flash the 3D transition involved the redesign of the device architecture, stacking vertically the charge trap memory cells [7]. This introduce a real "bit cost scaling" and functional devices with 32 cells, yielding 1 TB solid state drives (SSD) already on the market. 3D Flash using 64 layers has been already announced and will provide even higher density at reduced costs. Thanks to the aforementioned solutions the computer hierarchy as we all know it is expected to be extended for another decade.

However in the last 15 years, researchers have started exploring the possibility of new memory concepts [8]. Motivated by the creation of a "universal-memory" they have focused on solutions capable of merging the high density and non-volatility of Flash with the high endurance and high speed of DRAM [9]. Many new concepts have been explored to mitigate the large latency gap of flash (Fig. 1.1). In this quest many non-charge based alternatives have been proposed. Among those, promising candidates are: phase change memory (PCM) [10], spin-transfer-torque magnetic random access memory (STT-MRAM) [11], vacancy modulated conductive oxide (VMCO) [12], conductive bridge random access memory (CBRAM) [13] and valence change memory (VCM) often referred as oxide resistive random access memory [14]. They are all non-charge based devices as they exploit different solutions to store the logical bit. PCM relies on an amorphous-to-crystalline phase transition, STT-MRAM uses a magnetic tunnel junction with tunable magnetization, CBRAM and VCM are based on ionic movement e.g. conductive filament formation. They are all referred as resistance-based or resistive switching devices because the bit is stored in the form of device resistance. Today, the "universal-memory" concept has been widely abandoned, researchers have realized that the advent of portable/mobile devices and more recently cloud computing, wearable electronics and big-data analytics requires an application-driven memory design. In other words each level of the memory hierarchy is going to be optimized for its specific requirement and will use the proper memory technology.

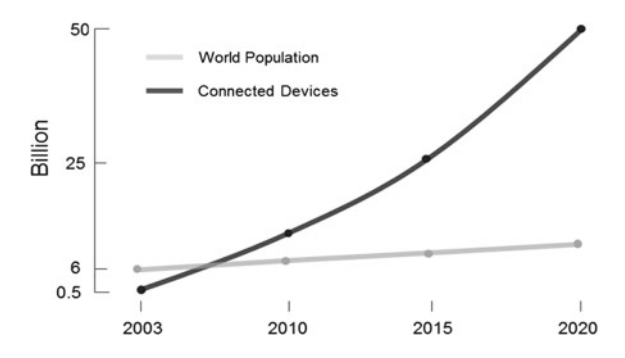
4 1 Introduction

1.2 New Applications, New Needs and Old Problems

In the zettabyte (10^{21} bytes) era, where a huge amount of data are delocalized and accessible from an ever increasing number of devices, the memory hierarchy will change. Most of the aforementioned emerging memory technologies are competing for the role of storage class memory (SCM) [9]. A type of memory which does not necessarily require 10 years of data retention, but will combine high density of Flash and high performance of DRAM. The growing server-market for social-media and cloud computing will tremendously benefit of a similar memory. In the meantime the so called mobile systems on chips (SoC) such as those powering our smartphones, are looking at the emerging solution for the introduction of an embedded nonvolatile memory (eNVM) [4]. This will provide a low-power, embedded nonvolatile solution for mobile applications and wearable electronics. The reasons for these changes relies on the big disparity between the processor speed and the data access time in the conventional Von Neumann architectures [15]. The most simple instruction on the core of the central processing unit (CPU) takes one cycle to be executed, hence less than a third of nanosecond at current speed $\approx 3.2\,\mathrm{GHz}$ (intel core i7). As the CPU works it must read from and write to caches (SRAM) and system memory (DRAM). When the contents of the system memory must be brought in the caches we have a massive ≈250 cycles of latency ≈60 ns. During this time the CPU has no work to do and waits. Interestingly this is the best scenario, because the access to any other storage data takes much longer. There is a famous pictorial example that translates CPU latency in human action time [16]. If reading data from the level 1 cache is like taking a piece of paper from our desk (3 s), level 2 cache is picking up a book from a nearby shelf (14s), the main system memory access is taking a 4-min walk down to the coffee machine and waiting for a hard drive seek is like leaving the building and take one year and three months sabbatical before coming back with the information. The big gap in the access speed among the memory hierarchy can be seen in Fig. 1.1 comparing the latency of different devices.

Next to the old problems, the advent of billions of connected devices is also creating new opportunities that require changes in the foundation of computing as we know it. The number of connected devices has largely exceeded the world population (Fig. 1.2), requiring new paradigms for the computation [17]. Such beyond Von-Neumann computing will be based on nonvolatile logic and neural networking system, in which logic circuits dynamically reconfigure in response to the input [18–20]. This will require memory elements with tunable, nonvolatile internal states. Compatibility with CMOS processes, long data retention, fast switching speed (<10 ns) and low-dimension scalability (<10 nm) are the shared requirements. Projects as "the machine" of Hewlett-Packard [21], memcomputers [22] and neuromorphic adaptive [19] are focusing on resistive memories. The first aims to fuse memory and storage to bring processing closer to data using electrons for computation, photons for communication and ions for storage. The second wants to replace standard circuits elements (transistors, capacitors and inductors) with memristors, memcapacitors and meminductors unifying computing and storage for a reinvented parallel computing

Fig. 1.2 Connected devices per person. Illustration of the growth trend of the world population as compared to the number of connected devices



[22]. Finally, neuromorphic and adaptive aim to realize on hardware level, neural networks and adaptive computation [19]. These would allow small and compact electronic devices to realize what supercomputers do on a software level using a significant amount of power. In addition, processes occurring in the human brain by synaptic operation could be replicated. Mechanisms as short-term plasticity and long-term potentiation, which are at the foundation of memory processes in the human brain, have been already successfully replicated using resistive switching devices [23]. The main result is a dramatic improvement in fields traditionally challenging for electronics, such as pattern recognition and fault tolerance.

1.3 Resistive Switching: Bits Made of Filaments

The focus of this dissertation will be on CBRAM and VCM [24, 25]. They have been considered for long time the only technologies that could have replaced Flash. They are still considered very promising for embedded applications (SRAM replacement), SCM and eNVM. Both types of memory store the logic bit in the form of a recoverable conductive filaments in a dielectric layer. This confers to both technologies the simplest integration scheme: two electrodes that sandwich a thin dielectric layer. The ionic movement combined to the electrochemical redox reaction inside the oxide layer, induce structural changes involving the local conductivity of the dielectric. The change in the resistance of the cell is used to store the logic bit of information [24]. To make a simplistic differentiation among CBRAM and VCM it can be said that the first class of devices is based on the migration of metal ions (cation) while the second on the generation/migration of oxygen defects (anion) [18]. The resistance switching of the metal-insulator-metal (MIM) cell is achieved by three main operations: forming, set and reset. The forming is generally considered as the breakdown of the oxide layer and initialization of a first conductive filament. After the forming the MIM structure shows a low resistive state (LRS). The reset is considered as the partial recovery of the CF previously induced, and brings back the device to a high resistive state (HRS). Finally the set restores the CF in the oxide and restores the

6 1 Introduction

LRS. These basic actions are repeated during the device operations. When forming/set/reset are done in the same voltage polarity the memory operates in unipolar mode, when forming/set and reset are done in opposite polarity the device is said to work in bipolar mode [13, 24]. In this dissertation we will focus only on bipolar devices which can be operated at lower current as compared to the unipolar.

1.4 Objectives and Outline of the Dissertation

This work is part of a global effort to understand and observe the physics of resistive switching in view of exciting new applications for memory and logic. Tuning the nonvolatile internal state of a sub-20 nm device by displacing ions in the space, can turn into a difficult task. In such conditions, the transport of ions lies at the boundary between classic physics and quantum mechanics. The whole switching mechanism takes place in a confined volumes (tens of nm³) and involves nanoscaled electrochemical redox reactions and ionic transport. The dominant transport mechanisms depend on the defect size, mean free path, metal precipitation and free energy of formation to name a few. The major challenge is represented by the intimate nature of the ions interaction with the surrounding material. In addition, the nucleation and growth of the CF are intrinsically stochastic processes. The analysis of structures different from the real integrated devices, are often not immediately representative of the reality due to the large amount of differences in the filaments formation conditions. Thus severe challenges in the observation are introduced by the ultra-confined characterization conditions. This has created a gap between physical understating and experimental device's results. The original research work reported in this dissertation is focused on the physical characterization and metrology of resistive switching. The major objectives of this thesis can be summarized as follows:

- Enable the use of electrical scanning probe microscopy (SPM) for the analysis of resistive switching at ultra-scaled dimensions without the need of a fully processed devices.
- Achieve a stable tip-induced formation and observation of conductive filaments in Cu-based CBRAM and HfO₂-based VCM.
- Generate fundamental understanding on the LRS and HRS states and their transitions.
- Development of a three-dimensional tomographic technique for the complete observation of the conductive filaments in integrated devices.
- Generate fundamental understanding of the RS in state-of-the-art integrated devices.
- Deliver understanding on common failure mechanisms and reliability threats in RS-devices by two- and three-dimensional characterization concepts.

The novelty of this work lies in the nanometer scale electrical characterization achieved with conductive atomic force microscopy (C-AFM). This is combined with a three-dimensional AFM-based tomographic technique developed for the electrical

characterization of confined volumes, thus enabling the direct observation of the CFs in 3D. Therefore the target of the work is to relate RS to the underlying nanoscopic effects. The results of this thesis are presented in six chapters.

Chapter 2 provides a review of filamentary-based resistive switching phenomena. The basic principles of CBRAM and VCM are introduced, followed by the description of the structures object of study in this work. The chapter closes with a short review on the filament observation to set the background in which our work has been performed.

Chapter 3 introduces the basics of electrical scanning probe microscopy. Atomic force microscopy (AFM) is introduced, and contact- and intermittent- electrical modes are discussed. The tip-sample interactions, the analysis conditions and the usage of diamonds tips are clarified. Based on point contact I–V curves, an original quantification technique for the electrical contact area is described. A dedicated solution based on parallel linear amplifiers, is introduced to extend the range of current sensitivity of C-AFM. In Sect. 3.3 the intermittent-mode (peak force) is described and compared to standard C-AFM. Different case studies are shown to highlight strengths and weaknesses of each approach. Finally, the chapter ends with the description of our AFM-based tomographic technique, used for tip-induced material removal and 3D observation of confined volumes.

Chapter 4 describes the formation, observation and manipulation of filaments by means of the nanosized C-AFM tip. The conductive tip is used as a movable electrode on a blanket sample. The electrical operations are matched by careful tip selection and the resistive states of CFs are investigated for each material system. By leveraging the high spatial confinement of the AFM tip, we investigate and model the reset transitions in sub-10 nm regime. Toward the end of the chapter, the basic concept of tip-induced material scraping is used to reverse engineer integrated devices and investigate different resistive states.

The original experimental work on the three-dimensional observation of filaments is reported in Chap. 5. The ON state of the Cu-based filament is observed providing insights on the CF growth dynamics. In Sect. 5.3 we unravel the dualism of abrupt and progressive reset-transitions by observing "broken" and "non-broken" filaments originated respectively from a constriction point in the current path and from an interrupted CF. The existence of both shapes is explained within one dissolution theory whether the starting point (i.e. the original size of the CF) determines the final shape. In Sect. 5.4 we report the tomographic observation of filaments in oxide VCM. High and low current operations are imaged and experimental evidences are provided for the nature of the CF as a defect modulated quantum point contact.

Chapter 6 presents the results obtained in the study of failure analysis and reliability threats of RS-devices using SPM tomography. We investigate failed devices and demonstrate the filaments multiplicity as a potential source of resistance states instability (Sect. 6.2) and unrecoverable failures (Sect. 6.3).

Finally, Chapter 7 provides a general comparison about the two material systems investigated in the dissertation and the general conclusions of the work. This is combined with the suggestions on the possible future research.

8 1 Introduction

References

 W.D. Brown, J.E. Brewer, Nonvolatile Semiconductor Memory Technology: A Comprehensive Guide to Understanding and Using NVSM Devices, 1st edition. IEEE Press, New Jersey (1997)

- 2. A. Pavlov, M. Sachdev, CMOS SRAM Circuit Design and Parametric Test in Nano-Scaled Technologies, Frontiers In Electronic Testing. (Springer, Netherlands, 2008)
- R. Micheloni, L. Crippa, A. Marelli, *Inside NAND Flash Memories*. (Springer, Heidelberg, 2010)
- ITRS consortium. International technology roadmap for semiconductors, memory report. Technical report, 2014
- D. Hisamoto, J. Kedzierski, E. Anderson, H. Takeuchi, K. Asano, T.-J. King, J. Bok, H. Chenming, A folded-channel MOSFET for deep-sub-tenth micron era. IEDM Tech. Dig. 38, 1032–1034 (1998)
- N. Chandrasekaran, Challenges in 3D Me emory Manufacturing and Process Inte egration. IEDM Tech. Dig. pp. 344–348 (2013)
- K-T. Park, Three-Dimensional 128Gb MLC Vertical NAND Flash-Memory with 24-WL Stacked Layers and 50MB/s High-Speed Programming. In proceedings of the International Solid-State Circuits Conference, 2014, p. 19.5
- 8. H.-S. Philip Wong, S. Salahuddin, Memory leads the way to better computing. Nat. Nanotechnol. **10**(3), 191–194 (2015)
- G.W. Burr, B.N. Kurdi, J.C. Scott, C.H. Lam, K. Gopalakrishnan, R.S. Shenoy, Overview of candidate device technologies for. IBM J. Res. Dev. 52(4), 449–464 (2008)
- S. Lai, Current status of the phase change memory and its future. In *Proceedings of the IEDM Tech. Dig.* 2003, pp. 255–258
- A.D. Kent, D.C. Worledge, A new spin on magnetic memories. Nat. Nanotechnol. 10(3), 187– 191 (March 2015)
- B. Govoreanu, A. Redolfi, L. Zhang, C. Adelmann, M. Popovici, S. Clima, H. Hody, V. Paraschiv, I.P. Radu, A. Franquet, J. Liu, J. Swerts, O. Richard, H. Bender, L. Altimime, M. Jurczak. Vacancy-Modulated Conductive Oxide Resistive RAM (VMCO-RRAM): An Area-Scalable Switching Current, Self-Compliant, Highly Nonlinear and Wide On/Off-Window Resistive Switching Cell, in *Proceedings of the IEDM Technical Digest* (2013), pp. 256–259
- I. Valov, R. Waser, J.R. Jameson, M.N. Kozicki. Electrochemical metallization memoriesfundamentals, applications, prospects. Nanotechnology 22(25), 254003 (2011)
- R. Waser, R. Dittmann, G. Staikov, K. Szot, Redox-Based Resistive Switching Memories -Nanoionic Mechanisms, Prospects, and Challenges. Adv. Mater. 21(25–26), 2632–2663 (2009)
- 15. M.R. Zargham. Computer Architecture: Single and Parallel Systems. (Prentice Hall, Upper Saddle River, 1996)
- G. Duarte, What Your Computer Does While You Wait. 2008. http://duartes.org/gustavo/blog/ post/what-your-computer-does-while-you-wait/
- 17. D. Evans, The Internet of Things How the Next Evolution of the Internet Is Changing Everything, Cisco IBSG 2011 (Technical Report April, Cisco, 2011)
- F. Yang, X. Ling, R. Zhang, L. Geng, L. Tong, X. Jun, S. Weining, Y. Yao, Z. Ma, K. Chen, Direct observation of phase transition of GeSbTe thin films by Atomic Force Microscope. Appl.Surf. Sci. 258(24), 9751–9755 (2012)
- S.D. Ha, S. Ramanathan, Adaptive oxide electronics: a review. J. Appl. Phys. 110(7), 071101 (2011)
- J. Borghetti, G.S. Snider, P.J. Kuekes, J.J. Yang, D.R. Stewart, R.S. Williams. 'Memristive' switches enable 'stateful' logic operations via material implication. Nature 464(7290), 873–876 (April 2010)
- Hewlett Packard laboratories. HP "The machine" (2014). http://www.hpl.hp.com/research/ systems-research/themachine/
- 22. M. Di Ventra, Y.V. Pershin, Just Add Memory. Sci. Am. **312**(2), 56–61 (2015)

References 9

23. S. Kim, C. Du, P. Sheridan, W. Ma, S. Choi, W.D. Lu, Experimental demonstration of a second-order memristor and its ability to biorealistically implement synaptic plasticity. Nano Lett. **15**(1), 2203–2211 (2015)

- R. Waser, M. Aono, Nanoionics-based resistive switching memories. Nat. Mater. 6(11), 833– 840 (2007)
- H.-S.P., Wong, H-Y. Lee, S. Yu, Yu-S. Chen, Y. Wu, P-S. Chen, B. Lee, F.T. Chen, M-J. Tsai, Metal-Oxide RRAM. Proc. IEEE 100(6), 1951–1970 (2012)

Chapter 2 Filamentary-Based Resistive Switching

2.1 Basic Operating Principles

The filamentary-based resistive switching (RS) phenomenon has been originally observed in the 1960s [1–3]. For almost 40 years it has received a limited attention, until the nanoscale realization of electronic devices based on RS has led to a considerable research interest [4]. Particularly due to the great potential for memory application, RS is nowadays at the forefront of non-charge based memory devices [5–7]. Conductive-bridge random access memory (CBRAM) and oxide-based valence change memory (VCM), prior to the introduction of 3D NAND they have been considered for long time as a possible replacements for Flash. They are still considered very promising for embedded applications (SRAM replacement), SCM and eNVM [7, 8]. Filamentary-based RS memories store the logic bit in the form of a recoverable conductive filament (CF) in a thin dielectric layer, this confers to these technologies:

- Simple metal/insulator/metal (MIM) structure.
- CMOS compatibility and cross-bar array integration.
- Small cell dimension and high scalability.
- Fast switching operation \approx sub 10 ns.
- Low power capability.
- Long endurance \approx billion of cycles.

To make a simplistic differentiation among CBRAM and VCM, it can be said that the conductive filament is induced by a metal ions (cation) migration in CBRAM, and by an oxygen (anion) migration in VCM [5, 6]. Figure 2.1a shows two electrodes that sandwich a thin dielectric layer. This can be thought as the elemental switching device, a large array of such devices can be considered for high density applications as in Fig. 2.1b. When a voltage is applied to the electrodes a structural change involving the local conductivity of the dielectric is induced. The local conductivity change is partially recoverable and allows to store a logical bit in the form of the MIM resistive state. The memory electrical switch is achieved by means of three main operations:

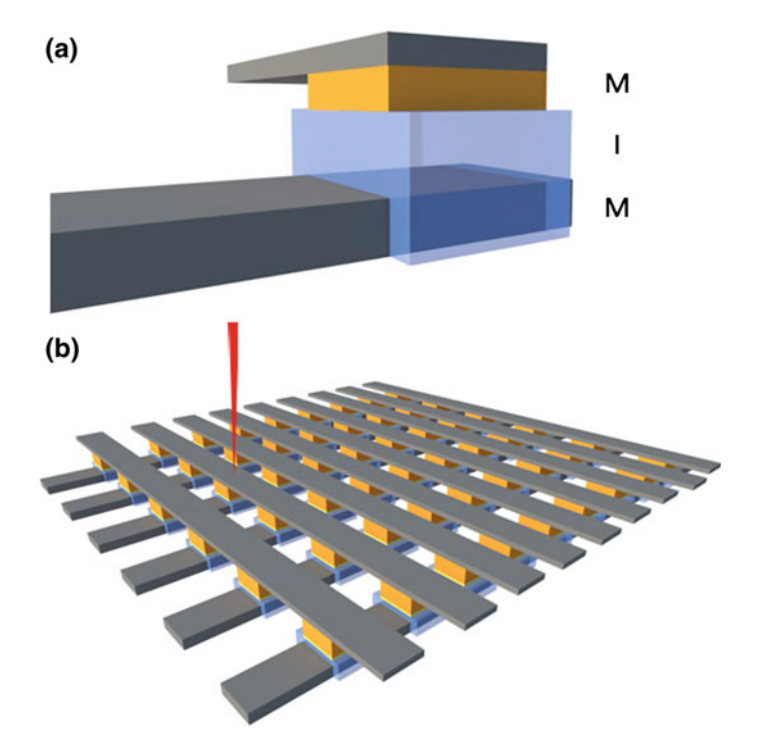


Fig. 2.1 General metal/insulator/metal device structure. **a** Illustration of the basic RS device structure. **b** The simple design and the small dimensions of the cells enable the fabrication of high density cross-bar array

forming, set and reset. The forming is generally considered as a soft breakdown of the oxide layer and the initialization of the CF. After the forming, the presence of the CF inside the MIM structure induces a low resistive state (LRS). The reset is considered as the partial recovery of the previously induced CF and brings the device again into a high resistive state (HRS). Finally the set restores the CF in the oxide and restores a LRS. During device operation a sequence of set and reset triggers the change in the resistance which is used to store the bit of information. Note, that the reset never takes back the MIM resistance to the level of the fresh device, indicating a deep structural change induced by the first programing step (forming). Proof of this is also the higher voltage required during the forming as compared to the set/reset transitions. RS can be classified based on the switching mode exhibited by the device, bipolar or unipolar as in Fig. 2.2. Bipolar switching requires opposite voltage polarities to switch ON and OFF whereas unipolar (also known as nonpolar) has no such requirement. When forming/set/reset are done in the same voltage polarity the memory operates in unipolar mode, when forming/set and reset are done in opposite polarity the device is said to work in bipolar mode (Fig. 2.2 top left). The structure of the device e.g. the asymmetry in the electrode materials, can impact the type of RS observed. It is generally accepted that the switching tends

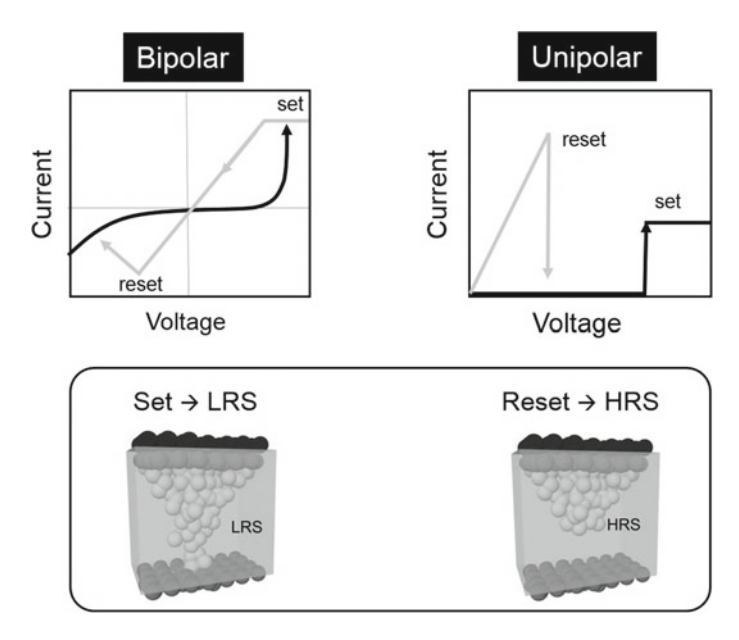


Fig. 2.2 Classification of resistive switching characteristics. Schematic representation of the bipolar and unipolar RS with the pictorial representation of the HRS and LRS filaments

to be bipolar if the electric field plays a significant role, whereas unipolar if thermal effects are dominant [6]. In case of unipolar switching the voltage used for writing is higher than that for erasing (Fig. 2.2 top right). The current required for the switching is in range of hundreds of μA to mA. For bipolar devices writing and erasing typically occur under different polarities and the switching current can be decreased to few tens of μ A. Therefore, this type of switching is more attractive for aggressive integration and low-power applications. In the rest of this dissertation only bipolar RS will be treated. An initial electroforming process is required to initiate the RS functionality. The forming process is done by applying an higher-than-usual voltage or current to a virgin device and enables the switchable state. It has to be considered as a precondition step to apply only once. A current limitation (compliance) is applied during the electrical programming to control the resistive state and avoid unrecoverable oxide breakdown. It is commonly assumed that the forming creates some nano channels in the oxide which are used during cycling as preferential paths for the CF growth and dissolution. Most of the RS devices show a cell size independence with the low resistance state (e.g. area independence with the LRS) [5]. This observation has been since the beginning considered as an experimental evidence of the presence of a single nanosized filament shorting the electrodes. The switching speed is one of the major properties of any memory device. Although is generally difficult to measure below the nanoseconds due to reflections and impedance mismatching, observation of switching time ≈ 0.1 ns has been recently reported [9]. Many other observations have confirmed the resistive switching speed in the \approx ns regime supporting that both CBRAM and VCM can rely on a fast pulsed switching operation [10–12].

2.2 Conductive Bridge Resistive Memory

CBRAM often referred as electrochemical metalization cells (ECM), programmable metalization cells (PMC) or atomic switches, bases its operation on metal cation transport for the filament formation. The memory element is based on a MIM structure, where a thin dielectric is sandwiched between an active electrode and an inert counter-electrode. Ag or Cu are commonly used as the active electrode in view of their property to inject metallic cations within the solid electrolyte. CBRAM uses a solid-state electrochemical reaction with Ag or Cu, to create or dissolve CFs. A variety of oxide, chalcogenide and sulphide thin films have been proposed for the solid electrolyte [13, 14]. The inert counter-electrode is generally made of Pt, W or TiN. When a positive voltage is applied to the active electrode, a field-assisted injection and transport of cations begins. This leads to the creation of the CF inside the switching layer. The presence of the CF lowers dramatically the resistance of the device thereby defining a LRS Fig. 2.2 (bipolar case). The CF can be dissolved by applying a negative voltage to the active electrode and thus restoring the HRS. The two different resistance states are used as the logic values "1" or "0". From here on in this work we will refer to the operation of a Cu/Al₂O₃/TiN-based cell. The latter has demonstrated good performance in combination with optimal CMOS compatibility [15, 16]. The memory element is shown in Fig. 2.3a. Amorphous Al₂O₃ (5 nm) is sandwiched between 10 nm TiN (bottom electrode) and 40 nm Cu (top electrode). The Al₂O₃ is deposited using a plasma enhanced atomic layer deposition (PE-ALD) at 45 °C, using O₂ plasma and Tri-Methyl Aluminum (TMA) precursor. Finally, the 30-nm Cu top electrode is deposited using physical vapor deposition (PVD). After deposition the sample is patterned by electron-beam lithography (e-beam). The memory cell is built on top of a 90-nm-wide TiN metal line connected to the drain of a transistor. This is a very common architecture (one-transistor-one-resistor, 1T1R) in which the selector transistor is used to limit the current that flows in the memory during the operations (Fig. 2.3b). The programming bias scheme is reported in

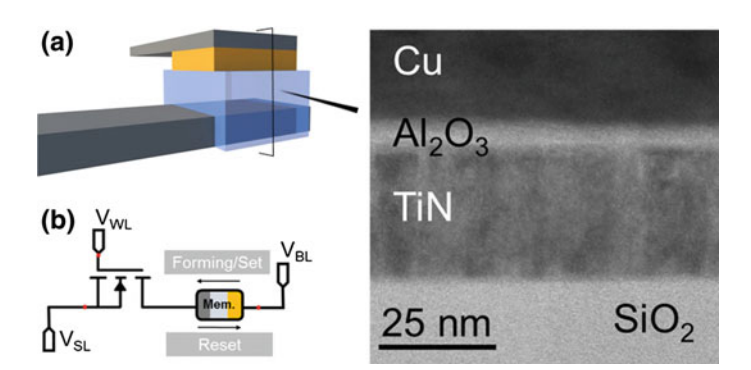


Fig. 2.3 Basic structure of conductive-bridge memory. **a** Schematic and cross-section TEM image of the Cu/Al₂O₃/TiN-based stack. **b** Switching scheme of the 1T1R structure for writing and erasing the memory cell

Fig. 2.3b, a positive bias is applied to bit line (BL) and word line (WL) with source line (SL) grounded for forming and set. While for reset, a positive bias is applied to SL and WL with BL grounded.

2.2.1 The Electrochemistry in CBRAM

Being primary based on a ultra-scaled electrochemical reaction it is important to recall the basic principles of the redox reaction at the foundation of RS in CBRAM. The device shows bipolar RS as presented in Fig. 2.2. The electrical programming (set) occurs if a sufficiently positive bias voltage is applied to the active electrode (Cu). At a microscopic level Cu undergoes anodic dissolution $Cu \rightarrow Cu^{n+} + ne^-$ at the Cu/Al_2O_3 interface, where n is the cation valence. This process is followed by the drift of the Cu^{n+} cations across the solid electrolyte. The final step is the reduction of Cu ions ($Cu^{n+} + ne^- \rightarrow Cu$) leading to CF growth. After the metallic filament has created an electronic contact between the two electrodes the cell is set in LRS. The process can be reversed by the application of sufficient high opposite polarity (Fig. 2.2). This triggers the reset of the cell (HRS) with partial dissolution of the CF. The kinetic of the electrochemistry processes impacts the overall CF growth and therefore have unparalleled importance on device performance.

Charge transfer reactions—the anodic dissolution of the Cu electrode and the cathodic reduction of the metal cation leading to the metallic filament formation, are charge transfer reactions between the Cu atoms and the electrolyte. They are often referred to as electrode reactions for their analogy with the operation of standard electrochemical cells. The charge transfer current for anodic/cathodic reactions at steady state conditions is provided by the Butler–Volmer equation [17]:

$$i = i_0 \left[\exp\left(\frac{(1-\alpha)ze}{k_B T}V\right) - \exp\left(-\frac{\alpha ze}{k_B T}V\right) \right]$$
 (2.1)

where i_0 is the exchange current; α is the charge transfer coefficient; z is the number of exchanged electrons; k_B is the Boltzmann constant; T is the temperature. Here V represents the electrochemical overpotential defined as the difference between the electrochemical potential at equilibrium and the actual electrode potential. If V >0 the first term of the equation (accounting for the oxidation reaction) dominates. Contrary, the reduction reaction prevails if V <0. In case of sufficiently high applied voltages (V $\gg k_BT/ze$) one of the terms in the equation becomes very small and can be neglected (Tafel approximation) [18]. This is the condition during device operation, and the equation becomes:

$$i = i_0 \exp\left(\frac{\alpha z e}{k_B T} V\right) \tag{2.2}$$

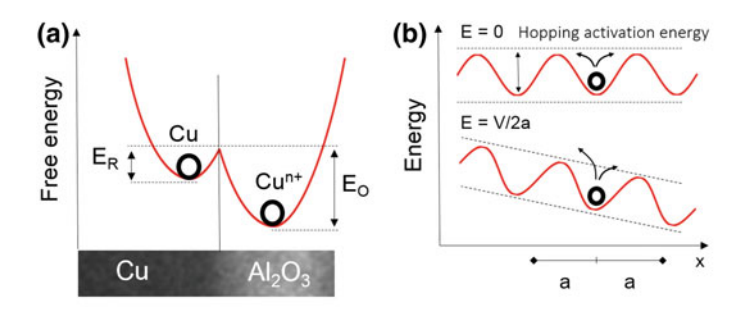


Fig. 2.4 Energy environment for charge transfer reactions. a Illustration of the energy profile of an electron transfer reaction at the Cu electrode surface and the corresponding Cu^{n+} cation inside the electrolyte. b Schematic representation of random ionic jump over a potential barrier, without external electric field applied (top figure) and with barrier lowering induced by the electric field (low figure)

Consequently, in case the reduction of Cu cations is the dominating term (V $\ll k_BT/ze$) the second exponential term in (Eq. 2.1) has to be considered. In these cases the exchange current i_0 is defined as:

$$i_0 = zeck_0 A \exp\left(-\frac{E_A}{k_B T}\right) \tag{2.3}$$

where c is the concentration of ions, k_0 is the reaction rate constant, A is the area involved in the electron transfer and E_A is the reaction energy barrier. The illustration of the energy profile of an electron charge transfer reaction at the interfaces between a Cu electrode is shown in Fig. 2.4a. Here the charge transfer between a Cu at the surface of the metal electrode and the cation in the electrolyte is represented. At equilibrium without any applied bias the activation energy for oxidation and reduction are the same at the Cu surface in contact with the Al_2O_3 . Application of a positive overpotential to the electrode induces Cu^{n+} cations diffusion toward the Cu/Al_2O_3 interface with consequent increase in Cu^{n+} cations concentration. The higher concentration increases the electrochemical potential of Cu^{n+} cations reducing the activation energy for reduction (E_R) . This process is determined by the electrochemical potential of the electrons e.g. their Fermi level in the metal. The applied electrostatic potential on the Cu electrode changes the height of the activation barrier.

Ionic transport—Assuming ionic Cu as the mobile species in the device, the ionic transport represents the drift of Cu cations through the solid electrolyte. This process is described as an ionic hopping from site to site over an energy barrier. The average distance between two sites is called hopping distance (a) and is estimated in the order of 0.2–0.5 nm [13]. At the equilibrium, thermal fluctuation and concentration gradient are the only driving forces for a net motion of ions in the solid electrolyte. The presence of the applied bias across the cell electrodes (V) induces an electric field E of strength E = V/d where d is the oxide thickness. Under these conditions

the Cu cations experience an electric field driven, thermally activated ion hopping. The corresponding current density can be calculated using the Mott–Gurney equation for ion hopping [19]:

$$i = 2zecavexp\left(-\frac{\Delta E_{hop,0}}{k_B T}\right) \sinh\left(\frac{azeE}{2k_B T}\right)$$
 (2.4)

where a is the mean ion hopping distance, ν is an attempt frequency factor, $\Delta E_{hop,0}$ is activation energy for the ion hopping in absence of the electric field. In other words the net motion of the ions becomes directional. According to this model the transport of ions is described by a series of thermally activated jumps between adjacent sites. The presence of the electric field lowers the activation energy for ion hopping enhancing the hopping rate in the direction of the field. For low electric fields $E \ll 2k_BT/aze$ the ion transport has a linear dependence with the electric field. For high electric fields $E \gg 2k_BT/aze$ the equation presents an exponential dependence on the field. A schematic of the random jump made by an ion overcoming a potential barrier $\Delta E_{hop,0}$ as shown with and without externally applied electric field (respectively low and high figure). The electric field lowers the potential barrier $\Delta E_{hop} = \Delta E_{hop,0} - \alpha qV$ where α is a barrier lowering coefficient.

Electrocrystallization—is defined as the process of nucleation of the Cu crystal on the inert electrode side prior to the CF growth. A stable nucleus is related to a critical number of atoms and consequently a critical size. The nucleation time is defined as the required time to form a stable nucleus and is related to the applied voltage by an exponential law [20].

$$t_n = t_o \exp\left[\frac{(N_c + \alpha)zeV}{k_B T}\right]$$
 (2.5)

where t_n is the nucleation time, t_0 is a prefactor depending on the density of the nucleation sites and ionic concentration, N_c is the number of atoms required for the critical nucleus and α is a charge transfer coefficient relating the fraction of voltage that is involved in the reaction. After nucleation a metal phase can grow. This is described by a growth rate directly proportional to the ionic current.

2.2.2 The Rate-Limiting Process

All the different electrochemical processes governing the CBRAM operations are contributing to the resistive switching e.g. CF formation/rupture. However, the slowest one will limit the switching kinetics and it is generally referred to as the rate-limiting step in the filament formation. Although the different physical nature of each process, the identification of the rate-limiting step is not simple. This has been treated by Menzel et al. [21] in the analysis of strongly non-linear switching kinetics. Independently from being field-induced or thermally activated, all the involved

processes are following an Arrhenius-law dependence so they will all be exponentially enhanced by a temperature increase. For example, due the high current densities in the CF, Joule heating increases the temperature inside the cell. Furthermore, the relative importance of each mechanism will not only depend on the material selected but also on the operating temperature [22, 23]. In real operating conditions moisture, surface roughness and residual OH⁻ groups acting as counter charges, complicate the interpretation [24]. Different solid electrolytes generally showing long-range disorder and good ionic conductivity, have shown a CF filament growth kinetics limited by charge transfer in accordance to Butler-Volmer equation [25]. However due to short transport paths for Cu cations, in low mobility switching layers (e.g. amorphous oxides) the charge transfer reactions are not considered as rate-limiting step in the CF formation. It is generally assumed that the metal dissolution (oxidation) is not the rate-limiting step due to the high electric fields ensuring sufficient decrease on the energy barrier maximum [13]. Few hundreds of mV are sufficient to initiate Cu-based electrochemical reaction. If electrochemical reactions are the rate-limiting processes it should be observed a non-linear dependence of the forming voltage with the oxide thickness, which is contradictory to the experimental observation. This indicates a complex ionic interaction with the solid electrolyte and the primary role of the electric field during switching. However any of the described processes, can be a potential rate-limiting step for the CF formation. A different selection of dielectrics, for instance, has shown to impact the switching time, E field required for CF formation and also the CF growth direction [26]. It has been demonstrated that cathodic charge-transfer reaction is the rate-limiting step in systems with high ionic mobility. While ionic diffusion can be responsible for the CF growth in poor ionic conductors or in general, for all the solid electrolytes that do not intrinsically contain metal cations. Due to the high number of factors contributing to the CF growth, a dedicated description and characterization of the material system of interest is required. It is worth noting that the results of this thesis are applicable to the class of CBRAM devices based on solid electrolytes such as thermally grown or ALD-deposited high-κ dielectrics (e.g. Al₂O₃, Ta₂O₅ to name a few). Here referred as solid electrolytes because they are used to transport ions. Other solid electrolytes such as ionic conductors or chalcogenides (Ag₂S or GeSe₂) are not covered by the experimental work of this dissertation.

2.2.3 CBRAM Device Operation

A complete switching cycle for our CBRAM stack is reported in Fig. 2.5a. The memory cell is operated by a quasi-static (DC) voltage sweep. The as-deposited device shows high resistance and requires an initial electroforming to activate the cell (step 1 Fig. 2.5a). After electroforming, the formation and rupture of the CF can be triggered respectively by means of a positive or negative voltage applied on the Cu electrode. The Cu electrode is negatively biased for the filament rupture (RESET step 2 Fig. 2.5a), and positively biased for the filament formation (SET step 3 Fig. 2.5a).

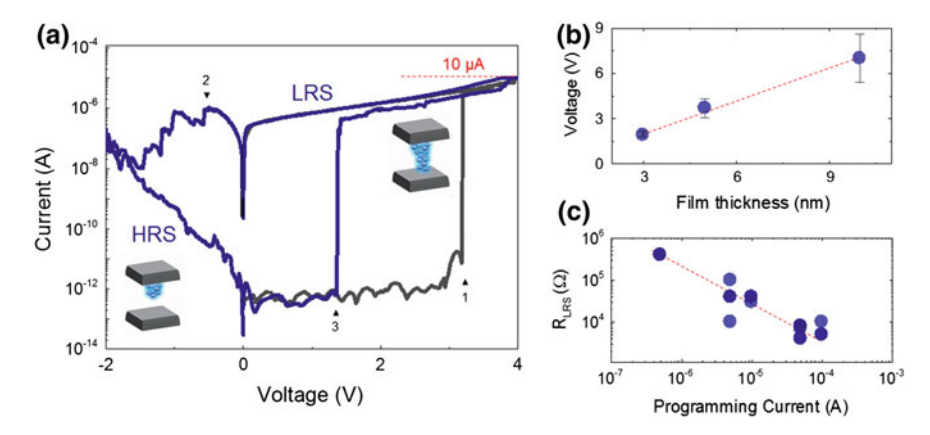


Fig. 2.5 *CBRAM device operation* a Current–voltage characteristic of CBRAM, forming reset and set are shown for a Cu/Al₂O₃/TiN cell. **b** Forming voltage dependence with oxide thickness. **c** LRS resistance modulation as function of programming current

In Fig. 2.5a the forming voltage is about $\approx 3.5 \,\mathrm{V}$ and the set and reset voltages are respectively ≈ 1.5 and -2 V. During forming and set operations the control transistor (Fig. 2.3b) delivers a current compliance of 10 μ A. As commonly reported also this device presents a linear dependence of the forming voltage (Fig. 2.5b) with the oxide thickness, whereas the set voltage is practically thickness independent (not shown). This is considered an evidence of the fact that after the first CF is formed, in the subsequent cycles the CF does not completely dissolve. In addition even after the CF reset, the HRS never reaches the pristine oxide resistive state thus indicating a permanent local modification of the solid electrolyte. Figure 2.5c shows how the CF resistance can be modulated using the current compliance (I_{cc}) during cycling e.g. larger I_{cc} leads to lower R_{LRS} . This among other properties make CBRAM extremely attractive for high density nonvolatile storage applications due to the possibility to implement multibit capability. The basic idea is to program the cell with different current compliances in order to induce multiple (distinguishable) resistive states. Note, that this analog-like resistance modulation common to most of the filamentary RS devices, is very attractive when trying to replicate artificial synapsis functioning in neuromorphic applications [27, 28]. Retaining data for long time is the ultimate goal of a nonvolatile memory. The (resistance) state stability or data retention is an important figure for filamentary-based memories. The data retention is the amount of time that a CF can maintain its resistance state without degradation i.e. inducing data loss. The target value for the retention is generally application specific, as example most of the nonvolatile consumer storage applications require 10 years retention at 85 °C but in the automotive sector the target is 10 years retention at 125 °C. In essence the CF has to maintain its resistance state for at least 10 years unaltered. Eventually this has to be guaranteed also in presence of disturbs. For example a temperature increase due to environmental conditions or a voltage stress on chip induced by the circuit-periphery. In Fig. 2.6a a retention test is shown for both HRS and LRS.

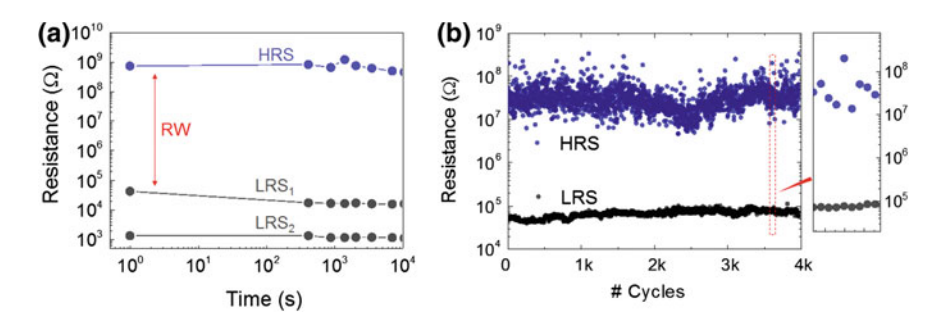


Fig. 2.6 CBRAM retention and endurance. a LRS and HRS show stable resistance retention for $10^4\,\mathrm{s}$ at $85\,^\circ\mathrm{C}$. A resistive window of $\approx 10^4\,\mathrm{is}$ visible. b Endurance test over few thousands of cycles is shown for our Cu/Al₂O₃/TiN cell. Note in the *inset*, the resistance fluctuations between consecutive cycles

The distance between the LRS and HRS resistances define another important figure of merit, namely the resistive window (RW). The RW represents indirectly how easily the coded "1" or "0" will be electronically interpreted. The ratio between the average OFF and ON states (R_{OFF}/R_{ON}) represents a number (in Fig. 2.6a $\sim 10^4$), which accounts for the orders of magnitude of electrical resistance separating the two or more bits. As a general rule, the higher the RW value the better the memory device, particularly for the potential multibit capability. In our example (Fig. 2.6a) by changing the current compliance two distinctive LRS can be induced 5 µA for LRS₁ and 50 µ A for LRS₂. During the test the sample is also baked, here at 85 °C in order to accelerate the degradation processes. Stable retention up to $\sim 10^4$ s is demonstrated for all the resistive states. By means of the baking test projected retention, for instance at 10 years can be extracted. In general both LRS and HRS can suffer from retention failures leading to drifts the resistive states through time. A certain tolerance on the resistance state degradation can be allowed in case of a resistive window wide enough to maintain two detectable "1" and "0" levels. Clearly the criteria becomes more stringent in case of multiple bits implementation, where each resistive states represent a different multibit combination. Also for the retention the programming current used during cycling has a major impact. Programming current below ($\approx 1 \,\mu\text{A}$) leads to weak CFs generally showing failure in the LRS retention while programming current over (\approx 100 μ A) induces strong CFs often impossible to reset.

As the memory device has to be cycled (i.e. reprogrammed) and show long and reliable operation, another important figure of merit is introduced in Fig. 2.6b, the *endurance*. The resistive values assumed by the device (CF) throughout continuous ON and OFF conditioning are shown. The device is first programmed and then read out. The read out is done after each cycle and plotted against number of cycles. A small voltage compared to that required for set/reset is used for the read-out (0.1 V). This avoids any perturbation on the resistance states during the read. The device presented in Fig. 2.6b shows \approx 4000 continuous cycles with a resistive window \sim 10 3 . It has to be noted that CBRAM is among RS devices the one that presents the larger

RW, up to 10⁸ has been demonstrated [13]. Regarding our device in Fig. 2.6a RW $>10^5$ can be achieved between HRS and LRS₂. Notably, in Fig. 2.6b the resistance of the LRS presents almost a constant value throughout cycling, while the HRS shows more fluctuations, as clearly visible in the inset. The latter indicates a smaller scattering in the resistance states assumed by the CF in the LRS which is generally following an Ohmic behavior (i.e. metallic conduction), and conversely wider dispersion for the HRS generally showing more complex conduction mechanisms. This will be treated in Chap. 5, where a detailed analysis of the HRS state and its manifold nature will be related to the CF structure. For memory storage applications, it is important to limit degradation mechanisms of the CF to avoid retention and endurance failures. Uncontrolled structural changes in the CF, such as those thermally activated or induced by concentration gradient, are undesired sources of instability for the resistance states. Thus impacting the overall reliability assessment of the filamentary-based RS devices. Such structural changes of the CF will be introduced in the Chap. 6, with the experimental observations of the degenerated Cu filament and of the filaments multiplicity as sources of resistance state variability.

2.2.4 Device Optimization

Though the Cu/Al₂O₃/TiN stack of the previous section shows attractive characteristics, such as: large R_{OFF}/R_{ON} resistance ratio, long data retention (10^4 s), high endurance, nanoseconds switching speed, small operation voltages (\approx 2 V) and multilevel capability [10, 16, 29]. This test vehicle is especially optimized for the characterization of the CF (i.e. 3D filament observation) of the following chapters. In reality, extensive engineering of the basic CBRAM stack has led to enhanced device performance (especially aiming at commercial applications). Now that the reader is familiar with the basic principles and figure of merits for CBRAMs, in this section a short overview of the state-of-the-art technologies aimed to the optimization of the memory cell is provided.

Cation supplier layer: though the metal cations are the foundation of the CF, the layer that supplies those ions does not have to be purely Cu or Ag. The active electrode has been often modified by introducing Ag- or Cu-based alloys [13]. Their fabrication is achieved by using sputtering, physical vapor deposition (PVD) techniques or chemical vapor deposition (CVD). For example, Cu has been alloyed with Te in a combinatorial co-sputtering approach [30, 31]. The impact of Cu and Te composition on the RS has been investigated and an optimal composition of $Cu_x Te_{1-x}$ in range 0.5 < x < 0.7 has shown improved control over CF formation [32]. Furthermore the CuTe layer has been also stabilized by the insertion of carbon which mitigate the impact of phase transformation shown by pure CuTe during thermal stress [31]. Binary alloying of Ag and Te has been also studied, showing improved switching properties for the use of Ag_2Te [33]. Alternatives for the active electrode may also comprise CuAg, AgTi, CuGe, CuGeTe, AgGe and others, getting to a discrete level

of complexity like Cu-doped $\text{TaW}_x \text{Si}_y \text{B}_z$ or $\text{TaW}_x \text{Si}_y \text{C}_z$ [34]. For most of these cases the alloying element may improve the thermal stability, interface quality, surface roughness, material homogeneity, tailor the work function of the active electrode or limit the injection of cations into the solid electrolyte. In some cases the alloying element is used also to influence the type of RS induced. As example, the introduction of a semiconductor as alloying element can reflect on new properties of the CF [35]. This is achieved by changing the Fermi wavelength of the CF material by semiconductors doping. Jameson et al. [36] demonstrated improved stability of the CF and enabled the usage of LRS resistances showing lower conductance as compared to the pure metallic case. One clear advantage of this approach is the reduced operative power on large arrays without compromise in CF stability.

Barrier layer: this is a common element to most of the high performance CBRAM devices. A thin layer (either metallic or insulating) is deposited between the solid electrolyte and the active electrode. This layer can promote adhesion between the layers but also provide a barrier for undesired ionic diffusion during device fabrication. Standard diffusion barriers available in the semiconductor industry have been proposed i.e. TaN, TiN, WN, Ru and others. In some cases the barrier layer has to react during a thermal annealing in order to intermix with the active electrode creating a concentration gradient for the metal cations in proximity of the solid electrolyte [37]. With the final result of having already some metal cations inside the solid electrolyte before forming.

Solid electrolyte: this layer is responsible for the ionic conduction and ultimately for most of the CF properties. Due to its great importance it has been subject to extensive studies in CBRAM optimization. A complete list of all the possible solutions is out of the scope of this dissertation and more information can be found in literature [13, 14]. Ionic conductors such as sulphides (Cu₂S, Cu-doped GeS₂ or $Zn_xCd_{1-x}S$), selenides (Cu-doped GeSe), chalcogenides (GeSbTe) and iodides (AgI, RbAg₄I₅) have been the first proposed solid electrolytes due to their known properties as ionic conductor and relatively possible CMOS manufacturability [38, 39]. But in the quest for improved performance and high CMOS compatibility insulating oxides and nitrides have been closely investigated. The list cannot be complete but the main ones are: SiO₂, Al₂O₃, Ta₂O₅, WO₃, ZrO₂, SrTiO₃, TiO₂, Si₃N₄ [10, 40-42]. Due to their large availability in standard CMOS process and to their good retention and endurance properties, oxides have rapidly received the attention particularly for nonvolatile memory applications. Due to the large set of oxide parameters which can be tuned during their deposition (e.g. quality, density, crystallinity, thickness and morphology) the deposition process becomes centric for the final device performance. A typical example is SiO₂ which can have completely different local microstructure depending on the deposition technique. Sputtered SiO₂ has a granular structure rich of defects and voids, while atomic layer deposited (ALD) or evaporated SiO₂ shows higher density and suppressed defectivity. This leads to a dramatic difference for the ionic mobility (higher in sputtered SiO₂) in the same material system as function of the deposition technique [43]. Recently also amorphous silicon (a-Si) is gaining increased attention as solid electrolyte [44, 45]. Contrary to crystalline Si, a-Si has

no long-range order in its atomic structure. It is rich of defects such as dangling bonds but their presence can be engineered by hydrogen passivation. This combined to the crystalline structure confer a simple way to control the ionic mobility in the layer to be exploited in the CF formation [25].

Inert electrode: the choice for the inert counter electrode, follows few simple guidelines. The material has to be stable, inert and do not electrochemically dissolve into the solid electrolyte. It has to provide minimal roughness, good adhesion and CMOS compatibility. W, Ru, TiW and TiN are all viable solutions because they all fulfil the requirements and are commonly used for metallization in microelectronics [46].

Architectures: when the optimal device structure is achieved a large number of cells have to be integrated and this requires the right integration architecture. The maximum storage density can be achieved using a crossbar array (Fig. 2.1b). This is generally referred as a 4F² integration, where F stands for minimum feature size e.g. the width of the electrode lines. 4F² represents the chip area occupied by a single memory element. Each cross-point device is formed at the intersection of the top and bottom electrodes, those are placed perpendicular to each other and sandwich the solid electrolyte. Though this configuration represents many advantages, the practical implementation requires an additional device to select the proper cell and to prevent parasitic access due to sneak paths [47]. In essence, when accessing a cell into a dense cross-point array, the resistance state of the neighboring devices can alter the read value due to sneak current from undesignated cells. A simple trade off is provided by the 1T1R configuration (Fig. 2.3b) requiring more chip area due to the integration of the transistor but enabling an easy way to suppress sneak paths and limiting the current during operation. Another solution is a rectifying device such a diode, to place in series of the memory element. Compared to the 1T1R configuration, this approach is more attractive since it reduces the required chip area. The rectifying diode should have a high on/off current ratio, high forward current density and low processing temperature. Oxide p-n diode, Zener-type and Schottky-type diodes have been studied [48–50]. IBM has demonstrated the integration of 512 kbit memory array using a mixed ionic-electronic conductors (MIEC) showing very high on/off current [51], Zhang et al. demonstrated using amorphous-Si a bidirectional selector exceeding 1 MA/cm² of drive current and high non-linearity [52]. Finally a more complex solution is provided by the redesign of original DRAM architectures. For example using a standard DRAM array technology a 6F² CBRAM array has been proposed where a modified buried recessed access device (BRAD) is used for accessing the devices [53]. Here two cells share the bottom electrode to increase density. By exploiting a combination of all the aforementioned solutions Zahurak et al. [53] introduces a 16 Gb Cu-based CBRAM array integrated in 27 nm technology. The latter shows 900 MB/s read speed and 180 MB/s for write. Jo and co-workers presented a functional 4Mb passive crossbar array based on a-Si as solid electrolyte [54]. Belmonte et al. demonstrated more than 10⁶ switching cycles using 10 ns pulses in integrated 90 nm W/Al₂O₃/TiW/Cu 1T1R cells [10]. Park et al. demonstrated the feasibility of multibit-bit operation at very low current ($<2\mu A$) [55]. Aratani et al. [56] presented four-level operation for a 20-nm scaled device structure with 10^7 cycles endurance. Finally, Jameson et al. [36] presented a 1 Mb array structure integrated in 1T1R showing 10 ns fast pulse operation with 1000 hours retention at 200 °C.

2.3 Oxide-Based Valence Change Memory

Valence change memory (VCM) is based on a redox process involving anion migration (opposite to CBRAM). In the majority of oxides such as transition metal oxides (TMO) for instance, the oxygen ions are considered more mobile than the metal species [57]. The local motion of these defects induces a local valence change of the cations triggering a resistance switching [5, 58]. For this reason oxide-based VCM are also referred as oxide resistive random access memory (ox-RRAM). Due to the large variety of defects present in dielectrics and their capability to alter the electrical properties in response of their motion, RS is observed in a long list of oxides, including large bandgap dielectrics (SiO₂), most of the existing TMOs (HfO₂, WO₃, TiO₂, Ta₂O₅, ZnO₂), rare-earths oxides (CeO₂) and perovskites (SrTiO₃, SrZnO₃) [6, 58, 59]. However for memory applications this list rapidly reduces to those oxides that show good switching performance and CMOS compatibility. Recently, material-systems as Ta₂O_{5-x}/TaO_{2-x} and HfO₂/Hf experienced an increasing scientific interest in view of their performance and CMOS compatibility [11, 60]. As these structures suggest, a dual layer approach appears privileged to achieve controllable RS. As will be explained next, this is used to engineer the defects profile in the oxide and increase the control of the RS. In this dissertation we will refer to the operation of a Hf/HfO₂/TiN-based VCM cell Fig. 2.7 for two main reasons. First HfO₂ is currently employed as high- κ gate dielectric in transistors and as such it is a well-known, available and fully CMOS-compatible material [61]. Second, as will

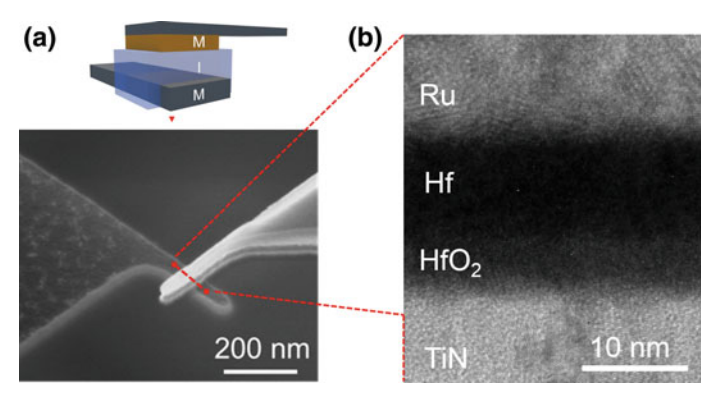


Fig. 2.7 Oxide-based VCM. **a** Schematic of the MIM structure for VCM and scanning electron microscopy (SEM) image of the 50×50 nm integrated cross-point device. **b** Transmission electron microscopy (TEM) image of the stack in the cross-point

be shown, defect-rich HfO₂ shows superior RS characteristics showing high speed (<10 ns) good resistive window (\approx 10²) and long endurance (>10⁶ cycles). The memory element is based on a 5-nm-thick amorphous HfO₂ sandwiched between metallic Hf and TiN. 30-nm-thick TiN is deposited by PVD as bottom electrode. The HfO₂ is deposited by means of ALD at 300 °C, using HfCl₄ as precursor and H₂O as oxidant. Finally 10-nm thick metallic Hf is deposited by PVD followed by 30 nm Ru to form the top-electrode. The TiN/HfO₂/Hf/Ru-structure (TEM in Fig. 2.7b) is patterned by dry etching to create the cross-point cell shown in Fig. 2.7a. The metallic Hf acts as an oxygen scavenging layer. The affinity of the metallic Hf with oxygen atoms partially extracts some oxygen from the stoichiometric HfO₂ layer. More details on the role of Hf thickness, thermal budget and composition can be found in dedicated studies on the subject [62]. In essence by tuning the composition and thickness of the metallic Hf it is possible to induce a gradient in the profile of oxygen vacancies at the Hf/HfO₂ interface. The latter is crucial for stable RS operation since it introduces a defects reservoir which is used to stabilize the CF during cycling. Also in this case the TiN bottom-electrode is directly connected to the drain of a selector transistor to form a 1T1R structure (Fig. 2.3b). This device shows bipolar RS behavior and has demonstrated remarkable performance [11, 63]. In common with CBRAM, the CF is created during the electroforming process, when the pristine cell is activated. Subsequent set and reset switching can be respectively triggered by means of positive and negative voltage applied to the Hf electrode.

2.3.1 VCM Device Operation

Device functionality of VCM has been reported for 10×10 nm device [11], and in this dissertation we investigate $50 \times 50 \text{ nm}^2$ cells. The electrical operation of VCM is presented in Fig. 2.8. The pristine device shows high resistance and requires the initial electroforming (step 1 Fig. 2.8a) to be activated. Once formed, the device can be cycled using negative and positive polarities on the Hf electrode for the reset and set respectively (step 2,3 Fig. 2.8a). During all the phases the selector transistor limits the current in our Hf/HfO₂-based at 50 µA. The forming voltage as shown in Fig. 2.8a is \approx 2.5 V, and the set and reset are triggered with ± 1 V. It can be noticed immediately that the level of resistance achieved after reset (HRS) is order of magnitudes far from the pristine cell values. This is a direct evidence of the presence of the CF in the HRS as a poorly conductive although highly defective region in the oxide. The relatively high conductive HRS leads to a narrowing in the resistive window in VCM as compared to CBRAM. Bipolar oxide VCM generally shows RW values ≈10. The linear dependence of the forming voltage with the oxide thickness is observed in VCM similarly to the CBRAM case (not shown). Once the oxide thickness (5 nm) is fixed, the forming voltage shows a weak dependence with the cell size until an increase appears in the 100 nm² size range. Figure 2.8c shows the observed independence of the R_{LRS} and the device size at fixed programming current (50 µ A). As for CBRAM, this indicates that a CF substantially smaller than

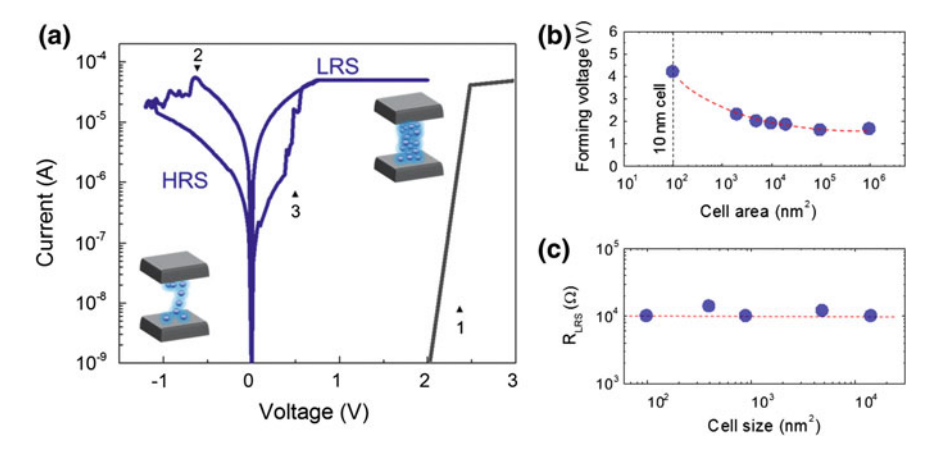


Fig. 2.8 VCM device operation. a Current voltage I–V characteristic of VCM, forming reset and set are shown for our Hf/HfO₂/TiN-based cell operated at $50\,\mu$ A. b Forming voltage as function of cell area. c Dependency of cell-size versus induced R_{LRS}

 $10 \times 10 \,\mathrm{nm^2}$ (in this case) is present. Though this effect is generally accepted for large cell-sizes its validation for a $100 \,\mathrm{nm^2}$ cell indicates that the CF lateral dimensions are smaller than 10 nm. In other words, the CF lateral growth is not limited by the physical device area even at $100 \,\mathrm{nm^2}$. The latter will be treated more in depth in the end of Chap. 5.

The data retention of VCM is reported in Fig. 2.9a, both LRS and HRS stably retain the resistance state for 10^5 s. During the test the sample is baked at $200\,^{\circ}$ C to accelerate the degradation processes. Compared to CBRAM, we observe an improved retention for VCM due to the reduced mobility of the defects constituting the CF (i.e. more stable CFs) [64]. The resistive window is ≈ 10 in case of VCM, which limits the multi-level bit applications for this technology. Finally, in Fig. 2.9b an endurance

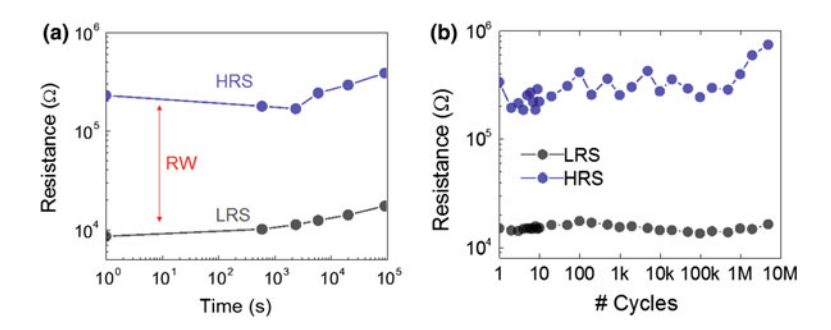


Fig. 2.9 VCM retention and endurance. a LRS and HRS show stable resistance retention for 10^5 s at $200\,^{\circ}$ C. A resistive window of ≈ 10 is visible. b Endurance test (median over a population of 18 cells), more then one million of cycles are shown. Set and reset are induced by $100\,\mathrm{ns}$ pulses as described elsewhere [63]

test of our Hf/HfO₂-based cell at $50\,\mu A$ is reported (median of 18 cells). More than one million cycles are induced and a RW ($\approx 10^2$) is clearly observable. In common with the CBRAM case, the LRS shows limited fluctuation compared to the HRS case. The latter can be ascribed to the stochastic nature of the switching transition, suggesting a metastable energetic configuration for the HRS state.

2.3.2 Switching Mechanism and Electron Transport in VCM

The switching mechanism in VCM is generally interpreted as a reversible (soft) dielectric breakdown of an oxide, associated with the generation and migration of oxygen vacancies (V_{ij} in the notation of Kröger and Vink) [65] through a field-assisted thermally activated hopping. On a pristine device, the high electric field during forming (>10 MV/cm) generates defects in the bulk of the oxide. When subjected to high enough energy, oxygen atoms start to leave their lattice position and drift towards the anode leaving behind a locally conductive path (Fig. 2.10). The filament growth is similar to the growth of a virtual cathode, due to the progressive extension of the reduced valence change in the filament location. Though the observable electrical characteristic of VCM is similar to the one of CBRAM the intimate physical mechanism is complementary. In one case (CBRAM), a foreign species (metal cations) is introduced into a solid electrolyte to short the two electrodes. In the other case (VCM) an intrinsic type of defect (oxygen vacancies) is generated in the oxide layer in order to short the electrodes by a conductive path (metallic-rich phase). At reset the oxygen ions migrate back and partially recombine with the V_a switching the memory in a HRS. The moving oxygen ions (for instance during forming and set) can easily get discharged $(O_o^x - 2e^- \rightarrow V_o^+ + \frac{1}{2}O_2)$ and become neutral oxygen when getting to

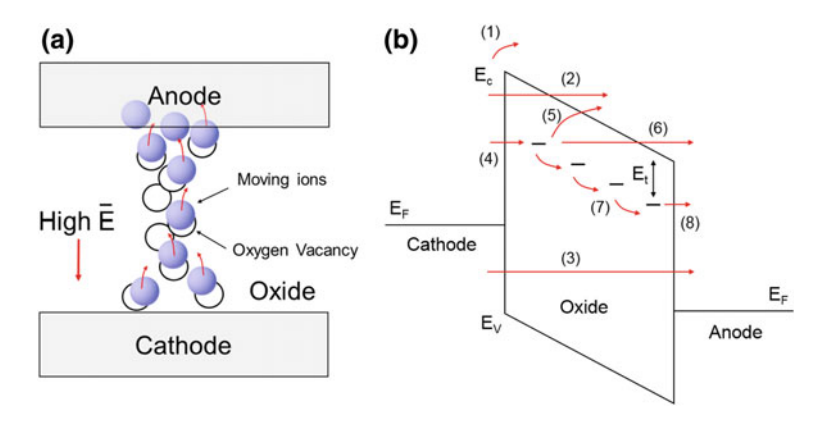


Fig. 2.10 Filament formation and electrons transport in VCM. **a** Schematic of the CF formation due to the electric-field-induced ionic motion. **b** Schematic of the possible electron transport processes in oxides [panel adapted from Yu et al. [67]]

the anode contact. The released neutral oxygen will start to accumulate at the anode interface. When this happens, the anode material can react getting oxidized in case of reactivity with oxygen, or if inert to oxygen it blocks the oxygen until the moment when the high pressure induces a small outbreak of the top electrode as often reported [66]. Obviously, this is not desirable and therefore the usage of bilayer structures such as HfO₂/Hf, where the sub-stoichiometric region behaves like an oxygen reservoir. This provides a controlled oxygen migration, limited neutral oxygen formation and thus improved device lifetime and stability.

The electric-field-induced ionic motion determines RS in VCM as schematically illustrated in Fig. 2.10a. Although the electrochemistry is at the foundation of RS also for VCM, the electrical conduction in the CF will be determined by the transport of electrons in a defect-rich oxide. Therefore the different transport phenomena involved in this type of conduction are central for the physical understanding of oxide RS [67]. For this reason their principles are briefly recalled in Fig. 2.10b as (1) Shottky emission which is a thermally activated injection of electrons through the barrier in the conduction band. (2) Fowler-Nordheim tunneling (FNT) where electrons tunnel from the cathode into the conduction band when subject to high electric field. (3) Direct tunneling (DT) in which case the electrons tunnel from cathode to anode directly in presence of a very thin oxide layer. In presence of traps in the oxide the mechanisms can intermix and we have possibility of (4) trapping of carriers into an oxide trap. (5) emission from a oxide trap to the conduction band (Poole-Frenkel emission); (6) tunneling from trap to conduction band. (7) Trap assisted hopping or tunneling and (8) tunneling from traps to anode. In Fig. 2.10b E_F is the Fermi energy level, E_V , E_C are the valence band and conduction band energy levels respectively and E_t is the trap barrier height.

2.3.3 The Filament as a Quantum Point Contact

The long list of mechanisms cooperating in the electron transport in the CF (Fig. 2.10b), contributes to increase the complexity of modeling the conduction in VCM. However, it has been soon recognized that RS in VCM has many similarities with bias-induced dielectric degradation which is generally described by percolation theory [68]. Indeed most of the stress-induced leakage measured in high- κ dielectrics for instance, can be attributed among other defects to oxygen vacancies [61]. For this reason, an analytical model based on conduction through a quantum point contact (QPC) [69] originally applied by Miranda et al. [70] for the oxide post-breakdown conduction was adapted to model the CF in VCM. For completeness, Terabe et al. [71] followed by other groups, observed conductance quantization also in CBRAM and applied a QPC description too.

The QPC model of the CF, uses the Landauer–Büttiker formalism treating the transport as a transmission problem for electrons at the Fermi level. The top and bottom electrodes of the RS device are modeled as current injecting and collecting reservoirs, in which all inelastic scattering takes place exclusively. The filament is

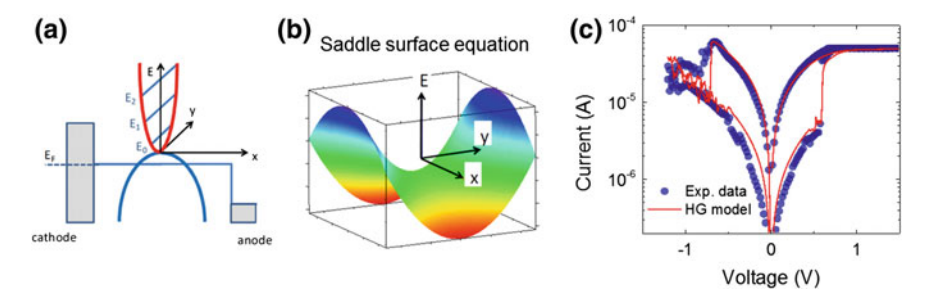


Fig. 2.11 Hour glass model and quantum point contact description of the CF. **a** The filament is described as 1D parabolic potential well with an addition potential barrier along the filament defining a saddle surface (**b**) in the x, y, E-space. The quantized energy levels E_n in the transverse direction depend on ω_y and V_0 only. The transmission probability is the sum of all transmission probabilities through all transverse channels and depends on ω_x . The total current is obtained by integrating the transmission probability over the voltage drop across the electrodes (i.e. V_{ox}). (**c**) Fitting of the experimental I–V is reported using our hour glass model. Experimental data find good agreement modeling the constriction with ≈ 100 particle for the LRS and ≈ 25 particles for the HRS [**a**, **b** reproduced from [73]]

described as a 1D parabolic potential well with an additional parabolic potential barrier along the filament as in Fig. 2.11a. The two potential barriers describe in the x, y, E-space a saddle surface as in Fig. 2.11b. The equation of the saddle surface is represented by:

$$E(x, y) = eV_0 - \frac{1}{2}m\omega_x^2 x^2 + \frac{1}{2}m\omega_y^2 y^2$$
 (2.6)

In which, V_0 relates the position of the Fermi level inside the constriction, ω_y defines the constriction width and the quantized energy levels E_n available for conduction, while ω_x determines the length of the tunnel barrier inside the constriction.

Using the Landauer formula [72] to relate the conductance to the transmission probability, the current inside the filament is obtained by integrating the transmission probability at each E_n over the available electron energy range.

$$T(E) = \sum_{n=0}^{N} \{1 + \exp[-2\pi(E - E_n)/\hbar w_x]\}^{-1}$$
 (2.7)

$$I = \frac{2e}{h} \int_{-qV_{ox}/2}^{qV_{ox}/2} T(E) \, dE$$
 (2.8)

The model is able to account quantitatively for the dynamic switching events (oxygen vacancies migration) as well as for resistance changes and their statistical distribution [73, 74]. The CF is treated as a single sub-stoichiometric HfO_x region where faster ion drift-diffusion occurs. In a first approximation we consider that ion diffusion takes place only inside the filament. The filament is in essence a container of V_a ,

where except during its forming, no generation or annihilation of vacancies can happen. In other words, the initial electroforming imposes the structure to the CF and the successive transitions between LRS and HRS are determined by changes in the number of V_a in the constriction. This model is often called hour-glass due to the pictorial representation of the CF as an atomic-scale constriction connecting two electrons reservoirs. The geometry of the constriction (width and length) is determined by the number of oxygen vacancies contained. From the saddle surface equation, two parameters define the shape of the constriction ω_x and ω_y their inverse provides the constriction's length and width respectively. Assuming a symmetric and abrupt potential drop at both electrodes as schematically drawn in (Fig. 2.11a), the quantized energy levels E_n in the transverse direction depend on ω_v and V_0 only. The transmission probability is the sum of all transmission probabilities through all transverse channels and depends on ω_r . The total current is obtained by integrating the transmission probability over V_{ox} . The modulation of the number of vacancies (ω_r) leads to different current values which are calculated by the model. In other words, wider constrictions corresponds to LRS states while narrow represents HRS. It is worth noting that once fixed a size for the volume of interaction of the oxygen vacancy the number of defects contained in the CF can be quantified starting from the I-V characteristic. In Fig. 2.11c the good agreement between the experimental I-V curve and the QPC model is reported for one of the device investigated in this work.

2.3.4 VCM Device Optimization

Although the material-system presented (Hf/HfO_2) shows good performance, in practice, the extensive engineering of the VCM stack (in particular for commercial applications) has led to devices with enhanced performance. Now that the reader knows about basic principles and figure of merits for oxide VCM, in this section some of the solutions designed to optimize the memory device are described.

Oxide selection: although the list of working materials for RS is extremely long, the major focus for high-performance application is currently on bilayer structures using HfO_2 and Ta_2O_5 [60, 63]. In particular to date Ta_2O_5 has provided record endurance and has been already introduced in commercial products [60, 75]. As explained the bilayer structure provides the V_o profile needed for formation/injection of defects in the CF. Many materials have been explored as oxygen scavenging-layer [62] but current designs are based on sputtered thin film of the related metal contained in the transition metal oxide i.e. Hf for HfO_2 and Ta for Ta_2O_5 . For the sake of large area integration and reliability amorphous materials is generally preferred versus crystalline oxides which are showing higher dispersion of median values due to local material fluctuation induced by crystalline grains and grains boundaries [63]. A known approach to limit the crystallization in HfO_2 is the alloying during the ALD deposition with aluminum. As often reported VCM based on $Hf_{1-x}Al_xO_y$ maintains

good switching performances improving device uniformity in high density applications [63, 76]. The oxygen partial pressure control in case of reactive sputtering deposition is another approach to modulate the properties of the switching oxides. Generally a more stoichiometric oxide leads to increased resistance for both LRS and HRS. This can be a possible solution to reduce the reset current, but it presents a trade off with the operative voltages which are also increased [60].

Oxygen-inert electrode: originally considered of minor importance, the role of the inert electrode becomes strategic for high performance application due to its interaction with the CF constriction. As will be presented in the next chapters the constriction of the CF is positioned next to the more oxygen-inert electrode (TiN in our case). Different studies have demonstrated that the chemical interaction between this electrode and the CF can be very detrimental for the switching [62, 77]. TiN has been traditionally used for integrated devices. Ab-initio modeling has shown that points defects such as nitrogen vacancies or dangling bonds in the TiN can locally reduce the energy barrier for oxygen to react with the metal and thus enhance the CF degradation [77]. For this reason materials showing high activation energy for oxygen in-diffusion such as ruthenium can offer extended endurance, robustness against breakdown and overall improved device lifetime.

Device encapsulation: due to the major role of oxygen in the switching mechanisms, it is extremely important to insulate the CF from any undesired oxygen interactions. To this end most of the high performance devices are carefully encapsulated limiting the oxygen in-diffusion from the outside. Another major issue can arise from regions where fabrication-induced damages (for example etching) increase the content of oxygen. Special care has to be taken in order to mitigate the possibility for the CF to be formed close to the edges of the device (where these damages are present). This approach has been recently proposed for the precise positioning of the CF in a 28-nm integrated TaO_x -based device [78].

Architectures: in common with CBRAM, the possibility to realize a dense crosspoint array of VCMs is also limited in reality by the sneak path problem [47]. Most of the characteristics previously defined in CBRAM hold true also for VCM. Highly non-linear devices providing sneak path current suppression when the cell is not accessed have been proposed also for VCM. Ovonic threshold switching, mixed ionic electronic conductors, Schottky emission-based diodes and complementary resistive switches are some of the explored solutions [48, 79, 80].

2.4 Review of Conductive Filaments Observation

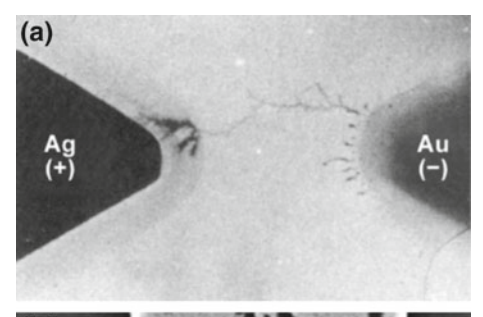
From the previous sections it is clear that the operation of any RS device is intimately correlated to the properties of the CF. Device physics, including speed, scalability, reliability and failures are all dependent on the CF and its characteristics. However, due to the extremely localized nature of the CF and its composition, the

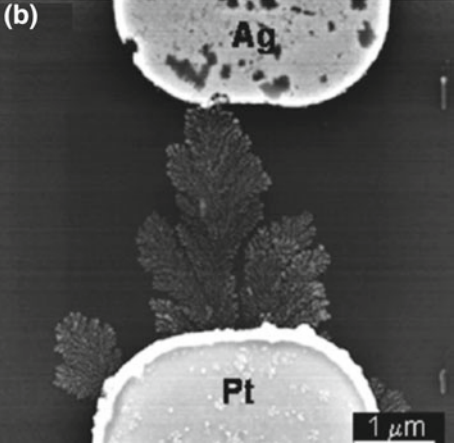
nanoscale observation of such filaments remains a key challenge for the community. In the last 40 years, most of the available (physical) characterization techniques have been used to directly image the CF. Beam-based and surface sensitive techniques such as transmission electron microscopy (TEM), electron energy loss spectroscopy (EELS), X-ray photoelectron spectroscopy (XPS), scanning electron microscopy (SEM), electron beam induced current (EBIC), secondary ion mass spectroscopy (SIMS) and scanning probe microscopy (SPM) to name a few, have been all used in the attempt to image the growth/dissolution processes in RS [81, 82]. The reason for this is the critical importance of a direct imaging of the CF, comprise of its compositional and chemical state characterization. To date, TEM and SEM coupled with SPM techniques have provided a good advance to the field, and CF observation has been achieved in different material systems for both CBRAM and VCM. This will be covered in this section with a short review of existing CF observations. This provides also the framework in which the original experimental work reported in this dissertation has been performed.

2.4.1 Filament Observation in CBRAM

A classic examples of CF observation in CBRAM is shown in Fig. 2.12, and is referred to the case of a Ag filament grown in two planar structures. Figure 2.12a, shows the first report from 1976 by Hirose and Hirose [83] where a Ag CF is visible on the surface of a As₂S₃ thin film. Figure 2.12b reports a more recent version of this experiment showing a Pt/H₂O/Ag cell, where de-ionized water is used as electrolyte [84]. During the switching phases a Ag CF grows with a dendritic morphology starting from the (Pt) inert electrode. Although based on a large planar structure and involving non-ideal materials for a CMOS integration, these experiments unambiguously demonstrate that formation and dissolution of a metallic CF is at the foundation of RS in CBRAM. Nevertheless the CF growth and dissolution dynamics are difficult to unravel starting from these observations. Furthermore, the structural changes observed on planar structures cannot be generalized to bulk structures, because diffusivity, solubility, redox activation energies to name few can be very different. For these reasons, systematic in- and ex-situ TEM analysis have been used to image structural changes of the CF during switching. TEM appears as a straightforward method to detect microstructural changes in the sample volume, even if CF localization and ex-situ sample preparation can be detrimental for the CF integrity. In-situ TEM, where the switching operations are induced in a TEM lamella simultaneously to the electron beam imaging, appears as a more reliable approach. In-situ TEM results are shown in Fig. 2.13a, for the case of a Ag/ZrO₂-based device [85] and in Fig. 2.13b for the case of CuGeTe [86]. In the scanning TEM (STEM) images of Fig. 2.13b LRS versus HRS state of the cell are shown. The CFs are clearly connected in the LRS case and ruptured at the Cu/CuGeTe interface for the HRS. From the comparison of Fig. 2.13a, b it is clear that the CFs assume a conical shape with a wide base. The position of the cone wide base is opposite to the CF growth direction and appears

Fig. 2.12 Planar observation of the conductive filament. a
Optical microscopy of a Ag (dendritic) CF grown on the top surface of a As₂S₃. b
Dendritic growth of CF imaged by SEM after switching process occurred in Pt/H₂O/Ag cell
[Reproduced from [83, 84]]





in opposite position in the two examples. The filament growth direction, its geometry and the location of CF dissolution, have been widely debated in the community due to the seemingly contradicting observations, arising from the analysis of different material systems [87–89]. The different geometries observed in Fig. 2.13a,b are good examples to support what was discussed in the Sect. 2.2.2 about filament growth dynamics and growth rate-limiting step. The overall CF properties (shape, size and growth direction) are determined by the rate-limiting factors affecting the material system under investigation. Specifically ion-solubility, mobility and oxidation/reduction rates are some of the main parameters influencing the charge transfer processes during the growth. For these reasons it is important to separate according to the ionic properties of the solid electrolyte the observed CBRAM switches. In essence, a solid electrolyte with good ionic mobility and low reduction rate will favor the growth direction of the CF from the inert toward the active electrode, as in Fig. 2.13a. On the contrary solid electrolyte with poor ionic conductivity and high reduction rate will lead to opposite filament growth Fig. 2.13b. Other reports with various CF geometries, have been imaged by in-situ TEM on a wide variety of solid electrolytes animating the debate in the community [43, 90–93]. Particularly because the set of phenomena involving metallic inclusions in dielectrics can be very rich just depending on the balance between ion mobility and oxidation/reduction rates in

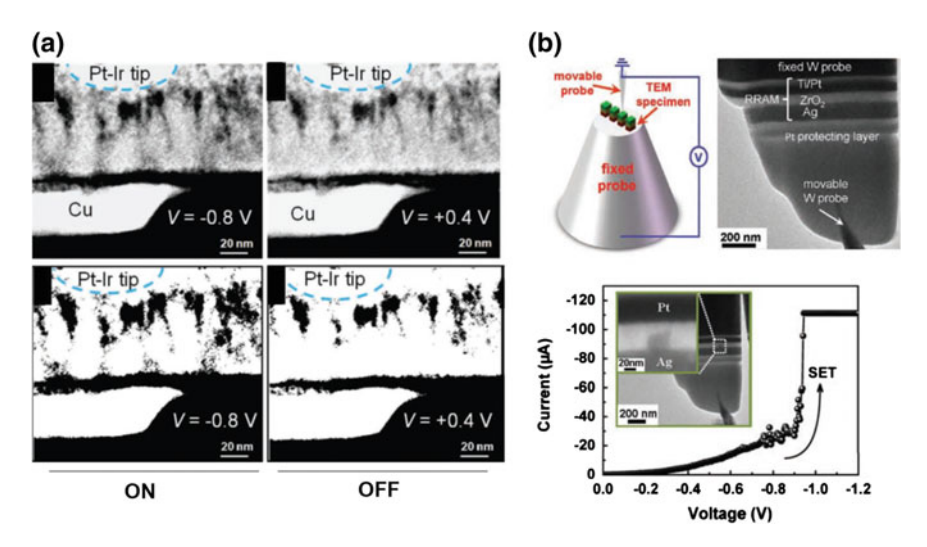


Fig. 2.13 *In-situ TEM experiment on dynamic filament observation.* **a** CFs observation in CuGeTe, STEM images are shown for the case of LRS and HRS. Raw TEM images are also shown and converted in *black* and *white* to enhance the contrast (*bottom insets*). **b** Schematic of in-situ TEM experiment and corresponding cross-section TEM image of fresh Ag/ZrO₂/Pt device. In the *inset* of the I–V cross-section TEM after electrical programming [Reproduced from [85, 86]]

the solid electrolyte. This has been the center of another in-situ TEM work, aimed to investigate the impact of CF growth condition as function of ionic mobility and redox/reduction rates [26]. The results are shown in Fig. 2.14 and present a model to explain most of the observed CFs geometries. It has to be mentioned that besides the cone-shaped CF, different combinations of the two parameters enable the evolution of conical CFs into more cylindrical geometry or clustered metallic inclusions in the oxide. Finally as will be covered in Chap. 5 the proper combination of ion mobility and redox rates can also induce CF wide at its ends and narrow in the middle (e.g. hourglass shape) showing specific electrical characteristic.

Next to the analysis with TEM, another set of techniques that have enabled good advances in the direct observation of the CF are scanning probe microscopies (SPMs). Thanks to their high lateral resolution and the capability to provide morphological and electrical information of the sample at the nanoscale, scanning tunneling microscopy (STM) as well as atomic force microscopy (AFM) have been extensively used for CFs observation [82, 94, 95]. Compared to TEM the use of SPM limits the effort in sample preparation and by means of the scanning conductive tip a movable (virtual) electrode can be easily realized. In addition the variety of electrical AFM modes gives access to different information such as local conductivity, surface potential and also structural/mechanical information. The unparalleled precision in tip positioning of STM has been used to investigate the CFs growth on the surface of super ionic solid electrolyte (Fig. 2.15) [94]. The STM tip is used to atomically control the growth of a Ag cluster on the surface of a RbAg₄I₅. A small (stable) Ag cluster is grown limited

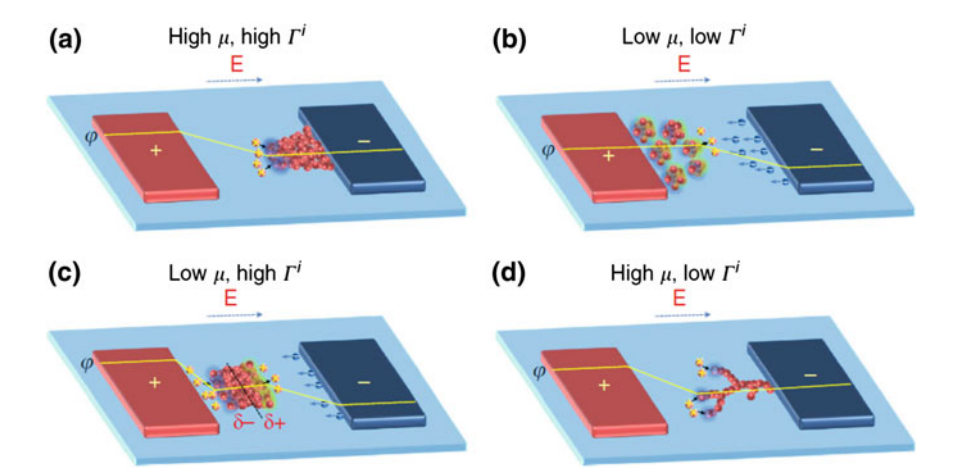


Fig. 2.14 Model for the filament growth based on kinetic parameters. Four schematics are presented for the possible combination of ionic mobility and reduction/oxidation rates in CBRAM. Γ represents oxidation (reduction) rate and μ is the ion mobility. As shown in figure, a and b represents the two conical geometry for the CF, while c accounts for all the formation of metallic clusters within the dielectric and d for branched CFs [Reproduced from [26]]

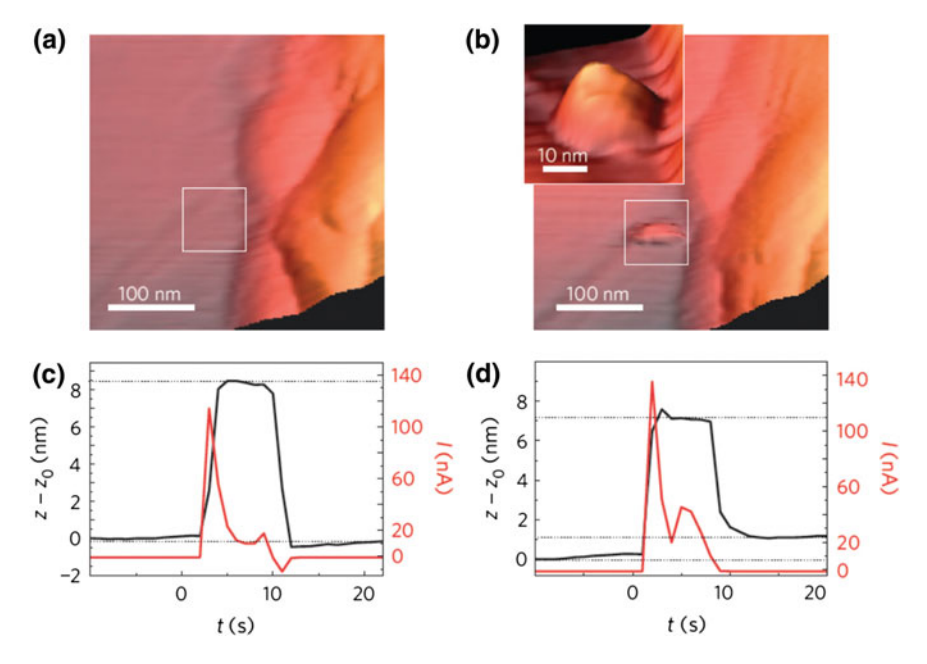


Fig. 2.15 STM observation of a tip-induced Ag cluster. $\bf a$ and $\bf b$ STM images of the RbAg₄I₅ before and after applying the voltage pulse. The pulse length is over imposed to the filament height induced by two different pulse amplitude $\bf d$ —250 mV and $\bf e$ —350 mV [Reproduced from [94]]

by the electron charge transfer at the STM tip. A minimum size for cluster stability has been observed at ≈ 5 nm in CF diameter and ≈ 3 nm in height. Similar results combined with the observation of quantized conductance steps were obtained by Wagenaar et al. in Ag₂ during the CF growth. Atomic force microscopy techniques, specifically with the conductive AFM (C-AFM) electrical mode, have provided various observation of the CFs as conductive spots. Yang et al. [96] investigated the presence of CFs in 30-nm-thick TiO₂-based device after the Cu top electrode has been removed by a FeCl₃ wet chemical etching. C-AFM revealed randomly distributed conductive hillocks with average diameter 100 and 40 nm height (the spots were still switchable by C-AFM tip). Similarly Park et al. [55] observed 5 nm-wide conductive spots in Cu/HfO₂-based cells where the Cu source was etched after CF formation. In this case the absence of hillocks could be explained with the control of the current during forming and cycling reducing the morphological changes associated to the CF formation. Celano et al. [15] have used C-AFM for the local formation and study of CFs induced by the conductive tip in CuTe/Al₂O₃ on blanket and also in integrated devices [97]. In this case the top electrode removal after device programming has been down by physical removal of the metal electrode by means of tip-induced physical scraping (as discussed in Chaps. 4–6 of this dissertation).

2.4.2 Filament Observation in VCM

The observation of the CF in bipolar oxide VCMs has been traditionally more challenging owing to a switching mechanisms based on the movement of oxygen vacancies. The local compositional change of the CF is often minimal compared to the surrounding material, and this poses strong limitations to the analysis. Ex-situ experiments and their preparation can induce undesired chemical and physical changes to the CF. This is due to the interaction of free oxygen with the V_a constituting the CF, and leads to the loss of information. One of the first attempt to relate RS to formation of CFs was done at IBM research [98] using electron beam-induced current (EBIC) on SrZrO₃ MIM capacitor. In EBIC an electron beam is scanned across the sample, and it locally generates charge carriers. In presence of an electric field (such as in a p-n junctions) or in a defective site there will be a local current induced by the e-beam that can be measured. The resultant current can be used as video signal of the SEM enabling the sensing the inhomogeneity in the electrical properties of the sample. After electroforming, EBIC evidenced few bright leakages posts with an average area of $10 \,\mu\text{m}^2$ in memory cells of $175 \,\mu\text{m}$ diameter (Fig. 2.16a,b). EBIC could not reveal any details on filament chemical composition but this work provided strong evidence of the filamentary nature of RS also for VCM. Although the number of published works is smaller as compared to CBRAM, in-situ TEM experiments have provided interesting results also for VCM. Park et al. [99] have demonstrated real-time measurements of a Ta_2O_{5-x} bilayer structure. A combination of high-angle annular dark-field (HAADF) and in-situ electrical probing enables the observation of conductive channels in the tantalum oxide layer. The observed CFs present a spatial

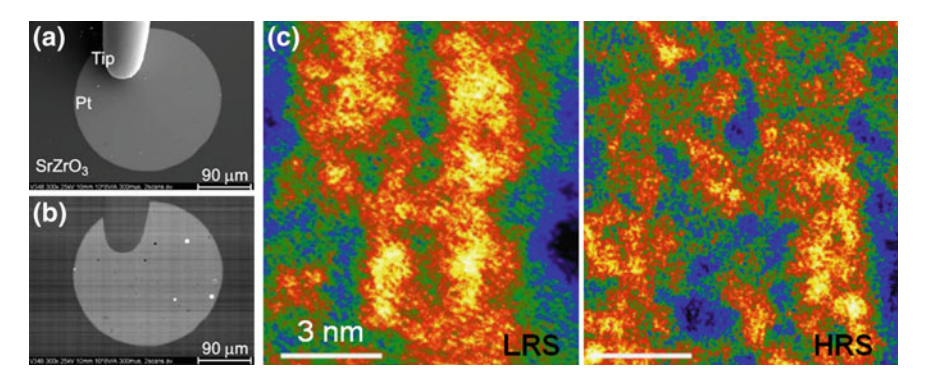


Fig. 2.16 VCM filament observation. a SEM image of the MIM capacitor. b Corresponding EBIC image with appearing conductive spots. c Micro-structural changes in Ta_2O_x -based bilayer VCM. Electron energy loss spectroscopy (EELS) analysis representing conductive channels consisting of a Ta-rich phase (*bright* and *yellow* regions). Structural evolution for LRS to HRS [Reproduced from [98, 99]]

extension of a few nanometers. By comparing the oxygen counts in the same region in LRS and HRS it is clear that the oxygen concentration in the CFs is lower for the LRS as compared to HRS, leading to a Ta rich phase for the CF in LRS as shown in Fig. 2.16c. The same group reported also the observation of a broken down Ta_2O_{5-x} studying the structural evolution and the oxygen composition. The result (not shown) is a degenerated and non-recoverable CF made of a Ta rich phase.

Due to the limited TEM observations, SPM has dramatically contributed also to the characterization of CF in VCM. One of the first materials to be investigated has been NiO known to be a nonstoichiometric compound in which oxygen can act as p-type dopant [100]. The passage of a biased AFM tip could induce the local conversion between Ni-rich and Ni-deficient domains with subsequent RS [101–104]. Fundamental studies using local conductance (LC-AFM same as C-AFM) have been conducted on perovskites such as crystalline SrTiO₃ [105–107]. Single crystalline SrTiO₃ has shown good switching properties in presence of dislocations and other extended defects. The conductive tip has been biased and used as a virtual electrode so that local conductance changes have been observed down to 1 nm conductive spot in SrTiO₃ single crystal [108]. Individual 30-nm-wide morphological protrusions on the SrTiO₃ surface, can be locally switched showing a resistance ratio of \approx 50 by Muenstermann and co-workers [106]. Owing to the role of oxygen, the RS can be observed only under vacuum conditions. SrTiO₃ study has been further extended for the case of Fe-SrTiO₃ where micro x-ray absorption has been used to related the distribution of oxygen vacancies to different resistive states Fig. 2.17a, b. A micro-focused x-ray beam is used to record the oxygen vacancy concentration on a MIM structure in LRS, by measuring the Fe K α fluorescence intensity. An homogenous increase in the vacancy concentration is observed in the CF and over the whole electrode area in electroformed devices. The introduced oxygen vacancies act as n-dopants and enhancing electron contribution in conduction band [109]. The

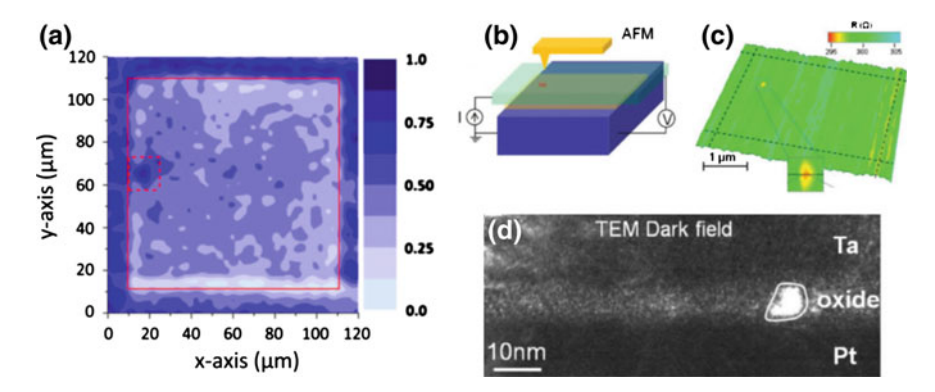


Fig. 2.17 *Ex-situ CF observation.* **a** Fe Kα fluorescence intensity map showing the area of the MIM device (*solid red line*). The CF appears as local vacancy enriched spot *dashed red line*. **b** Schematic representation of the PMCM setup, used for the localization of the CF in the Ta_2O_5 -based VCM. **c** Resistance map showing the position and size of the CF area. **d** Cross-sectional observation and dark-field TEM analysis of the CF structural composition [Reproduced from [109, 115]]

same group also combined a cleaving delamination technique to C-AFM to study the switching interface after metal top electrode removal [105]. Large part of the understanding gained on perovskites could be extended to other material systems such as TMO-based bipolar VCM. C-AFM for example, has been extensively used in the characterization of TiO2, ZnO2, HfO2, SiO2, WO3 and Ta2O5 [110-115]. A combination of SPM and TEM has been proposed by Miao et al. [115] at Hewlett-Packard labs, they have used ex-situ TEM and pressure-modulated conductance microscopy (PMCM). The CF is induced in a Pt/TaO_x/Ta device, and subsequently located by PMCM. A non-conducting AFM tip it is scanned over the device area at high pressure. By monitoring the device resistance it is possible to obtain a spatially correlated map of resistance as function of the tip position (Fig. 2.17b). The CF appears as a local lowly resistive spot of \approx 100 nm within the device area. A TEM lamella is taken in correspondence of the CF and the structural composition of the CF is investigated by means of high resolution TEM. In dark-field TEM the CF is shown next to a 5 nm wide nanocrystal indicating a local phase change in the amorphous Ta₂O₅. Due to the high crystallization temperature required, the presence of this local crystallization indicates that very high temperature is locally induced during RS. Consistently with previous observations the presence of oxygen in the CF central region is decreased to less than one third of that of pristine film. As will be shown in Chaps. 4 and 5, Celano et al. [116] have used an SPM-related techniques to visualize in three-dimension the CF in Hf/HfO₂ blanket sample and integrated device.

2.5 Summary of the Chapter

In this chapter we have reviewed the possible implementation of bipolar resistive switching devices, focusing on two specific material systems, Cu/Al₂O₃ for CBRAM and Hf/HfO₂ for VCM. The basic operative principles have been introduced for both technologies. Details on the devices fabrication and the main figure of merits have been provided for the test vehicle studied in this thesis. The advantages offered from each material system have been outlined and a review of the possible optimizations strategies has been provided. Finally, since this thesis is devoted to the study of resistive switching physical mechanisms, a brief literature review of the physical characterization of conductive filaments has been reported. The CF has shown scalability of its dimensions in the nanometers regime for both technologies. While filaments based on metal cations have proved increased stability enabling their direct observation by means of SEM, TEM and SPM. The observation of the CF in VCM is hampered by the interaction of the CF with the environmental oxygen. Thus requiring often, indirect CF observation techniques such as ex-situ XPS or EBIC. However, the observation of the CFs in three-dimension or in integrated devices has always represented a further challenge whose solution is presented in the rest of this dissertation.

References

- T.W. Hickmott, Low-frequency negative resistance in thin anodic oxide films. J. Appl. Phys. 33(9), 2669 (1962)
- T. Prodromakis, C. Toumazou, L. Chua, Two centuries of memristors. Nat. Mater. 11(6), 478–481 (2012)
- L. Chua, Resistance switching memories are memristors. Appl. Phys. A 102(4), 765–783 (2011)
- D.B. Strukov, G.S. Snider, D.R. Stewart, R. Stanley Williams, The missing memristor found. Nature 453(7191), 80–83 (2008)
- R. Waser, M. Aono, Nanoionics-based resistive switching memories. Nat. Mater. 6(11), 833– 840 (2007)
- J. Joshua Yang, D.B. Strukov, D.R. Stewart, Memristive devices for computing. Nat. Nanotechnol. 8(1), 13–24 (2012)
- H.-S. Philip Wong, S. Salahuddin, Memory leads the way to better computing. Nat. Nanotechnol. 10(3), 191–194 (2015)
- 8. G.W. Burr, B.N. Kurdi, J.C. Scott, C.H. Lam, K. Gopalakrishnan, R.S. Shenoy, Overview of candidate device technologies for. IBM J. Res. Dev. **52**(4), 449–464 (2008)
- A.C. Torrezan, J.P. Strachan, G. Medeiros-Ribeiro, R. Stanley Williams, Sub-nanosecond switching of a tantalum oxide memristor. Nanotechnology 22(48), 485203 (2011)
- A. Belmonte, W. Kim, B.T. Chan, N. Heylen, A. Fantini, M. Houssa, M. Jurczak, L. Goux, 90nm WAl2O3TiWCu 1T1R CBRAM cell showing low-power, fast and disturb-free operation, in 5th IEEE International Memory Workshop (IMW) (2013), pp. 26–29
- B. Govoreanu, G.S. Kar, Y.-y. Chen, V. Paraschiv, S. Kubicek, A. Fantini, I.P. Radu, L. Goux, S. Clima, R. Degraeve, N. Jossart, O. Richard, T. Vandeweyer, K. Seo, P. Hendrickx, G. Pourtois, H. Bender, L. Altimime, D.J. Wouters, J.A. Kittl, M. Jurczak. 10x10nm 2 Hf / HfO x

- crossbar resistive RAM with excellent performance, reliability and low-energy operation, in *IEDM Technical Digest* (Washington, DC, 2011), pp. 31.6.1–31.6.4
- 12. N. Onofrio, D. Guzman, A. Strachan, Atomic origin of ultrafast resistance switching in nanoscale electrometallization cells. Nat. Mater. **14**, 440–446 (2015)
- I. Valov, R. Waser, J.R. Jameson, M.N. Kozicki, Electrochemical metallization memoriesfundamentals, applications, prospects. Nanotechnology 22(25), 254003 (2011)
- 14. I. Valov, Redox-based resistive switching memories (ReRAMs): electrochemical systems at the atomic scale. ChemElectroChem 1(1), 26–36 (2013)
- U. Celano, L. Goux, K. Opsomer, A. Belmonte, M. Iapichino, C. Detavernier, M. Jurczak, W. Vandervorst, Switching mechanism and reverse engineering of low-power Cu-based resistive switching devices. Nanoscale 5(22), 11187–11192 (2013)
- A. Belmonte, W. Kim, B.T. Chan, N. Heylen, A. Fantini, M. Houssa, S. Member, M. Jurczak, L. Goux, A thermally stable and high-performance 90-nm. IEEE Trans. Electron Devices 60(11), 3690–3695 (2013)
- C. Schindler, G. Staikov, R. Waser, Electrode kinetics of Cu-SiO₂-based resistive switching cells: overcoming the voltage-time dilemma of electrochemical metallization memories. Appl. Phys. Lett. 94(7), 072109 (2009)
- A. Bard, L. Faulkner, Electrochemical Methods-Fundamentals and Applications, 2nd edn. (Wiley, New York, 2001)
- N.F. Mott, R.W. Gurney, Electronic Processes in Ionic Crystals, 2nd edn. (Dover, New York, 1940)
- G. Staikov, Electrocrystallization in Nanotechnology (Wiley-VCH Verlag GmbH & Co. KGaA, Weinheim, 2007)
- S. Menzel, U. Böttger, M. Wimmer, M. Salinga, Physics of the switching kinetics in resistive memories, in Advanced Functional Materials (2015)
- S. Menzel, S. Tappertzhofen, R. Waser, I. Valov, Switching kinetics of electrochemical metallization memory cells. Phys. Chem. Chem. Phys.: PCCP 15(18), 6945–6952 (2013)
- 23. S. Kim, S.H. Choi, L. Wei, Comprehensive physical model of dynamic resistive switching in an oxide memristor. ACS Nano 8(3), 2369–2376 (2014)
- 24. T. Tsuruoka, K. Terabe, T. Hasegawa, I. Valov, R. Waser, M. Aono, Effects of moisture on the switching characteristics of oxide-based. Gapless-type atomic switches. Adv. Funct. Mater. **22**(1), 70–77 (2011)
- Y. Yang, L. Wei, Nanoscale resistive switching devices: mechanisms and modeling. Nanoscale 5(21), 10076–10092 (2013)
- Y. Yang, P. Gao, L. Li, X. Pan, S. Tappertzhofen, S.H. Choi, R. Waser, I. Valov, W.D. Lu, Electrochemical dynamics of nanoscale metallic inclusions in dielectrics. Nat. Commun. 5, 4232 (2014)
- D. Kuzum, Y. Shimeng, H.S.P. Wong, H.S.P. Wong, Synaptic electronics: materials, devices and applications. Nanotechnology 24(38), 382001 (2013)
- R. Yang, K. Terabe, Y. Yao, T. Tsuruoka, T. Hasegawa, J.K. Gimzewski, M. Aono, Synaptic plasticity and memory functions achieved in a WO₃-based nanoionics device by using the principle of atomic switch operation. Nanotechnology 24(38), 384003 (2013)
- L. Goux, A. Fantini, B. Govoreanu, G. Kar, S. Clima, Y.-Y. Chen, R. Degraeve,
 D.J. Wouters, G. Pourtois, M. Jurczak, Asymmetry and switching phenomenology in TiN\(Al₂O₃)\HfO₂\Hf systems. ECS Solid State Lett. 1(4), P63–P65 (2012)
- L. Goux, K. Opsomer, R. Degraeve, R. Muller, C. Detavernier, D.J. Wouters, M. Jurczak, L. Altimime, J.A. Kittl, Influence of the Cu-Te composition and microstructure on the resistive switching of Cu-Te/Al₂O₃/Si cells. Appl. Phys. Lett. 99(5), 053502 (2011)
- W. Devulder, K. Opsomer, F. Seidel, A. Belmonte, R. Muller, B. De Schutter, H. Bender, W. Vandervorst, S. Van Elshocht, M. Jurczak, L. Goux, C. Detavernier, Influence of carbon alloying on the thermal stability and resistive switching behavior of copper-telluride based CBRAM cells. ACS Appl. Mater. Interfaces 5(15), 6984–6989 (2013)
- L. Goux, K. Opsomer, R. Schuitema, R. Degraeve, R. Müller, C. Detavernier, D.J. Wouters, M. Jurczak, L. Altimime, J.A. Kittl, Self-limited filament formation and low-power resistive

References 41

- switching in Cu x Te 1-x/Al₂ O₃/Si CBRAM cell, in *Memory Workshop (IMW), 2011 3rd IEEE International, number c* (Monterey, CA, 2011), pp. 1–4
- W. Devulder, K. Opsomer, J. Meersschaut, D. Deduytsche, M. Jurczak, L. Goux, C. Detavernier, Combinatorial study of Ag-Te thin films and their application as cation supply layer in CBRAM cells. ACS Comb. Sci. 17(5), 334–340 (2015)
- 34. S. Mege, Memory cell device and method of manufacture, US Patent 8952493 B2 (2015)
- J.R. Jameson, Nonvolatile memory with semimetal or semiconductors electrodes, US Patent WO 2014146003 A1 (2014)
- 36. J.R. Jameson, P. Blanchard, C. Cheng, J. Dinh, A. Gallo, V. Gopalakrishnan, C. Gopalan, B. Guichet, S. Hsu, D. Kamalanathan, D. Kim, F. Koushan, M. Kwan, K. Law, D. Lewis, Y. Ma, V. Mccaffrey, S. Park, S. Puthenthermadam, E. Runnion, J. Sanchez, J. Shields, K. Tsai, A. Tysdal, D. Wang, R. Williams, M.N. Kozicki, J. Wang, V. Gopinath, S. Hollmer, M. Van Buskirk, Conductive-bridge memory (CBRAM) with excellent high-temperature retention. *IEDM Technical Digest* (2013), pp. 738–741
- 37. D.W. Collins, Memory cells including top electrodes comprising metal silicide, apparatuses including such cells, and related methods (2013)
- 38. D.-Y. Cho, S. Tappertzhofen, R. Waser, I. Valov, Chemically-inactive interfaces in thin film Ag/AgI systems for resistive switching memories. Sci. Rep. 3, 1169 (2013)
- 39. D. Kamalanathan, U. Russo, D. Ielmini, M.N. Kozicki, Voltage-driven on off transition and tradeoff with program and erase current in programmable. **30**(5), 553–555 (2009)
- C. Schindler, M. Weides, M.N. Kozicki, R. Waser, Low current resistive switching in Cu-SiO₂ cells. Appl. Phys. Lett. 92(12), 122910 (2008)
- W. Guan, M. Liu, S. Long, Q. Liu, W. Wang, On the resistive switching mechanisms of Cu/ZrO₂:Cu/Pt. Appl. Phys. Lett. 93(22), 223506 (2008)
- A. Nayak, T. Tsuruoka, K. Terabe, T. Hasegawa, M. Aono, Switching kinetics of a Cu₂ S-based gap-type atomic switch. Nanotechnology 22(23), 235201 (2011)
- 43. Y. Yang, P. Gao, S. Gaba, T. Chang, X. Pan, L. Wei, Observation of conducting filament growth in nanoscale resistive memories. Nat. Commun. 3, 732 (2012)
- 44. Nano letters CMOS compatible nanoscale nonvolatile resistance switching memory. **8**(2), 392–397 (2008)
- 45. W. Lu. Silicon based nanoscale crossbar memory, US Patent US 8071972 B2 (2011)
- S. Tappertzhofen, R. Waser, I. Valov, Impact of the counter-electrode material on redox processes in resistive switching memories. ChemElectroChem 1(8), 1287–1292 (2014)
- 47. E. Linn, R. Rosezin, C. Kügeler, R. Waser, Complementary resistive switches for passive nanocrossbar memories. Nat. Mater. 9(5), 403–406 (2010)
- 48. Takhee Lee, Yong Chen, Organic resistive nonvolatile memory materials. MRS Bull. **37**(02), 144–149 (2012)
- 49. J. Woo, D. Lee, E. Cha, S. Lee, S. Park, H. Hwang, Vertically stacked ReRAM composed of a bidirectional selector and CB-RAM for cross-point array applications. **34**(12), 1512–1514 (2013)
- S.H. Jo, T. Kumar, S. Narayanan, W.D. Lu, H. Nazarian, P. Henry, S. Clara, 3D-stackable crossbar resistive memory based on field assisted superlinear threshold (FAST) selector. 408, 160–163 (2014)
- 51. R.S. Shenoy, K. Gopalakrishnan, B. Jackson, K. Virwani, G. W Burr, C.T. Rettner, A. Padilla, D.S. Bethune, R.M. Shelby, A.J. Kellock, M. Breitwisch, E.A. Joseph, R. Dasaka, R.S. King, K. Nguyen, A.N. Bowers, M. Jurich, A.M. Friz, T. Topuria, P.M. Rice, B.N. Kurdi, Endurance and scaling trends of novel access-devices for multi-layer crosspoint-memory based on mixed-ionic-electronic-conduction (MIEC) materials (2011), pp. 94–95
- 52. L. Zhang, B. Govoreanu, A. Redolfi, D. Crotti, H. Hody, V. Paraschiv, S. Cosemans, C. Adelmann, T. Witters, S. Clima, P. Hendrickx, D.J. Wouters, G. Groeseneken, M. Jurczak, High-drive current (>1MA/cm2) and highly nonlinear (>103) TiN/amorphous-Silicon/TiN scalable bidirectional selector with excellent reliability and its variability impact on the 1S1R array performance, in *IEDM Technical Digest IEEE International Electron Devices Meeting* (IEEE, 2014), pp. 6.8.1–6.8.4

- 53. J. Z.ahurak, K. Miyata, M. Fischer, M. Balakrishnan, S. Chhajed, D. Wells, A. Torsi, M. Korber, K. Nakazawa, S. Mayuzumi, M. Honda, S. Sills, S. Yasuda, A. Calderoni, B. Cook, G. Damarla, C. Cardon, K. Karda, J. Okuno, A. Johnson, T. Kunihiro, M. Tsukamoto, K. Aratani, N. Ramaswamy, W. Otsuka, K. Prall, Process integration of a 27nm, 16Gb Cu ReRAM, in 2014 IEEE International Electron Devices Meeting (IEEE, San Francisco (CA), 2014), pp. 6.2.1–6.2.4
- S.H. Jo, K.-H. Kim, W. Lu, High-density crossbar arrays based on a Si memristive system. Nano Lett. 9(2), 870–874 (2009)
- 55. J. Park, W. Lee, M. Choe, S. Jung, M. Son, S. Kim, S. Park, J. Shin, D. Lee, M. Siddik, J. Woo, G. Choi, E. Cha, T. Lee, H. Hwang, Quantized conductive filament formed by limited Cu source in sub-5nm era, in 2011 International Electron Devices Meeting (2011), pp. 3.7.1–3.7.4
- K. Aratani, K. Ohba, T. Mizuguchi, S. Yasude, T. Shiimoto, T. Tsushima, T. Sone, K. Endo, A. Kouchiyama, S. Sasaki, A. Maesaka, N. Yamada, H. Narisawa, Katsuhisa. Arataniojp. sony.com, in *Electron Devices Meeting*, 2007. IEDM 2007. IEEE International (Washington, DC, 2007), pp. 783–786
- S. Clima, K. Sankaran, Y.Y. Chen, A. Fantini, U. Celano, A. Belmonte, L. Zhang, L. Goux,
 B. Govoreanu, R. Degraeve, D.J. Wouters, M. Jurczak, W. Vandervorst, S. De Gendt, G.
 Pourtois, RRAMs based on anionic and cationic switching: a short overview. *physica status solidi (RRL) Rapid Research Letters* (2014), 11:n/a–n/a
- H.-S. Philip Wong, H.-Y. Lee, S. Yu, Y.-S. Chen, Y. Wu, P.-S. Chen, B. Lee, F.T. Chen, M.-J. Tsai, Metal-oxide RRAM, Proc. IEEE 100(6), 1951–1970 (2012)
- R. Waser, R. Dittmann, G. Staikov, K. Szot, Redox-based resistive switching memories nanoionic mechanisms, prospects, and challenges. Adv. Mater. 21(25–26), 2632–2663 (2009)
- 60. M.-J. Lee, C.B. Lee, D. Lee, S.R. Lee, M. Chang, J.H. Hur, Y.-B. Kim, C.-J. Kim, D.H. Seo, S. Seo, U.-I. Chung, I.-K. Yoo, K. Kim, A fast, high-endurance and scalable non-volatile memory device made from asymmetric Ta₂O₍5-*x*)/TaO₍2-*x*) bilayer structures. Nat. Mater. **10**(8), 625–630 (2011)
- 61. M. Houssa, High-k Gate Dielectrics (CRC Press, Boca Raton, 2003)
- 62. Y.Y. Chen, Electrical Characterization of Functional Oxides for Resistive RAM Memory Applications. Ph.D. thesis, KU Leuven (2013)
- 63. A. Fantini, L. Goux, S. Clima, R. Degraeve, A. Redolfi, C. Adelmann, G. Polimeni, Y.Y. Chen, M. Komura, A. Belmonte, D.J. Wouters, M. Jurczak, Engineering of Hf 1-x Al x O y amorphous dielectrics for high-performance RRAM applications. (c) (2014)
- 64. A. Belmonte, R. Degraeve, A. Fantini, W. Kim, M. Houssa, M. Jurczak, L. Goux, Origin of the current discretization in deep reset states of an Al₂O₃/Cu-based conductive-bridging memory, and impact on state level and variability. Appl. Phys. Lett. 104(23), 233508 (2014)
- 65. F.A. Kröger, H.J. Vink, Solid State Physics, vol. 3 (Academic Press, New York, 1956)
- J.J. Yang, F. Miao, M.D. Pickett, D.A.A. Ohlberg, D.R. Stewart, C.N. Lau, R. Stanley, Williams. The mechanism of electroforming of metal oxide memristive switches. Nanotechnology 20(21), 215201 (2009)
- S. Yu, X. Guan, H.S.P. Wong, Conduction mechanism of TiN/HfOx/Pt resistive switching memory: A trap-assisted-tunneling model. Appl. Phys. Lett. 99(6), 063507 (2011)
- 68. R. Degraeve, G. Groeseneken, R. Bellens, J.L. Ogier, M. Depas, P.J. Roussel, H.E. Maes, New insights in the relation between electron trap generation and the statistical properties of oxide breakdown. IEEE Trans. Electron Devices 45(4), 904–911 (1998)
- 69. B.J. van Wees, H. van Houten, C.W.J. Beenakker, J.G. Williamson, L.P. Kouwenhoven, D. van der Marel, C.T. Foxon, Quantized conductance of point contacts in a two-dimensional electron gas. Phys. Rev. Lett. 60(9), 848–850 (1988)
- E.A. Miranda, C. Walczyk, C. Wenger, T. Schroeder, Model for the resistive switching effect in HfO 2 MIM structures based on the transmission properties of narrow constrictions. IEEE Electron Device Lett. 31(6), 609–611 (2010)
- K. Terabe, T. Hasegawa, T. Nakayama, M. Aono, Quantized conductance atomic switch. Nature 433(7021), 47–50 (2005)

References 43

 R. Landauer, Electrical resistance of disordered one-dimensional lattices. Phil. Mag. 21(172), 863–867 (1970)

- R. Degraeve, L. Ph Roussel, D.Wouters Goux, J. Kittl, L. Altimime, M. Jurczak, G. Groeseneken, Generic learning of TDDB applied to RRAM for improved understanding of conduction and switching mechanism through multiple filaments. IEDM Tech. Dig. IEEE Int. Electron Devices Meet. 1, 632–635 (2010)
- R. Degraeve, A. Fantini, S. Clima, B. Govoreanu, L. Goux, Y.Y. Chen, D.J. Wouters, G.S. Ph Roussel, G.Pourtois Kar, S. Cosemans, J.A. Kittl, G. Groeseneken, M. Jurczak, L. Altimime, Dynamic 'hour glass' model for SET and RESET in HfO₂ RRAM, in *Symposium on VLSI Technology (VLSIT)*, number 1 (Honolulu, HI, 2012), pp. 75–76
- Panasonic. Panasonic (press release), Panasonic Starts World's First Mass Production of ReRAM Mounted Microcomputers (2013)
- A. Fantini, L. Goux, A. Redolfi, R. Degraeve, G. Kar, Y.Y. Chen, M. Jurczak, Lateral and vertical scaling impact on statistical performances and reliability of 10nm TiN / Hf (Al) O / Hf / TiN RRAM devices (2014), pp. 2013–2014
- C.Y. Chen, L. Goux, A. Fantini, A. Redolfi, S. Clima, R. Degraeve, Y.Y. Chen, G. Groeseneken, M. Jurczak, Understanding the impact of programming pulses and electrode materials on the endurance properties of scaled Ta₂O₅ RRAM cells, in *IEDM Technical Digest* (IEEE, 2014), pp. 14.2.1–14.2.4
- 78. Y. Hayakawa, A. Himeno, R. Yasuhara, W. Boullart, E. Vecchio, T. Vandeweyer, T. Witters, D. Crotti, M. Jurczak, S. Fujii, S. Ito, Y. Kawashima, Y. Ikeda, A. Kawahara, K. Kawai, Z. Wei, S. Muraoka, K. Shimakawa, T. Mikawa, S. Yoneda, Highly reliable TaOx ReRAM with centralized filament for 28-nm embedded application, in *Symposium on VLSI Technology (VLSIT)*, vol. 724 (IEEE, 2015), pp. T14–T15
- Y. Yang, J. Lee, S. Lee, C.-H. Liu, Z. Zhong, W. Lu, Oxide resistive memory with functionalized graphene as built-in selector element. Adv. Mater. (Deerfield Beach, Fla.), 26(22), 3693–3699 (2014)
- 80. G. Wang, A.C. Lauchner, J. Lin, D. Natelson, K.V. Palem, J.M. Tour, High-performance and low-power rewritable SiOx 1 kbit one diode-one resistor crossbar memory array. Adv. Mater. (Deerfield Beach, Fla.), **25**(34), 4789–93 (2013)
- D.S. Jeong, R. Thomas, R.S. Katiyar, J.F. Scott, H. Kohlstedt, A. Petraru, C.S. Hwang, Emerging memories: resistive switching mechanisms and current status. Rep. Prog. Phys. Phys. Soc. (Great Britain). 75(7), 076502 (2012)
- 82. M.H. Lee, C.S. Hwang, Resistive switching memory: observations with scanning probe microscopy. Nanoscale 3(2), 490–502 (2011)
- 83. Y. Hirose, Polarity-dependent memory switching and behavior of Ag dendrite in Agphotodoped amorphous As₂S₃ films. J. Appl. Phys. **47**(6), 2767 (1976)
- X. Guo, C. Schindler, S. Menzel, R. Waser, Understanding the switching-off mechanism in Ag⁺ migration based resistively switching model systems. Appl. Phys. Lett. 91(13), 133513 (2007)
- 85. Q. Liu, J. Sun, H. Lv, S. Long, K. Yin, N. Wan, Y. Li, L. Sun, M. Liu, Real-time observation on dynamic growth/dissolution of conductive filaments in oxide-electrolyte-based ReRAM. Adv. Mater. (Deerfield Beach, Fla.). **24**(14), 1844–1849 (2012)
- S.-J. Choi, G.-S. Park, K.-H. Kim, S. Cho, W.-Y. Yang, X.-S. Li, J.-H. Moon, K.-J. Lee, K. Kim, In situ observation of voltage-induced multilevel resistive switching in solid electrolyte memory. Adv. Mater. (Deerfield Beach, Fla.). 23(29), 3272–3277 (2011)
- I. Valov, R. Waser, Comment on real-time observation on dynamic growth/dissolution of conductive filaments in oxide-electrolyte-based ReRAM. Adv. Mater. (Deerfield Beach, Fla.).
 25(2), 162–164 (2013)
- 88. I. Valov, R. Waser, Comment on "Dynamic Processes of Resistive Switching in Metallic Filament-Based Organic Memory Devices" (2013), pp. 8–10
- S. Gao, C. Song, C. Chen, F. Zeng, F. Pan, Reply to "Comment on 'Dynamic Processes of Resistive Switching in Metallic Filament-Based Organic Memory Devices" (2013), pp. 6–7

- 90. S. Gao, C. Song, C. Chen, F. Zeng, F. Pan, Dynamic processes of resistive switching in metallic filament-based organic memory devices. J. Phys. Chem. C 116(33), 17955–17959 (2012)
- 91. S. Gao, C. Song, C. Chen, F. Zeng, F. Pan, Formation process of conducting filament in planar organic resistive memory. Appl. Phys. Lett. **102**(14), 141606 (2013)
- 92. H. Sun, Q. Liu, C. Li, S. Long, H. Lv, C. Bi, Z. Huo, L. Li, M. Liu, Direct observation of conversion between threshold switching and memory switching induced by conductive filament morphology. Adv. Funct. Mater. **24**(36), 5679–5686 (2014)
- 93. W.A. Hubbard, A. Kerelsky, G. Jasmin, E.R. White, J. Lodico, M. Mecklenburg, B.C. Regan, Nanofilament formation and regeneration during Cu/Al2O3 resistive memory switching. Nano Lett. (2015)
- I. Valov, I. Sapezanskaia, A. Nayak, T. Tsuruoka, T. Bredow, T. Hasegawa, G. Staikov, M. Aono, R. Waser, At superionic solid electrolyte surfaces. Nat. Mater. 11(6), 530–535 (2012)
- 95. M. Lanza, A Review on Resistive Switching in High-k Dielectrics: A Nanoscale Point of View Using Conductive Atomic Force Microscope (2014), pp. 2155–2182
- 96. J.J. Yang, J. Borghetti, D. Murphy, D.R. Stewart, R. Stanley Williams, A family of electronically reconfigurable nanodevices. Adv. Mater. 21(37), 3754–3758 (2009)
- U. Celano, L. Goux, K. Opsomer, M. Iapichino, A. Belmonte, A. Franquet, I. Hoflijk, C. Detavernier, M. Jurczak, W. Vandervorst, Scanning probe microscopy as a scalpel to probe filament formation in conductive bridging memory devices. Microelectron. Eng. 120, 67–70 (2014)
- 98. C. Rossel, G.I. Meijer, D. Bremaud, D. Widmer, Electrical current distribution across a metal-insulator-metal structure during bistable switching. J. Appl. Phys. **90**(6), 2892 (2001)
- 99. G.-S. Park, Y.B. Kim, S.Y. Park, X.S. Li, S. Heo, M.-J. Lee, M. Chang, J.H. Kwon, M. Kim, U.-I. Chung, R. Dittmann, R. Waser, K. Kim, In situ observation of filamentary conducting channels in an asymmetric TaO₅-x/TaO₂-x bilayer structure. Nat. Commun. **4**, 2382 (2013)
- D. Adler, J. Feinleib, Electrical and optical properties of narrow-band materials. Phys. Rev. B 2(8), 3112–3134 (1970)
- C. Yoshida, K. Kinoshita, T. Yamasaki, Y. Sugiyama, Direct observation of oxygen movement during resistance switching in NiO/Pt film. Appl. Phys. Lett. 93(4), 042106 (2008)
- F. Nardi, D. Deleruyelle, S. Spiga, C. Muller, B. Bouteille, D. Ielmini, Switching of nanosized filaments in NiO by conductive atomic force microscopy. J. Appl. Phys. 112(6), 064310 (2012)
- J.Y. Son, Y.-H. Shin, Direct observation of conducting filaments on resistive switching of NiO thin films. Appl. Phys. Lett. 92(222106), 222106 (2008)
- W. Polspoel, High resolution study of high-k layers using C-AFM. Ph.D. thesis, KU Leuven (2012)
- 105. R. Dittmann, R. Muenstermann, I. Krug, D. Park, T. Menke, J. Mayer, A. Besmehn, F. Kronast, C.M. Schneider, R. Waser, Scaling potential of local redox processes in Memristive SrTiO₃ thin-film devices. Proc. IEEE 100(6), 1979–1990 (2012)
- R. Muenstermann, R. Dittmann, K. Szot, S. Mi, C.-L. Jia, P. Meuffels, R. Waser, Realization of regular arrays of nanoscale resistive switching blocks in thin films of Nb-doped SrTiO₃. Appl. Phys. Lett. 93(2), 023110 (2008)
- 107. C. Rodenbücher, W. Speier, G. Bihlmayer, U. Breuer, R. Waser, K. Szot, Cluster-like resistive switching of SrTiO₃: Nb surface layers. New J. Phys. 15(10), 103017 (2013)
- K. Szot, W. Speier, G. Bihlmayer, R. Waser, Switching the electrical resistance of individual dislocations in single-crystalline SrTiO₃. Nat. Mater. 5(4), 312–320 (2006)
- 109. Ch. Lenser, A. Kuzmin, J. Purans, A. Kalinko, R. Waser, R. Dittmann, Probing the oxygen vacancy distribution in resistive switching Fe-SrTiO₃ metal-insulator-metal-structures by micro-x ray absorption near-edge structure. J. Appl. Phys. 111(7), 076101 (2012)
- S.C. Chae, J.S. Lee, S. Kim, S.B. Lee, S.H. Chang, C. Liu, B. Kahng, H. Shin, D.-W. Kim, C.U. Jung, S. Seo, M.-J. Lee, T.W. Noh, Random circuit breaker network model for unipolar resistance switching. Adv. Mater. 20(6), 1154–1159 (2008)
- 111. X. Zhu, W. Su, Y. Liu, B. Hu, L. Pan, W. Lu, J. Zhang, R.-W. Li, Observation of conductance quantization in oxide-based resistive switching memory. Adv. Mater. (Deerfield Beach, Fla.). 24(29), 3941–3946 2012

References 45

112. S. Brivio, G. Tallarida, E. Cianci, S. Spiga, Formation and disruption of conductive filaments in a HfO₂/TiN structure. Nanotechnology **25**(38), 385705 (2014)

- 113. A. Mehonic, S. Cueff, M. Wojdak, S. Hudziak, C. Labbé, R. Rizk, A.J. Kenyon, Electrically tailored resistance switching in silicon oxide. Nanotechnology, **23**(45):455201 (2012)
- 114. M. Lanza, G. Bersuker, M. Porti, E. Miranda, M. Nafria, X. Aymerich, Resistive switching in hafnium dioxide layers: Local phenomenon at grain boundaries. Appl. Phys. Lett. 101(19), 193502 (2012)
- 115. F. Miao, J.P. Strachan, J.J. Yang, M.-X. Zhang, I. Goldfarb, A.C. Torrezan, P. Eschbach, R.D. Kelley, G. Medeiros-Ribeiro, R. Stanley Williams, Anatomy of a nanoscale conduction channel reveals the mechanism of a high-performance memristor. Adv. Mater. 53(47), 5633– 5640 (2011)
- 116. U. Celano, L. Goux, A. Belmonte, K. Opsomer, A. Franquet, A. Schulze, C. Detavernier, O. Richard, H. Bender, M. Jurczak, W. Vandervorst, Three-dimensional observation of the conductive filament in nanoscaled resistive memory devices. Nano Lett. 14(5), 2401–2406 (2014)

Chapter 3 Nanoscaled Electrical Characterization

3.1 Overview

The nanoscale control afforded by scanning probe microscopy has rapidly made it a key tool for nanotechnology [1]. The development of SPM in many directions has led to unprecedented access to the nanoscaled properties of materials [2–6]. The idea of obtaining information from an object by scanning a small tip on its surface is very old. We use it to find the light switch in a dark room or to play music in old-fashion record players. At the beginning of the 80s G. Binnig and H. Rohrer decided to apply a similar approach to image surfaces of solids with a lateral precision down to 10 pm. The invention for which they have been awarded with the Nobel prize for physics in 1986 is the scanning tunnel microscope (STM) [7]. A sharp metallic tip is scanned over the surface at a distance of less than 1 nm. This distance can be kept constant with pm precision thanks to a quantum mechanical effect namely the electron tunneling. In essence, a tunneling current is flowing between two electrodes when they are spaced by a small distance although not in contact. This is due to the delocalized wave function of the electrons of the outmost atoms constituting the two electrodes. Interestingly, the intensity of this tunneling current decays exponentially with the tip-sample (electrodes) distance, enabling the current to flow from the very last atom of the tip apex. Having a single atom responsible for the conduction of the tunneling current leads to atomic resolution. Figure 3.1a, represents the standard measurement setup for STM. The tip is moved in three-dimensions (3D) by piezoelectric actuators. Once the level of tunneling current is fixed, an electronic controller is used to keep the value of the current constant by changing the position of the tip and thus creating a nanometer precise profilometer. The tip displacement is recorded by a computer during the raster scan of a portion of space and the surface image is generated. Although the invention of the STM determined a milestone for physics, in the original design it required conducting surfaces to operate and this limited its application.

To overcome this limitation, AFM originated as an extension of STM. The first design proposed by G. Binning et al. [8], was based on a sharp probe attached to a cantilever (spring) which was brought in contact with the sample surface. The forces

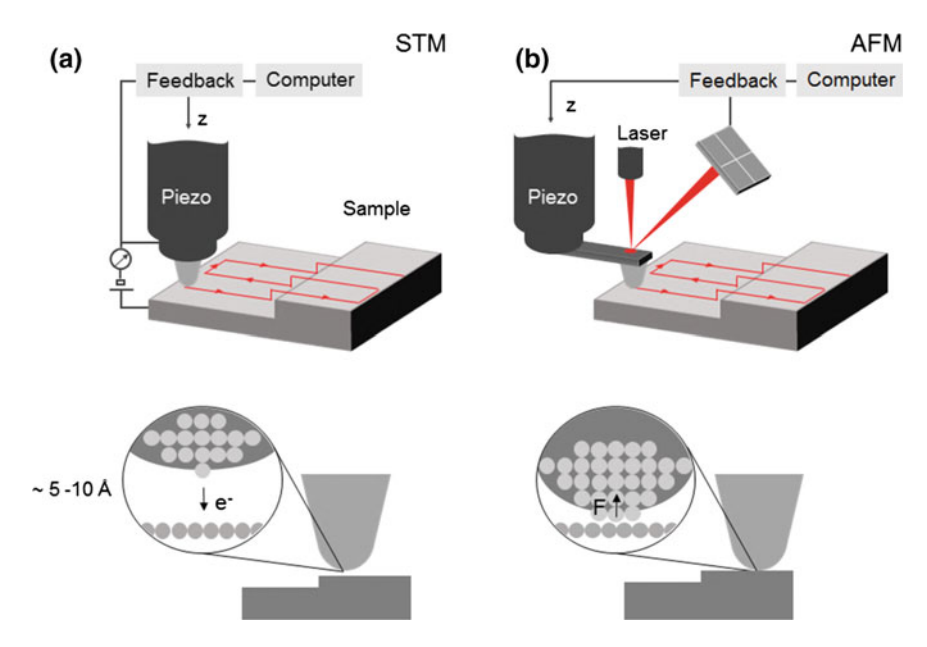


Fig. 3.1 *General SPM setup.* **a** Schematic of STM, where the z distance is controlled by a feedback circuit (driving the piezoelectric scanner) keeping constant the tunneling current flowing between the last atom of the tip and the (conducting) sample. Tip-surface detailed illustration is in the *inset*, note the distance between the tip and the conducting sample. **b** Schematic of AFM configuration, the tip is mounted at the edge of a micro fabricated cantilever, and brought in repulsive force regime on the sample. The beam deflection is recorded by a position-sensitive detector (4-quadrant photodiode)

acting between the sample and the tip induced a displacement of the tip (deflection) on the cantilever. A second STM tip was used to control the tunneling current between tip and the backside of the cantilever. The latter approach enabled the precise force control between the tip and the sample surface during the scan. This configuration has been exceeded when Meyer and Amer [9] proposed the usage of a laser beam reflection on the backside of the cantilever to observe the tip-sample forces. This is still the most common configuration for AFMs (known as beam-deflection design) and it is based on a position-sensitive quadrant photodiode in which the laser beam is reflected from the backside of the cantilever. The output of the photodiode is converted to tip displacement and recorded by a computer during the raster scan to directly image the surface morphology (Fig. 3.1b). It goes without saying that all kind of surfaces (conductive and insulating) can now be investigated. In addition this approach enabled the simultaneous sensing of other surface properties such as mechanical and electrical parameters by selecting different tip materials or by applying a tip-sample voltage [10]. This has been probably the most disruptive innovation that led to the big success of AFM-based techniques. After few years from its introduction AFM has rapidly found applications in a wide range of fields spanning from

3.1 Overview 49

semiconductor physics [3] to biological materials [11]. However, the wide AFM application came at the price of reduced lateral resolution. The latter is now limited to the tip-radius of the micro-machined tip and not anymore to the outmost single atom of the STM tip, thus reducing the lateral resolution from Å to few nanometers. The atomic force microscopy has proved to be tremendously adaptive to assess not only topography but also a wide range of other properties. Among various application in physics, chemistry and biological science AFM-based techniques have been extensively applied to micro and nano electronics [6, 10]. By using a biased conductive tip, AFM has enabled the sensing of electrical properties at the nanoscale in a wide range of applications [10]. Exploiting the measurement of local current, voltage, resistance or capacitance, the nanoscopic access to a wide range of material properties has rapidly increased revealing surface charges [12], dopant profiles [13], piezoelectricity [14], and others. For the characterization of electronic devices AFM offers different techniques: conductive atomic force microscopy (C-AFM), which represents the main topic of this dissertation, then scanning capacitance microscopy (SCM) and scanning spreading resistance microscopy (SSRM) for dopant profiling and implant mapping, magnetic force microscopy (MFM) and kelvin probe force microscopy (KPFM) to study respectively magnetic field and surface potential distribution.

The ample set of tip-sample interactions and their different detection led to the development of different AFM operation modes. These can be divided in static and dynamic modes, where the static bending of the cantilever or its dynamic properties are respectively measured. For example, an effective way to record the topography of the sample is maintaining the cantilever bending constant during the scan. This is a static mode called contact mode. One might be interested in recording the long-range forces such as magnetic or capacitance and in this case, it is more effective to scan the tip at a constant height from the surface recording any cantilever deflection. This is a dynamic mode, wherein other properties rather than cantilever bending are measured i.e. vibrational eigenfrequency, oscillation amplitude or phase shift. Maybe the most famous dynamic mode is represented by intermittent non-contact AFM often referred as tapping mode. Here the cantilever is excited by a piezoactuator to oscillate at a frequency near to its mechanical eigenfrequency (10–500 KHz). The tip oscillation has an amplitude of 20-100 nm, and is progressively reduced in order to achieve an intermittent contact ("tap"). The tip-sample interaction is measured by the frequency shift. This induces high sensitivity for the existing forces and provides higher lateral resolution to the technique. In addition the reduced tip-sample contact and minimal lateral forces reduce the tip degradation. Unfortunately the limited contact does not allow current measurements in tapping mode. Similarly also SCM, MFM and KPFM are based on dynamic modes where long-range force (E field, H field and contact potential) are responsible for the cantilever deflection. On the other hand, C-AFM and SSRM require a physical contact to exist between tip and sample. They belong to the family of contact modes and enable the recording of an electrical current flowing in the tip-sample system. Recently, static and dynamic modes have been combined into a powerful hybrid technique named Peak Force TappingTM, this will be introduced in Sect. 3.4. Finally, due to the growing interest in confined volumes

characterization in Sect. 3.5, we discuss the original experimental work to achieve 3D analysis using SPM. This is done in view of the extensive use of this technique in the following chapters particularly for the observation of conductive filaments in resistive switching memory.

3.2 Conductive Atomic Force Microscopy

C-AFM is a sensing technique to probe local conductivity variations in high to medium resistive samples such as thin dielectrics deposited on conductive substrate (e.g. n-doped Si for example). A conductive tip is scanned in contact with a biased sample, meanwhile the topography and current are simultaneously recorded. The conductive tip is used as a virtual electrode scanning at constant force onto the sample surface. The lateral resolution in this configuration is determined by the radius of the tip-apex (tens of nm). The current noise level is determined by the low-noise current amplifier and by the stability of the tip-sample electrical contact. A typical value for the AFM scan size varies from $100\times100~\text{nm}^2$ to $10\times10~\text{μm}^2$. In this area C-AFM enables the direct correlation of local topography and electrical properties. A schematic representation of the C-AFM setup is illustrated in Fig. 3.2. C-AFM has two modes of operations: the imaging- and the spectroscopy-mode.

Imaging mode—when used in imaging mode, the current flowing through the tip is recorded while the tip is scanned on the biased sample. The bias is applied to the sample and the tip is grounded (connected to the virtual ground of the current amplifier). The result is a nanometer-resolved image where morphology and conductivity of the sample are correlated. Since the tip is physically dragged on the sample surface, mechanical parameters such as tip-velocity, load force, surface quality and applied bias determine the tip degradation. The tip velocity is imposed by the scan

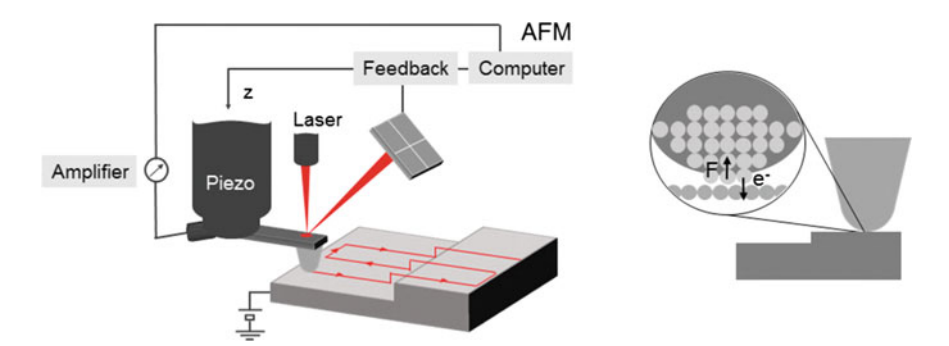


Fig. 3.2 *C-AFM schematic.* Based on contact mode AFM, during the measurement the tip experiences a repulsive force due to the physical contact with the surface (as in the *inset*). The sample is biased and the tip is connected to a current-to-voltage low-noise amplifier (C-AFM sensor). In this configuration the electronic current that flows through the tip-sample system is recorded

frequency (e.g. the time for the tip to draw a scan line), the latter is generally kept in range 0.2–1 Hz. The tip load force is strongly dependent on the sample, tip material and application. For example, C-AFM is generally performed from a fraction of nN to several µN while SSRM requires the µN force regime. Surface properties are often independent from the user choice, sample roughness, water affinity and the presence of contaminants can dramatically affect the measurement. For instance an hydrophilic material will easily contaminate the tip apex or a rough sample will accelerate the wear of the tip coating. In the standard configuration C-AFM is usually done in air. The usage of vacuum, controlled humidity and inert atmosphere can improve the result by removing the thin layer of water adsorbed on the tip and sample (meniscus), and minimizing the potential surface oxidation [15]. Finally, the applied bias between tip and sample induces a high electric field under the tip that can affect the results. A notorious case is the tip oxidation induced by a positively biased tip in presence of adsorbed water and therefore OH⁻ groups [16]. Similarly, by reversing the bias, if the sample is prone to oxidation the high field could induce surface modification (hillocks or bumps). This simple effect has been extensively studied as a probe-based patterning technique in literature [4], but it can be very detrimental when undesired. In general when working in air, the voltage is applied negative to the sample and the tip acts as an electron collector. In other words, the degradation of the surface is minimized at the price of a shorter tip lifetime. Additionally, when studying dielectrics layers such as high- κ , the electron barrier is provided by the semiconductor/oxide interface, enabling the study of the conduction band offset between Si and oxide. However, as will be discussed in Chap. 4, due to the bipolar nature of resistive switching (RS) is not possible to limit the C-AFM to operate in a single polarity.

Spectroscopy mode—in this configuration the tip is held steady in position in contact with the sample (constituting a nanosized capacitor). A voltage is ramped and simultaneously the current is measured thus recording current–voltage (I–V) and current–time (I–t) characteristics. In a simple approximation the setup is described by a capacitor (C) in parallel with a resistor R. Depending on the application it can be relevant to divide the R in the series of resistances representative for the tip, the sample and the back contact. This is the case of SSRM, where the tip-sample resistance has to dominate the series of resistances to successfully measure [17]. Also in case of conductive filament (CF) formation, the tip resistance has a primary role since it will limit the current flowing into the CF during the tip-induced operations. The speed of the voltage ramp is limited by the presence of the tip capacitance (\approx pF), inducing a displacement current $I_{disp} = CdV/dt$. Such displacement current scales linearly with the ramp speed and it adds to the measured current. For this reason, the voltage is generally swept in a quasi-static DC mode at a rate of 10 V/sec at maximum. An example of the two imaging modes is provided in Fig. 3.3.

Independently from the mode, the electronics of the AFM is limited to a voltage range from -12 V to 12 V. Current-to-voltage (transimpedance) linear amplifiers are preferred for current sensing in view of their faster response to the input changes. This generally imposes some limitations for their dynamic range and for this reason

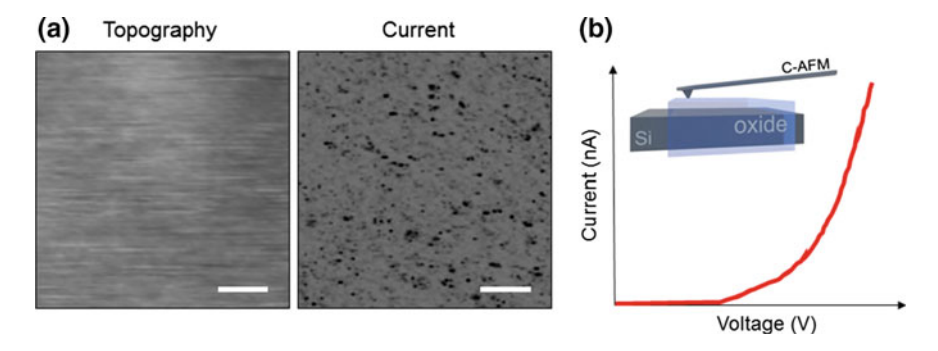


Fig. 3.3 *C-AFM operation modes.* **a** In imaging mode the topography (z range 2 nm) and current (z range 50 pA) is reported for a thin SiO₂ layer (1.5 nm) grown on n-type Si (scan bar 200 nm). **b** The output of the spectroscopy mode is the tip-sample I–V characteristic

more than one amplifier is often required depending on the application. The C-AFM sensor measures current from 100 pA to $1\mu A$ while tunneling AFM (TUNA) sensor records current from 1pA to 100 pA. The maximum measurable current does not limit the current that flows in the tip-sample system, although the sensors have an internal 1 k Ω resistor to limit the current below 1 mA and to protect the hardware. Later in this chapter, the parallel use of multiple linear amplifiers is proposed in order to extend the dynamic range with no impact on the scan speed. Thanks to our custom configuration in this work we could access current sensitivity from 1 pA/V up to 100 μ A/V leading to measurable current from 1 pA to 2 mA. In this dissertation different AFM systems have been used: Digital instrument Dimension 3100 (Bruker), EnviroScope AFM (Bruker), Dimesion Icon (Bruker) and Agilent 5500 AFM (Agilent). Various operational modules have been alternatively applied: C-AFM, TUNA and Peak Force TUNA (Bruker), Resiscope (CSI) and external variable gain amplifiers (FEMTO DHPCA-100). For the sake of simplicity whether not specified with the term C-AFM we refer to any of the aforementioned sensors.

3.2.1 Conductive Tips

Thanks to the major advance of semiconductor fabrication processes, AFM tips are generally manufactured starting from silicon. Alternatively silicon nitride is used for the tip body, the cantilever (spring) and also for the tip-apex. For the electrical measurements however, the silicon tip-apex is not a good solution due to oxidation of silicon in air. Therefore, for electrical SPM the tip is coated with a thin metal layer after fabrication. Originally, in view of their inertness noble metals such as gold or platinum have been used, tip radii of 20–50 nm have been achieved. They are still very common for dynamic electrical modes such as KPFM or SCM, but due to fast wear of the coating those tips are not commonly used in contact modes.

Alternative coatings such as Al, Pt/Ir, Pt/Si, Cr, Co/Cr, TiN, W and diamond have demonstrated improved performance [18, 19]. All metal tips have been proposed too [20]. Interesting new concepts have been recently suggested, carbon nanotubes and nanowires for an increased lateral resolution [21], or small metallic inclusion at the apex of tip coated by a thin oxide [22]. Although in an exploratory phase these solutions can considerably improve the resolution of the measurements.

When contact mode is combined with high load forces, the only viable solution to limit tip wear is represented by doped-diamond tips. There are two major solutions proposed: (1) a CVD coating of diamond nanocrystallites combined with an in-situ gas-phase boron doping. This results in an increased tip radius due to the average size of the crystallites (20–50 nm). In addition, despite the diamond coating, the Si tip can still be fragile, and commercially available high aspect ratio diamond coated tips can break close to the apex. (2) The other solution is offered by the full diamond tips (FDT) where molding technique is used to fabricate a bulky diamond tips which offer better resistance to wear [23, 24]. They also demonstrate excellent spatial resolution \approx 5 nm since the apex of the tip may consist of a single nanocrystal enhancing the tip sharpness [25]. In-house fabricated diamond-tips (FDT) have a low aspect ratio pyramidal shape that provides an enhanced mechanical stability enabling superior performance in SSRM or high force C-AFM. The current design of FDT uses a Ni cantilever with integrated boron-doped diamond pyramids. A pyramidal mould is patterned on silicon wafer and filled with diamond deposited by hot-filament CVD (HFCVD). A gap-phase boron doping during the HFCVD deposition allows the resistivity of the diamond layer to get $\approx 0.005 \Omega$ cm [25]. Three tips are mounted on different cantilevers to provide different spring constant (k) values as shown in Fig. 3.4a. As discussed in the following sections the usage of FDT for C-AFM can

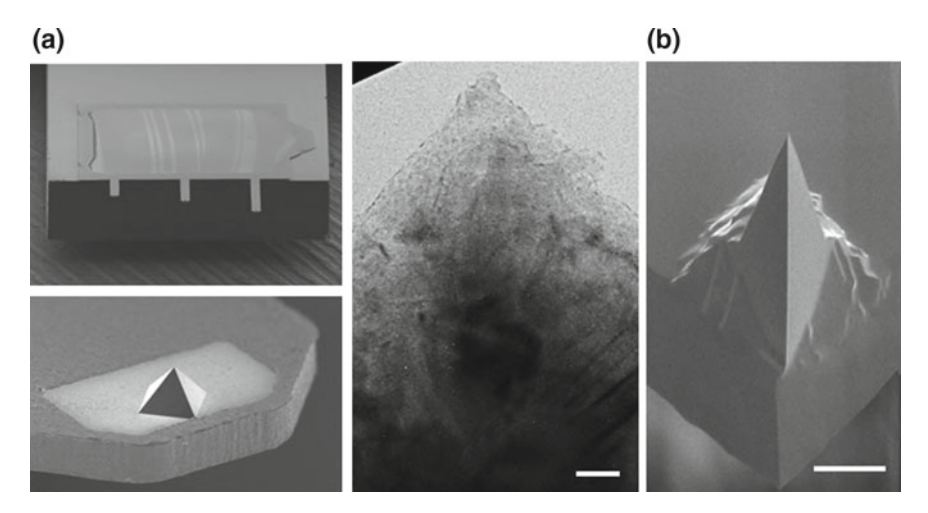


Fig. 3.4 Scanning electron microscopy of conductive tips. **a** Mosaic of boron-doped diamond tip (FDT). The three-cantilever design and the pyramidal tip are shown in SEM. TEM cross-section shows details of the tip-apex (scale bar 20 nm). **b** Commercial metal coated Pt/Ir tip (scale bar 5 μ m)

be beneficial for their high electrical resolution as described in Sect. 3.3, and for the application of high load forces (scalpel SPM).

Due to existing physical contact between tip and sample the stiffness of a cantilever is very important for C-AFM. The stiffness is given by the spring constant, and for a rectangular cantilever this can be calculated with:

$$k = \frac{Ewh^3}{4l^3} \tag{3.1}$$

where E is the Young's modulus of the cantilever material, h is the thickness, w is the width and l the length of the lever. The tip spring constant is a variable parameter and it ranges from below 0.01 N/m to hundreds of N/m. In Fig. 3.4 full diamond tip (a) and commercial Pt/Ir coated tip (b) are shown. For the type of applications in this dissertation, the range of spring constant goes from 2–30 N/m and the experimental work is done with both types of tips shown in Fig. 3.4.

3.2.2 Contact Forces

The quality of the physical contact existing between the tip and the sample reflects on the topographic and electrical images. Contact mode AFM relies on the repulsive force regime acting on the AFM tip. Similar to any mass and spring system the deflection of the cantilever can be described by the Hooke's law. The normal force acting on the tip is calculated by multiplying the spring constant with the deflection, where the tip spring constant (k) is a variable parameter depending on tip geometry and material. The final position of the tip is provided by the equilibrium of forces acting on the tip-sample system. Attracting long-range forces have to be compensated by short-range repulsive force and the force exerted by the cantilever (spring) has to be summed (Fig. 3.5a).

Electrostatic forces (F_E) are generally considered long-range forces because they can influence the tip at a mesoscopic scale (the whole cantilever), although their main contribution is due to the E field fringing induced at the tip-apex (inset Fig. 3.5b). While Van der Waals forces based on dipoles interaction, are considered at the limit between short and long range forces since they don't act only on the tip-apex but they don't affect the whole cantilever ($\approx 10\,\mathrm{nm}$ interaction range) [26]. However, when working in air, the force exerted by the layers of absorbed water, surface contaminates i.e. meniscus (F_M) or capillary force, become dominant.

In the presence of an external voltage, the tip-sample capacitor will experience also an electrostatic force. In the simple approximation of a parallel plate capacitor, the electrostatic force experienced by the tip can be approximated by:

$$F_{elect} = \frac{Q^2}{4\pi\epsilon_0 kd} \tag{3.2}$$

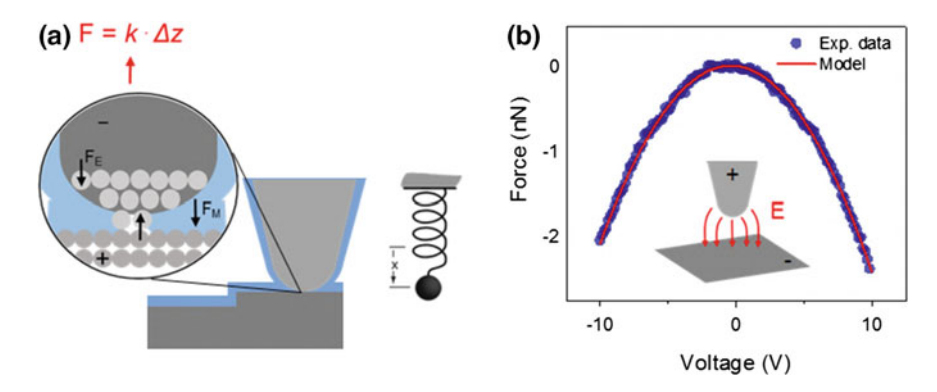


Fig. 3.5 Force balance on the AFM tip. **a** Schematic of attractive and repulsive forces acting on a contact AFM measurement. The force exerted by the cantilever is chosen in order to minimize the resulting force but avoiding the tip jump-of-contact. **b** Electrostatic force experimentally measured on a Pt/Ir tip having a *k* value of 0.2 N/m. The tip is lifted (non-contact few nm from the surface) and the cantilever deflection is measured as function of the applied voltage

In which $Q^2 = C^2V^2$ is the square of the charge stored in the capacitor, ϵ_0 is the dielectric constant of the air, k the dielectric constant of the oxide layer and d the thickness of the oxide. By inserting some reasonable numbers for the capacitance (\approx pF), oxide thickness (d = 3 nm), SiO₂ as oxide (k = 3.9) and voltage (V = 5 V) the approximated electrostatic force lies below 5 nN. It is worth noting that in a standard C-AFM measurement the force acting on the tip goes from tens to hundreds of nN, therefore the contribution of the electrostatic force does not affect the results unless a soft tip and smaller forces are involved e.g. organic materials. However, the presence of the electrostatic force can be easily measured by lifting the tip (in non-contact few nm far from the surface) and observing the tip deflection as a function of the applied voltage. In this configuration every added force during the voltage sweep induces a measurable deflection on the tip. Figure 3.5b shows an example using a Pt/It tip having k = 0.2 N/m. The quadratic dependence of the force with the voltage is clearly visible as the experimental data are fitted with a simple $F_{elect} = \alpha Q^2$ function.

Van der Waals forces originate from dipole-dipole interaction (inset Fig. 3.5a). Their decay distance is considered in the order of few nm (\approx 10 nm) [26]. Their intensity is however limited to few nN and thus not exactly relevant in this context [1]. On the contrary the presence of a thin layer of absorbed water vapor on the tip and the surface induces capillary forces. As reported elsewhere, [27, 28] their maximum contribution can be estimated as:

$$F_{max}^{capil} = 4\pi R \gamma cos\theta \tag{3.3}$$

where R is the radius of curvature, γ the surface tension of the absorbed liquid, and θ the contact angle. As reported by Stifter et al. [28] capillary forces can reach tens of nN and therefore they are more relevant of Van der Waals forces. They represent a lower

limit for the minimum force applied between tip and sample when working in air, because they have to be compensated by the repulsive force. Owing to this, humidity in contact mode AFM affects contact size and degrades the lateral resolution. Due to the absence of the absorbed meniscus layer in ultra-high vacuum conditions, it has been often reported an improved (topographical) resolution. Another solution to remove the capillary forces is the immersion of tip-sample and the measurement in liquid (not easily applicable to electrical modes). Finally, short-range forces can arise from the overlap of electron wave functions or ionic interaction. They can be attractive or repulsive although their short extension (<1 nm). Those forces are generally in the order of few nN and therefore they affect more dynamic AFM modes (non-contact).

3.2.3 Artifacts in C-AFM

In this section the possible artifacts of C-AFM are discussed. In common to all the AFM techniques, topography artifacts arise mostly from the tip geometry. As introduced in the first section of this chapter a degraded tip apex limits the lateral resolution of the topographic features. This is the most common artifact in contact AFMs; such that can limit the observation of the convolution between the real surface and the tip apex. This impacts on the size, shape and aspect ratio of the measured object. For example a spherical shape could appear as a square if probed with a blunt tip. Figure 3.6a shows the case of a 3×3 array of Si cylindrical nanopillars

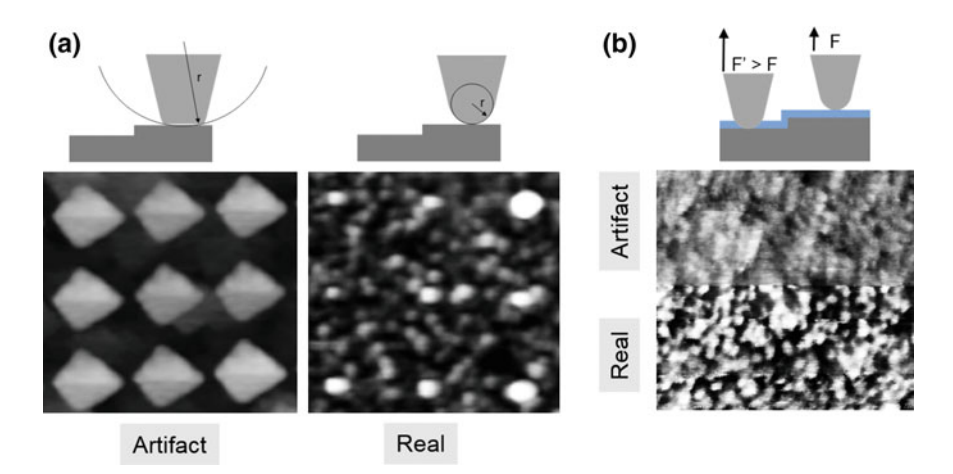


Fig. 3.6 Topography artifacts in C-AFM. a Comparison between a blunt and a new tip in imaging the topography of vertical Si nanopillars (z range 30 nm, scale size = $1.3 \times 1.3 \ \mu m^2$). **b** Highly porous Si is imaged using low and high load force respectively for the *top* and *bottom* half of the scan (z range 5 nm, scan size = $300 \times 300 \ nm^2$)

the information on their shape is completely lost due to the squared tip-apex. More complicated geometries, such as multiple tips can create fake repetitive features in the acquired image. A detailed treatment of morphological artifacts for dynamic and static AFM modes can be found in the work of Meyer [1]. Another common artifact in contact mode AFM, is induced by the absorbed layer of water (meniscus) on the sample surface. In Fig. 3.6b the micro porosity of a Si surface is imaged; a low force is used for the top half of the image and the force is increased in the bottom part. The thin meniscus layer shields the observation of the fine porosity inducing the tip to scan on the water layer. In both cases the tip experienced a repulsive force regime although only the highest load force enabled a good imaging. It is clear from these examples that the optimal combination of tip and load force can be determined only once the sample and its properties are well known.

Beside the topography, in C-AFM also the current channel can be affected by artifacts. A standard C-AFM current map is shown for a thin (3 nm) SiO₂ layer scanned by a biased-tip in (Fig. 3.3a). The result is a uniform and random distribution of leakage spots in the current map. The electrical resolution, treated more in detail on Sect. 3.3, can be defined by the portion of the tip-sample contact-area having minimum resistance for the current. The size of this conductive spot in C-AFM ($\approx 10 \, \text{nm}^2$) has been experimentally evaluated [29]. This area can be thought as the conductive spot through which the current is physically flowing. Once this area comes across a conductive area of the sample there will be a geometrical convolution between the conductive spot and the surface conductive feature. This leads to the existence of electrical artifacts (similar to the topographic) depending on the geometrical shape and quality of the electrical contact area. This will affects the electrical analysis with artifacts directly visible on the C-AFM current map (Fig. 3.7).

In common with the morphological artifacts induced by tip-shape effect (Fig. 3.6a), a degraded electrical contact area will affect the conductive lateral resolution. In these situations all the conductive features in the current map will appear with the same shape (Fig. 3.7a). This condition is often not recoverable and the tip has to be changed. Another possible source of artifacts is the contamination of the conductive tip with a consequent increase in the tip-sample contact resistance. Two cases can be observed: (1) a partial contamination, leading to tip-contact resistance enhancement and (2), a full contamination leading to tip isolation. Working in air and especially for hydrophilic materials (high- κ or organic materials) this is a common artifact due to the presence of meniscus and other contaminants on the surface. The first type of contamination can be identified due to a progressive reduction on the intensity in the measured current during continuous scan or alternatively, for the evolution of a fully conductive spot into a spiked-type of conduction (Fig. 3.7b, c). Since the partial tip contamination does not completely insulate the tip, this artifact can be more difficult to identify as compared to the second. Indeed, when the tip completely loses its conductivity, the current map shows a sudden change similar to Fig. 3.7b but more severe. Different solutions can be proposed to get rid of the tip contamination such as increasing the load force on the cantilever trying to remove the contaminant, this can be done in scan mode or also in repeated point-contact mode alternatively with or without voltage applied. Finally when operating C-AFM with soft cantilevers,

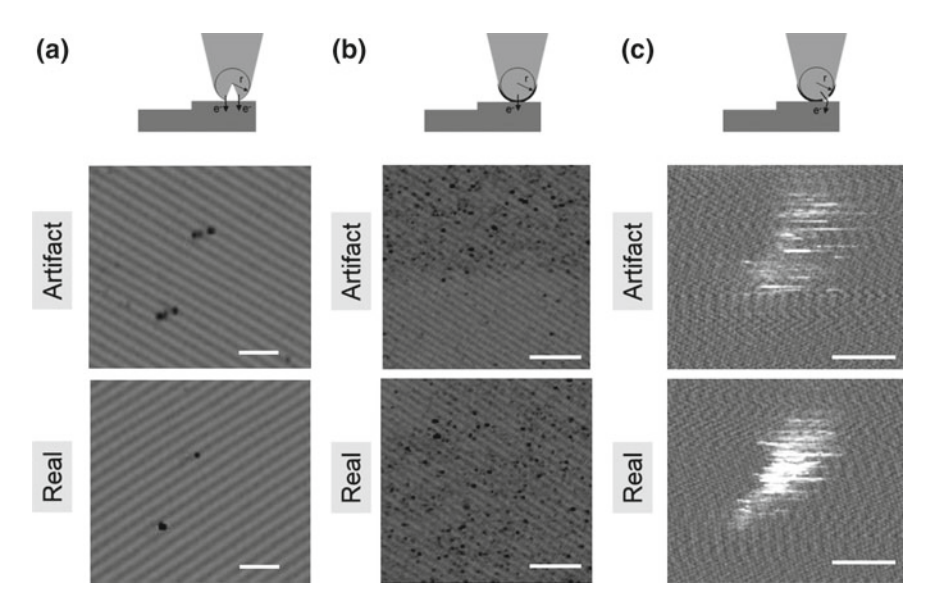


Fig. 3.7 Electrical artifacts in C-AFM. **a** Electrical version of the tip geometrical artifact, two single conductive spots imaged by a degraded tip with a double electrical contact are imaged as multiple spots (z range 20 pA, scale bar 10 nm). **b** Uniform contamination of the tip results in an enhanced tip-sample contact resistance inducing a (sudden) decrease in conductivity (z range 10 pA, scale bar 500 nm). **c** Partial tip contamination can induce a partial loss of conductivity reflected as a peaked-signal when scanning a conductive spot (z range 50 pA, scale bar 20 nm)

frictional and lateral forces can induce severe bending. These effects are known to induce in topography artifacts known as parasitic deflection [1, 5]. They can effect the electrical contact area inducing an undesired enhancement of the tip-sample contact resistance similar to the partial tip contamination. Meyer [1], proposes the usage of triangular cantilever in these cases to minimize the impact of lateral forces.

C-AFM has often been described as an STM whereas the vacuum gap between tip and sample is replaced by a thin oxide [10]. As such the tunneling current through the thin dielectric can be measured and the defects states probed. The presence of highly conductive features in a insulating material can induce a proximity-effect leading to lateral transport due to tunneling currents that contributes to an overestimation of the conductive spot. This can be seen in Fig. 3.8a where a conductive wire, (for instance a CF) appears as a circular conductive spot. Due to the high conductivity of the metal, the tip will start to experience a tunneling current already when in proximity of the wire. The exponential decay of the tunneling current will lead to an overestimation of the spot size in the order of ≈ 1 nm. This type of artifact becomes relevant when the features investigated are within the $10 \, \mathrm{nm}^2$ regime. The last electrical artifact described can be considered more an instrumental effect, due to the AFM electronics. However this is a relevant artifact because it can easily be confused with a real physical measurement. As introduced in Sect. 3.2, the reduced dynamic range of

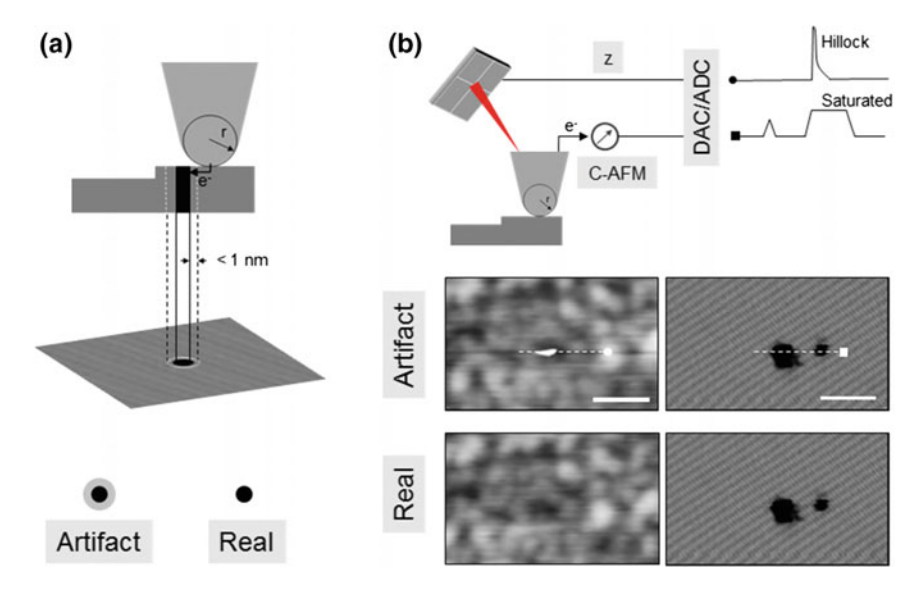


Fig. 3.8 Technique induced and instrumental artifacts in C-AFM. **a** Electrical resolution of C-AFM can be enhanced when the tip goes in proximity of a highly conductive region due to a lateral tunneling effect. **b** Hillocks in topography can also appear when the current amplifier saturates due to channel coupling in the DAC and ADC converters with the AFM controller. In the example a breakdown spot in $10\,\mathrm{nm}$ TiO₂ is investigated (scale bar = $100\,\mathrm{nm}$). Hillock appears in correspondence of pixel saturated in current map. A second scan with reduced or null bias, avoids the sensor saturation and confirm the absence of any standing surface modifications

linear amplifiers is the price to pay for their fast response. This implies that a (standard) C-AFM amplifier, will often saturate during measurements if the current exceeds the value of 1 µA. Fast (100 kHz) and ultra-low noise digital-to-analog (DAC) and analog-to-digital (ADC) converters are used for fast acquisition of the x-y scanning and the z deflection in many AFM designs. Similarly, also the electronics of the C-AFM sensor lies in the same circuit. The saturation of their inputs induces the generation of a saturated output acting as a parasitic also for the z deflection signal. This induces the formation of an artificial spike signal erroneously converted by the AFM controller as a hillock in topography. The effect is very distinctive and it can be seen as one or more spikes in the topography map in correspondence of the saturated pixels in current (Fig. 3.8b). In essence, the observed hillocks are not real surface modifications and a simple second scan (avoiding the sensor saturation) will show the real surface morphology (Fig. 3.8b). Hillocks have been often related to transient phenomena such as the sudden removal of the electrostatic force during uncontrolled discharge through the oxide. And in this framework, they might be seen as very interesting for a transient electrostatic characterization [30]. But unfortunately this does not correspond to the reality, indeed by connecting the C-AFM sensor directly to a current source, it can be easily demonstrated that when the current injected overcomes the nominal value of 1 µA, hillocks are introduced in the topography. The

latter can be reproduced during scan or even with the tip in false-engage. Finally, the same effect can be also observed at lower current if the sensitivity in the C-AFM sensor is reduced (for example at 101 nA if the sensitivity is set at 10 nA/V = 100 nA max detectable current).

3.2.4 Electrical Lateral Resolution

The lack of a true atomic resolution in topography for C-AFM has been traditionally explained by the fact that the tip-sample contact is larger than atomic dimensions. This is generally true for the topography of all the contact modes, which is assumed to be limited to $\approx\!10$ nm (depending on the tip radius). Unfortunately, in contrast to the physical contact area which can be calculated by geometrical considerations based on tip shape and tip-radius, [26, 31] the effective electrical contact area needs a different treatment as it depends on the local work function, oxide thickness, dopant concentration and pressure distribution. On the other hand, C-AFM as well as SSRM have reported $\approx\!1$ nm electrical resolution as indication of a higher confinement of the electrical processes within the tip-sample contact area. A notorious case illustrating the difference between physical and electrical contact area relates to SSRM, where the confined pressure transformation resulting from the high force applied to the tip, leads to an electrical contact area $5{\text -}10\,\mathrm{x}$ smaller than the geometrical one [32]. Figure 3.9a shows the case of SSRM where a thin 0.5 nm oxide is detectable.

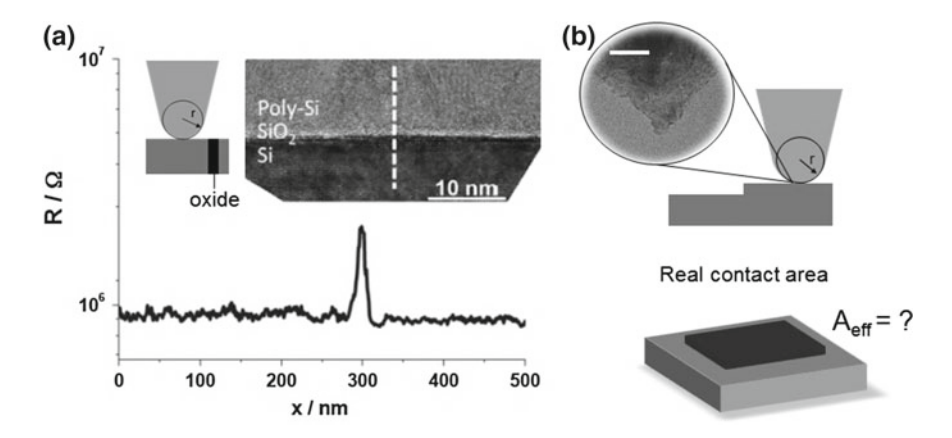


Fig. 3.9 Electrical SPM lateral resolution. **a** Test structure made of an ultra-thin 0.5 nm oxide grown between conductive layers (TEM reported in the *inset*). C-AFM and SSRM can successfully detect the presence of the sub-nm conductivity change in the sample. **b** Schematic for the tip-sample interaction, the effective physical contact area is determined by the contacting asperities of the two surfaces. In the *inset* the tip apex is imaged by high-resolution TEM showing the presence of diamonds crystals covering the tip-apex (scale bar 20 nm)

In principle the tip contact area could be estimated from the tip shape and its end radius in agreement with continuum mechanics models [17]. However the underlying assumption of a perfectly smooth surface interacting with an hemisphere, is rarely justified as both surfaces typically have some asperities. Hence, the real interaction area differs from the theoretical calculation and in particular for the electrical measurements might be more dominated by the tip-surface asperities rather than by the global contact area. The main consequence is that the effective contact area, which can be considered as the size of the virtual tip-sample capacitor (Fig. 3.9b), will be much smaller than the real contact area. Since the effective contact area is frequently a parameter required for the quantitative interpretation of electrical results, we present in this section a procedure for its evaluation (Fig. 3.9b). The latter is based on the I-V curve measured with C-AFM on a 1.5-nm-thick SiO₂ film grown on Si. From this curve we extract the electrical contact area for commercial platinum (Pt/Ir) tips as well as for our in-house developed doped-diamond tips [29]. The conductive tip is used as a virtual metal electrode scanning in contact onto the sample surface. Its effective electrical contact area is primarily related to the asperities interacting between the tip and the surface. As shown in Figs. 3.4b and 3.9b for the case of diamond tip, the presence of the diamond nanocrystals at the tip apex create an effective electrical contact area which will be hardly predictable with traditional Hertz contact theory. In this section we evaluate the effective electrical contact area of the tip-sample nanocapacitor (Fig. 3.9b) and provide quantitative values for two commonly used C-AFM tips. We characterize the electrical contact area for coated metal and doped-diamond tips operated at in contact mode with load forces < 200 nN. In both cases we observe that only a small fraction ($<10 \text{ nm}^2$) of the physical contact ($\approx 100 \text{ nm}^2$) is effectively contributing to the transport phenomena. Assuming this reduced area is confined to the central area of the physical contact, these results explain the sub-10 nm electrical resolution observed in C-AFM measurements.

3.2.5 Effective Emission Area Evaluation

From Celano, U. et al., *Journal of Applied Physics*, 117(21), 214305, 2015.

To accurately quantify the electrical contact area, we measure point contact I–V curves on a 1.5 nm-thick oxide layer, and we fit them with a Fowler Nordheim tunnel (FNT) [33] model for thin dielectrics [34]. In FNT the current through the oxide is described as field assisted tunneling through the barrier formed at the injection electrode-oxide interface and has an explicit dependence on the emission area of the electrical contact (equal to the tip electrical contact area in our configuration). In view of the relation between the current and the oxide thickness, this model was originally introduced by Frammelsberger et al. [34] for the oxide thickness calibration of thin oxides, whereby the Hertz contact theory was used to estimate a value for the electrical contact area within the FNT equation and the oxide thickness was calculated as a fitting variable. Depending on the coating or shape of the tip e.g. Co/Cr, Pt/Ir or diamond, the values for the emission area in literature range from 10 to 500 nm² [34, 35].

Our approach is exactly the opposite in the sense that we fix the thickness (1.5 nm) of a very well know material system (Si/SiO₂) and use the FNT-model to fit the I-V characteristics as obtained with C-AFM whereby the only unknown variable in this fit is the effective electrical contact area. The C-AFM measurements are performed in high vacuum ($\approx 10^{-5}$ mbar). We bias the sample negatively and ground the tip, in order to achieve substrate injection and minimize tip-induced anodic oxidation [36]. Commercial Pt/Ir coated tips and FDT have been used at load levels in the range ≈50–150 nN which are representative values for contact-AFM. For an accurate estimate of the load force, the spring constants and deflection sensitivity of both cantilevers have been experimentally calibrated. The Pt/Ir commercial cantilever has a value of k = 5.24 N/m whereas the diamond-tip shows k = 7.5 N/m. The oxide thin film used is a thin SiO₂ film grown on a n-type Si substrate with a thickness of 1.5 nm as determined with ellipsometry and X-ray photoemission spectroscopy (XPS). The roughness of the sample is ≈ 0.12 nm RMS over 1 μ m scan size as determined with tapping AFM. In Fig. 3.10a the measured I-V curve is shown together with a fit based on the FNT. It is clear that the latter fits the experimental data quite well. The parameters used in the FNT-description are the standard ones relevant for our SiO₂-Si system, i.e. the SiO₂ thickness is set to 1.5 nm, the SiO₂/Si energy barrier for electrons (Φ_B) is considered to be 3.25 eV and the electron effective mass (m_{eff}) is chosen as $0.42m_e$. It is important to clarify that this evaluation procedure could be extended to other material systems, provided that the set of parameters used for the fit are accurately known. In particular due to the exponential dependence of the tunneling current with the dielectric thickness, the latter is the most sensitive parameter in order to extend the usage of the proposed method. The FNT current approximation is based on the description proposed by Schuegraf and Hu. and co-workers [33]. In this formulation the FNT model is optimized for oxides below 2 nm and has a correction factor taking into account when one is in the direct tunnel (DT) regime $(V_{ox} < \Phi_B/q)$

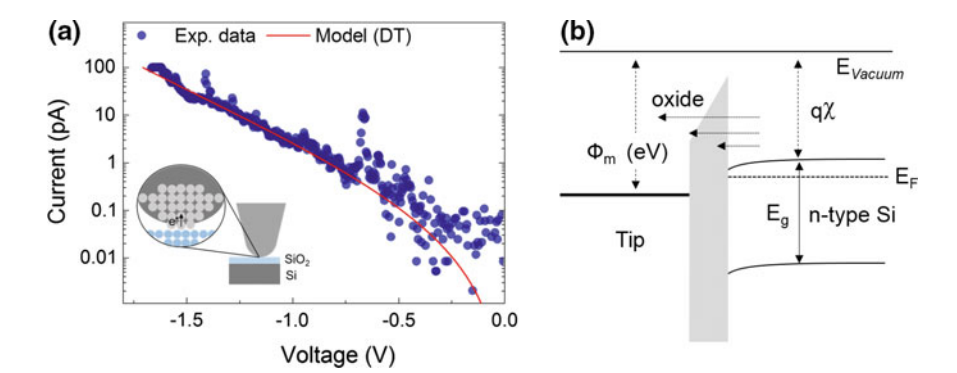


Fig. 3.10 Area evaluation procedure. **a** I–V curves as measured with C-AFM versus a fit based on Fowler Nordheim tunneling. In the *inset* the tip-sample configuration is shown; the tip is grounded and the bias is applied to the sample with the n-type Si in accumulation as in **b** the idealized band diagram

or in the FNT regime $(V_{ox} \ge \Phi_B/q)$. In this description, V_{ox} is the voltage drop across the oxide, Φ_B is the barrier height in electron volts for substrate injection of the electrons, and q the electron charge. Owing to the flatband voltage (V_{FB}) and the band bending in the silicon (V_{Si}) during the bias ramp, the voltage drop across the oxide (V_{ox}) is only a fraction of the total voltage applied (Fig. 3.10b). Indeed a fraction of V_{tip} is used to balance the work function difference between tip and substrate (Φ_{ms}) whereas the substrate surface potential (Ψ_{si}) is considered negligible since the n-type Si will be in accumulation. Therefore V_{ox} is equal to:

$$V_{ox} = V_{sample} - \Phi_{ms} \tag{3.4}$$

where $\Phi_{ms} = \Phi_m - \chi$ and Φ_m is the work function and χ is the electron affinity of the substrate (4.05 eV) [37]. On the basis of these considerations, the I–V curves measured with C-AFM have to be shifted with the amount ($\Phi_m - \chi$) in order to represent the real I–V dependence. This poses the problem of determining Φ_{ms} . To this end we have used KPFM on a freshly cleaved highly ordered pyrolytic graphite (HOPG) surface for the calibration of the tip work function. The results indicate for the Pt/Ir-tip a work function of 4.75 ± 0.05 eV and for our diamond tip a value of 4.1 ± 0.05 eV. Figure 3.11a,b shows the measured I–V curves together with I–V curves estimated with the FNT model using different sizes of the electrical contact area. The I–V curves related to the Pt/Ir tip are shifted over 0.7 V ($\Phi_{ms} = \Phi_m - \chi = 4.75-4.05$ eV) and plotted in Fig. 3.11a. Two different data sets are compared related to two different load forces (78 and 157 nN). In both cases the effective emission areas are below 10 nm² while nevertheless a clear increase of the effective emission area with increasing load force is observed. This translates for the Pt/Ir tip assuming a circular electrical contact area into a contact radius of ≈ 0.69 nm at 78 nN and ≈ 0.97 nm at 157 nN.

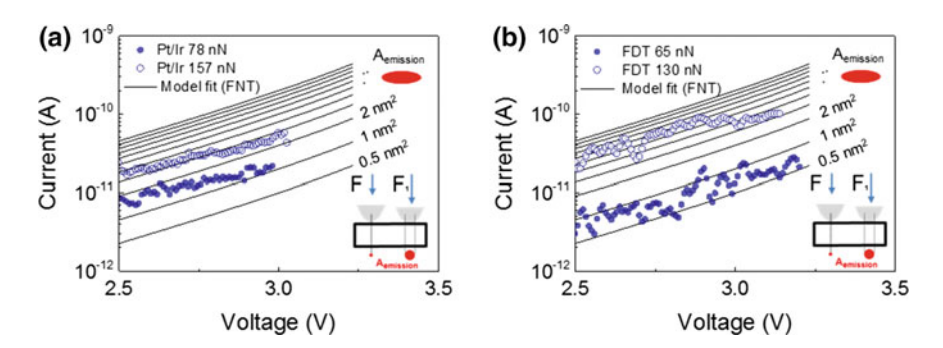


Fig. 3.11 FNT fit evaluation. I–V curves recorded for different forces on the Si/SiO₂/tip-MOS system using (a) Pt/Ir or (b) diamond tips. Theoretical I–V curves based on the FNT-model are added to the plot having as (changing) parameter the electrical contact area

For our diamond tips we observed a tip work function of $\Phi_{ms} = 4.1$ eV. The I–V curves relative to the diamond tip are offset of 0.05 V ($\Phi_{ms} = \Phi_m - \chi = 4.1 - 4.05 \text{ eV}$) and plotted in Fig. 3.11b. At a load force ≈ 65 nN the tip shows a remarkably small electrical contact area of 0.5 nm² which is equal to an (circular) electrical contact radius of ≈ 0.39 nm. This very small value might originate from the micro roughness of the diamond tip which can induce the electrical contact at one single diamond crystallite under moderate pressure. Increasing the load force to ≈130 nN the area increases to 4-5 nm² leading to an electrical contact radius of ≈1.11-1.26 nm. A comparison between the contact area obtained by continuum mechanics model and our experimental evaluation is presented in Fig. 3.13a. In Fig. 3.13a the continuous line represents the simulated Hertz contact model for a diamond tip with 30 nm tip radius. The experimental values for DMT model were estimated for our full diamond tips using the pull-off forces extracted at different load forces according to model proposed by Carpick [38]. The evaluations are done in the range of load forces 0-500 nN. Note, the range of load forces is limited to 500 nN to avoid damages on the ultra-thin SiO₂ layer. Our results demonstrate that the electrical contact area is much smaller than the estimated physical contact area, implying that only a fraction of the contact area contributes to collect current, likely the point of higher pressure. These evaluations for the contact area are consistent with the apparent electrical resolution obtained with these probes. For instance in Fig. 3.12a, b we use the (calibrated) tips to scan at a constant bias across the surface of the 1.5nm-thin SiO₂ layer.

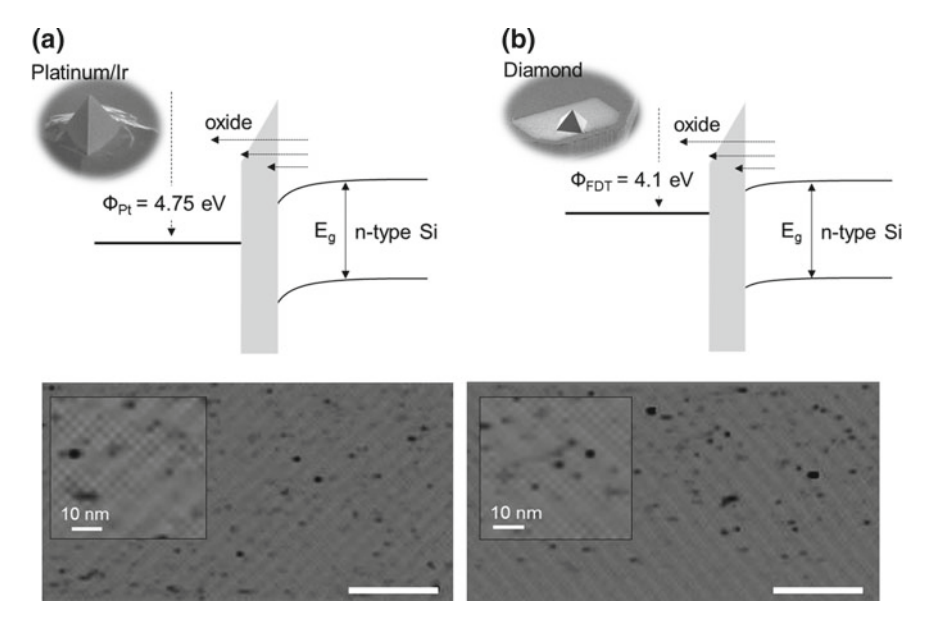


Fig. 3.12 Experimental evaluation $\bf a$ Idealized band diagram for the n-type Si with substrate injection for the case of the Pt/Ir tip and $\bf b$ doped diamond tip using the experimental work functions. The two tips are also used to image sub-10 nm features in a stressed SiO₂ 1.5nm-thick layer (scale bar 100 nm, z range 10 pA)

Both tips are scanned at a load-force ≈ 100 nN with a negative bias (-3V) which is applied to the sample. The inset shows the idealized band diagram for the experiments (substrate injection on n-type Si) for both Pt/Ir and diamond tips. The recorded current maps show current variations due local deficiencies in the oxide leading to larger/smaller leakage currents. Within these maps features as small as 10 nm² can be observed. Realizing that the size of these features are already too large due to the convolution of the tip area and their intrinsic dimension, it is fair to state that the electrical contact area must be smaller than 10 nm² consistent with our calibration procedure. It has to be mentioned that the proposed method is intrinsically based on a point-contact IV curve, and the extracted contact-area values can be considered valid for point-contact electrical measurements. During AFM scanning conditions these values can be slightly different due to lateral-forces, friction, tip-contamination and other factors, but the consistency observed in the experimental observation between predicted values and observed conductive-spots sizes in Fig. 3.12a, b are good indicators for the consistency of our method. It is worth noting that the FNT fit for FDT tips shown in Fig. 3.11b follows the fitting trends with more fluctuation as compared to Pt/Ir case. The same effect can be observed also comparing the I–V characteristics of the two types of tips in Fig. 3.13b. The scattered transport in FDT compared to Pt/Ir it is ascribed to the higher presence of defects states and grain boundaries in the boron-doped diamond layer (inset Fig. 3.13b). Those are responsible for the noisy current fluctuation which can be detected measuring small currents and are finally converted in the scattered FNT fitting of Fig. 3.11b.

Our results are also in line with the pioneering results of Salmeron, [39] who could demonstrate atomic resolution on graphite using the contact current channel of a C-AFM which can only be possible by assuming an ultra-scaled electrical contact area as small as 0.9 nm. Using our procedure electrical contact areas below

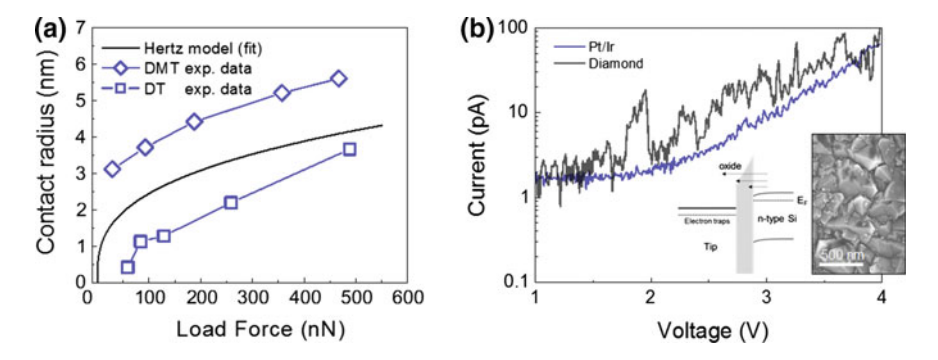


Fig. 3.13 Contact area models comparison. **a** We compare our observation with two continuum mechanics models: (1) standard Hertz contact model and (2) Derjaguin–Muller–Toporov (DMT). **b** I–V curves (on log scale) acquired with the Pt/Ir tip and our diamond tip. Note, the different fluctuations in the measured current which are consistently higher in the case of the diamond tips. This is likely due to the higher presence of defects states in the doped-diamond tips as compared to Pt/Ir (inset showing SEM image of the diamond film)

 10 nm^2 are observed for a physical contact of 100 nm^2 . The latter translates into radii ranging from 0.3 (diamond) to 1.2 (Pt/Ir) nm and explains the ultra-high electrical resolution observed in C-AFM electrical measurements. This evaluation procedure can be easily extended to other types of contact mode electrical AFM techniques where the effective size of the tip-sample contact area is an important parameter.

3.2.6 Extending C-AFM Current Range

A current-to-voltage low-noise linear amplifier is the active element for the measurement of current in C-AFM. This is generally realized by a shunt reference resistor placed in the feedback loop of a current-amplifier. Good signal-to-noise ratio (SNR), short integration time (speed) and the ability to measure small currents are among the main requirements for a C-AFM-type of amplifier. A linear amplifier can guarantee most of these requirements, at the price of a small dynamic range (DR). The DR is defined as the difference between the maximum and minimum input level for the proper amplifier operation. The minimum input level is determined by the SNR of the specific amplifier electronics and the maximum input level is limited by the nonlinearity or amplifier saturation due to power supply. This translates in a small DR for the detectable currents in the majority of commercially available C-AFM sensors (generally ≈ 100 pA-1 μ A). One possible solution to widen the DR is the use of a logarithmic amplifier. The latter is currently used for SSRM and offers a larger DR $(\approx 5-6 \text{ decades})$. The main difference with linear amplifiers lies on the usage of a diode (or a nonlinear element) in the feedback loop of the current-amplifier. Unfortunately a nonlinear element in the feedback loop induces large integration time, not acceptable to detect rapidly changing conductive features. In addition, it degrades the SNR in the small currents range not acceptable to detect weakly conductive features. Therefore although with small DR linear amplifiers are the common choice for C-AFM and related measurements. A possible solution to overcome this limitation comes from the parallelization of multiple linear amplifiers covering a wide dynamic range. Parallel linear amplifiers with complementary current ranges can enable the desired DR. For example Blasco et al. [40] replaced the standard hardware of the AFM biasing system with a source monitor units (SMU). In this way they could achieve enhanced current range in point contact measurements taking advantage of the SMU capability. Nonetheless, this approach does not allow scan imaging due to the decoupling of the SMU from the AFM tip-motion system. In this section by using 6 parallel linear amplifiers controlled by a labVIEW interface, we achieve C-AFM acquisition with extended current range from ≈100 pA to 10 mA capability for both imaging and I-V spectroscopy modes. For this purpose we select a commercial FEMTO DHPCA-100 variable gain, high speed current amplifier. It combines 6 switchable transimpedance amplifiers with gain from 10^2 to 10^8 V/A. The bandwidth (20 MHz) and cut-off frequency (10 MHz) enable fast integration time. In addition the possibility to remotely control the switching function by a universal serial bus (USB) controller guarantees the dynamic selection of different amplifier during the

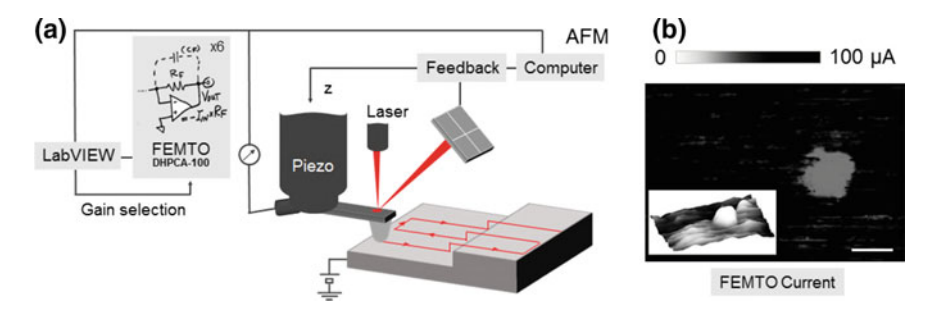


Fig. 3.14 Extended range C-AFM. a Six linear amplifiers in parallel are dynamically selected to increase the input dynamic range of standard C-AFM. The standard sensor is replaced with an external FEMTO DHPCA-100 amplifier directly connected to the tip. b Large current ($\gg 1~\mu A$) is measured on a Pt surface (topography in the *inset*), in correspondence of a contaminant (insulating) particle (scale bar = 250 nm). The current range achieved by using 3 of the 6 FEMTO amplifiers span from ≈ 50 nA to $100~\mu A$

AFM scan. In a simplified configuration the output of the FEMTO amplifier can be directly connected to one of the external inputs provided with the AFM controller. This simple solution does not allow dynamic selection of different amplifiers but can provide large dynamic range using one at a time each amplifier. The other possibility requires the formation of the current map in a second computer equipped with a labVIEW input card for the signal acquisition. This approach enables more flexibility since the selection of the amplifier can be realized by the labVIEW routine depending on the required DR. The simple schematic of our custom design is presented in Fig. 3.14a. By synchronization with the end-of-line pulses of the AFM controller, we select two or more amplifiers to alternatively recorder subsequent scan lines. In this way, after a gain conversion the final image will be constituted of lowly and highly conductive features recorded with the same accuracy. Figure 3.14b shows an example using three amplifiers on a Pt sample. A large insulating contamination particle is visible, in the same image we detect few tens of nA (on the insulating particle) and a maximum current measured on Pt of $\approx 100 \,\mu\text{A}$, this corresponds to a 100× improved detection capability as compared to standard C-AFM sensor.

3.3 Peak Force: Intermittent Contact Mode

An innovative solution to combine the advantage of dynamic and contact AFM modes has been recently introduced with the commercial name of PeakForce Tapping TM mode [41]. The cantilever is driven with a low frequency oscillation (1–2 KHz) creating an intermittent contact between tip and sample (Fig. 3.15a). In each tapping cycle the tip displacement is monitored and tens of force-curves are recorder for each pixel during the few microseconds of physical contact. Here the tip is oscillated at a lower frequency as compared to the mechanical eigenfrequency of the cantilever (\approx 10–500 KHz). The oscillation has an amplitude between 100 and 150 nm excited

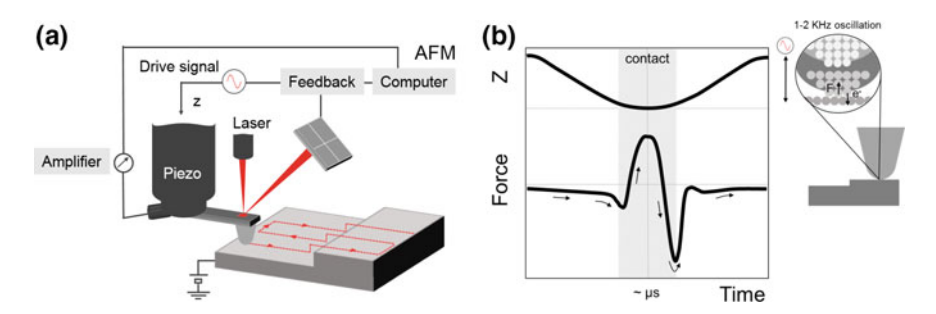


Fig. 3.15 PeakForce TUNA mode. a PFTUNA combines the advantages of dynamic and static AFM modes, by using a low frequency oscillating tip-sample contact. b The tip is oscillated at a \approx 1–2 KHz with an amplitude of \approx 150 nm. During each tap the tip experiences the force shows in the graph, with a fraction of time spent in contact with the sample surface

by the z piezoactuator. The reduced speed of the oscillation enables the sampling of the cantilever deflection at each tap, thus collecting multiple force curves on each pixel. Thanks to the higher bandwidth of the amplifier (≈15 KHz) it is possible to sample the current during the fraction of time spent by the tip in contact ($\approx \mu s$), thus measuring the electrical properties of the sample (Fig. 3.15b). This mode combines a lateral resolution comparable to tapping mode (\approx 5 nm) and the possibility to record the electrical properties of the sample as in C-AFM. In other words the best of two techniques are combined. The advantage is that the sensing of sample properties is done by a static contact mode (cantilever deflection), while the minimization of the deformation depths and later-forces is achieved by a dynamic (customized) tapping mode. The commercial name of this mode is Peak Force Tunneling AFMTM (PFTUNA). Compared to the standard C-AFM it enables higher lateral resolution for the topography and higher precision in the tip positioning due to the introduction of drift correction algorithms. Among other advantages the low frequency oscillation enables the use of various tips without limitation for the mechanical eigenfrequency, it minimizes the tip damages and additionally it also improves the quality of the measurements. Extension of this mode is PeakForce QNMTM (quantitative nanomechanics) that enables the quantitative analysis of material properties such as modulus, adhesion, deformation and dissipation at the nanoscale. The latter is provided by the real time analysis of the multiple force curves collected for each pixel during the PeakForce tapping. Fig. 3.16a, b shows a typical AFM force curves composed of the tip approach (a) and tip retract (b). Force distance curves, generally referred to as force curves, show the evolution of the interaction force experienced by the tip as it gets closer to the sample (approach) and back to the rest position (retract). These two phases are presented as function of the cantilever deflection (y-axis), which is finally converted into force. In Fig. 3.16a black trace, the cantilever approaches the surface. At some tip-sample distance (grey area), the attractive long-range forces become stronger than the tip spring constant inducing the jump-into-contact with the sample. Once the tip is in contact, short-range forces cause the deflection of the cantilever in the repulsive contact region until the value established by the user. During the

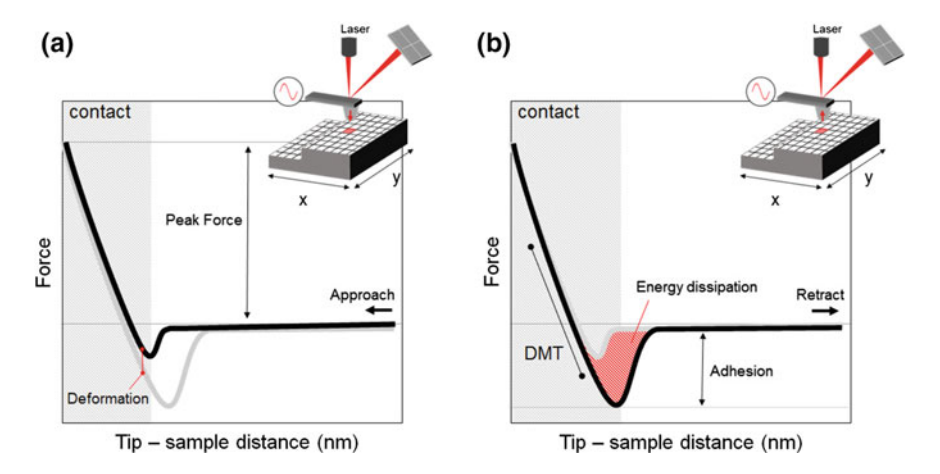


Fig. 3.16 Intermittent force curve. **a** Schematic force interaction of the tip approaching the sample and **b** of the tip withdrawal. The different properties sensed by the intermittent AFM-analysis (e.g. deformation, energy dissipation, adhesion and modulus) are indicated

retrace Fig. 3.16b, the deflection follows the same load curve as the force is released, but the presence of surface adhesion requires higher force to release the tip that goes back to the rest position ready to start another approach. The higher force induces a shift in the jump-out-contact (grey area) as compared to the jump-into-contact as in Fig. 3.16b. By studying a force curve a plethora of information is accessible on the contact quality and sample properties. In PeakForce QNMTM different force curves are collected on each pixel constituting the sample (inset). The online fitting of these curves enable the extraction of reduced Young's modulus, adhesion, deformation and energy dissipation. The reduced Young's modulus E^* is obtained by fitting the contact region of the retract curve (Fig. 3.16b) with the Derjaguin, Muller, Toporov (DMT) model [42] using equation:

$$F_{tip} = \frac{4}{3}E^* \sqrt{R_d^3} + F_{adh} \tag{3.5}$$

where F_{tip} is the force on the tip, F_{adh} is the adhesion force, R the tip radius and d the tip sample separation. The adhesion is calculated on the retrace curve as the force before the tip loses the contact (Fig. 3.16b). The peak force is shown in Fig. 3.16a as the maximum force experienced by the tip during the approach. The deformation caused by the probe on the sample can be estimated by the difference between the two contact branches of the curves approach vs. the retract (as in Fig. 3.16b). Finally, the integral over the oscillation period of the force times the velocity is the energy dissipation. This is considered as the hysteresis between the load and unload curves Fig. 3.16b.

3.3.1 Peak Force TUNA Case Studies

From Celano, U. et al., Microelectronic Engineering, 109, 318–321, 2013.

In this section, the extended capability of PFTUNA are introduced with three practical examples. First, a combinatorial study using TEM and PFTUNA for the analysis of poly-crystalline Ta₂O₅. Second, PFTUNA is used in combination with an array of Si nanopillars to demonstrate the capability to probe buried structures by the observation of mechanical channels. Finally we demonstrate the capability to discriminate between different materials based on the mechanical information.

Recrystallization of Ta₂O₅—The high electrical permittivity of high- κ materials, enables the further reduction of the equivalent oxide thickness (EOT) while maintaining low gate leakage for MOSFET transistors delivering better performance. This feature has stimulated the introduction of high- κ materials in many other applications such as: DRAM, storage capacitors and VCM [43]. Despite their widespread adoption in the semiconductor technology, a lot of issues on their electrical properties and reliability are still open. In particular for the case of poly-crystalline high- κ dielectrics, an important issue that remains is the non-uniform leakage distributions that gives rise to large variations of the electrical properties among devices on a chip. These could originate from different grain orientations and/or local variations in composition [44]. In this section amorphous Ta₂O₅ is recrystallized by high temperature annealing. The latter induces major structural and electrical changes in the film providing a good test vehicle for a complementary study with TEM and PFTUNA. A Ta₂O₅ layer is deposited by atomic layer deposition (ALD) with TaCl₅ as precursor in combination with H₂O as the oxidant. Details about the entire deposition can be found in literature [45]. The thin film is grown on a 300 mm p-type Si (1 0 0) substrate, after a standard (IMEC-clean) process which leads to the formation of ≈1.1 nm of chemical SiO₂ layer. A 15 nm-thick layer of Ta₂O₅ is grown and recrystallized with a thermal treatment. A crystallization temperature higher than 760 °C is generally required to induce crystallization. In this work we have used a spike anneal (1.5 s) at 1030 °C as thermal treatment. Figure 3.17a represents the PFTUNA images of the crystallized Ta₂O₅ film, note that compared to C-AFM in this case we can achieve surface topography with a quality comparable to tapping mode. The higher value of PFTUNA for such application is represented by the enhanced topography sensitively coupled with the information on the sample's mechanical properties. On Fig. 3.17a one can notice that the crystallization led to the formation of clearly defined grains and that the GBs form a network of interconnected gaps (≈10-20 nm) in between crystalline grains across the entire sample surface [46]. According to the AFM analysis, the GBs correspond to a \approx 2 nm depression in topography as compared to the crystalline grains. PFTUNA current map (-0.5 Vbias) shows different conductive domains. Unexpectedly, no clear correlation exists between height and current in the GBs transition regions, which actually conduct less current than the rest of the sample despite the reduced thickness (Fig. 3.17b). The latter is opposite to the trends reported elsewhere where a higher leakage current is seen in the GBs which was assigned to the thinner oxide and also to the higher density of defect generally present on GBs [47]. It is known that grain boundaries may possess different conductivity associated to the higher concentration of defects, vacancies and other contributor to tunneling and trap assisted leakages. In addition the particles decorating the grain boundaries appear as highly conductive and harder than the surrounding material as in Fig. 3.17c. In order to clarify this effect and the nature of the highly conductive particles, TEM has been used. Figure 3.18 shows the cross section of the crystalline sample. The thickness of the Ta₂O₅ layer is not constant and, as observed by the AFM the GBs are associated with a reduced layer thickness that appears to be filled with an amorphous material. The region under the GB in Fig. 3.18a, b also shows an amorphous layer of Si at the interface with the substrate. In fact, the formation of an amorphous layer within the Si substrate is observed in most locations where the Ta₂O₅ layer is not continuous such as at the grain boundaries. The thickness of the SiO_2 layer is close to the expected ≈ 1.3 nm, but the presence of amorphous Si in combination with SiO₂ induce an effective thickness higher than the nominal under the GBs. The TEM analysis of the highly conductive particles indicates that they have an average diameter of \approx 30 nm. EELS analysis indicates a composition close to TaN. The crystalline lattice of TaN can be distinguished in the inner region of the particle by their lattice parameters (inset of Fig. 3.18a). At the edges of the crystalline grains, TEM reveals a clear reduction in thickness which could be responsible for the increased leakage current. Moreover, the crystalline lattice is less ordered in these regions compared to the core of the crystalline islands (not shown for brevity) which also can lead to an increased number of defects and oxygen vacancies with a consequently enhancement of leakages. The larger leakage current observed at the position of the TaN clusters can originate from a partial or complete short in the dielectric in correspondence of the particle. The nature of the highly conductive particles (in particular requiring the presence of N) has to be related to some contamination during the thermal annealing process which is out of the scope of this discussion. The presence of amorphous material combined with the amorphous Si at GBs can explain their unexpected insulating behavior and mechanical properties. In summary the peculiar recrystallization of Ta₂O₅ provided a good platform for PFTUNA to demonstrate its capability to detect different material phases and study their electrical properties.

Probing the invisible—as a second example, in this section we show that the mechanical properties of a sample can in some cases enhance the observation capability and reveal buried structures. A buried array of vertical poly-Si channels (pillar) is used. These structures are originally deposited as vertical gate for 3D NAND application and their fabrication process can be found elsewhere [48]. The height of the pillar is 200 nm with a 80 nm diameter, they are grown to form an array structure with 500 nm pitch between neighbor pillars. After their growth a 20 nm-thick SiO₂ is deposited leading to a uniform surface covering the pillars that leaves visible only the roughness of the SiO₂ (Fig. 3.19a). In this case, the collection of multiple force curves on each pixel, enables to detect a different material deformation in correspondence of the Si pillars that become visible in the adhesion map (Fig. 3.19b). The adhesion

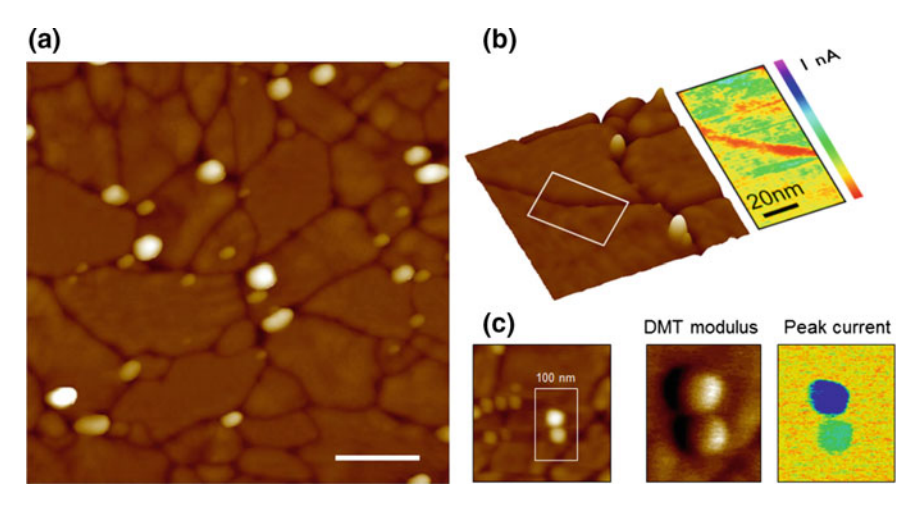


Fig. 3.17 *PFTUNA analysis of crystalline Ta*₂**O**₅. **a** Topography image of poly-crystalline Ta₂O₅ showing crystalline islands surrounded by grain boundaries. Large particles are located at the grain boundaries (z range 20 nm, scale bar 100 nm). **b** 3D topography of 500×500 nm² scan and current map as measured by PFTUNA (-0.5 V bias applied to the sample) in correspondence of grain boundaries. **c** Topography, modulus and current channel for a different 400×400 nm² scan area

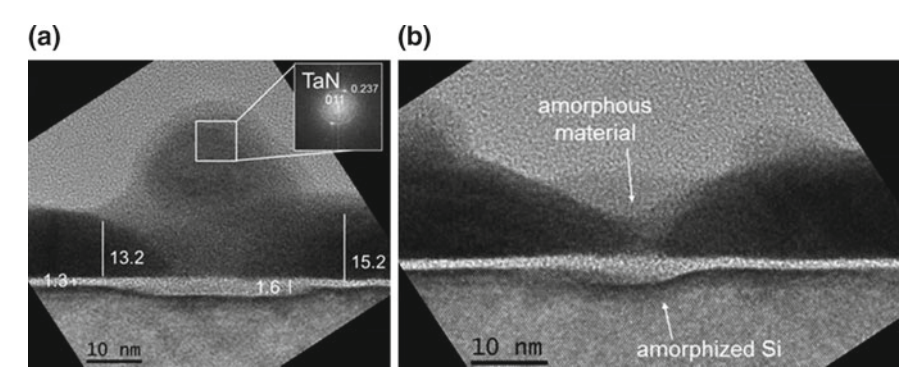


Fig. 3.18 $TEM image \ a$ Cross section image of poly-crystalline Ta_2O_5 . In the region of the GBs the silicon shows a small amorphous depression which increases locally the amount of poorly conductive material. b High resolution TEM, the conductive particles are indexed with TaN (reported in the inset), the GBs region is filled with an amorphous material which combined with the amorphization of the underlying silicon could explain the high insulating behaviors of GBs

map in Fig. 3.19b clearly shows the appearance of the 3×3 array of pillars spaced by 500 nm which is the structure buried under the 20 nm SiO₂ top surface.

Material sensitivity—The third example applies to samples with very distinctive mechanical properties. In this situation PFTUNA can be useful to identify the constituting elements due to their distinctive mechanical response. This is the case of cellulose nanofiber paper, often referred as nanopaper [49]. This is an emerging

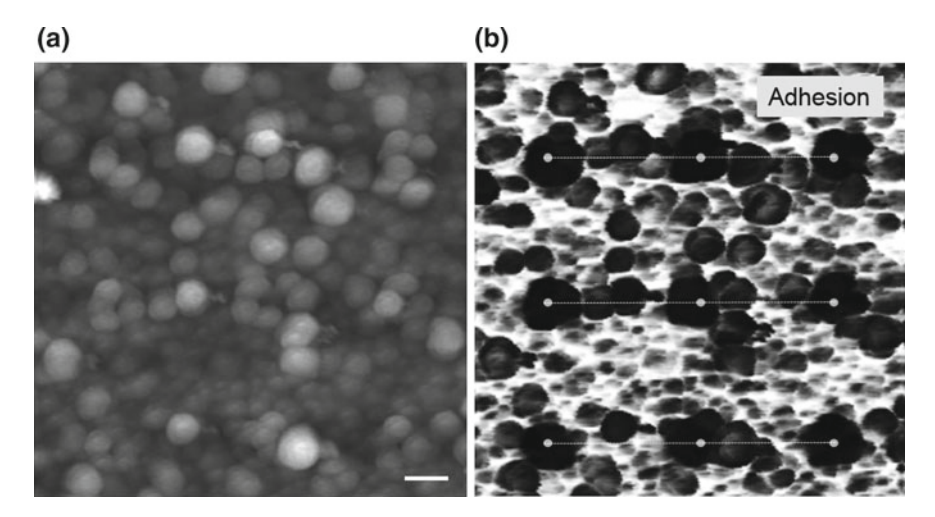


Fig. 3.19 Peak Force on vertical Si pillars. **a** Topography of 20 nm SiO₂ deposited on top of an array of 80 nm-wide Si pillar (z range = 16 nm, scale bar = 150 nm). **b** The adhesion map of the same area reveals the presence of the 3×3 array due to the different tip-sample deformation in presence of the buried Si pillar. Note the 3×3 dots array to guide the eyes

material in the field of flexible electronics and in the appendix we report on the usage of nanopaper for the fabrication of flexible cellulose-based CBRAMs [50]. Here we focus on the mechanical properties and the localization by PFTUNA of nanosized cellulose fibers deposited on a Ag substrate. Those will be locally switched by C-AFM in the appendix. The nanofibers is deposited by drop casting of the nanosized cellulose slurry onto Ag/Ti/SiO₂/Si substrate and it is dried at 40 °C for 24 h. By selecting a low density slurry it is possible to achieve a limited coverage of the substrate and locate single cellulose nanofibers. In some cases due to their reduced dimensions the roughness of the Ag layer can be comparable to the cellulose nanofibers leading to difficult localization on the surface. On the other hand, the peculiar adhesion properties of cellulose enhance the sensitivity of detection also in case of ultra-thin cellulose bundles. Figure 3.20 shows an example where the characteristic adhesion of cellulose can assist the detection of the fiber evolution in on the Ag surface.

3.3.2 Electrical Tip-Contact: Dragged Versus Intermittent

In intermittent contact modes (Fig. 3.16a) the peak force is equivalent to the load force (deflection setpoint) of standard contact mode. In other words, by scanning the same sample with the same tip with C-AFM and PFTUNA we should obtain the same electrical results using the equal values of load force. This experiment can be easily realized by measuring a highly conductive point defect in a thin dielectric, under the same conditions using C-AFM and PFTUNA. The result Fig. 3.21a, b shows the

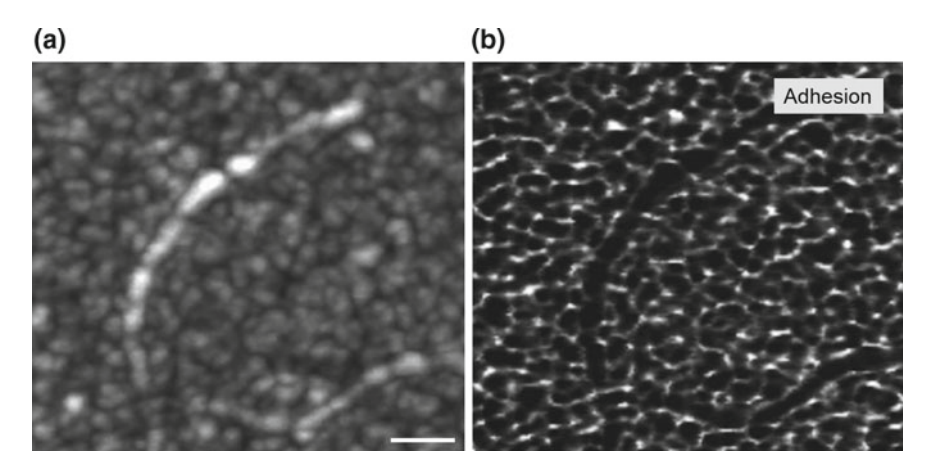


Fig. 3.20 *PFTUNA on cellulose nanofiber*. **a** Topography of a single cellulose nanofiber (z range = 10 nm, scale bar = 120 nm). **b** The adhesion map of the same area reveals the spatial distribution of the cellulose fiber

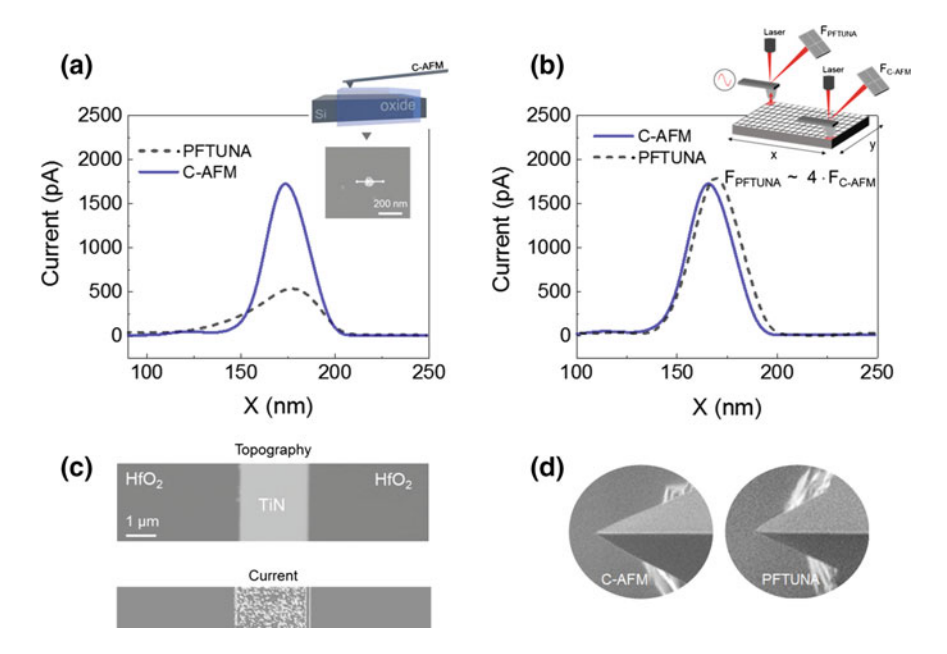


Fig. 3.21 Dragged versus intermittent contact. a Comparison between C-AFM and PFTUNA current, scanning the same tip on the same conductive spot at equal value of load force. b The peak force value is raised (\approx four times) to match the level of current flowing in the two setup. c Topography and current of a TiN metal line used as reference sample for the experiment. d SEM inspection of the tips used in the comparison

unexpected higher current measured with C-AFM as compared to PFTUNA although using the same tip at the same nominal load force value. In order to balance the observed discrepancy in the current amplitude the peak force value is increased for PFTUNA and the load force for C-AFM is kept constant until the two experimental values are matched (Fig. 3.21b). The same experiment is repeated on other type of samples, such as metallic lines (Fig. 3.21c) with the same results. Consistently, we observe that a higher force is required for PFTUNA to reach the same electrical contact quality of standard C-AFM. As in Fig. 3.21b the measured current values are equaled only when the peak force reaches four times the load force (deflection set-point) used for C-AFM. Similar values are obtained also for other samples, thus indicating an intimate difference between the two type of contacts i.e. the vertically intermittent and the laterally dragged. This can be qualitatively explained by the contribution of lateral and capillary forces induced by the absorbed water layer in the case of intermittent contact not present for the dragged contact. On every tap of PFTUNA the tip encounters the meniscus layer that has to be penetrated, while with the dragged contact the tip punches the meniscus layer with the first contact and on its scan the tip slides through the meniscus layer which is removed by the tip passage. This is consistent with the molecular dynamics simulation work of Yue et al. [51] and Shimizu and co-authors [52]. In view of this, the force discrepancy is generally more pronounced in hydrophilic surfaces (organic materials). In other words, to achieve the same electrical contact quality the intermittent contact has to be operated at higher force compared to the case of contact mode AFM.

The higher force required by PFTUNA to achieve the same electrical contact of C-AFM could reduce the benefits of the intermittent contact in term of tip wear. In order to compare the impact on the tip degradation we have compared the quality of the Pt/Ir coating on the tip-apexes for two tips scanned for $\approx\!10\,\text{cm}$ (200 AFM scans) over a biased 2 μm wide metal line (Fig. 3.21c). During the test the root mean square (RMS) value of the current channel has been kept constant for both techniques in order to equal the electrical contact quality. Also in this case the average value of force required by PFTUNA has been 4 times the value used for C-AFM. Figure 3.21d shows the comparison between two tips after the accelerated degradation test. Both tips still present a sharp apex (at SEM inspection) after the test. This suggests that although requiring a 4 times larger load-force used by C-AFM, the reduced tip-sample interaction of PFTUNA, mitigate the tip degradation. Note that in this experiment we have used a relatively low value for the load force ($\approx\!200\,\text{nN}$).

3.4 Three-Dimensional SPM Tomography

From Celano, U. and Vandervorst, W., IEEE IIRW final report, 1–5, 2014.

The introduction of three-dimensional devices like finFET and stackable architectures like 3D-NAND, poses unparalleled challenges to the semiconductor metrology. To the point that the cost of testing is now one of the primary source of cost of transistors. Conventional characterization methodologies start to be ineffective applied

to structures <100 nm. Furthermore, characterization of electronic devices needs to include structural, compositional and electrical sensing capability. Therefore the main requirements for a valuable 3D characterization technique are: (1) nanoscale spatial resolution (e.g. sub-10 nm observation capability). (2) Sensitivity (e.g. electrical and structural) and (3) nanometer accuracy in probing the third dimension. In this section we propose an approach, termed SPM tomography or scalpel SPM, which is based on extending the 2D-analysis capabilities of SPMs towards 3D, thereby creating a valuable technique for the electrical 3D characterization of ultra-confined volumes. In Chap. 5 the concepts introduced here will be applied for the analysis and 3D observation of the conductive filaments in VCM and CBRAM.

3.4.1 Overview of 3D Tomography

Although SPM provides revolutionizing techniques for surface analysis, these are clearly limited to the observation in 2D. However, the continuous scaling of electronic devices led to the introduction of 3D device structures like finFET and architectures such as nanowire-based transistor and 3D NAND memory. Although the production of such devices can be achieved by standard semiconductor fabrication techniques, the 3D metrology still represents a major challenge. Doping control in 3D structures, sub-nm spatial resolution of complex geometries and chemical-electrical sensitivity of confined volumes are only some of the complications faced by the semiconductor metrology.

Existing 3D imaging solutions are generally based on beam analysis such as: scanning electron microscopy in dual beam configuration, transmission electron microscopy, electron tomography and X-ray tomography. SEM in combination with an ion beam can be used to image and mill material from the sample surface. While not limited by the lateral resolution, the poor control on the material slicing induced by the ion beam (\approx 10 nm) does not allow tomography of highly confined volumes with this method. Similarly X-ray tomography is generally limited to ≈µm resolution. The latter can be improved using synchrotron radiation and a highly coherent X-ray source but this is of impractical use. TEM combined with a large variety of imaging modes, can provide 3D structural and chemical information of the sample. For example, electron holography uses an interference pattern (hologram) in the TEM. The electron wave emitted by the field emission gun serves as highly coherent source of electrons. The beam is partially deflected to the sample and partially passed through the vacuum, the two waves are then overlapped and interfere. By the interference pattern the phase shift of the electron wave is determined enabling the sensing of variation in the magnetic and electrostatic potential within the sample. Promising results have been reported on the 3D electrostatic potential in p-n junctions and electrostatic potential in MOSFETs [53]. TEM can also record images at progressively increasing tilt angles and a 3D reconstruction is "back-projected". However, in most cases the reconstruction becomes complicated due to artifacts, specimen-induced shadowing and precise control of the angular increment. Finally, atom probe tomography (APT)

is based on field ion microscopy and delivers the highest spatial resolution available for 3D analysis (sub-nm) [54]. Here the sample has to be shaped as a sharp needle and is subjected to a very strong electric field. The outmost atoms in the sample are ionized and projected onto a position sensitive detector. In essence, the sample is peeled apart atom by atom, and by adding a time-of-flight mass detector it is also possible to allow chemical identification. The high electric field ($\approx 10 \text{ V/nm}$) is induced by the application of several kilovolts to the shaped sample, leading to the field evaporation of the sample. During the analysis, the sample is kept at cryogenic temperature in order to suppress the transverse kinetic energy to the emitted ions. Unfortunately, the complicated sample preparation the use of high voltages and the cryogenic conditions are still limiting the diffusion of this technique. In addition, although APT localizes atoms with excellent spatial resolution, no information can be obtained about charge carriers or electrical properties.

Scanning probe microscopy had already a fair share of attention for 3D characterization. A schematic of the proposed solutions can be seen in Fig. 3.22a-c. Magerle et al. [55] used SPM in combination with subsequent calibrated chemical etching for the reconstruction of the sample volume in 3D. They could demonstrate volume images of semicrystalline polypropylene revealing the differences between crystalline and amorphous regions [56]. However, the same area has to be repeatedly located in every etch cycle leading to complex operations (Fig. 3.22a). To overcome this problem a dedicated liquid cell for in-situ etching and sensing has been developed to enable the inlet and outlet of the etching solution without moving the sample [57]. Alekseev et al. [58] have proposed to combine C-AFM with a microtome to cut extremely thin slices of the sample (Fig. 3.22b). With a slice space of \approx 12 nm they could image the 3D volume of a conductive nanocomposite filled with multi walls carbon nanotubes (MWCNTs) and reconstruct the conductive sub-networks by C-AFM. Bailey et al. [59] have proposed a combination of AFM and ion milling, providing the possibility to perform morphological 3D observation (Fig. 3.22b). Unfortunately as for the dual-beam SEM, the limited control of the ion milling leads to limited slicing capability or complicated sample preparation. For specific applications, dedicated sample structures can be fabricated in order to have repeated features staggered by a certain well defined distance (Fig. 3.22c). The cross-sections are generally obtained by a combination of cleaving, mechanical- and chemical-mechanical polishing (CMP) as

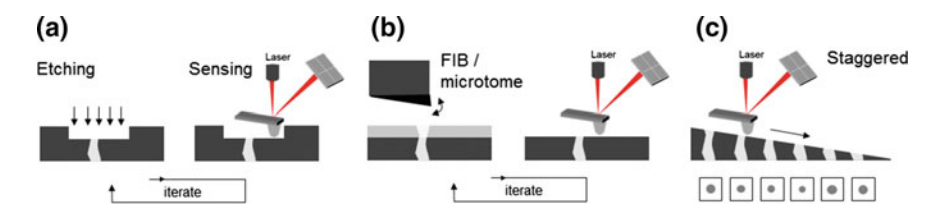


Fig. 3.22 *SPM toward three-dimension.* **a** Alternating chemical etching and SPM sensing. **b** Physical removal by ion beam or microtome followed by SPM sensing. **c** Dedicated staggered structure for a 3D volume replica

described elsewhere [17]. In this way different 2D AFM profiles across each of the staggered devices can be acquired and finally interpolated providing a replica of the 3D volume. This approach has been used by Mody et al. [60] in order to evaluate the gate overlap and dopant conformity over a fin cross-section, and by Schulze et al. [61] to map the distributions of carriers in nanowire-based transistors. Nevertheless, this concept is based on the assumption of identical properties to nearby structures and therefore cannot provide information on a single device or for failure analysis.

As an alternative, in this section we demonstrate a 3D-tomographic technique based on a slice-and-view approach whereby we add a depth profiling capability, to the 2D-mapping of electrical AFM by tip-induced material removal. We named this approach *SPM tomography* or *scalpel SPM*.

To accomplish the depth profiling we make use of conductive, wear-resistant diamond-tips [23]. The hardness of diamond is exploited to physically remove (scraping) material during the scan. We slice in a controlled manner through the sample collecting AFM profiles at different depths. The consecutive planar AFM images are then stacked and interpolated for the formation of the 3D tomogram. In SPM tomography we can achieve sub-nm vertical removal-rates which provides ample depth resolution for the application of this technique in various emerging electronic devices.

3.4.2 SPM Tomography

Like the word suggests (ancient Greek tomos, "slice" and graphō, "to write") with SPM tomography we reconstruct a 3D volume from a series of 2D sections of the sample. The sectioning is achieved by a tip-induced removal of sample material. The possibility to induce material removal with contact mode AFM is known since the early days. Hu et al. [62] observed the formation of 1 nm deep hole on mica after tip scanning (Fig. 3.23a). The latter could be induced either by one single scan at high loads or multiple low load scans, indicating for the first time a controllable tip-induced removal of material. Xu et al. [63] demonstrated depth control in the material removal in InP by successive scans with diamond tip at constant load force. By reducing the scan size continuously the authors induced a staircase structure and probed in depth the dopant profile with SSRM. A similar approach has been used also by Ou et al. [64] for 3D carrier profiling in Si nanowires. More recently, Schulze et al. [65] have applied it to characterize the resistance distribution within contact holes filled with carbon nanotubes and the carrier distribution in nanowire-transistors [66].

From a pure solid mechanics standpoint, a sharp tip sliding on a flat surface, has enabled many studies on wear, friction and contact mechanics [5, 67]. Specifically at the nano scale the wear is described as an atom-by-atom removal of material, which is defined by Jacobs and Carpick as a stress assisted chemical reaction [67]. The atom-by-atom wear mechanism can be described by a single process where the atoms at the interface between the two sliding bodies, undergo a chemical bonding

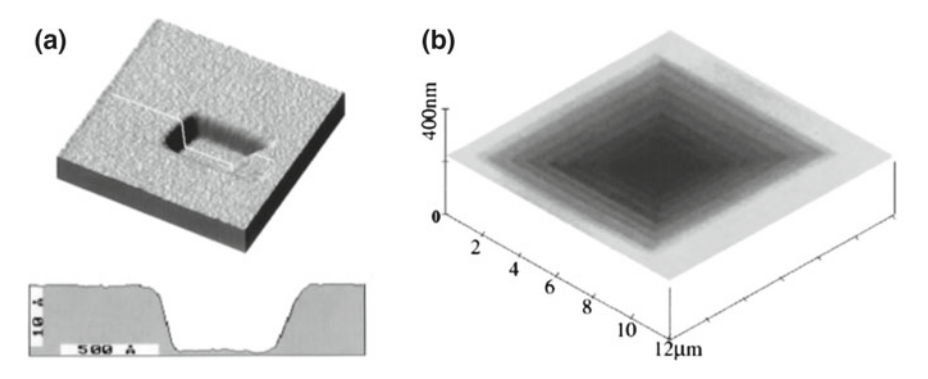


Fig. 3.23 *Tip-induced material removal*. a Removal of a single layer of mica. b Subsequent scans on InP inducing a controlled stepped morphology to the surface (reproduced from [62, 63])

reaction. The reaction rate theory can therefore describe the rate of atom removed as $\Gamma_{atom-loss}$ (units s⁻¹) according to the equation:

$$\Gamma_{atom-loss} = \Gamma_0 \exp\left(-\frac{\Delta G_{act}}{k_B T}\right)$$
 (3.6)

where Γ_0 is a pre-factor (an effective attempt frequency), k_B is the Boltzmann constant and T the absolute temperature. The ΔG_{act} represents the free energy of activation which is reduced to the mechanical work done on the system as reported by Jacob and co-workers [68]. As a practical consequence of this, one can explore the wear phenomena as a possibility to induce controlled removal of material by means of a continuous tip scanning against a solid surface. The wear control arises from the precise load-force application enabled by the AFM feedback-system. The large variety of tip materials provides a wide range of hardness to exploit. For practical reasons in SPM tomography, we generally limit ourself to the usage of our in-house fabricated conductive diamond-tips which proves to be a wear-resistant tool for material removal. Figure 3.24a shows a practical example where a 30nm-thick Cu electrode is progressively eroded until the complete removal by continuous AFM scanning at constant load force. In this case the purpose was only to expose the layer below the Cu electrode, but this can be representative for applications such as layer removal or circuit-editing, as in Fig. 3.24b where scalpel SPM is used to locally disconnect a part on a fabricated chip for failure analysis purpose.

By coupling the hardness of diamond and tip load force we can access material removal-rates that span from zero to hundreds of nm per scan (depending on the sample). The main result is that sub-nm removal-rates can easily be achieved with our tip-induced erosion. Particularly the sub-nm removal capability should not surprise since a standard contact AFM measurement is not supposed to remove any material from the sample surface, thus representing a zero nm/scan removal rate. This high control enables high resolution in the third dimension to be summed with the

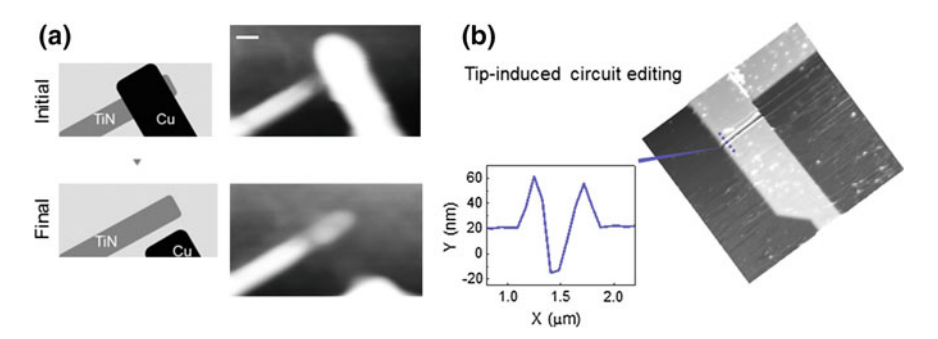


Fig. 3.24 *Tip-induced material removal applications*. **a** Removal of 30 nm-thick Cu electrode and exposure of layer underneath. **b** A small opening is induced by the tip along a metal interconnection in order to disconnect a failed device

nanometer lateral resolution of the AFM techniques. In essence SPM tomography is now based on the fact that through the combination of high-force and diamond tip, we probe in each AFM scan the local variations in conductivity (C-AFM or SSRM) and also partially erode a controlled amount of the sample surface. The collection of 2D AFM conductivity profiles are finally aligned and interpolated to generate a 3D tomogram. Fig. 3.25 shows a schematic of the SPM tomography work-flow.

Through the use of a special design, our wide base pyramid-shaped tips overcome the tip rupture problems experienced with high aspect ratio coated Si-tips when attempting scalpel SPM. Based on the pressure (\approx few GPa) needed for the tip-induced material removal of metals and dielectrics, a cantilever spring constant >10 N/m is generally required. As visible in Fig. 3.25 SPM tomography is a destructive technique. After the complete material removal a crater is left in the place of the region of interest. A large fraction of the material removed is accumulated on the

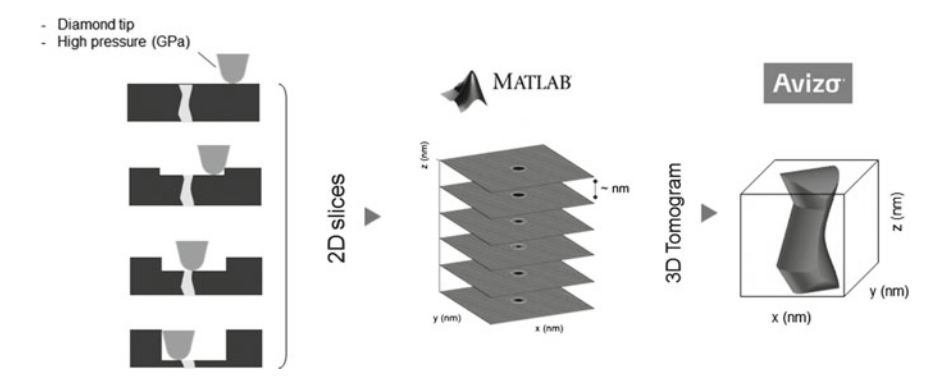


Fig. 3.25 SPM tomography procedure. The wear resistant diamond tip, is scanned on the surface at high pressure (\approx GPa) inducing a controlled material removal. The acquired 2D images are aligned and interpolated by a dedicated software to generate a 3D tomogram

side of the scan area and on the tip body (Fig. 3.26). Different materials will show different removal rate (nm/scan) depending on their hardness. Note that the actual value for the removal rate depends on many parameters such as: material type and deposition technique, layer thickness and absorbed contaminants. For this reason, a reliable evaluation of the material removal rate for a specif material can only be obtained by a load force calibration on the material of interest (e.g. blanket sample). The tip can be scanned and the removal rate (nm/scan) versus the applied force is evaluated [69]. One could assume that due to the stress continuously applied to the scanning probe, only soft materials can be removed in order to limit tip degradation and loss of the lateral resolution. In reality, as partially introduced already by Hu et al. [62] one can trade off the load force with time and achieve the same removal of material in a longer amount of time. By means of this approach, tip-induced material removal has been carried out on a wide range of materials such as: TiN, Cu, Ti, TaN, Ru and Au [65, 70–72].

In combination with the intrinsic tip and material properties, the AFM scanning conditions play an important role in the removal rate. Tip velocity, number of lines per scan, tip-sample biasing and environment conditions (e.g. air, vacuum or controlled humidity) are some of the tunable parameters. Here we provide some of the practical values used in this work and a brief description of their effect. The speed at which the tip scans the surface is defined as tip-velocity and it is reported in μ m/s. Scanning the surface at low speed translates in a longer time spent on the same location exerting high pressure and leading to more stable tip-sample interactions. The usage of a small tip velocity has a dramatic impact on the time for each acquisition but it also improves the quality of the removal and increases the removal rate. A commonly used value is in the range 0.5–1.5 μ m/s. The number of lines acquired on each 2D AFM scan is generally associated to the graphical resolution of the final AFM image. While removing material, this parameter plays a crucial role in the quality of the removal. A high number of lines translates into a denser and less spaced passages of the tip in the same portion of area. In extreme cases e.g. very small scan sizes, the tip can

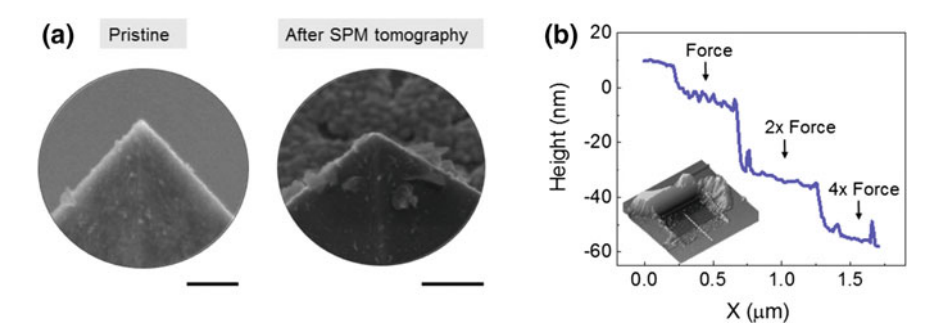


Fig. 3.26 *Material removal rate.* **a** A pristine FDT is compared with one used for multiple tomographic analysis. Residues of the material removed are visible on the tip body. **b** A Cu blanket sample is used as calibration structure for the removal rate evaluation at different load forces

pass many times on the same location within a single AFM scan improving the effectiveness in the removal. In this work we generally use 512 lines per scan which does increase the acquisition time but also provides high-resolution 2D AFM images. The latter is beneficial for the resolution of the final 3D interpolation. During the SPM tomography the DC bias between the tip and the sample has to fulfill two main requirements: (1) it has to be sufficiently high to induce a measurable current flow leading to the detailed contrasts in the current map. (2) It should not interfere with the measurement e.g. affecting the material removal rate. It is clear that this value is highly dependent on the characteristic conductivity of the sample and will vary among different type of observation. For example Rodembücher et al. [73] have used a diamond tip at high pressure to access the bulk properties of Nb doped SrTiO₃. In general if the DC bias is not intentionally used as a mechanism for material removal during the scan, a low value is preferable; in this work we use always (negative) voltage in the range of 10–100 mV with the tip grounded and the bias applied to the sample. However, thermal effects due to Joule heating can contribute to the eroding process since also at reduced values of applied voltage tens to hundreds of nA can flow (especially for conductors). Finally, the dependence of the material removal on the environmental conditions during the analysis is another major parameter since it can induce structural and mechanical changes in the materials under investigation. In our measurements we work generally at high vacuum ($\approx 10^{-5}$ mbar) although we were also able to obtain similar results when working in air at ambient conditions. Due to the aforementioned scanning conditions the duration of the entire analysis can take several hours; during this time any system-induced drift in the x-y plane needs to be compensated either by the operator or by dedicated control software.

Three-dimensional reconstruction—after the acquisition of the set of 2D images, the three-dimensional reconstruction enables the final structural and electrical analysis. This procedure starts with the displacement of the 2D images set in a 3D matrix by means of a dedicated MATLAB routine [65]. The slices are generally assumed as evenly spaced in the third dimension although each slice can be positioned at a desired point. The newly generated 3D matrix is imported in a graphic rendering software (e.g. Avizo) here each slice is aligned. This step can be done using dedicated error-minimization algorithms between subsequent slices, or manually aligning consecutive slice by means of alignment markers. At this point the software can execute different interpolations, to reconstruct the missing information between slices. Generally a linear interpolation based on the value of the nearby slices is preferred for our purpose.

3.5 Summary of the Chapter

In this chapter standard and non-conventional measurement techniques used in this work were introduced. Basic principles of electrical SPM for nanometer electrical characterization have been presented. Traditional electrical contact mode (e.g. C-AFM) has been presented and compared with a recent intermittent contact analysis technique. Some of the most common measurement artifacts observed during our original experimental work have been reported together with the possible solution. By the adoption of 6 parallel linear amplifiers we have improved the existing technique by extending the current sensitivity of C-AFM of three order of magnitudes. When needed, we have exploited the intermittent contact PFTUNA to correlate electrical and mechanical sample's properties. We also presented an original evaluation method to calibrate the electrical contact area of the tips for contact-based electrical AFM techniques. Finally, after a review on potential 3D analysis technique, we have described our newly developed 3D-tomographic technique namely SPM tomography. This exploits an elegant slice-and-view approach where sub-nm material removal is induced by a diamond tip to record consecutive 2D images. Those are finally interpolated by a dedicated algorithm for the 3D analysis of confined volumes. The main parameters to control the tip-induced material removal have been described together with the list of potential applications, however scalpel SPM will be extensively used in Chaps. 5 and 6 for the tomographic observation of conductive filaments in RS memory devices.

References

- E. Meyer, H.J. Hug, R. Bennewitz, Scanning Probe Microscopy: The Lab on a Tip (Springer, Berlin, 2003)
- 2. L. Gross, Scanning probe microscopy. Nat. Chem. 3(April), 273–279 (2011)
- P.M. Koenraad, M.E. Flatté, Single dopants in semiconductors. Nat. Mater. 10(2), 91–100 (2011)
- R. Garcia, A.W. Knoll, E. Riedo, Advanced scanning probe lithography. Nat. Nanotechnol. 9(8), 577–587 (2014)
- R.W. Carpick, Miquel Salmeron, Scratching the surface: fundamental investigations of tribology with atomic force microscopy. Chem. Rev. 97(4), 1163–1194 (1997)
- R.A. Oliver, Advances in AFM for the electrical characterization of semiconductors. Rep. Prog. Phys. 71(7), 076501 (2008)
- G. Binning, R. Heinrich, W. Pauli, The scanning tunneling microscope. Sci. Am. 253, 50–56 (1985)
- 8. G. Binning, C.F. Quate, Ch. Gerber, Atomic force microscope. Phys. Rev. Lett. **56**(9), 930–933 (1986)
- G. Meyer, Nabil M. Amer, Novel optical approach to atomic force microscopy. Appl. Phys. Lett. 53(12), 1045 (1988)
- J.Y. Park, S. Maier, B. Hendriksen, Miquel Salmeron, Sensing current and forces with SPM. Mater. Today 13(10), 38–45 (2010)
- X.D. Cui, A. Primak, X. Zarate, J. Tomfohr, O.F. Sankey, A.L. Moore, T.A. Moore, D. Gust, G. Harris, S.M. Lindsay, Reproducible measurement of single-molecule conductivity. Science 294(5542), 571–574 (2001)
- L. Collins, S. Jesse, J.I. Kilpatrick, A. Tselev, O. Varenyk, M. Baris Okatan, S.A.L. Weber, A. Kumar, N. Balke, S.V. Kalinin, B.J. Rodriguez, Probing charge screening dynamics and electrochemical processes at the solid-liquid interface with electrochemical force microscopy. Nat. Commun. 5(May), 3871 (2014)

- P. De Wolf, J. Snauwaert, T. Clarysse, W. Vandervorst, L. Hellemans, Characterization of a point-contact on silicon using force microscopy-supported resistance measurements. Appl. Phys. Lett. 66(12), 1530 (1995)
- J. Seidel, L.W. Martin, Q. He, Q. Zhan, Y.-H. Chu, A. Rother, M.E. Hawkridge, P. Maksymovych, P. Yu, M. Gajek, N. Balke, S.V. Kalinin, S. Gemming, F. Wang, G. Catalan, J.F. Scott, N.A. Spaldin, J. Orenstein, R. Ramesh, Conduction at domain walls in oxide multiferroics. Nat. Mater. 8(3), 229–234 (2009)
- L. Aguilera, W.A. Volodin Polspoel, C. Van Haesendonck, M. Porti, W. Vandervorst, M. Nafria, X. Aymerich, Influence of vacuum environment on conductive atomic force microscopy measurements of advanced metal-oxide-semiconductor gate dielectrics. J. Vac. Sci. Technol. B 26, 4 (2008)
- A.E. Gordon, Mechanisms of surface anodization produced by scanning probe microscopes.
 J. Vac. Sci. Technol. B: Microelectron. Nanometer Struct. 13(6), 2805 (1995)
- A. Schulze, Two- and Three-Dimensional Dopant and Conductivity Profiling in Confined Volumes, Ph.D. thesis, 2013
- 18. M.R. Waser Wojtyniak, K. Szot. The thermal stability of Pt/Ir coated AFM tips for resistive switching measurements. Appl. Surf. Sci. 257(17) (2011)
- 19. H. Bhaskaran, A. Sebastian, Michel Despont. Res. Lett. **8**(1), 128–131 (2009)
- T. Hantschel, A. Schulze, U. Celano, A. Moussa, K. Arstila, P. Eyben, B. Majeed, D.S. Tezcan, T. Werner, W. Vandervorst, TiN scanning probes for electrical profiling of nanoelectronics device structures. Microelectron. Eng. 97, 255–258 (2012)
- N.R. Wilson, J.V. Macpherson, Carbon nanotube tips for atomic force microscopy. Nat. Nanotechnol. 4(8), 483–491 (2009)
- 22. S.S. Hong, J.J. Cha, Y. Cui, One nanometer resolution electrical probe via atomic metal filament formation. Nano Lett. **11**(1), 231–235 (2011)
- 23. T. Hantschel, P. Niedermann, T. Trenkler, W. Vandervorst, Highly conductive diamond probes for scanning spreading resistance microscopy. Appl. Phys. Lett. **76**(12), 1603 (2000)
- T. Hantschel, C. Demeulemeester, P. Eyben, V. Schulz, O. Richard, H. Bender, W. Vandervorst, Conductive diamond tips with sub-nanometer electrical resolution for characterization of nanoelectronics device structures. Physica Status Solidi (a) 206(9), 2077–2081 (2009)
- M. Tsigkourakos, Nucleation and growth of Boron-doped diamond films for electrode application. Ph.D. thesis, 2015
- B. Cappella, G. Dietler, Force-distance curves by atomic force microscopy. Surf. Sci. Rep. 34, 1–104 (1999)
- 27. J.N. Israelachvili, Intermolecular and Surface Forces, 3rd edn. (Elsevier, Amsterdam, 2011)
- T. Stifter, O. Marti, Theoretical investigation of the distance dependence of capillary and van der Waals forces in scanning force microscopy. Phys. Rev. B 62(20), 667–673 (2000)
- U. Celano, T. Hantschel, G. Giammaria, R.C. Chintala, T. Conard, H. Bender, W. Vandervorst, Evaluation of the electrical contact area in contact-mode scanning probe microscopy. J. Appl. Phys. 117(21), 214305 (2015)
- M. Porti, M. Nafria, M.C. Blum, X. Aymerich, S. Sadewasser, Atomic force microscope topographical artifacts after the dielectric breakdown of ultrathin SiO₂ films. Surf. Sci. 532–535, 727–731 (2003)
- B. Luan, M.O. Robbins, The breakdown of continuum models for mechanical contacts. Nature 435(7044), 929–932 (2005)
- P. Eyben, J. Mody, A. Nazir, A. Schulze, T. Clarysse, T. Hantschel, W. Vandervorst, Fundamentals of Picoscience (CRC Press, Boca Raton, 2013)
- 33. K.F. Schuegraf, CH. Hole, Injection Si0₂ breakdown model for very low voltage lifetime extrapolation. IEEE Trans. Electron Devices **41**(5), 761–767 (1994)
- W. Frammelsberger, G. Benstetter, R. Stamp, J. Kiely, T. Schweinboeck, Simplified tunnelling current calculation for MOS structures with ultra-thin oxides for conductive atomic force microscopy investigations. Mater. Sci. Eng.: B 116(2), 168–174 (2005)
- E. Atanassova, P. Lytvyn, R.V. Konakova, V.F. Mitin, D. Spassov, Conductive-atomic force microscopy characterization of Ta₂O₅/SiO₂ stacks and the effect of microwave irradiation. J. Phys. D: Appl. Phys. 42(14), 145301 (2009)

References 85

36. W. Polspoel, High resolution study of high - k layers using C-AFM, Ph.D. thesis, KU Leuven, 2012

- 37. S.M. Sze, *Physics of Semiconductor Devices*, 3rd edn. (Wiley, New York, 2007)
- 38. W. Robert, D. Carpick, F. Ogletree, M. Salmeron, A general equation for fitting contact area and friction vs load measurements. J. Colloid Interface Sci. 400, 395–400 (1999)
- M. Enachescu, D. Schleef, D. Ogletree, M. Salmeron, Integration of point-contact microscopy and atomic-force microscopy: application to characterization of graphite/Pt(111). Phys. Rev. B 60(24), 16913–16919 (1999)
- X. Blasco, X. Aymerich, W. Vandervorst, Nanoscale Post-Breakdown Conduction of HfO SiO MOS Gate Stacks Studied by Enhanced-CAFM. 52(12):2817–2819 (2005)
- 41. B. Pittenger, M. Erina, C. Su, Quantitative Mechanical Property Mapping at the Nanoscale with PeakForce QNM (2010)
- 42. B.V. Derjaguin, V.M. Muller, Y.P. Toporov, Effect of contact deformations on the adhesion of particles I-. J. Colloid Interface Sci. **53**(2) (1975)
- 43. G.D. Wilk, R.M. Wallace, J.M. Anthony, High- κ gate dielectrics: current status and materials properties considerations, J. Appl. Phys. **89**(10), 5243 (2001)
- J. Petry, Microstructural and electrical characterization of thin dielectrica with high k values. Ph.D. thesis, 2005
- C. Adelmann, A. Delabie, B. Schepers, L.N.J. Rodriguez, A. Franquet, T. Conard, K. Opsomer,
 I. Vaesen, A. Moussa, G. Pourtois, K. Pierloot, M. Caymax, S. Van Elshocht, Atomic layer deposition of tantalum oxide and tantalum silicate from chloride precursors. Chem. Vap. Depos. 18(7–9), 225–238 (2012)
- U. Celano, R.C. Chintala, C. Adelmann, O. Richard, W. Vandervorst, The unexpected effects of crystallization on Ta₂O₅ as studied by HRTEM and C-AFM. Microelectron. Eng. 109, 318–321 (2013)
- K. McKenna, A. Shluger, V. Iglesias, M. Porti, M. Nafria, M. Lanza, G. Bersuker, Grain boundary mediated leakage current in polycrystalline HfO₂ films. Microelectron. Eng. 88(7), 1272–1275 (2011)
- 48. J.G. Lisoni, A. Arreghini, G. Congedo, K. Huet, E. Capogreco, L. Liu, C. Tan, R. Degraeve, G. Van Den, J. Van Houdt, Laser Thermal Anneal of polysilicon channel to boost 3D memory performance. **95**(2009) (2014)
- M. Nogi, S. Iwamoto, A.N. Nakagaito, Hiroyuki Yano. Optically transparent nanofiber paper. Adv. Mater. 21(16), 1595–1598 (2009)
- K. Nagashima, H. Koga, U. Celano, F. Zhuge, M. Kanai, S. Rahong, G. Meng, Y. He, J. De Boeck, M. Jurczak, W. Vandervorst, T. Kitaoka, M. Nogi, T. Yanagida, Cellulose nanofiber paper as an ultra flexible nonvolatile memory. Sci. Rep. 4, 5532 (2014)
- 51. D. Yue, T.B. Ma, Y. Hu, J. Yeon, A.C.T van Duin, H. Wang, J. Luo, Tribochemical mechanism of amorphous silica asperities in aqueous environment: a reaxff molecular dynamics study. Langmuir: the ACS J. Surf. Colloids (2015)
- 52. J. Shimizu, L. Zhou, H. Eda, Molecular dynamics simulation of the contact process in AFM surface observations. Tribotest 9(2), 101–115 (2002)
- D. Cooper, Alison C. Twitchett, Philippa K. Somodi, P.A. Midgley, R.E. Dunin-Borkowski, I. Farrer, D.A. Ritchie, Improvement in electron holographic phase images of focused-ion-beam-milled GaAs and Si p-n junctions by in situ annealing. Appl. Phys. Lett. 88(6), 063510 (2006)
- 54. W. Erwin, Muller, Atom-probe field-ion microscopy. J. Vac. Sci. Technol. **8**(1), 89 (1971)
- 55. R. Magerle, Nanotomography. Phys. Rev. Lett. pp. 2749–2752 (2000)
- C. Dietz, M. Zerson, C. Riesch, A.M. Gigler, R.W. Stark, N. Rehse, R. Magerle, Nanotomography with enhanced resolution using bimodal atomic force microscopy. Appl. Phys. Lett. 92(14), 143107 (2008)
- C. Dietz, S. Röper, S. Scherdel, A. Bernstein, N. Rehse, R. Magerle, Automatization of nanotomography. Rev. Sci. Instrum. 78(5), 053703 (2007)
- A. Alekseev, A. Efimov, L. Kangbo, J. Loos, Three-dimensional electrical property mapping with nanometer resolution. Adv. Mater. 21(48), 4915–4919 (2009)

- R.J. Bailey, R. Geurts, D.J. Stokes, F. de Jong, A.H. Barber, Extending AFM phase image of nanocomposite structures to 3D using FIB, in MRS Proceedings, 1421(August 2015):mrsf11– 1421–pp. 07–09 (2012)
- J. Mody, G. Zschätzsch, S. Kölling, A. De Keersgieter, G. Eneman, A.K. Kambham, A. Schulze, T. Chiarella, N. Horiguchi, T.-y Hoffmann, P. Eyben, W. Vandervorst, K.U. Leuven, K. Arenberg, 3D-carrier profiling in finFETs using scanning spreading resistance microscopy, pp. 119–122 (2011)
- A. Schulze, A. Florakis, T. Hantschel, P. Eyben, A.S. Verhulst, R. Rooyackers, A. Vandooren, W. Vandervorst, Diameter-dependent boron diffusion in silicon nanowire-based transistors. Appl. Phys. Lett. 102(5), 052108 (2013)
- 62. J. Hu, X.-D. Xiao, D.F. Ogletree, M. Salmeron, Atomic scale friction and wear of mica. Surf. Sci. 327(3), 358–370 (1995)
- M.W. Xu, T. Hantschel, W. Vandervorst, Three-dimensional carrier profiling of InP-based devices using scanning spreading resistance microscopy. Appl. Phys. Lett. 81(1), 177 (2002)
- X. Ou, P. Das Kanungo, R. Kögler, P. Werner, U. Gösele, W. Skorupa, X. Wang, Threedimensional carrier profiling of individual Si nanowires by scanning spreading resistance microscopy. Adv. Mater. (Deerfield Beach, Fla.), 22(36):4020–4 (2010)
- A. Schulze, T. Hantschel, A. Dathe, P. Eyben, X. Ke, W. Vandervorst, Electrical tomography using atomic force microscopy and its application towards carbon nanotube-based interconnects. Nanotechnology 23(30), 305707 (2012)
- A. Schulze, T. Hantschel, P. Eyben, A.S. Verhulst, R. Rooyackers, A. Vandooren, J. Mody, A. Nazir, D. Leonelli, W. Vandervorst, Observation of diameter dependent carrier distribution in nanowire-based transistors. Nanotechnology 22(18), 185701 (2011)
- D.B. Tevis, J.R.W. Carpick, Nanoscale wear as a stress-assisted chemical reaction. Nat. Nanotechnol. 8(2), 108–112 (2013)
- D.B.T. Jacobs, B. Gotsmann, M.A. Lantz, R.W. Carpick, On the application of transition state theory to atomic-scale wear. Tribol. Lett. 39(3), 257–271 (2010)
- U. Celano, W. Vandervorst, Scanning Probe Tomography for Advanced Material Characterization, in 2014 IEEE International Integrated Reliability Workshop Final Report (IIRW), pp. 1–5 (2014)
- U. Celano, L. Goux, K. Opsomer, M. Lapichino, A. Belmonte, A. Franquet, I. Hoflijk, C. Detavernier, M. Jurczak, W. Vandervorst, Scanning probe microscopy as a scalpel to probe filament formation in conductive bridging memory devices. Microelectron. Eng. 120, 67–70 (2014)
- U. Celano, L. Goux, A. Belmonte, A. Schulze, K. Opsomer, C. Detavernier, O. Richard, H. Bender, M. Jurczak, W. Vandervorst, Conductive-AFM tomography for 3D filament observation in resistive switching devices, in 2013 IEEE International Electron Devices Meeting (IEDM), pp. 21.6.1–21.6.4 (2013)
- U. Celano, L. Goux, A. Belmonte, K. Opsomer, A. Franquet, A. Schulze, C. Detavernier,
 O. Richard, H. Bender, M. Jurczak, W. Vandervorst, Three-dimensional observation of the conductive filament in nanoscaled resistive memory devices. Nano Lett. 14(5), 2401–2406 (2014)
- 73. C. Rodenbücher, W. Speier, G. Bihlmayer, U. Breuer, R. Waser, K. Szot, Cluster-like resistive switching of SrTiO₃: Nb surface layers. New J. Phys. **15**(10), 103017 (2013)

Chapter 4 Conductive Filaments: Formation, Observation and Manipulation

4.1 Tip-Induced Filament Formation and Observation

For memory applications the conductive filament represents the bit of information, its creation and dissolution mechanisms are of primordial importance to provide insights on the device performance. Programming speed, power consumption, retention, cyclability and thermal stability are all intimately related to the physical structure of the CF. For instance the retention of the information depends on the filament stability which is related to the atomic structure of the CF. Similarly, the endurance (i.e. filament cyclability) is determined by the CF's apex and its continuous nanoscopic rearrangements during formation and rupture. Electrical characterization methods based on scanning probe microscopy have the potential to provide the required spatial resolution and thus enable the physical characterization of the RS mechanisms. As introduced in Chap. 2, SPM and C-AFM in particular, have been often proposed to study the local effects of RS on the sample surface [1, 2]. Among other advantages, this configuration facilitates the device fabrication. The switching materials can be deposited on blanket wafers, saving time and costs related to the mask design and lithography. In this section RS in Cu/Al₂O₃ and Hf/HfO₂ is investigated using the C-AFM tip twofold. (1) As a virtual ultra-scaled top electrode thus allowing to induce filament formation and cycling, and (2) as a probe during the analysis phase whereby the local changes in current flow (resistivity) detects the presence and state of a filament. The role of the conductive tip on the resistive switching by C-AFM is investigated in the following sections. In particular we describe the tradeoffs between tip-resistance, tip-radius and tip-material to provide a good correspondence between standard RS-device and tip-induced RS experiments. After the CFs formation, they are observed and manipulated in order to understand the scaling potential of resistive switching. This combined to the analytical fitting of the I–V characteristics recorded by C-AFM, is used to elucidate the physics of the reset mechanisms in the sub-10 nm² dimensions.

4.1.1 Areal Switching

The usage of C-AFM for investigation of RS, has been often associated with areal switching [3]. Many material system such as perovskites (e.g. SrTiO₃, Pr_{0.7}Ca_{0.3}MnO₃ PCMO) and binary transition metal oxides (e.g. NiO and TiO₂) exhibit a continuous RS related to a gradual modulation of the Schottky barrier at the interface with the electrode due to a voltage-induced variation of the defects densities (V_a) in the film [4]. The barrier modulation induces a local resistance variation which is often studied with C-AFM as region locally ON or OFF within the scan area [5, 6]. In the material systems studied in this dissertation this effect is generally absent. This can be considered as an indication of the specific RS mechanism in purely filamentary-based RS as compared to the large range of RS events. Although triggered by a voltage-induced defect modulation, our CFs require a local electroforming to be activated. Scanning a local portion of sample with the required forming bias leads generally to surface damages. These unrecoverable modifications are induced by a combination of high electric field and high current density combined to the lateral motion of the tip. In Cu/Al₂O₃ for example, the smooth surface easily evolves into rough when subject to these conditions. Figure 4.1a shows the Auger spectrum after scanning the surface with the tip biased at 6 V. The area originally flat (not shown), is investigated with Auger electron spectroscopy (AES) to detect the chemical species on the surface which is now very rough. AES is carried out in a Thermo VG350f Microlab tool with beam energy of 10kV and beam current ≈3 nA. After the AFM scan with the biased tip, the morphology changes with the appearance of unrecoverable bumps that AES reveals to be Cu-rich. Those features affect the entire layer integrity and are not representative for the RS events happening in the devices since they are not observed. Similarly, for the Hf/HfO₂/tip-system every attempts to induce areal RS leads to morphological changes of the surface, those are generally less severe of

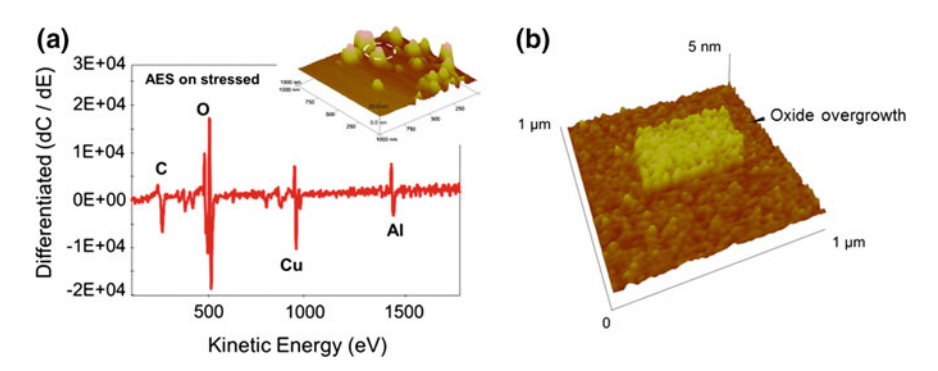


Fig. 4.1 Areal switching. **a** Auger electron spectroscopy is used on the Al_2O_3 surface after scanning the biased-tip. Severe structural modification of the surface with intermix of the constituting materials is induced, as seen with AES. **b** Surface modification induced by the attempt to form a $500 \times 250 \text{ nm}^2$ region on HfO₂ surface

the one presented in Fig. 4.1a and they belong to the class of the tip-induced bias assisted anodic oxidation phenomena [7]. In Fig. 4.1b a central 500×250 nm² region has been modified while attempting to form that area. The morphology of the film is locally changed with a thicker oxide grown in the 500×250 nm² area. The increase in thickness of the oxide layer shift the value of forming voltage over 10 V, and thus limits any possible measurement. Furthermore, these type of morphological changes are not observed in integrated devices (for example by TEM) also after prolonged operations. Suggesting that these are tip-induced (C-AFM specific) artifacts when working in air. Thus they are not very representative for the filamentary-based RS mechanism.

In general, in this dissertation we focus on point-contact CF formation and all the reported RS events are not associated to any large morphological changes of the oxide surface. For this reason since topography images are generally constant, in this dissertation primarily current maps are shown.

4.1.2 Ultra-Scaled Device Sizes with C-AFM

The evaluation of the electrical contact area (Sect. 3.2.5), indicates that the FDT tips at moderate load force (\approx 200 nN) can easily replicate a 10 nm² (or smaller) movable top electrode [8]. Two blanket samples are prepared in order to investigate with C-AFM the cation- and anion-based RS. In case of CBRAM the stack is 15 nm Cu deposited by PVD on a standard 300 mm p-type Si(100), followed by 3 nm amorphous Al₂O₃ deposited using a plasma enhanced ALD deposition technique at 45 °C, using O₂ plasma and tri-methyl aluminium (TMA) precursor. In the case of VCM, 30 nm TiN layer is deposited on a standard 300 mm p-type Si(100) wafer, followed by 10 nm metallic Hf grown by low-temperature PVD and finally 3 nm HfO2 layer is deposited with a standard water-based ALD process. Both samples present smooth surfaces with roughness in range 0.1 to 0.3 nm (RMS) for 1 µm area. Different oxide thicknesses have been investigated resulting in a optimal value of 3 nm when working with C-AFM. Similar to the MIM devices, an electroforming is required also with C-AFM to trigger the RS. Figure 4.2 shows the forming voltage dependence as function of device size with the values of C-AFM, here considered as a 10 nm² device. The increasing trend of forming voltage with reduction of device size is maintained, values over 6 V are consistently observed when forming with C-AFM. The observed high values can be partially attributed to the transition of the electric field from a planar toward an hemispherical distribution as in (Fig. 4.2b top inset) [9, 10]. This is specific for the sharp AFM tip (radius \approx 20 nm) that induces a strong localization of the E field at the edge of the tip sample contact. This is generally approximated with a radial field distribution, with the highest field strength close to the tip apex and rapidly decaying [1, 9]. However, in view of the aggressive integration of the RS devices these values of forming voltages have to be taken into account. Consistently with devices, the forming voltage presents a linear dependence with oxide thickness and the set voltage seams independent as in Fig. 4.2b. This indicates that although

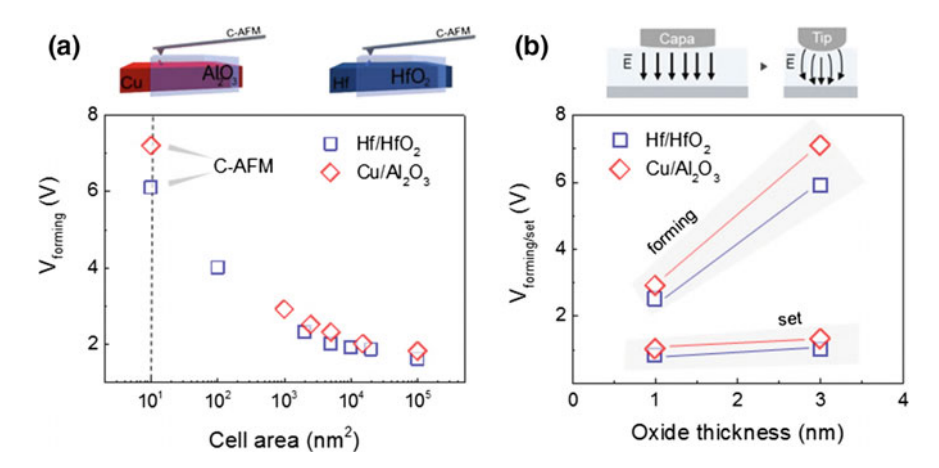


Fig. 4.2 *Tip-induced forming.* **a** Forming voltage dependence as function of the cell area. Integrated devices data are complemented with C-AFM. **b** Forming voltage depends linearly on the oxide thickness, while the set voltage is almost constant, as an indication that the CF does not completely recover on every cycle

the E field-driven migration of the defects is responsible for both the CF formation and the set/reset. During the first CF formation the voltage drops across the entire oxide thickness while during the set/reset the voltage will drop only on the fraction of the original oxide thickness constituted by the recovered part of the CF.

Figure 4.3 provides a clear overview of the dimensions involved in the tip-induced RS events. Both samples are illustrated schematically and imaged using cross-section TEM. Figure 4.3a, c represent respectively the Hf/HfO₂ and Cu/Al₂O₃ stacks. A high resolution TEM image of the tip apex of our FDT is added to the figures (scale bar 10 nm). For the electrical programming, the tip is grounded and the bias is applied to the sample, which has been previously prepared to contact the TiN or the Cu layer respectively. This preparation often referred as "back-contact" is realized by scribing the sample with a diamond pen and filling the scribe with a GaIn eutectic finally covered with a Ag paint. In this way, an ohmic contact is established between the buried (metal) layers and the sample holder where the bias is applied. After the electroforming the C-AFM tip can be used to locally trigger RS. As shown in Fig. 4.3b, d when held stationary in one point the tip can record I–V characteristics. Two RS cycles respectively for the Hf/HfO₂/tip- and Cu/Al₂O₃/tip-structure are presented. According to the biasing scheme of Chap. 2 (Fig. 2.3), we observe set and reset using positive and negative polarities (applied to the sample) consistently with the bipolar type of RS. A sudden increase in current (Fig. 4.3b, d) during the positive voltage ramp clearly demonstrates the creation of a filament ("set" stage). Conversely filament disruption ("reset" stage) is visible when the opposite polarity is applied. After the reset transition both switching layers behave as a normal thin oxide with associated current leakage due to direct or trap-assisted tunneling (inset Fig. 4.3b), this will be treated more in details in the following sections.

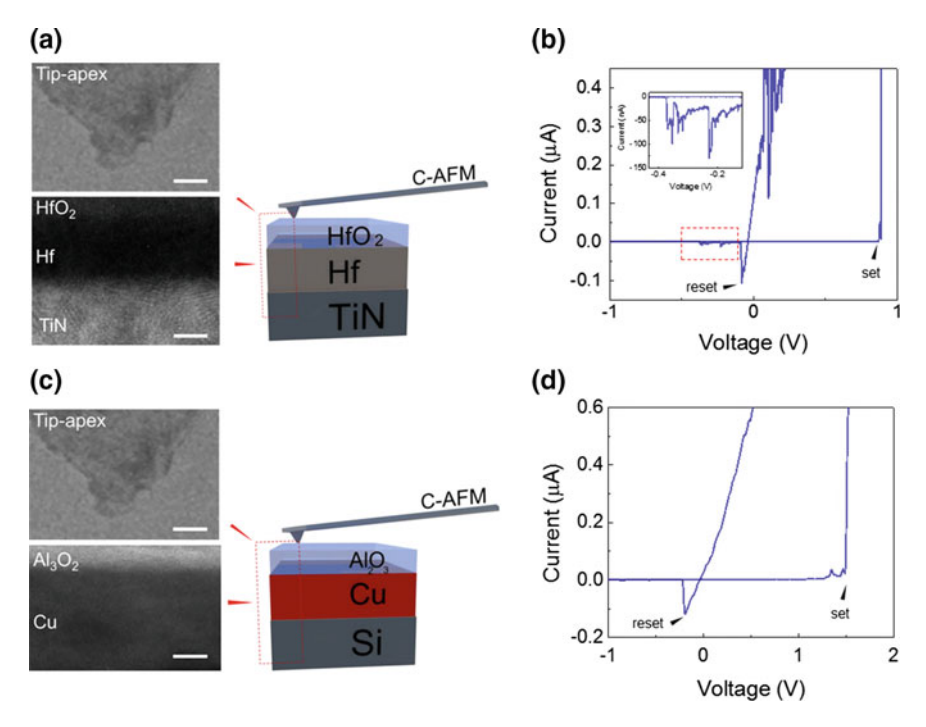


Fig. 4.3 *Tip-induced resistive switching*. **a** Schematic and cross-section TEM of the C-AFM setup for HfO₂-based VCM (scale bars: tip 10 nm, sample 5 nm). **b** Tip-induced switching cycle in Hf/HfO₂-tip system. The inset shows current fluctuation associated with reset. **c** Schematic and cross-section TEM of the C-AFM setup for Cu/Al₂O₃-based CBRAM (scale bars: tip 10 nm, sample 5 nm). **d** Tip-induced switching cycle in Cu/Al₂O₃-tip system

These observations, clearly show that it is possible to induce filament formation and dissolution using C-AFM. Furthermore, due to the size of the tip-induced electrode, the physical mechanism of RS shows strong scaling potential in the sub-10 nm² dimensions.

4.1.3 The Role of the Tip

Acting as a movable top electrode the conductive AFM tip has a primordial importance in tip-induced RS. Before proceeding with the rest of the experimental work, in this section the importance of the conductive tip (e.g. material, resistance and tip-apex) is clarified. In common with the inert electrode of the integrated devices, the AFM tip has to be conductive. To avoid the oxidation of the tip during RS, the use of materials electrochemically inert to oxygen is required. In addition, due to the absence of any selector device (as the 1T1R transistor), in a C-AFM experiment

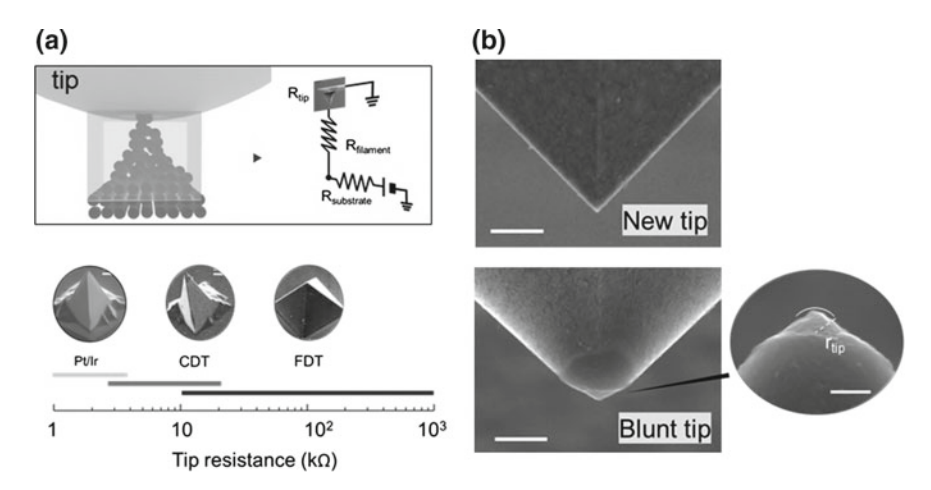


Fig. 4.4 *The role of the tip.* **a** Schematic of the total resistance in the tip-CF-sample system. In the inset, the resistance of different conductive tips is reported. **b** SEM inspection of a sharp FDT tip (scale bar 500 nm), compared to an intentionally blunted tip (scale bar 500 nm and inset 200 nm)

the tip acts also as a current limiter during the filament formation. In essence, once the CF forms the series resistance constituted by R_{substrate}, R_{filament} and R_{tip} is the limiting element for the flowing current (Fig. 4.4a). R_{substrate} is generally negligible due to the sample back-contact. R_{tip} can be considered as constituted of two terms. One accounting for the tip-sample resistance and a second bulk tip resistance, considered as the contribution of the remaining parts of the tip. When the CF is formed and a galvanic contact is (locally) created between tip and sample the first term is negligible. Therefore the second term, the bulk tip resistance becomes a relevant parameter. In the ideal case of a negligible filament-resistance, the current limitation is entirely set by the tip resistance. In reality, the tip resistance will always be in series with a non-negligible filament resistance and thereby their sum acts as a current limiter (Fig. 4.4a). Hence the choice of a lowly resistive tip can lead to a high programming current, destroying (by thermal dissipation) the sample. Conversely, a highly resistive tip could limit the current to levels at which RS is not induced. In view of this current limiting function, the conductive tip in C-AFM can be compared to the control-transistor in a 1T1R configuration. As example in Fig. 4.3b considering a set voltage of 1 V, one can now calculate the maximum current flowing through the electrical circuit formed by the series resistance of the tip and the filament similarly to a current compliance as extrapolation of the ohmic part of the I–V ($\approx 2 \,\mu$ A).

Figure 4.4a (bottom inset) shows different tips and their relative values of bulk tip resistance. Metal coated tips, provide low resistance values while diamond tips are generally showing high resistance. In addition, diamond tips show large variability of the nominal resistance value due to the conductivity variations of the doped diamond layer. However, the tip resistance can be calibrated on a Pt reference sample before the usage by a simple I–V measurement. To meet the low-current operation used for

devices (1–50 μ A), in this work where not specified, we use FDTs with resistance >10 k Ω . The use of resistive tips (i.e. low-switching currents) mitigates the thermal dissipation leading to morphological changes of the sample surface [11].

If the tip resistance is important to limit the current in the CF, the tip-radius is another relevant parameter as it can determine the final size of the tip-induced virtual capacitor. The electrical contact area evaluated for a new tip (Sect. 3.2.5), is estimated below $10\,\mathrm{nm}^2$. Assuming a current of $100\,\mathrm{pA}$ flowing in the tip-sample system, a current density of $1000\,\mathrm{A/cm}^2$ is easily reached. For point-contact measurements it might be important to achieve larger contact sizes. For example, to minimize the current density and associated heat dissipation, or to replicate larger device sizes with C-AFM (as shown in the next section). To this end a fresh tip can be intentionally blunted in order to enlarge the electrical contact-area. This can be achieved by ion beam milling [12] or by prolonged scanning of the tip. The result of this second approach can be seen in Fig. 4.4b. In this case the tip has been scanned for $\approx 20\,\mathrm{h}$ at high pressure (GPa) against a Pt surface. The SEM image shows the apexes of a pristine versus an intentionally blunted tip, the latter shows an increased tip radius compared to fresh tips (Fig. 3.4a).

4.1.4 Resistive Switching C-AFM Versus Devices

Aiming to gain insights on the physical mechanisms of RS, C-AFM must be able to reproduce electrically the same CF formation and switching observed in devices. We have partially introduced how to match operative current and device size by tuning the tip parameters. In this section those concepts are used in order to achieve good agreement between C-AFM experiments and MIM devices. Figure 4.5a shows

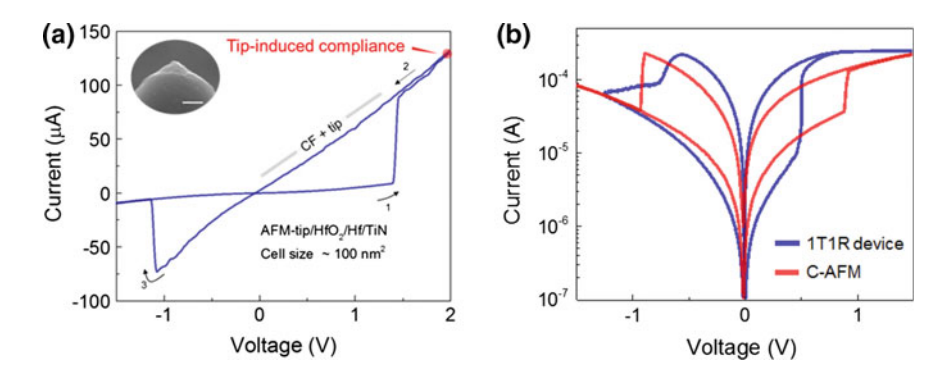


Fig. 4.5 Matching device operation in VCM. a An intentionally blunted tip is used to replicate the operation of a $100\,\mathrm{nm}^2$ MIM device. The stop voltage of the C-AFM bias sweep is used to impose the compliance current. Note, the current is measured with a C-AFM equipped with our custom FEMTO amplifier for the extend current sensitivity. b Comparison between C-AFM and integrated device both operated at $\approx 250~\mu\mathrm{A}$ current compliance

a C-AFM switching cycle of Hf/HfO₂. After the CF formation (Fig. 4.5a step 1), the current is limited by the series of CF + tip (Fig. 4.5a step 2). By modulating the voltage sweep it is possible to force the desired current in the CF, as in Fig. 4.5a we stop at 2 V with 125 μA . In Fig. 4.5b the C-AFM I–V characteristic is compared to a 1T1R device (50 \times 50 nm²), both electroformed and programmed at 250 μA . In the attempt to replicate the operations of a 50 \times 50 nm device as in Fig. 4.4b, a blunt AFM tip is used thus leading to a contact area of $\approx \! 100 \, \text{nm}^2$. A slightly higher set voltage is observed in C-AFM likely due to hemispherical electric field distribution induced by the conductive tip acting as a virtual electrode. For the rest, both I–Vs i.e. AFM tip-induced and MIM device, show good agreement.

It is worth noting, that when a sharp tip is used (independently from the tip material), it becomes difficult to force currents over 50 μA in the CF. The observed I–V curves are similar to the one showed in Fig. 4.3a, b where the CF resistance dominates the CF + tip series. This indicates that a highly resistive CF ($\approx\!M\Omega$) is formed when the contact size is below $10\,\text{nm}^2$. This will be clarified in Chap. 5 when the sizes of the CFs induced at different programming conditions are directly observed in two- and three-dimensions. However, the present observations indicate that the filaments programmed at current regime $>\!50\,\mu A$, require a later growth which exceed the sub- $\!10\,\text{nm}^2$ contact size provided by our sharp C-AFM tip. As a consequence, scaled contact sizes will induce highly resistive CFs and therefore limit the accessible currents to few tens of μA , independently on the tip resistance. This does not represent a problem for our study since the interest on RS phenomena is especially related to low-current operations.

With the setup shown in Fig. 4.5a (blunt tips) it is possible to achieve stable and repeatable cycling of the conductive filament for both CBRAM and VCM. Hundreds of cycles can be achieved using the C-AFM tip; ultimately limited by the quality of the tip-sample contact which is affected by many factors such as tip-forces, surface asperities, lateral drift and sample adhesion. Although far below regular device performance, is impressive that C-AFM in a single point-contact measurement can repeatedly induce hundreds of cycles. The latter suggests that conceptually a C-AFM-induced device is the same as a lithographically defined one.

By using a sharp tip the cycling stability reduces, resulting in few tens of consecutive cycles. This can be partially ascribed to the formation of weaker CFs, combined to a stronger impact of the contact-related issues when the contact size is very small. However, these are interesting results as they prove that (1) a minimum later growth (e.g. physical space) is required for the CF to achieve low resistance ($<100\,\mathrm{k}\Omega$). (2) The capability of C-AFM to mimic the RS mechanisms can be exploited to investigate the filament formation on blanket samples obtaining operations consistent with devices. The case of VCM is reported in Fig. 4.5b while CBRAM is reported in Fig. 4.6a, b. Good agreement is observed in the I–V characteristics of C-AFM and device operations. In Fig. 4.6a the LRS resistance R_{LRS} and I_{reset} are presented as function of the programming current for standard probe measurements of 0T1R and 1T1R devices and C-AFM in Fig. 4.6a. The results show the role of the compliance current in the formation of the resistance for the CF in LRS. By comparing our measurements with standard probe measurements, it is clear that C-AFM provides a

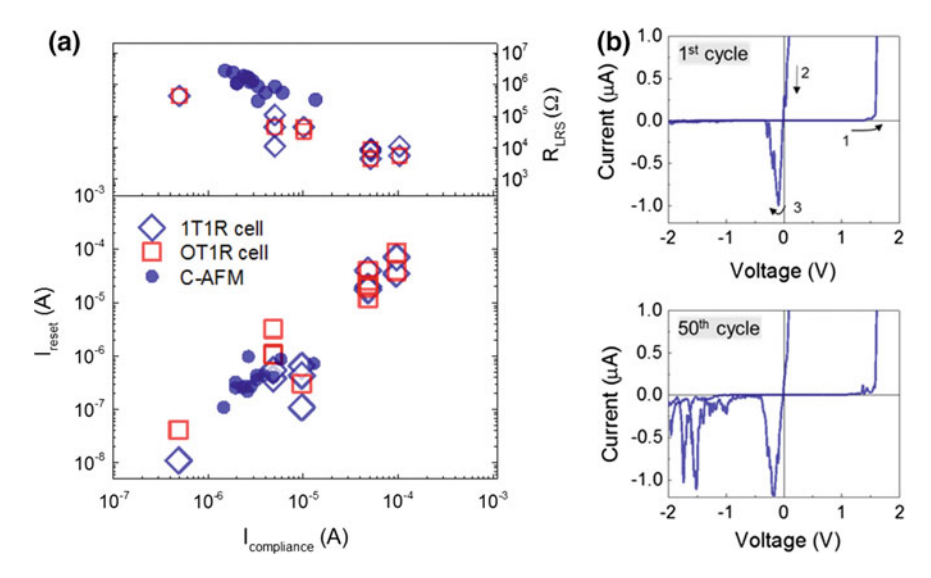


Fig. 4.6 Matching C-AFM with devices for CBRAM. **a** R_{LRS} resistance and resent current are shown as function of the compliance current for 0T1R, 1T1R and C-AFM. As visible, C-AFM can be used as a complementary analysis technique as the experimental observation are well in *line* with device results. **b** The first and the fiftieth cycles are shown for the Cu/Al_2O_3 -tip. The induced LRS is practically the same suggesting the same CF to be consequently formed and ruptured. Note, after prolonged cycling a leakage current appears after the reset, as indication of a progressive oxide degradation

complementary analysis tool specifically to study the physics of RS at low-current on the nanometer scale. In addition, by tuning the load force on the tip, C-AFM enables the modulation of the electrical contact size and therefore the analysis of RS at ultra-scaled dimensions as treated in the following sections. Remaining in the case of CBRAM, Fig. 4.6b compares the first and the last I–V characteristics after 50 cycles induced by C-AFM. The little variation of the R_{LRS} and reset voltages among the subsequent cycles may be an indication of the continuous formation and dissolution of the same conductive filament. On every formation and disruption the conductive filament likely undergoes some small changes in shape and size. On the last cycle of Fig. 4.6b after the reset transition, a certain leakage current appears in the reset sweep at -1 V, due to the oxide degradation during cycling. The latter effect is prominent especially after may cycles, indicating that this is a mechanism ultimately responsible for the degradation of these devices when too many defects in the oxide are generated [13].

4.1.5 Filament Observation

From Celano, U. et al., *Nanoscale*, 5, 11187, 2013.

From the previous sections, it is clear that the electrochemically-assisted formation/annihilation of Cu or V_{a} filaments described in Chap. 2 is feasible using a C-AFM tip. The added value of C-AFM relies in the possibility to probe also the shape and size of the CFs. In order to create a CF and inspect it with C-AFM, a simple four-step approach can be used: the conductive tip is used for (1) filament formation (2) LRS characterization (3) filament disruption (4) HRS characterization. Filament formation refers to create a CF and leave it in the LRS. This can be achieved by applying only the voltage sweep for the CF formation (avoiding the negative sweep) as in Fig. 4.7a from 0 to 2 V. Afterwards, the region where the point-contact I-V has been done, is scanned with C-AFM at low bias (10-100 mV read-out). This is done to observe the CF and its conductivity in the current map of C-AFM, without perturbating it. After the CF visualization the tip is positioned again onto the CF and the CF reset is achieved by point-contact voltage sweep, as in Fig. 4.7a this time applying a negative bias (from 0 to -0.5 V). The C-AFM read-out is repeated in the same region also for the HRS state. In this way the same CF can be inspected in its LRS and HRS state. The result is shown in Fig. 4.7b, whereby the same conductive filament is observed in LRS after the formation and HRS after the reset. In the LRS a highly conductive spot with a diameter \approx 20 nm is visible in the current map of C-AFM. The conductivity is highly localized in the inner part of the spot and tens of nA flow as measured by C-AFM with-10 mV applied to the sample with the tip grounded. After the LRS characterization the conductive tip is placed on the conductive filament and a reset DC sweep is ramped. Once in HRS the observation with C-AFM is repeated. The highly conductive spot is now carrying a very small current in the range of pA as compared to the nA of the LRS. Despite this 10³ fold decrease in current, the shape

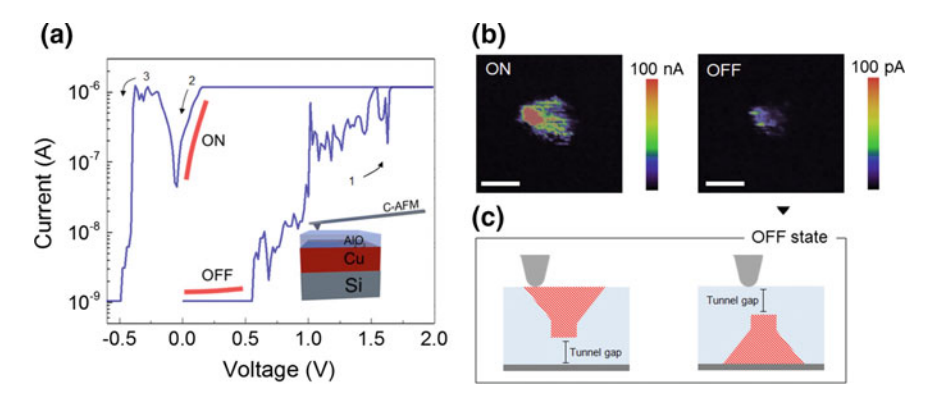


Fig. 4.7 *ON and OFF observation.* **a** C-AFM point contact I–V trace showing the CF formation and reset. **b** The same CF is observed with C-AFM (current map) in the ON (*top*) and OFF (*bottom*) state (scale 20 nm). Note the large difference in current visible in the current data scales

and size of the conductive spot is similar in both LRS and HRS. In this scenario, the tunneling gap created at the point of rupture of the conductive filament would be responsible for the leakage current observed in the HRS. This leaves the shape and size of the conductive spot in the C-AFM current map unchanged, and affects only the absolute value of the current that flows. However, this does not allow to unambiguously determine if the gap is formed on the top or the bottom interface as the results would be similar in both cases (inset Fig. 4.7c). Note, the spots are measured on the top surface of the sample as in the inset of Fig. 4.7a. Our results show conductive filament in LRS with a diameter of $\approx 20 \, \text{nm}$ on the surface of Al_2O_3 (note this is the side of the inert counter electrode).

Reduced dimensions for the CFs can be observed by using a sharp tip at moderate load force. However, in this case the repositioning of the tip with Å precision onto the CF for subsequent set and reset could be difficult. Despite the limitations, the LRS and HRS states of different CFs can still be individually induced and observed. Figure 4.8 shows two CFs respectively induced on Cu/Al₂O₃/ and Hf/HfO₂. The I–V curves related to the visualized CFs are shown in Fig. 4.3b, d. The conductivity of the CFs is highly localized and each spot presents a more conductive (core) region as also visible by a 2D cross-section in Fig. 4.8a, b (current profiles in the insets). The highly conductive sub-region of the CF can be quantified, and in both cases we obtained values well below 100 nm². As the reader will have noticed, the CF visualized for the HfO₂ shows a poor conductivity although in LRS (Fig. 4.8b). This is likely due to a fast passivation of the defects constituting the CF with the oxygen present on the sample surface once the tip is removed from the point-contact. This effect imposes severe limitations to the inspection of the CF in case of VCMs. This problem is mitigated in case of Cu-filament (Fig. 4.8a) due to reduced reactivity of Cu with the environmental oxygen. In this case the HRS, can be visualized after CF rupture as a spot with reduced conductivity (Fig. 4.7b). However, also the tip-induced Cu filaments show the tendency to recover (i.e. increase the CF resistance) with time. This is clearly visible in Fig. 4.8c, where the evolution of the $CF_{resistance}$ and CF_{area} is shown as function of time. The same CF is observed and the evolution of its size and conductivity is recorded during the continuous AFM scans. The tip is biased with 100 mV read-out voltage (similar results are observed also with opposite polarity). After $\approx 6 \,\mathrm{min}$, we observe a size reduction of the highly conductive area inside the CF. The latter is not associated with a large change in resistance, calculated as 0.1 V divided by the highest value of current measured in the CF. In the following read-out the CF resistance has a sudden increase, this is associated with a structural change in the CF visible as a size reduction (from \approx 38 to 19 nm²) and conductivity change. The CF is almost completely recovered in the last read-out (\approx 15 min). The current flowing is in the range of pA and the sizes are dramatically reduced to $\approx 10 \text{ nm}^2$. This effects which is consistent in all the tip-induced CFs, indicates a natural tendency of the CF to evolve into the HRS, when induced on blanket layers. It has to be considered that, the tip acts as nucleation site for the Cu-filament and therefore once it is removed to scan, the CF is exposed to the oxygen in-diffusion from the meniscus and surface contaminants accelerating its passivation. However, a poor LRS retention is often reported also for devices if programmed at low current ($<10 \,\mu\text{A}$). In addition, these

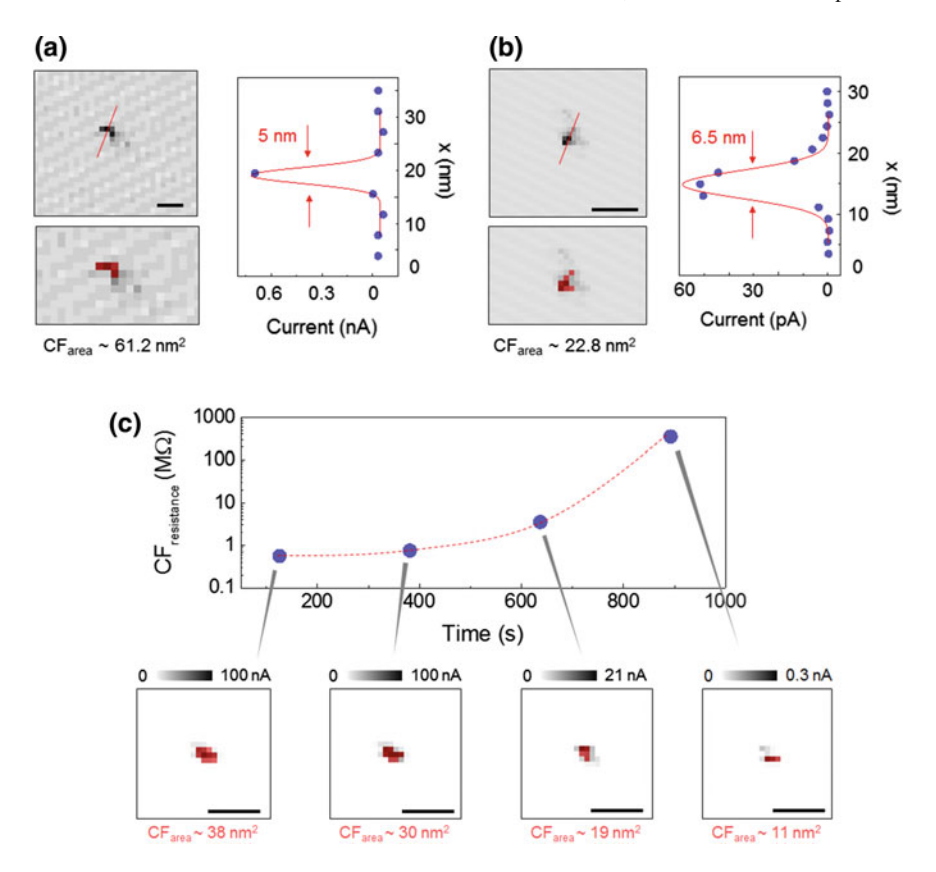


Fig. 4.8 Filaments at reduced dimensions. **a** Using a sharp tip at moderate force we induced and observe CF in the case of **a** Cu/Al₂O₃/ and **b** Hf/HfO₂. A 2D cross-section of the conductive profile and the quantification of the highly conductive area within the CF is provided. **c** The evolution of the conductivity and the dimensions is reported as function of time for a Cu-filament. Note, the values of the CF's area evolution is shown in the inset pictures as a transparent red area

resistive states tend to spontaneously drift toward higher values of resistances in pulse programming, a problem known as state relaxation [14]. Therefore our observations have to be likely considered as the direct experimental evidences of the metastable nature of the LRS.

Despite the short stability, the possibility to inspect CFs after their formation leads to the possibility to correlate geometrical parameters to electrical properties of the CFs. This is shown in Fig. 4.9a, where the CF area is plotted as function of the filament resistance (for Cu-filaments). The filament resistance is extracted from the ohmic branch of the I–V curve at the CF formation after subtracting the value of the tip resistance. The independence of the experimental values of filament area with the CF resistance suggests an irregular geometry for the CF in the third dimension. The CF is certainly not cylindrical because resistance and area would

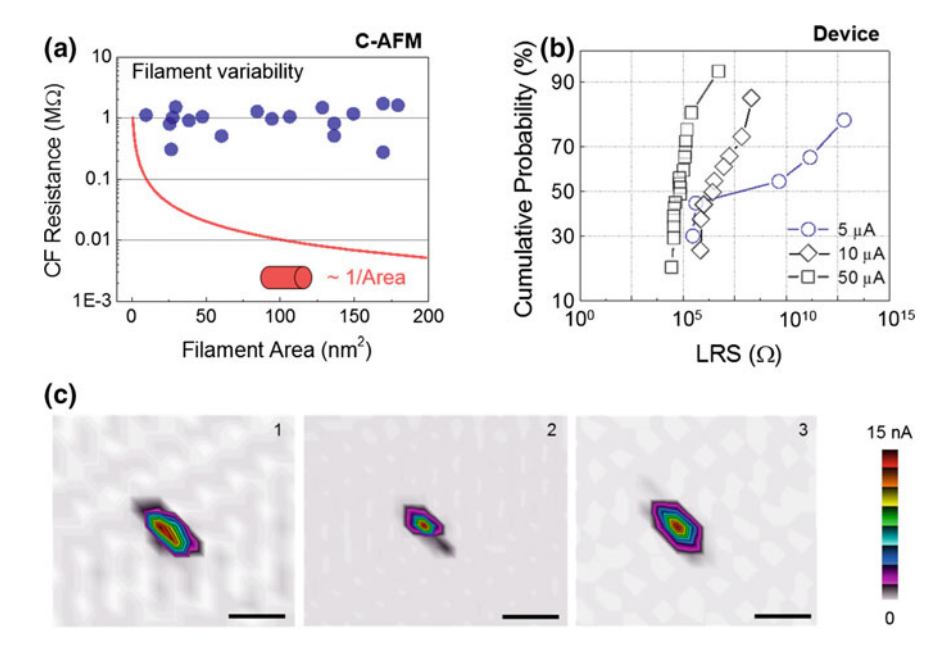


Fig. 4.9 Filament geometry considerations. **a** The area of various CFs formed under the same conditions is shown as function of the CF resistance. **b** R_{LRS} distribution observed in device when programmed under comparable current levels. **c** Conductivity, shape and size are compared for the same Cu-based filament after three subsequent formations (scale bar 20 nm)

have shown a \approx 1/A proportionality with A CF area (red trace Fig. 4.9a). While a truncated-cone geometry approximation is still possible due to the proportionality of the resistance with \approx 1/ab where a and b are respectively the major and minor bases of the truncated cone. Note that we can observe only the face of the CF measurable by C-AFM on the oxide surface, therefore the size/shape of the CF at the oxide/Cu (i.e. bottom) interface is unknown. Interestingly, filaments showing comparable value of resistance (and induced with similar conditions), present a large spread in the measured sizes as indication of two major facts. (1) The complex atomic structure of the CF in the third dimension contributes greatly to set the CF resistance. And (2) that the local properties of the solid electrolyte (e.g. density, porosity, thickness variation and absorbed moisture) can induce a large variation in the CFs formed under similar conditions. The same process is likely the physical explanation for the very large dispersion experimentally observed in the LRS distribution of MIM devices programmed with low current compliance as in Fig. 4.9b.

To elucidate this phenomenon, we repeatedly formed the same CF, and study the evolution of its dimensions and conductivity on three subsequent cycles. Figure 4.9c shows an example where the same CF is induced and inspected three times. The read-out scans after each formation are presented in Fig. 4.9c. Although with minimal differences in all the cases the spots have almost identical sizes while different

conductivity is observed (i.e. different current flowing at same read-out bias). This indicates that (1) the same CF tends to re-form on subsequent cycles, and (2) that atomic rearrangement of Cu in the CF can induce changes in the CF resistance even with no major CF geometrical modifications. This topic will be covered also in Chaps. 5 and 6 with the 3D observation of CFs and the tomography of multiple parasitic filaments.

Finally, these results partially show some limitations of the standard C-AFM technique. The observation of the CFs as (2D) conductive profiles on the surface of the solid electrolyte, cannot provide information of the entire CF and in particular of its constriction. As demonstrated in this section, the electrical properties of the CF are greatly dependent on those parts not directly accessible with the standard C-AFM.

4.2 C-AFM Probing the Reset State

Due to its remarkable spatial confinement C-AFM is a privileged tool to investigate at the nanoscale the structural changes of the CF during RS. While the LRS can be programmed and observed, the HRS is generally more complex to characterize in view of its reduced conductivity. In this section, to elucidate the nature of the CF in the HRS, we form and cycle CFs with the C-AFM and model their rupture based on the analytical fitting of the I-V characteristics. We explore the description of the erased CFs as either a tunnel-barrier or a quantum-point-contact. For CBRAM we demonstrate the formation of a tunnel barrier associated with the HRS state when the CF is confined under the C-AFM tip. For VCM, the modes of operation observed, can be related to the number of defects contained in the CF and modeled through a low-defects assisted quantum-point-contact (QPC) conduction. We assume that a generic reset transition can be considered as constituted by two main parts (Fig. 4.10). (1) An initial part where the CF is still present often showing fluctuations, which is considered characteristic for the creation of the conductive path for the HRS (dashed red line). And (2), a more stable part (termed as static) representative for the final state assumed by the CF in the HRS after the reset (solid blue line). As reference Fig. 4.10 shows this separation in the reset transition of a CBRAM device.

4.2.1 Gap Formation in Cu Filaments

From Celano, U. et al., *IEEE IEDM Tech. Dig.*, 14.1–14.4, **2014**.

In case of CBRAM, the reset operation starts when the negative polarity is applied at the Cu electrode. A large current flows through the CF due to its low resistivity and the temperature of the CF increases by Joule heating. The thermal conductivity of the Al_2O_3 is about 10 times smaller than that of Cu, and thus the temperature increase is mostly confined in the CF. The Cu atoms of the CF are thermally oxidized

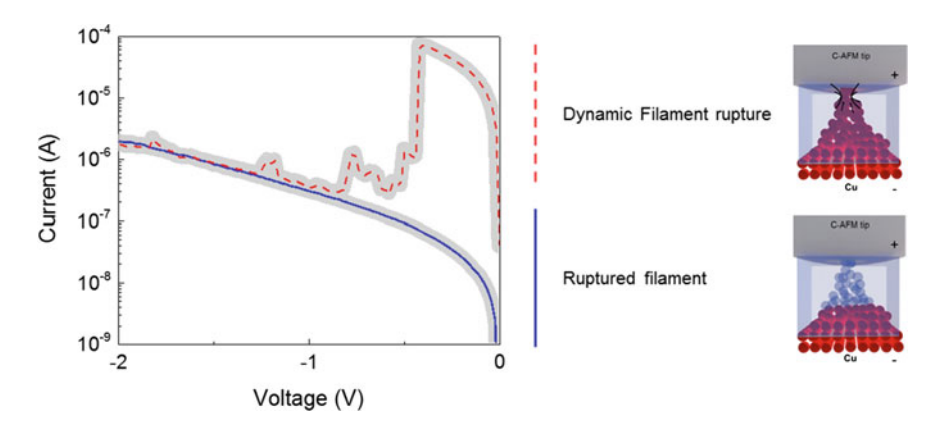


Fig. 4.10 Analysis of the reset transition. A general reset sweep can be divided in two main components: first, the dynamic transition of the CF from LRS to HRS associated with current fluctuations (red dashed line). Second, the final (static) HRS leakage baseline after the CF has changed its conductance (blue static line)

and they diffuse in the surrounding medium due to concentration gradient. Finally, electric-field driven and thermally activated hopping of Cu ions induces a structural rearrangement of the CF (enhanced at its constriction). In these conditions, the rupture of the CF takes place due to an electrochemical and Joule-heating assisted process [15–17].

When the reset is triggered, C-AFM detects a leakage current in correspondence of the CF rupture, immediately after the reset transition (on Cu/Al₂O₃). Figure 4.11a shows that after the CF rupture, clear steps appear in the reset sweep. These can be considered as the intermediate steps toward the final HRS which is induced in the CF at the end of the bias sweep (Fig. 4.11b). The different branches of the measured current leakage obey a Fowler-Nordheim tunnel (FNT) dependence (e.g. tunneling across an insulator gap of increasing thickness). In essence the observed jumps after the CF rupture are a signature of steps occurring during the tunnel-barrier (gap) formation. Note that different conduction mechanisms have been tried such as Schottky emission, Poole–Frenkel and QPC conductance but they did not provided satisfactory fitting to our curves [18]. In Fig. 4.11a, the provided fit demonstrate that the I–V curve for the leakage after the CF reset can be described with an analytical tunneling current description (as proposed by Schuegraf and Hu for a tunnel barrier) [19].

$$J = \frac{q^3}{16\pi^2\hbar} \frac{m_e}{m_{ox}} \frac{1}{\phi_B} F_{ox}^2 \times exp\left(-\frac{4}{3} \frac{\sqrt{2m_{ox}}}{q\hbar} \frac{\phi_B^{3/2}}{F_{ox}} \left(1 - \left(1 - \frac{vV_{ox}}{\phi_B}\right)^{3/2}\right)\right)$$
(4.1)

where q is the electron charge, m_e is the free electron mass, m_{ox} is the effective electron mass in the band gap of Al_2O_3 , \hbar is the reduced Planck constant, ϕ_B is the barrier height in electron volts for injection of the electrons, $F_{ox} = V_{ox}/d_{ox}$ is

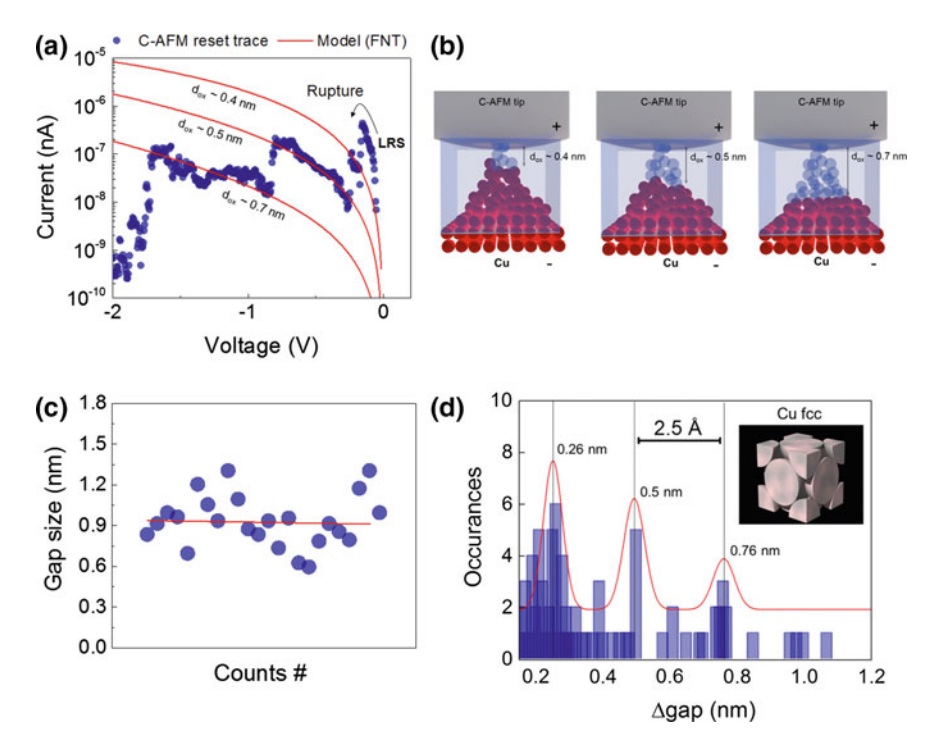


Fig. 4.11 *Tip-induced filament rupture in CBRAM*. **a** Tip-induced reset trace, the rupture of the CF and the transition between LRS to HRS presents a leakage current which follows a FNT dependence with increasing thickness of the tunnel barrier. **b** A three-steps gap formation process is schematically described in figure. **c** Values of d_{ox} extracted by the FNT fitting for the static part of the I–V, an average 0.9 nm gap is induced. **d** We introduce Δ gap as the difference between two consecutive barrier thicknesses $(d_{ox_n} - d_{ox_n-1})$. Δ gap can be interpreted as the size of the consecutive steps done by the CF during the formation of the tunneling gap after filament rupture. We plot all the steps into a histogram, and we clearly observe peaks appearing at integer of 2.5 Å. Those are fitted with a series of Gaussian distributions as a guide to the eyes. In the inset conventional cell with cannonballs at each point of the Bravias lattice is shown for Cu fcc

the electric field across the oxide (V_{ox} is the bias across the oxide, d_{ox} is the oxide thickness). In this formulation the model is optimized for oxides below 2 nm and has a correction factor for direct tunnel (DT) regime for $V_{ox} < \phi_B/q$ and FNT regime for $V_{ox} > \phi_B/q$. The set of parameters used for the fitting are experimentally extracted by internal photo emission spectroscopy (IPE) analysis carried out on Cu/Al₂O₃ reference stack ($\phi_B = 3.5$ eV and $m_{ox} = 0.4$ eV) [20].

Using the FNT equation, to fit the HRS baseline after CF rupture, we can extract the thickness of the tunnel-barrier induced at the end of the reset transition (4.11c). This is in the order of \approx 0.9 nm. Due to the appearance of intermediate steps in the reset transition (Fig. 4.11a), we can quantify the steps between subsequent jumps (e.g. step = $d_{ox2} - d_{ox1}$) to account for the intermediate tunnel-barrier growth. Interestingly, when we repeat this experiment on several reset traces and plot the histograms of

the subsequent steps we observe clear peaks at integers of 2.5 Å which is in the same order as the lattice parameter of the Cu metallic-phase. This proves that due to the high spatial confinement of C-AFM a limited number of Cu atoms are in the constriction which dissolves leading to a tunnel gap formation. The latter is achieved by a quantized evolution of the originally connected CF with steps on average of 2.5 Å. It is worth noting that using the $\text{Cu/Al}_2\text{O}_3$ -tip configuration, we consistently observe the formation of a tunnel gap associated to a abrupt type of reset. A more complete CF rupture dynamic will be discussed in the next chapter for the case of integrated devices. There, our observation will be integrated by a complementary phenomenon which is the size modulation of the filament constriction. This is also associated to a different type of reset namely "progressive".

4.2.2 Low-Defects Assisted Quantum-Point-Contact

For the Hf/HfO₂ material system in Chap. 2 we have described a quantum point contact conductance model that well describes the device operations [21]. The QPC model describes the behavior of a physical constriction with a current-controlling energy barrier. Using as fitting parameter the geometrical dimensions of the filament constriction e.g. the number of particles in the constriction. The model provides a good fitting also for the I–Vs recorded with C-AFM. However also in this case, the high spatial confinement provided by C-AFM enables the analysis of the reset transition at very low dimensions, and thus unfolds the related switching mechanisms.

CFs are formed using FDT in sub- $10\,\mathrm{nm}^2$ configuration with programming currents below $10\,\mu\mathrm{A}$. Similarly to CBRAM, the CFs' resistance is in the order of M Ω also in this case. This is a known condition, often reported for MIM devices [22]. The LRS starts to increase and the ON state of the I–V characteristic deviates from the standard ohmic behavior especially at the zero crossing point. The stability of the CFs is often affected and the majority of the CFs does not maintain the state after removing the voltage stimulus [23]. It has been often debated if in such conditions the CF undergoes a complete rupture (similar to CBRAM case) or it is still constituted of few connected defects [24, 25]. We repeated the analytical study of the negative part of the C-AFM I–V characteristics also for Hf/HfO2. Different conduction models are tried to fit the leakage current during reset transition (Schottky emission, Poole–Frenkel, direct and Fowler-Nordheim tunnel). It is worth noting that in this case the only model providing satisfactory fit is QPC. We observe three main RS behaviors.

In Figure 4.12 linear and log scales are provided for each I–V curve. Traces of the QPC model are shown in red as function of decreasing number of defects in the CF constriction. As example, in a population of 100 tip-induced RS events, a small fraction (\approx 5–10%) presents the standard RS behavior as in Fig. 4.12a. This is associated with an ohmic LRS which is lost when the CF is ruptured during the negative I–V sweep. The rest (\approx 90%) of the RS events present a strongly rectifying or a threshold-switching (TS) behavior Fig. 4.12b, c. Note, that QPC provides a good fit for all the observed I–Vs (Fig. 4.12a–c), whereby the different modes can be induced

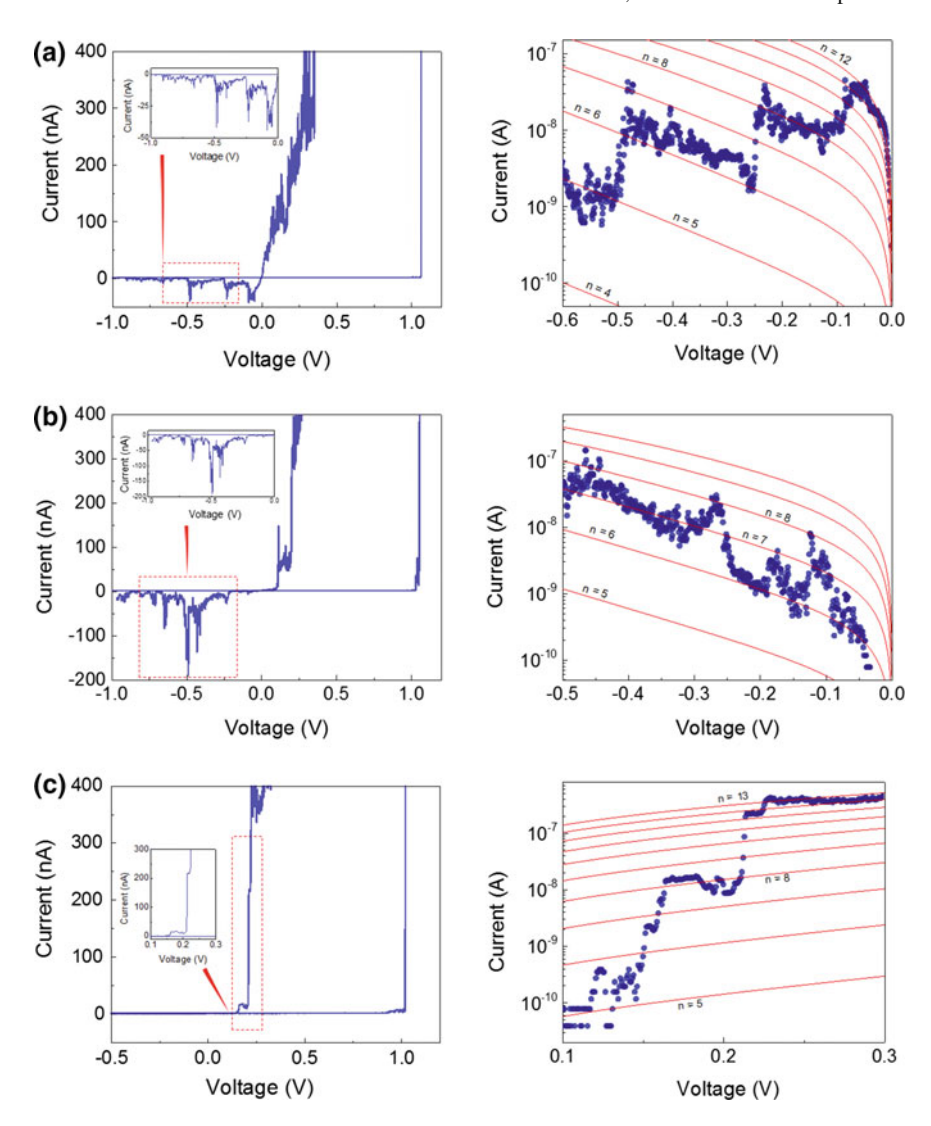


Fig. 4.12 *Tip-induced RS in VCM*. **a** Standard RS showing ohmic LRS behavior is shown in linear and log scale with QPC fitting provided. **b** Rectifying RS showing fluctuations during reset, indicating some structural rearrangements of the CF during the reset and **c** threshold switching behavior also associated with unstable CF (note the reset at low positive bias). By looking all the I–Vs in logarithmic scale, the transition from LRS to HRS presents a leakage current which follows a QPC dependence for all the cases with an decreasing number of V_o : in the CF constriction, we over impose the QPC fit (*red solid lines*) using limited number of oxygen vacancies (n represents the number of V_o :)

solely by changing the number of V_o as indicated by the red lines (fitting curves) in Fig. 4.12a–c. The number of V_o in the tip-induced CFs is in range 10–20. All the induced CFs have in common the highly resistive LRS and the small number of V_o . Note that previous studies on integrated devices operated at low-current, presented similar values of the induced LRS but a high percentage of CFs showing direct tunnel (DT) behavior with CF resistances over 100 M Ω [24]. In our C-AFM study, the number of CFs showing DT behavior is practically negligible also for highly resistive CFs. It is worth noting that for Fig. 4.12c the CF starts to erase already at positive polarity nevertheless in agreement with the QPC description (as visible in the fitting).

Hence, the three different I–V characteristics observed are function of the number of defects constituting the reduced cross section part of the CFs. Furthermore, on subsequent set/reset transitions we observe a continuous fluctuation among the different types of the possible I–V characteristics. The latter proves that the CF filament geometry undergoes small structural changes on every cycle due to the electrical stress. Due to the ultra-scaled volume sampled by the AFM-tip, the impact of this nanosized rearrangement is amplified indicating an instability of the atomic-size CF. Our experiments suggest that the CFs continue to behave like a QPCs in non-linear regime also when programmed at low-current and ultra-scaled dimensions. In other words, the CF created as a local valence change within the HfO₂ presents an atomic-scale constriction thus behaving like a QPC. Owing to the high confinement e.g. <100 nm² and the low operative current e.g. <10 µA, very few defects are constituting the constriction thus increasing the energy barrier for the first available subband limiting the electron transport. In essence, the electrons which are energetically positioned at the Fermi level of the two reservoirs will depend on the applied voltage to increase their probability to tunnel through the QPC subband leading to a strongly nonlinear zero-crossing characteristic. This is at the origin of the CF instability and also of the observed TS. Furthermore microscopic changes of the defect arrangement in the OFF-state CF have a big influence on the CF stability explaining the pronounced cycle to cycle variability that is observed also in integrated devices [23]. Our results are in agreement with Long et al. [23] in their work on low current RS in large MOS structures.

Based on our observation, the final configuration of the filament for any value of the programming current below $10\,\mu A$ is not deterministic. In other words, at low current there is an intrinsic stochastic nature of the RS-phenomenon leading to formation of CFs where the atomic constriction has such a small number of defects that the two electron reservoirs are connected through a tunnel mechanism. Independently of the forming conditions when the programming current is below $10~\mu A$ we observe a non-zero probability for the CF configuration to show this bimodal behavior. This is not surprising if one considers that the RS is only a subset of the soft (SBD) and progressive (PBD) breakdown theory [26]. The final configuration of the filament is bimodal with a finite non-zero probability of being QPC mode or tunnel barrier (TUN) mode.

A model for CFs at reduced dimension—Although the differences observed in the I–Vs (Fig. 4.12a-c) suggest different structural properties for the CFs, they might be viewed as the extreme case of QPC conductance (Fig. 4.13). During the electroforming the electric field induces the formation and the rearrangement of oxygen vacancies in the HfO2, converting de facto a fraction of the oxide volume into the CF i.e. local valence-change. With drastically decreasing dimensions (3 × 3 nm and below) the number of available defects cannot be described as an average density identical at all locations, but needs to be viewed as a stochastic variable creating local different probabilities for the CF formation. This explains the variability observed. On the other hand, the QPC theory can still account for all the observed RS characteristics including the evolution into TS (Fig. 4.12c) when a low number of defects (below ≈ 10) is used. As the number of defects within the constriction reduces the barrier height of the first available electrons subbands in the QPC and the Fermi level position of the electrons reservoir determines the transport in the CF (Fig. 4.13 inset), as also reported by Long et al.[23] for devices in low-current regime.

In our C-AFM experiments, the reduced appearance of DT behaviors, suggests that the limited spatial dimensions and the high field-confinement can contribute to the formation of QPC-behaving CFs. Those are generally more desirable for their higher stability. The number of defects effectively constituting the CF's constriction, will determine the filament electrical behavior. In essence, our results indicate that the CF stability in ultra-scaled devices will depend on the maximization of the oxide volume

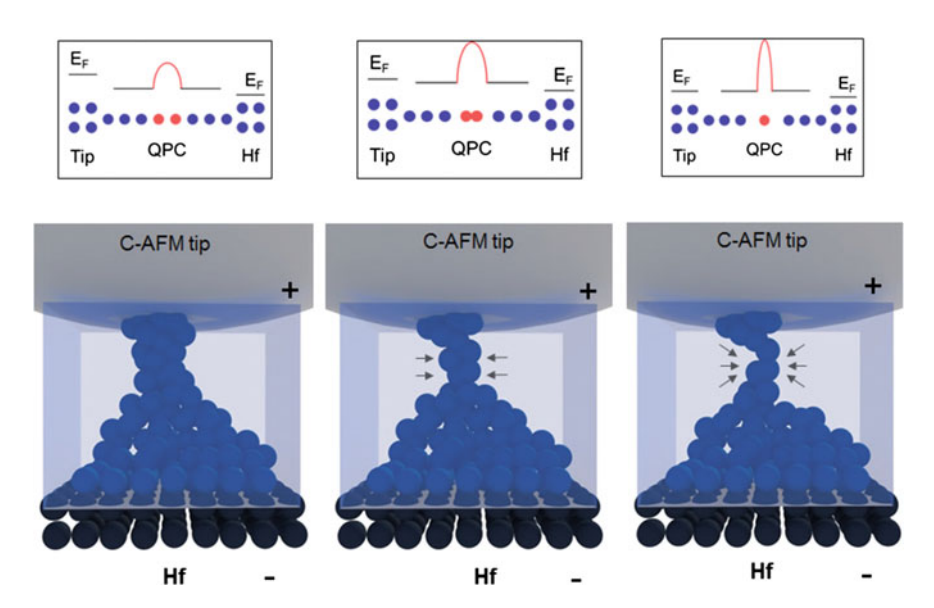


Fig. 4.13 *Tip-induced filament rupture in VCM*. Three configurations of the CF constriction are schematically described. The *top inset* shows the schematic of the energy diagram for the three cases, emphasizing the role of the barrier height of the first available electrons subbands and the Fermi level position of the electrons reservoir as the number of V_o decreases in the QPC constriction

effectively converted into active (defects rich) filament volume. Before closing, it has to be mentioned that working with C-AFM in air, the presence of absorbed water (meniscus) on the tip and the blanket sample can affect our measurements. In particular the availability of oxygen in proximity of the tip-sample physical contact enhances the possibility of undesired interaction between V_o s of the CF and oxygen atoms. The major impact of this can be an enhanced cycle-to-cycle variability and CF instability both observed in our experiments. Although working in controlled environment this effect is hardly controllable due to the extremely reduced number of V_o s constituting the CF.

4.3 Device De-Process: Filament Observation

From Celano, U. et al., *Applied Physics Letters*, 102, 121602, **2013**. From Celano, U. et al., *Microelectronic Engineering*, 120, 67-70, **2014**.

In this section, to elucidate the nature of resistive switching on MIM cell structure, C-AFM is used in a reverse engineering fashion. In integrated capacitor-like devices the layers of interest (Al_2O_3 or HfO_2) are buried under several tens of nm (top electrodes) [27, 28]. In this situation, the electrical information is averaged due to the presence of the electrodes. C-AFM can be used only after the metal electrode shielding the oxides is removed. There are three possibilities for the removal of the top electrode: (1) wet chemical etching (2) ion milling (3) physical scraping. The chemical removal by means of etchants might be detrimental for the stability of the conductive filament. The use of focus ion milling has been demonstrated by Singh et al.[29] on large devices, but in real cases higher accuracy is needed due to the highly scaled device dimensions. Muenstermann et al.[6] have used a removal technique based on delamination by adhesive tape to investigate TiO_2 under Pt electrodes.

As introduced in Chap. 3, we have developed a nanometer precise removal technique by means of diamond tips and C-AFM [30]. The combination of high pressure and high hardness of the FDTs is exploited here to physically remove the top electrode by mechanical scraping. In this manner the surface of the dielectrics becomes accessible and the conductive filament can be characterized with C-AFM. The advantages of this approach are threefold: First, the presence of the electrode during the cycling phase, allows to stress the device in the real operative conditions and actual devices can be used. Second, the electrical programming is done ex-situ and the C-AFM is used at low bias only for the subsequent characterization. Third, all the materials softer than diamond can be removed with nm-precision [27, 31].

Electrode removal in HfO₂ VCM—the memory element in our study is a capacitor-like structure based on HfO₂, as shown in Fig. 4.14. A 30 nm-thick TiN layer is deposited on a standard p-type Si(100) wafer, followed by 10 nm of metallic Hf grown by low-temperature PVD and 10 nm HfO₂ deposited with a standard water-based ALD process. Finally, a 30 nm TiN top electrode is deposited on top of the

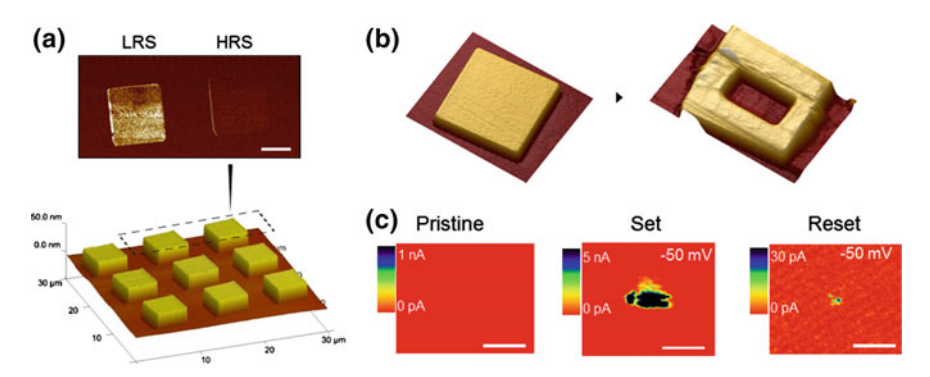


Fig. 4.14 Top electrode removal VCM. a The array of $5 \times 5~\mu\text{m}^2$ cells is shown in 3D by AFM. In the inset, two devices respectively programmed in LRS and HRS are image by C-AFM (current map). The LRS is characterized by a high leakage current ($\approx 1~\text{nA}$), while the HRS shows a low but non-negligible (\approx) pA leakage. Both electrodes are visible indicating, th presence of CF with different resistive states. b The 30-nm TiN top electrode is imaged before and after material removal. (c) The oxide interface is exposed and observed with C-AFM at read-out bias ($\approx 100~\text{mV}$) for pristine memory element, where no filaments are observed, LRS where highly conductive CFs with diameter of the filament $\approx 50~\text{nm}$ are observed. Finally for HRS, C-AFM current map presents filament with diameter in range 5–10 nm carrying currents in the pA range (scale bars 50 nm)

HfO $_2$. The sample is then patterned, creating $5\times 5~\mu m^2$ cells (inset Fig. 4.14a). Figure 4.14a top inset shows two C-AFM current maps of different cells (metal electrode still present) respectively programmed in LRS and HRS. The device on the left is formed and the one on the right has been formed and then reset. Though the leakage current flowing in the HRS cell is dramatically lower than for the LRS, it remains non negligible and the device can still be observed relative to the surrounding insulating material. This confirms the presence of conductive filaments under the top electrode in both cases. It is important to stress that the uniformity of the current maps in Fig. 4.14a is due to the highly conductive electrode, still present at this stage, which shields all electrical differences and thus prevents the local filament observation. For the sake of completeness, it is worth mention that the measured C-AFM map on a fresh cell does not present any current, which indicates the absence of any filaments shortening the two electrodes before the electro forming step.

Once the state of the memory element has been programmed, the top electrode can be removed to be able to investigate the buried HfO₂ layer with C-AFM. Hence we have used our material removal procedure using the FDT (diamond-based) tips. As reported in Chap. 3, we slow down the scan speed to (0.4 Hz) and increase the load force on the tip in the GPa regime. Finally, the number of lines acquired is increased to 512. Under these conditions the AFM performs hundreds of scans on the 5×5 μm^2 cell progressively opening a window into the TiN top electrode (Fig. 4.14b). With this procedure an extremely precise removal rate in range 1-2 nm/hour has been achieved. The equality of the heights of the de-processed region and of the TiN top electrode is used as the stopping criterion for the material removal (Fig. 4.14b). Once

the interface of interest is reached, we reduce the load force to μN and bias the tip with a read-out voltage.

One sample for each of the three states: fresh, LRS and HRS has been subjected to this procedure. First, the pristine cell Fig. 4.14b does not show any leakage current under a read-out bias voltage (-100 mV) in C-AFM. This is expected since the 10 nm HfO₂ layer is thick enough to prevent any visible current in this stress regime. Second, the LRS (set) presents multiple filaments with an observed diameter ranging between 30 and 50 nm when "read" at—50 mV. The current carried by these conductive paths is on the order of 1 nA. The conduction is fairly homogeneous within the conductive spot. Finally, in the reset state, many filaments are also present. These filaments, however, have smaller diameters (5-10 nm) and their leakage current is in the pA range. In other words, while no current is measured in the fresh state, a non-negligible leakage current is detected both in the set and reset cells, which indicates the clear role of the forming step as a trigger for the filament formation and the fact that even after a reset operation the material does not return to its initial pre-formed state but rather to a situation where the conductivity of the filamentary conduction path is drastically reduced. Note, that after top electrode removal, the spots are randomly distributed on the exposed HfO₂ surface, and afterward, centered in the C-AFM. These measurements were repeated in four different cells (two in LRS and two in HRS) showing similar results. It has to be mentioned that, due to the reduced electrode sizes $5 \times 5 \mu m^2$ the C-AFM tip has been used also to form and cycle the MIM structures with a very limited control on the compliance current. Therefore, the cells often required multiple electroforming steps, thus it is not surprising the presence of multiple filaments experimentally observed. Higher accuracy in the electrical programming is achieved in Chap. 5 where we will present the observation in 1T1R devices.

Top electrode removal for CBRAM—the memory device in this case is a capacitor-like structure stacked on top of a selector transistor e.g. 1T1R scheme. The memory cell is built on top of a 100-nm-wide TiN metal line connected to the drain of the transistor (Fig. 4.15a). The entire stack of the cell is deposited and when the sample is patterned by mean of electron-beam lithography (e-beam) the final memory structure is located at the point of intersection between TiN bottom electrode (BE) and the top electrode (TE). Amorphous Al₂O₃ 3 nm is used as switching layer. This is deposited using a plasma enhanced atomic layer deposition technique (PE-ALD) at 45 °C, using O₂ plasma and Tri-Methyl Aluminum (TMA) precursor. To prevent in-diffusion processes of the Cu species into the Al₂O₃ we insert 3 nm-thick Ti layer before the 20 nm Cu electrode acting as cation supplier. Finally, Au (20 nm) is deposited on top of Cu in order to avoid oxidation of the Cu and to provide the contact for the final device. Note, that after the e-beam patterning the layer of Al₂O₃ remains only in the cross-point and its sizes are $\approx 100 \times 100 \text{ nm}^2$ (inset Fig. 4.15a).

The devices are electrically programmed using a conventional parameter analyzer (HP4156). Exploiting the selector transistor, the C.C. is kept at 100 μ A during forming and set operations. In this regime the memory state can be set and reset many times showing a stable $\approx 2-3$ order of magnitude resistance window R_{HRS}/R_{LRS}

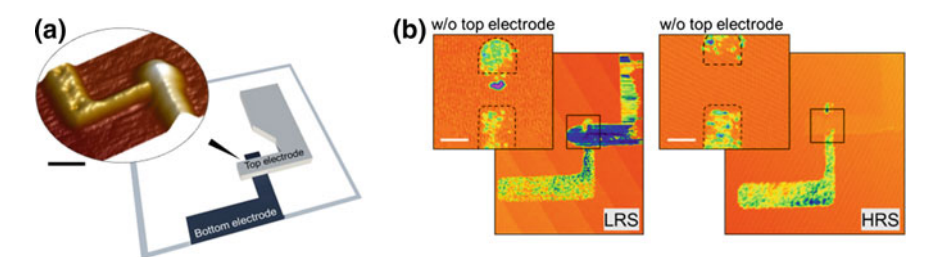


Fig. 4.15 *Top* electrode removal of CBRAM. **a** Cross-point memory device before the *top* electrode removal. In the inset AFM topography is shown (scale bar 100 nm). **b** C-AFM current maps (50 mV bias) are shown for LRS and HRS devices. LRS is characterized by a high leakage current and both electrodes are clearly visible. While the HRS presents lower leakage and the *top* electrode is barely visible indicated reduced conductivity for the CF. In the *inset* the active area of both devices is shown without *top* electrodes (scale 80 nm). The CF is clearly visible as a conductive spot for the LRS case, while in HRS due to the reduced conductivity no clear CF is detected

(as reported elsewhere) [27]. Figure 4.15b shows the C-AFM current maps of the LRS and HRS respectively. Though the top electrode is still present thus inhibiting the observation of the details of the filament, the state of the cell is clearly visible by the observed leakage current with higher leakage current in the LRS (4.15b) than for the HRS case. The values of leakage measured with C-AFM are in agreement with the resistance values previously reported by the semiconductor parameter analyzer. The leakage current flowing in both the LRS and HRS is dramatically higher than the case of fresh device. In fact the top electrode of a pristine cell is completely invisible in the C-AFM current map (not shown for brevity) because no filaments has formed i.e. no electrical connection exists between top and bottom electrodes.

In order to remove the 20-nm Au/20-nm Cu/3-nm Ti (top electrode) scalpel SPM is used. In case of Au and Cu (softer than TiN), few tens of AFM scans are sufficient to expose the oxide interface. The CF is unambiguously revealed in the LRS figure inset, after top electrode removal. The CF appears as a highly conductive spot with diameter $\approx\!30\,\text{nm}$, carrying tens of nA (on read-out bias—10 mV). Comparing the HRS and LRS with the top electrodes still present, it is clear that the CF has now a reduces conductivity. Although, no conductive spots are observed when the electrode is removed (inset), the dielectric layer has been repeatedly stressed during the cycling and this can give rise to the increased leakage current compared to the fresh state. However, the current in the HRS is in the pA range as stressed with $10\,\text{mV}$ applied by the C-AFM and this is generally not sufficient to observed by standard C-AFM (used for this experiment). In the next chapter HRS CFs are investigated using higher sensitivity for 2D and 3D observation.

4.4 Summary of the Chapter

In this chapter, conductive atomic force microscopy has been used to investigate the local nature of resistive switching by using the tip as a movable top electrode. First the benefits of using C-AFM and the possibility to match device operation using the nanosized tip have been demonstrated. We have optimized the tip parameters in order to replicate the device operations and to induce CFs with sub-10 nm² dimensions. The tip-induced CFs have showed cyclability up to hundreds of cycles with few μA operative current, providing a good indication for the high scalability of this memory technology. Cu- and V_{α} -based CFs have been induced at the nanoscale and visualized. This allowed the study of their dimensions and relate them to their electrical behaviors. The high spatial confinement of C-AFM has enabled the analysis on scales which are of major interest to study the scaling trends of RS devices (below 10 nm²). We have used analytic fitting of the I-Vs recorded by C-AFM to clarify the nature of the CF rupture for CBRAM and VCM. In case of Cu-based CFs we have observed the tendency to form CFs which undergo a physical rupture on reset with consequent formation of a tunnel barrier, possible to fit only with a Fowler-Nordheim tunnel model. On the other hand for the filaments of VCM a quantum point contact conductance model is required for a proper fitting. Indicating that the reduced number of defects in the CF constriction, can account for all the observed electrical behaviors within the framework of the OPC conduction also at very scaled dimensions. Finally, a tip-induced material removal technique has been exploited for the observation of the filaments (LRS and HRS) in conventional MIM devices by removal of the top electrode and observation of the CFs. The high hardness of diamond-based conductive tips has been used to physically remove the top electrodes MIM devices after setting their memory state. For this purpose, an high precision top electrodes removal technique with controllable removal rate in range 0.1–10 nm/scan has been developed and successfully applied to TiN, Au, Cu and Ti. The latter represents the ancestor of our SPM tomography introduced in the next chapter.

References

- 1. M.H. Lee, C.S. Hwang, Resistive switching memory: observations with scanning probe microscopy. Nanoscale 3(2), 490–502 (2011)
- K. Szot, W. Speier, G. Bihlmayer, R. Waser, Switching the electrical resistance of individual dislocations in single-crystalline SrTiO₃. Nat. Mater. 5(4), 312–320 (2006)
- R. Dittmann, R. Muenstermann, I. Krug, D. Park, T. Menke, J. Mayer, A. Besmehn, F. Kronast, C.M. Schneider, R. Waser, Scaling potential of local redox processes in memristive SrTiO₃ thin-film devices. Proc. IEEE 100(6), 1979–1990 (2012)
- J. Lee, M. Jo, D-j Seong, J. Shin, H. Hwang, Materials and process aspect of cross-point RRAM (invited). Microelectr. Eng. 88(7), 1113–1118 (2011)
- Polspoel, W.: High resolution study of high—k layers using C-AFM. Ph.D. thesis, KU Leuven (2012)

- R. Muenstermann, R. Dittmann, K. Szot, S. Mi, C-L. Jia, P. Meuffels, R. Waser, Realization of regular arrays of nanoscale resistive switching blocks in thin films of Nb-doped SrTiO₃. Appl. Phys. Lett. 93(2), 023110 (2008)
- R. Garcia, A.W. Knoll, E. Riedo, Advanced scanning probe lithography. Nat. Nanotechnol. 9(8), 577–587 (2014)
- 8. Celano, U.: Evaluation of the electrical contact area in contact-mode scanning probe microscopy. J. Appl. Phys. (2015)
- F. Peter, J. Kubacki, K. Szot, B. Reichenberg, R. Waser, Influence of adsorbates on the piezoresponse of KNbO 3. Physica Status Solidi (a) 203(3), 616–621 (2006)
- S. Kremmer, S. Peissl, C. Teichert, F. Kuchar, H. Hofer, Modification and characterization of thin silicon gate oxides using conducting atomic force microscopy. Mater. Sci. Eng. B 102(1–3), 88–93 (2003)
- W. Polspoel, P. Favia, J. Mody, H. Bender, W. Vandervorst, Physical degradation of gate dielectrics induced by local electrical stress using conductive atomic force microscopy. J. Appl. Phys. 106(2), 024101 (2009)
- M. Kopycinska-Müller, R.H. Geiss, D.C. Hurley, Contact mechanics and tip shape in AFM-based nanomechanical measurements. Ultramicroscopy 106(6), 466–474 (2006)
- 13. S. Balatti, S. Ambrogio, Z. Wang, S. Sills, A. Calderoni, N. Ramaswamy, D. Ielmini, Pulsed cycling operation and endurance failure of metal-oxide resistive (RRAM), in *IEDM Technical Digest*, pp. 359–362 (2014)
- 14. A. Belmonte, A. Fantini, A. Redolfi, M. Houssa, M. Jurczak, L. Goux, Excellent Roff/Ron ratio and short programming time in Cu/Al₂O₃-based conductive-bridging RAM under low-current (10 μA) operation, in *physica status solidi* (a), **213**(2), pp. 302–305, February (2016)
- S. Larentis, F. Nardi, S. Balatti, D.C. Gilmer, D. Ielmini, Senior Student Member, Resistive switching by voltage-driven ion migration in bipolar RRAM—Part II: Modeling. IEEE Elect. Device Lett. 59(9), 2468–2475 (2012)
- I. Valov, R. Waser, J.R. Jameson, M.N. Kozicki, Electrochemical metallization memoriesfundamentals, applications, prospects. Nanotechnology 22(25), 254003 (2011)
- 17. Y. Yang, P. Gao, S. Gaba, T. Chang, X. Pan, L. Wei, Observation of conducting filament growth in nanoscale resistive memories. Nat. Commun. 3, 732 (2012)
- U. Celano, L. Goux, A. Belmonte, K. Opsomer, R. Degraeve, C. Detavernier, M. Jurczak, W. Vandervorst, Understanding the dual nature of the filament dissolution in conductive bridging devices. J. Phys. Chem. Lett. 1919–1924 (2015)
- F. Klaus, Schuegraf and Chenming Hu. Hole Injection Si02 Breakdown Model for Very Low Voltage Lifetime Extrapolation. IEEE Trans. Electr. Devices 41(5), 761–767 (1994)
- F. De Stefano, V.V. Afanas'ev, M. Houssa, A. Stesmans, K. Opsomer, M. Jurczak, L. Goux, Control of metal/oxide electron barriers in CBRAM cells by low work-function liners. Microelectr.c Eng. 109, 156–159 (2013)
- R. Degraeve, L. Ph Roussel, D.Wouters Goux, J. Kittl, L. Altimime, M. Jurczak, G. Groeseneken, Generic learning of TDDB applied to RRAM for improved understanding of conduction and switching mechanism through multiple filaments. IEDM Tech. Dig. IEEE Int. Electr. Devices Meeting 1, 632–635 (2010)
- 22. L. Goux, A. Fantini, G. Kar, Y. Chen, N. Jossart, R. Degraeve, S. Clima, B. Govoreanu, G. Lorenzo, G. Pourtois, D.J. Wouters, J.A. Kittl, L. Altimime, M. Jurczak, Ultralow sub-500 nA Operating Current High-performance TiN \ Al₂O₃ \ HfO₂ \ Hf \ TiN Bipolar RRAM Achieved Through Understanding-based Stack-engineering. pp. 159–160 (2012)
- S. Long, M. Liu, X. Saura, E. Miranda, D. Jime, J.M. Rafi, F. Campabadal, J. Suñé, Threshold Switching and Conductance Quantization in Al/HfO₂/Si (p) Structures. Jpn. J. Appl. Phys. 52(4) (2013)
- N. Raghavan, R. Degraeve, L. Goux, A. Fantini, D.J. Wouters, G. Groeseneken, M. Jurczak, RTN Insight to Filamentary Instability and Disturb Immunity in Ultra-Low Power Switching HfO x and AlO x RRAM 84(2012), 159–160 (2013)
- F.M. Puglisi, L. Larcher, A. Padovani, P. Pavan, A complete statistical investigation of RTN in HfO₂-Based RRAM in High Resistive State. IEEE Trans. Electr. Devices 62(8), 2606–2613 (2015)

References 113

 R. Degraeve, G. Groeseneken, R. Bellens, J.L. Ogier, M. Depas, P.J. Roussel, H.E. Maes, New insights in the relation between electron trap generation and the statistical properties of oxide breakdown. IEEE Trans. Electr. Devices 45(4), 904–911 (1998)

- U. Celano, L. Goux, K. Opsomer, M. Iapichino, A. Belmonte, A. Franquet, I. Hoflijk, C. Detavernier, M. Jurczak, W. Vandervorst, Scanning Probe Microscopy as a scalpel to probe filament formation in conductive bridging memory devices. Microelectr. Eng. 120, 67–70 (2013). (in press)
- U. Celano, Y.Y. Chen, D.J. Wouters, G. Groeseneken, M. Jurczak, W. Vandervorst, Filament observation in metal-oxide resistive switching devices. Appl. Phys. Lett. 102(12), 121602 (2013)
- B. Singh, B.R. Mehta, D. Varandani, A.V. Savu, J. Brugger, CAFM investigations of filamentary conduction in Cu(2)O ReRAM devices fabricated using stencil lithography technique. Nanotechnology 23(49), 495707 (2012)
- U. Celano, L. Goux, A. Belmonte, K. Opsomer, A. Franquet, A. Schulze, C. Detavernier,
 O. Richard, H. Bender, M. Jurczak, W. Vandervorst, Three-dimensional observation of the conductive filament in nanoscaled resistive memory devices. Nano Lett. 14(5), 2401–2406 (2014)
- 31. U. Celano, W. Vandervorst, Scanning probe tomography for advanced material characterization, in 2014 IEEE International Integrated Reliability Workshop Final Report (IIRW), pp. 1–5 (2014)

Chapter 5 Three-Dimensional Filament Observation

5.1 Scalpel SPM for Filament Observation

In the previous chapter, by means of the C-AFM tip we have demonstrated the possibility to induce the CFs and study them on blanket samples. Although relevant information of the resistive switching mechanisms has been unraveled by this approach, two major limitations have clearly appeared. First, creating CFs on blanket samples by using the tip for the electrical programming can replicate the device operation but it will never achieve the precise control offered by the 1T1R configuration. Second, the scaled tip dimensions, ultra-small contact vibrations and the abundance of surface adsorbates (at the tip-sample interface) create particular conditions for the nucleation of the CF. Such may not be present in a real device, therefore the tip-induced CF formation cannot be completely representative for the CF growth dynamic inside a standard MIM devices constituted of thousands of nm² of contact area.

This indicates that the CF observation in devices represents an important step to elucidate the physics of RS inside integrated devices. Here, the nucleation and growth of the CF are based on stochastic processes that occur in a highly confined volume e.g. few hundreds of nm³ [1–4]. As these CFs are embedded in nanoscaled devices, their physical characterization is generally further complicated by the presence of many surrounding layers (conducting and insulating). These obstacles have hampered the observation of CFs in integrated devices with most of the known techniques. Though the morphology and chemical composition of the conductive filament has been observed using scanning electron microscopy (SEM) and transmission electron microscopy (TEM) [5–8], complete observation in three-dimensions of the CF in a scaled device has been missing for long time. Nevertheless, the full characterization of the conductive filament in real device would be beneficial for three main reasons.

Electronic supplementary material The online version of this chapter (doi:10.1007/978-3-319-39531-9_5) contains supplementary material, which is available to authorized users.

- It would dramatically enhance our understanding of the filament growth dynamics.
- 2. It would provide more insight to locate the critical interface during filament cycling, which is essential in device optimization.
- 3. The information about the shape and size of the CF would clarify the underlying physical mechanisms and contribute to advancing filamentary-based memory technology toward a reliable mature technology.

At the end of Chap. 4, we have removed the top electrodes of MIM devices, enabling the observation of the CF at the electrode-oxide interface. This has been the first step towards the usage of C-AFM to probe the CFs' that were induced using the 1T1R configuration. Although this unambiguously confirmed the filamentary nature of RS and provided insights on the switching mechanism, the analysis was still limited to a two-dimensional (2D) observation, while our results on tip-induced CF switching indicate that relevant information about the filament are dependent on its 3D atomic structure. However, with the work reported at the end of the Chap. 3, we have achieved precise control in tip-induced material removal (for the top electrode removal). The natural extension of this approach leads to the continued material removal also inside the oxide containing the CF, to probe the structural evolution of the CF in 3D. In other words, instead of limiting the observation to the oxide top surface we explore the possibility to slice through the oxide until the bottom electrode exposure. Oxides are generally tougher than metals and they show (during tip scraping) reduced material removal rates. One can stop after top electrode removal, recalibrate the load force or change the tip, before continuing to collect 2D conductive profiles. The CF is embedded in the oxide as a local highly conductive region. The collection of 2D conductive profiles acquired in the oxide at different depths, will reveal the CF shape in the third dimension. In the following sections of this chapter, starting from this simple idea we refine our tip-based material removal technique into what we call scalpel SPM or SPM tomography, for the analysis of ultra-confined volumes $(\approx 100 \, \text{nm}^3)$ and the three-dimensional CF observation.

5.2 Tomographic Observation of Cu-Based Filaments

From Celano, U. et al. Nano letters, 14, 2401, 2014.

For the observation of the CF in CBRAM, the device under investigation is a $\text{Cu/Al}_2\text{O}_3/\text{TiN}$ -based memory, integrated in a one-transistor-one-resistor configuration (Fig. 5.1). The device is placed at the cross-point between the bottom and top electrode (BE and TE). The memory element is based on a 5 nm amorphous Al_2O_3 sandwiched between 10 nm TiN (BE) and 40 nm Cu (TE), as shown in Fig. 5.1a, b. In Fig. 5.1a a cross-sectional TEM image clearly shows the integration scheme (1T1R). The inset of the figure shows the details of the $\text{Cu/Al}_2\text{O}_3/\text{TiN}$ memory element. The AFM-topographical image in Fig. 5.1b presents the memory cell $(100 \times 20 \, \text{nm}^2)$ created by electron beam patterning. The BE is directly connected to the drain of

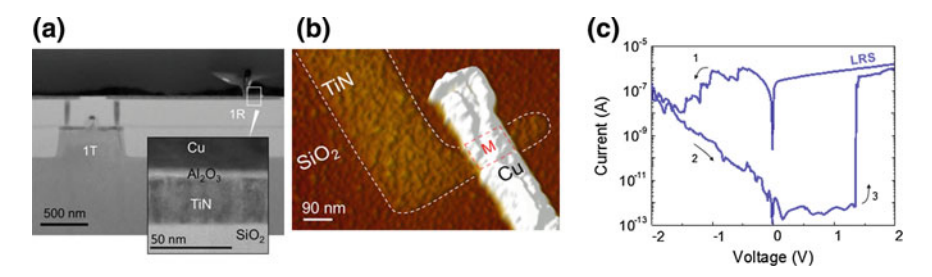


Fig. 5.1 Cross-point integrated CBRAM. a Cross-section TEM image of our device. The inset shows details of the cross-bar memory element. b Topographical AFM image of the cross-point area $100 \times 200 \, \mathrm{nm}^2$. c I–V characteristic of the cell under study

the control transistor which is used to limit the current during the device operations. As previously introduced, this type of nonvolatile memory device shows attractive characteristics such as: high ON/OFF resistance ratio ($>10^6$), good retention (10^4 s), high endurance ($>10^6$ cycles) and multilevel capability, similarly to the stacks we have reported elsewhere [9, 10].

Figure 5.1c shows the I–V characteristic of the cell during the electrical programming, prior to the C-AFM tomography. The as-deposited device is normally in the OFF-state showing high resistance. The pristine cell requires an initial electroforming to activate the device. After electroforming, the formation and rupture of the CF can be triggered respectively by means of a positive or negative voltage on the Cu electrode. The Cu electrode is positively biased for the filament formation, and negatively biased for the filament rupture. In our studies the memory element is programmed using a semiconductor parameter analyzer. The control transistor delivers a current compliance of $10\,\mu\text{A}$ during all the programming phases. In Fig. 2.5 the forming voltage is about $\approx\!3.5\,\text{V}$ and the set and reset voltages are respectively $\approx\!1.5\,\text{and}-2\,\text{V}$. The device was subjected to a few tens of cycles and is then placed in the AFM system for the scalpel C-AFM.

5.2.1 CBRAM: Low-Resistive-State Observation

As introduced in Chap. 4, the presence of the top electrode shields the observation of the CF by C-AFM (Figs. 4.14a, 4.15b). This layer has to be removed before any CF observation. Our scalpel SPM concept is based on a slice-and-view approach where the AFM tip is used also to remove material from the sample surface, in a very controlled manner. In each planar C-AFM scan, we probe the local variations in conductivity and partially erode a controlled amount of the sample surface. Hence in essence, we use the conductive-diamond tip as a scalpel for a controlled material removal [11] by physical scraping, and as a conductive probe to record the spatial variations of the tip-sample current. When applied to our programmed mem-

ory device, we thus collect 2D current maps of the CF at different depths (Fig. 5.2a). Finally, (Fig. 5.2b) the 2D images are combined into a 3D representation (tomogram) by a dedicated software interpolation (MATLAB and Avizo). The C-AFM tomogram starts after the removal of the top electrode [12]. Once the top electrode is removed and the Al_2O_3 surface is exposed, we record the first C-AFM slice of the collection (Fig. 5.2c1). The CF is now clearly visible as a highly conductive spot in the middle of the active area, in contrast with the rest of the Al_2O_3 surface, which is still highly insulating (red background in Fig. 5.2c). Different slices are collected at constant load force as in Fig. 5.2c1–7. Using a removal rate of ≈ 0.5 nm/scan the final collection constitutes 10 slices for the 5 nm-thick switching layer. We stop the acquisition when the switching layer is completely removed and the highly conductive bottom electrode, e.g. TiN, becomes visible. An analysis of the consecutive images clearly indicates that in contrast with the first C-AFM slice the last one before the bottom electrode presents a CF with a much smaller size, indicating the shrinkage of the CF from the active electrode (Cu) to the inert counter electrode (TiN).

The conical shape, ending at the bottom electrode, becomes very clear from the 3D-representation in Fig. 5.3. In Fig. 5.3b, c the CF shows a shrinkage in the shape moving from TE to BE i.e. from Cu/oxide-interface to oxide/TiN. The area of the CF shrinks from \approx 493 nm² on the Cu-side down to \approx 200 nm² on the side of the inert-electrode. The morphology of the CF clearly presents two branches evolving through the Al₂O₃ toward the inert-electrode following a conical shape. Of the two branches, the major one is fully connecting the electrodes, while the small one may be not fully

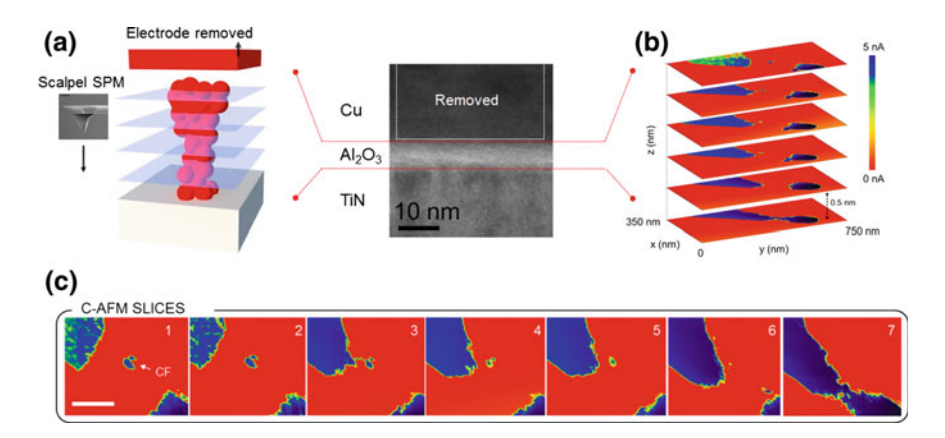


Fig. 5.2 C-AFM tomography on CBRAM. a Schematic of the C-AFM tomography procedure, the diamond tip is exploited to collect several slices at different heights of the CF after the removal of the TE. b Superimposition of the collected 2D C-AFM slices, prior to the 3D interpolation. Note, the average space between each slice is \approx 0.5 nm. c Collection of 2D slices (current map) constituting the dataset for the 3D interpolation (scale bar 80 nm). The CF appears in the middle of the active area after top electrode removal. The highly conductive features on the top-left and bottom-right corners are the exposed parts of the TiN BE, which is progressively exposed during the removal of Al₂O₃

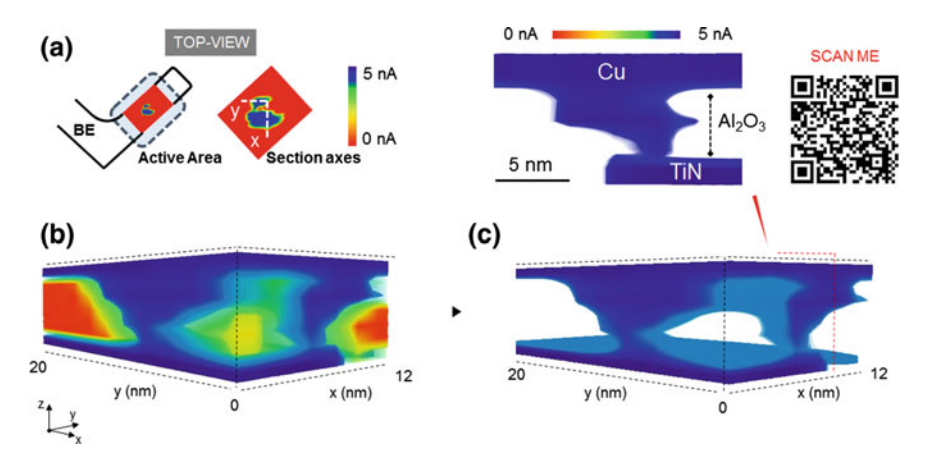


Fig. 5.3 Cu filament 3D tomogram. a Schematic of the CF position, note the section axes for 3D observation. b Observation of the reconstructed 3D tomogram for the CF under investigation, in 5 nm thick Al_2O_3 . c The low-current contribution in the tomogram is suppressed to enhance the contrast of the highly conductive features. The *inset* shows a cross-section of the smaller CF branch. The animated cross-section of the tomogram is available by clicking here or by scanning the QR tag

connected. This cannot be detected by C-AFM due to the presence of a non-negligible tunneling current flowing through a possible non-connected filament's branch. The same effect imposes some limitations in the characterization of the reset (OFF) state using this technique, as presented later in this chapter. In Fig. 5.3c we subtract all the low-current contribution in the 3D tomogram in order to show only the highly conductive features. This is likely representative for the shape of the CF, which is supposed to be the lower resistive path for the current inside the Al_2O_3 . The animated cross-section of the tomogram and the shape evolution of the CF are available by the hyperlink in the figure caption or by scanning the quick response code (QR) next to the figure with any device equipped with a QR code reader.

5.2.2 CBRAM: High-Resistive-State Observation

For the characterization of the reset state we repeated the SPM tomography on a device in HRS. To this end, one memory cell has been formed and cycled using $50\,\mu\text{A}$ current compliance. A higher operative current is needed in order to induce a more stable CF and to avoid the formation of weak filaments which could not be detected by C-AFM owing to the sensitivity of the current amplifier. Prior to the C-AFM tomography the device undergoes a reset voltage sweep which induces a high resistance to the memory element (Fig. 5.4a). C-AFM tomography is carried out at low read-out bias $\approx 10\,\text{mV}$ to minimize the impact of the tip-bias on the analysis. This combined to the higher resistance of the filament in HRS leads to a

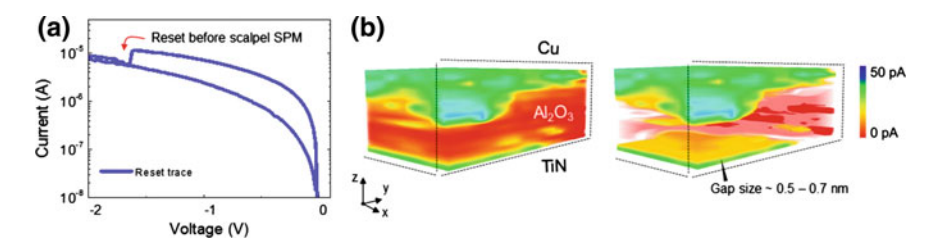


Fig. 5.4 HRS state, 3D tomogram. a Electrical programming of the reset state, under negative DC voltage sweep. Note, the current is limited to $50\,\mu\text{A}$ during forming and set. b Observation of the reconstructed 3D tomogram for the CF in the OFF state, in 5 nm thick Al₂O₃. Cross section observation of the gap size is $\approx 0.5-0.7$ nm (the low-current contribution is suppressed to enhance the contrast in the volume rendering)

lower current measured (data scale of Fig. 5.4b). However, during the tip-induced slicing, the current leakage in the CF shows a gradual recover in proximity of the inert-electrode interface until the bottom electrode is exposed. The latter once interpolated is converted into a small gap between the CF and the bottom electrode. Two 3D interpolations of the 2D slices collected for the device in OFF state are shown in Fig. 5.4b. The tomographic reconstruction of the CF by volume rendering (redfog) and iso-surface at fixed threshold (green-shape) is shown, note the presence of an unconnected filament between the two electrodes in the case of the OFF state. Although the irregular geometry of the ruptured CF complicates the quantification of the gap size, by suppressing the low-current contribution the gap size can be estimated as ≈ 0.5 –0.7 nm. The value obtained is in agreement with the results obtained with the tip-induced gap formation experiment of the previous chapter (Sect. 4.2.1). Precise modeling of the broken CF and gap size quantification will be treated in detail in Sect. 5.3.2).

Although the existence of a broken filament for the HRS and previously our C-AFM reset study (Sect. 4.2) suggest a dissolution of the Cu-filament leading to a tunnel gap formation this is not the only possible configuration for the HRS. In Sect. 5.3 we will show that the CF assumes different shapes in the HRS depending on the original volume of the CF (i.e. LRS resistance). This will unravel the nature of the multiple reset transitions experimentally observed in real devices, and clarify the filament rupture physics for the case of CBRAM.

5.2.3 Cu-Filament Growth Model in Low-Mobility Media

Based on the present observations of the CF, the shape observed by scalpel SPM is opposite to the one predicted for chalcogenide-based ECM cells [3, 13]. The difference emphasizes the critical role of the cation-transport through the electrolyte and thus the need for an optimized material-selection when targeting resistive switching. For chalcogenides, sulphites or ionic-conductors, the cation mobility is much higher

as compared to the case of amorphous dielectrics. Therefore, the cations can easily reach the counter-electrode, where they are reduced thereby initiating the nucleation of the CF. In this scenario the reduction and nucleation of the filament are the rate-limiting processes for the filament growth, and the CF starts to grow from the inert-electrode to the active electrode. Such a shape has experimentally been observed by Sang-Jun Choi et al. in Cu-doped GeTe using TEM [14]. In this case the CF present a conical shape with the filament constriction close to the active electrode interface. On the other hand, our 3D tomogram unambiguously reveals that the CF has the narrow part close to the inert-electrode.

To explain this different shape we suggest that the cation-transport is the rate-limiting process for the CF formation in our devices [15, 16]. In such condition, the injected cations get reduced within the electrolyte nearby the injection interface and start forming the CF from the active anode side. Our observations are in agreement with TEM observations by Yang et al. [6] in amorphous-silicon and by Liu et al. in ZrO_2 [17]. In those cases we can expect solubility and diffusion coefficients similar to the case of amorphous- Al_2O_3 . Those works have raised debates in the community about the possible mechanisms for reversed filament growth [18–20]. Now unified under the framework of a cation-transport centric theory [21].

To explain our results in more detail we describe the CF filament formation in our oxide-electrolyte-based CBRAMs as a field-assisted ion transport inside the Al₂O₃ (Fig. 5.5). Under the effect of positive bias, Cu atoms are ionized and diffuse into the switching layer, Fig. 5.5a. At the same time the high electric field, $\approx 10^9 \, \mathrm{Vm^{-1}}$, might generate oxygen vacancies within the Al₂O₃. These might contribute to electronic leakage current throughout the electrolyte and also have an impact on the Cu migration due to the ionic transport along chains of O-sites of the Al-O bonding in the amorphous matrix [22]. However, given the low cation mobility in the Al₂O₃, the Cu cations may only travel a short distance inside the dielectric before they are reduced by capturing electrons injected in the electrolyte under the high electric field. The Cu⁺ are reduced back to Cu near the active electrode and become an extension of it. The Cu⁺ ions that are subsequently injected will preferentially become reduced at the end of the already existing filament, as its end constitutes the point with the highest electric field. Hence the filament growth can be viewed as based on this repetition of ionization and injection, slow (limited) migration and reduction processes. Under these assumptions the filament grows from the active electrode e.g. Cu, towards the inert-electrode consistently with our 3D observations. Note, our C-AFM tomography does not provide any compositional analysis of the filament, leaving the debate on its chemical composition still open. The final conductive filament can be constituted of different conductive species such as Cuⁿ⁺ ions, Cu⁰ or Al-Cu-O phases. During the reset operation when an opposite polarity is applied, the rupture of the CF takes place due to an electrochemical and Joule-heating assisted process, restoring the high resistance state for the device [23]. It is clear that the CF will rupture at the position where the current density is the highest. As experimentally observed this point will be placed in proximity of the TiN bottom electrode.

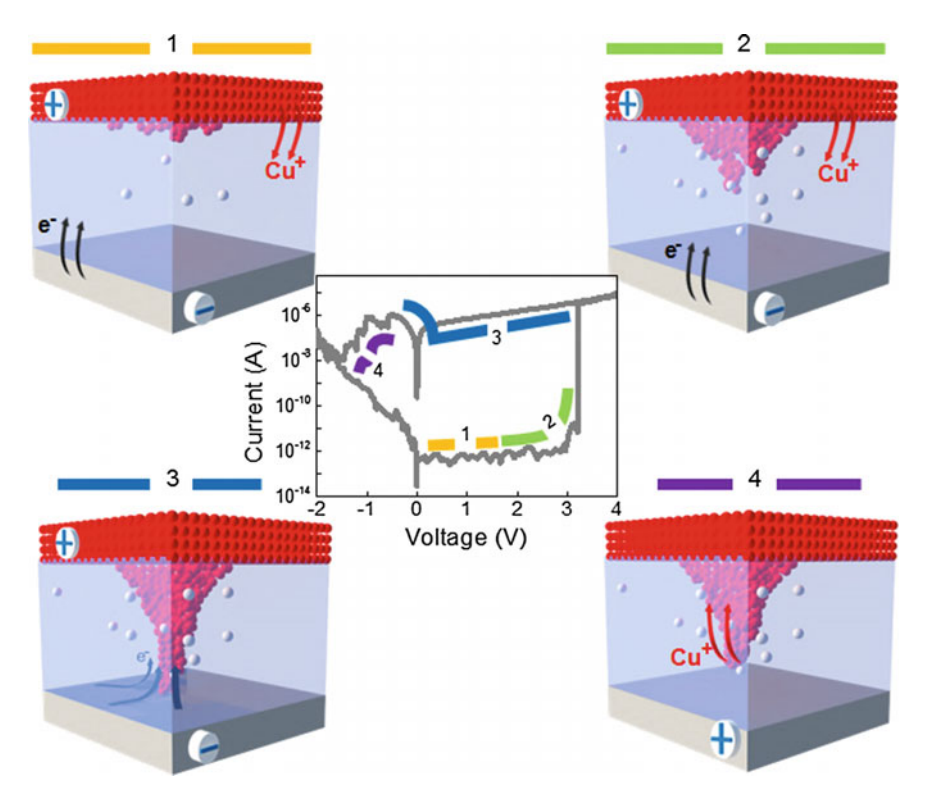


Fig. 5.5 Cu-filament growth model. Illustration of the electrochemical processes during resistive switching. I First, the Cu oxidizes and Cu⁺ ions are injected in the Al₂O₃. Second, the high electric field might lead to the formation of oxygen vacancies in the dielectric layers (white balls in the cartoon). 2 The slow migration of Cu⁺ ions in the switching layer implies that a reduction reaction occurs before the Cu⁺ reaches the inert-electrode. 3 The filament growth continues and the CF eventually shorts the two electrodes thereby creating the low resistive state. 4 When the bias is reversed a Joule-heating assisted electrochemical reaction is responsible for the rupture of the CF in the point of max power dissipation i.e. CF constriction

5.2.4 Filament Volume Modulation and Multibit Capability

The possibility to probe the CF in 3D, allows to further elucidate the relationship between the programming conditions and the CF volume. The modulation of the Cu-filament resistance with the programming current has been often reported [24] and experimentally observed also in our device (Fig. 4.5). This effect is of particular interest because it can be used to achieve multibit operation by multiple resistance-state formation [25]. As introduced in Chap. 2, the capability of storing multiple resistance-states in a single memory cell is one of the most important requirements for non-volatile memory because it can dramatically enhance the data density without increasing the number of devices. Specifically, in the case of CBRAM, different

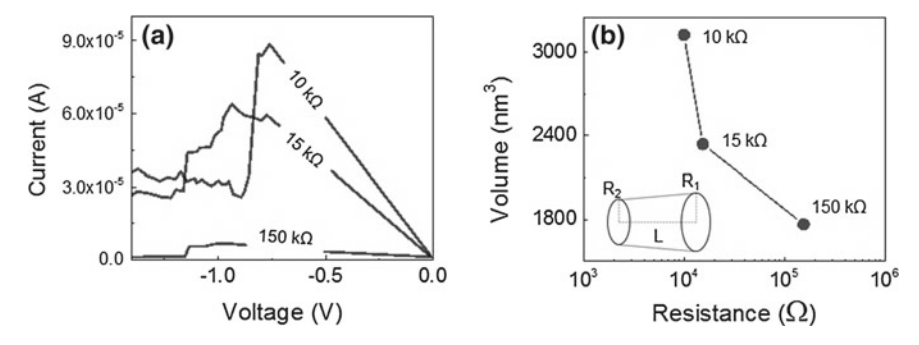


Fig. 5.6 Filament volume and programming conditions. **a** Typical reset sweep for three different programming currents. The resistance of the CF tends to decrease as the programming current is increased. **b** Correlation between the resistance value and the physical-volume of the CF as induced by different programming currents. The values for the CF physical volumes are extracted using the obtained 3D tomograms

programming currents (Fig. 5.6a) can be utilized to induce multiple resistance-states and therefore, multiple logical bits [24]. It is commonly assumed that after the CF formation as long as the voltage is applied the CF radial growth will continue leading to a larger amount of ion injection into the CF. In order to elucidate the nature of this multilevel bit capability we study the physical volume of the CFs in relation to the differences in their resistance as induced by different programming currents. Three different devices are programmed while limiting the programming current to 10-50-100 μA. The corresponding reset sweeps (Fig. 5.6a) clearly indicate that filaments with different resistances have been formed. We measured the resistance of the CF's after the electrical programming and then performed the C-AFM tomography. From the obtained 3D tomograms we calculated the physical volume of the CF in the Al₂O₃ for each case. The correlation shown in Fig. 5.6b indicates very clearly that a larger programming current induces a larger physical volume and that the larger volume leads to a lower resistance value. Hence by controlling the programming current, the volume of the CF and thus the resistance can be modulated. Based on our observation, the mechanisms of multi-level switching in our material system can be explained as follows: during the set process at high current compliance, more Cu atoms are injected increasing the final volume of the CF. While the operation at low current compliance results in a reduced metal-ions injection as demonstrated by the smaller volumes experimentally observed. Known the sizes and shape of the CF we can calculate the resistivity of the Cu-filaments with a truncated cone approximation as in the equation:

$$\rho = \frac{R}{L} \cdot \pi R_1 R_2 \tag{5.1}$$

where R is the resistance, L, R_1 and R_2 are respectively the length and the two radius of the truncated cone as in the inset of Fig. 5.6b. Interestingly, all the three

cases of Fig. 5.6b do not match the actual value of the Cu resistivity ($\approx\!1.68\times10^{-8}\,\Omega\cdot m$). The two CFs induced at 50 and 100 μA present values in range $\approx\!10^{-6}$ and $10^{-5}\,\Omega\cdot m$ while $\approx\!10^{-7}$ is obtained for the CF programmed with $10\,\mu A$. This can be explained by the fact that our scalpel SPM provides only a conductivity map, therefore we don't know where the Cu atoms are positioned within the observed volume. In other words, a truncated cone approximation might not be correct and the conductive volumes observed is likely constituted of a more complex intermix of Cu, defects-rich Al_2O_3 and Al-Cu-O inter phases.

5.3 On the Dual Nature of Cu Filament Dissolution

From Celano, U. et al. J. Phys. Chem. Lett., 6, 1919, 2015.

Contrary to the CF's formation that is an additive process, the filament erase (reset) is generally considered as the subtraction of conductive metal atoms from the CF [1, 3, 26]. The latter induces a rearrangement of the filament's atomic structure and changes its conductivity [27]. We have previously reported the formation of a tunnel gap, with our tip-induced filament rupture experiment (Chap. 4) and by the 3D observation of the HRS state in the previous section. Nonetheless, this description doesn't fully account for the rich set of phenomena observed during the reset in CBRAM. The limited understanding of the filament dissolution process, hampers at present the comprehension of certain undesired sources of variability in these devices. In particular the state stability, that is, retention, immunity to disturbances, and the resistive window (R_{HRS}/R_{LRS}) are some of the main features showing substantial variability. In addition, nearly identical devices often show different reset behaviors such as demonstrated in Fig. 5.7, clearly suggesting that different mechanisms are operative concurrently. Those are often observed but not described within a unified theory. The clear observation of the shape and properties of erased CFs would dramatically improve the understanding in the reset mechanisms, also enabling the device optimization. In this section we present a three-dimensional (3D) characterization of the CFs in the reset state. Different reset behaviors are repeatedly induced in scaled conductive-bridging memory devices and their electrical properties are modeled and correlated to the experimentally observed (erased) CFs. Figure 5.7 shows two currentvoltage (I-V) reset characteristics for similar (but distinct) devices operated at the same conditions. The device under investigation is again our Cu/Al₂O₃/TiN-based cell, integrated in a 1T1R configuration. The memory element is reported in Fig. 5.1b and is based on 5 nm amorphous Al₂O₃ sandwiched between 10 nm TiN and 40 nm Cu, the cell size is $100 \times 200 \,\mathrm{nm^2}$. Figure 5.7 shows the large difference between the two reset IV characteristics. Although the CF erase starts at similar voltages (V_{reset}) \approx -0.5 V and reaches comparable resistances (HRS) in both devices, the processdynamics are dramatically different. The red trace (Fig. 5.7) shows a progressive decrease in current with concurrent current fluctuations throughout the reset voltage sweep, whereas the blue trace exhibits a sudden current drop at V_{reset} . Figure 5.7 also shows that despite having reached the same HRS value, the I-V characteristic

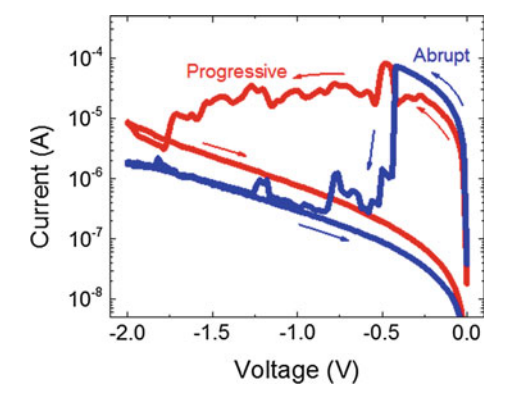


Fig. 5.7 Progressive versus abrupt reset. Two different reset types are observed in similar devices operated under the same conditions. The red trace (progressive) shows fluctuations in the current that progressively evolves to a lower value (HRS). The blue trace (abrupt) shows a steep reduction of current in correspondence of \approx -0.5 V taking the device in the HRS. The final resistive state induced is comparable for both devices. The forming and set voltages are not shown but they do not present differences

in the backward sweep (from -2 to $0\,V$) exhibits very different trends for each of the two observed devices. This part of the I–V characteristic can be considered as the electrical signature of the stationary CF-state after the dynamic reset transition and thus representative for the current conduction mechanisms within the "erased" filament. Specifically we observe that for the abrupt-reset device the backward I–V can be fitted with a direct tunnel (DT) conduction model (i.e. tunneling across an insulator gap), whereas for the progressive reset case it follows the I–V behavior of a quantum-point-contact, i.e. implying that the filament is not completely broken. [28]. Note, that the appearance of one of the two types of reset is not related to any clear difference in the forming or set voltages (not shown).

In Fig. 5.8a, we demonstrate that the I–V curve for the abrupt reset case can be described with an analytical tunneling current description (similar to the one of Chap. 4) [27]. The set of parameters used for the fitting (inset Fig. 5.8a) are experimentally extracted by internal photoemission spectroscopy analysis carried out on Cu/Al_2O_3 reference stack [29, 30]. The proposed fit leads to a good agreement in the cases of abrupt reset, using as unique fitting parameters the thickness of the tunnel barrier (d_{ox}) and emission area (A_{em}). In Fig. 5.8b (progressive reset) the I–V curve can be described using the QPC model which delineates the behavior of a physical constriction with a current-controlling energy barrier (inset of Fig. 5.8b). This model already introduced for the dynamic switching events in HfO_x-based VCM [31] has recently been adapted to the case of CBRAM as well [32]. In our model the CF is described as a region connecting two ion reservoirs where faster ion diffusion/drift occurs [28]. The proposed QPC-fit finds good agreement in the cases of progressive reset, using as fitting parameter the geometrical dimensions of the filament constriction. Note that the use of the two models for the two cases is mandatory as we are

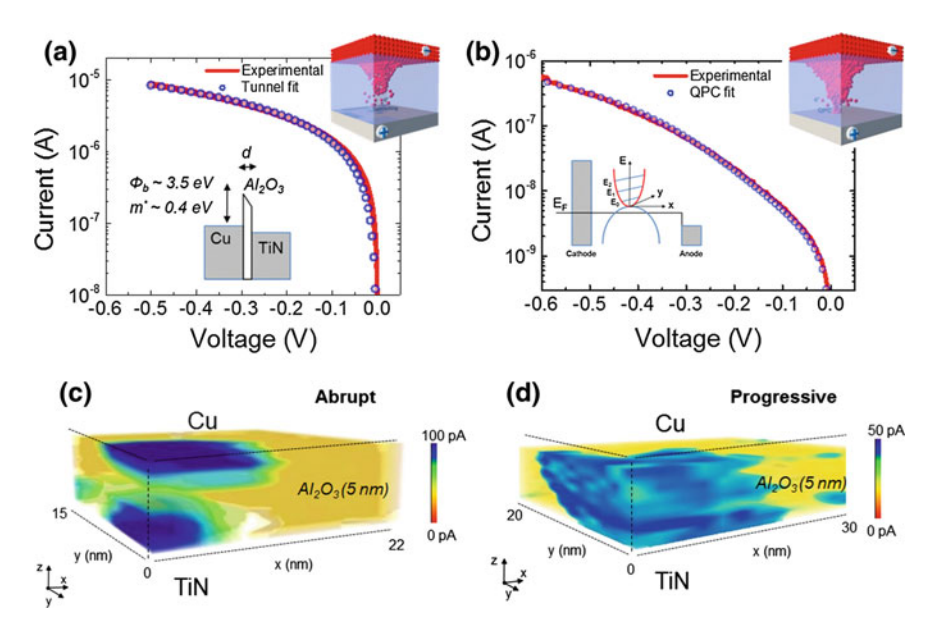


Fig. 5.8 A model for each reset transition. **a** The abrupt type can be fitted with a direct tunneling transport-mechanism whereas **b** the progressive reset finds agreements with a quantum point contact description. **c** Tomographic reconstruction of the CF by volume rendering (*yellow-fog*) and isosurface at fixed threshold (*blue-shape*) for the abrupt type of reset as shown in 3D cross-section, note the presence of a tunneling gap. **d** Tomographic reconstruction of the CF by volume rendering of the CF relative to the progressive type of reset as shown in 3D cross-section, note the presence of a non-broken lowly-conductive filament

unable to fit the I–V curves for the abrupt case with the QPC description and vice versa with DT for the progressive. Hence, this bimodal behavior suggests that the reset filaments have two different shapes. First, in the abrupt case the filament looks like partially disrupted, with electrons being forced to tunnel across an insulating barrier. Second, in the progressive case the filament is developing a reduced cross section (partially dissolving) with the electrical characteristics of a QPC.

To confirm these conclusions we investigate the shape of the erased CFs using C-AFM tomography. Prior to the C-AFM tomography each device is programmed and cycled for few tens of cycles. The control transistor delivers a current compliance of $100\,\mu\text{A}$ during all the programming phases. After electroforming, the formation and rupture of the CF can be triggered respectively by means of a positive or negative voltage on the Cu electrode (respectively ≈ 1.5 and $-2\,\text{V}$) as shown elsewhere [15]. For the experimental CF observation, we program devices exhibiting the desired type of reset and we submit them to C-AFM tomography. C-AFM tomography is always carried out at very low bias $\approx 10\,\text{mV}$ to minimize the impact of the tip-bias on our analysis. The CF becomes visible (in the C-AFM current map) when the Cu top-electrode is completely removed. Figure 5.8c shows the 3D tomogram of the erased CF for the abrupt transition. The abrupt device exhibits a broken CF with a

gap of \approx 0.4 nm. On the contrary, the device showing progressive reset presents a continuous lowly-conductive CF running through the 5 nm-thick switching layer i.e. a non-broken CF. Figure 5.8d shows the 3D tomogram.

5.3.1 A Model for Broken and Nonbroken HRS Filaments

From Celano, U. et al. *IEEE IEDM Tech. Dig.*, 14.1–14.4, **2014**.

Although the existence of broken and nonbroken filaments for the HRS suggests different structural properties for the CFs, they might be viewed as being induced by the same process. This can be considered as the dissolution of Cu atoms from the CF, whereby the original shape of the CF controls the distinction between abrupt and progressive reset. Indeed previously we have demonstrated that the LRS resistance is related to the volume of the CF which is controlled by the current flowing during the forming/set operations [15]. This implies that different CFs may have different volumes [33]. The reset operation starts when the negative polarity is applied at the Cu electrode. As previously described, the rupture of the CF takes place due to an electrochemical and Joule-heating assisted process [3, 23, 27]. This is limited in time and thus in the number of atoms which can be displaced. Starting from a weak/strong CF (low/high volume at the constriction) it is then not surprising that, under the assumption of displacing only a limited number of Cu atoms, in one case the CF completely dissolves at the constriction (leading to the gap formation) whereas in the other case it merely reduces its dimension creating a OPC-like constriction. Figure 5.9 shows a schematic for the proposed model. Hence, although driven by the same phenomenon, its impact on the final CF-shape creates a gap behavior or QPC behavior. On the basis of this reasoning, a relation between the shape/size of the CF and the reset type is expected. As the size of the CF is reflected in the value of the LRS, one thus also expects a correlation between the LRS and the reset type. Such a correlation is clearly present when plotting the statistical distribution of the LRS values and overlying them with the region characteristic for the reset type (Fig. 5.10a). In other words, the LRS-resistance of the device, i.e. the CF's volume, determines which type of reset will be more favored during filament erase. The latter is presented in Fig. 5.10a where a clear relationship is found for devices showing lower R_{LRS} and progressive reset, and conversely for those presenting a higher R_{LRS} and abrupt reset. Between two CFs in LRS, the filament constituted of fewer Cu atoms (smaller volumes and higher- R_{LRS}) will have the tendency to reset abruptly whereas the CF with a lower R_{LRS} (higher Cu volume) will show progressive reset as shown in Fig. 5.10a. To further confirm the result, Fig. 5.10b, c shows the area comparison between two LRS CFs as observed after top electrode removal. The cut orientation of the 2D planes are shown in the inset of Fig. 5.10b, c. Once the top electrode is removed, at the Cu/Al₂O₃ interface the CF appears as a conductive spot. Figure 5.10b shows the planar observation of the CF belonging to a device that has shown progressive reset during cycling, while Fig. 5.10c reports the case of the abrupt reset. The 2D observations confirm that the area of the CF belonging

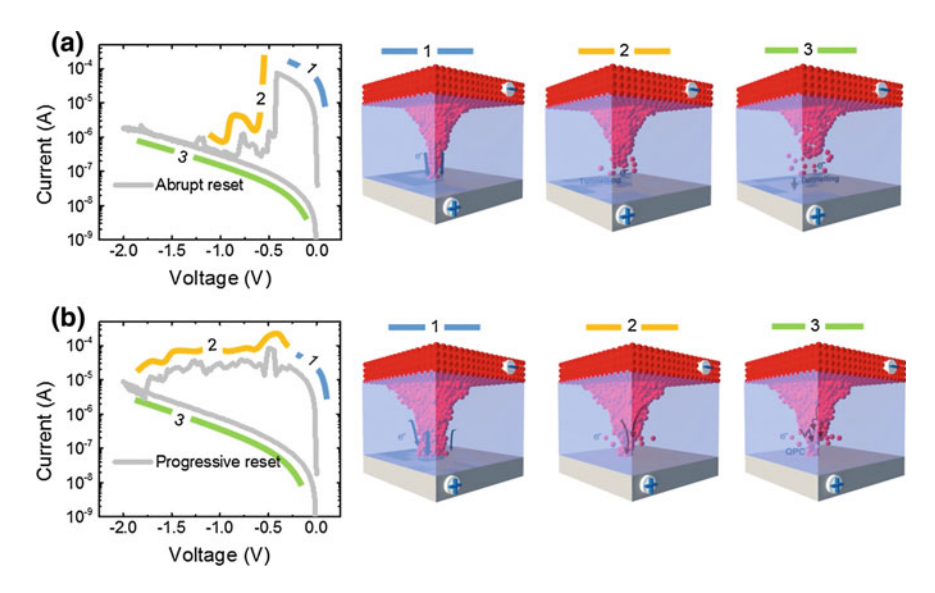


Fig. 5.9 Proposed model for abrupt and progressive reset. **a** Electric-field driven and thermally activated hopping of Cu ions induces in weaker CFs the formation of a tunneling gap in the CF. **b** The same process produces a different effect in CFs with high volume where the structural rearrangement of Cu atoms induces the formation of a QPC-like constriction

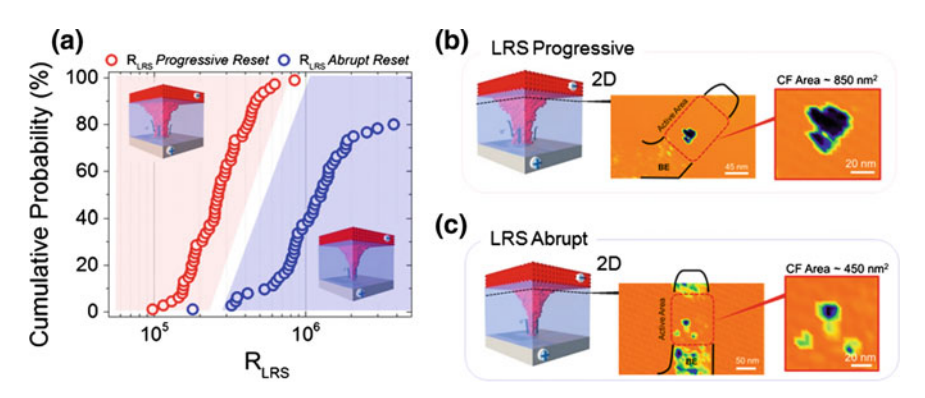


Fig. 5.10 Filament volume—reset type dependence. a Correlation between R_{LRS} cumulative distribution of devices showing abrupt or progressive reset. Weaker/stronger CF (i.e. higher/lower R_{LRS} values), can be clearly linked to abrupt or progressive behaviors. **b–c** C-AFM planar observations of the LRS CFs contained in devices exhibiting **b** progressive reset and **c** abrupt reset, during programming cycling

to the progressive reset device (Fig. 5.10b) is almost double (Area_{CF} \approx 850 nm²) as compared with the one of the abrupt reset (Area_{CF} \approx 450 nm²), thus supporting a relationship between filament volume and the type of reset transition.

5.3.2 A Ruptured Filament Is Not a Conventional Tunnel Junction

Based on the previous section, the I–V curves presenting abrupt reset should follow a FNT dependence after the CF rupture. While this appears generally true for the midhigh bias range of the I–V, it is very common to observe a misfit in the low-voltage range. Figure. 5.11a shows this effect for a device programmed at $50\,\mu$ A, presenting abrupt type of reset. The 3D tomogram in the inset of Fig. 5.11a shows the presence

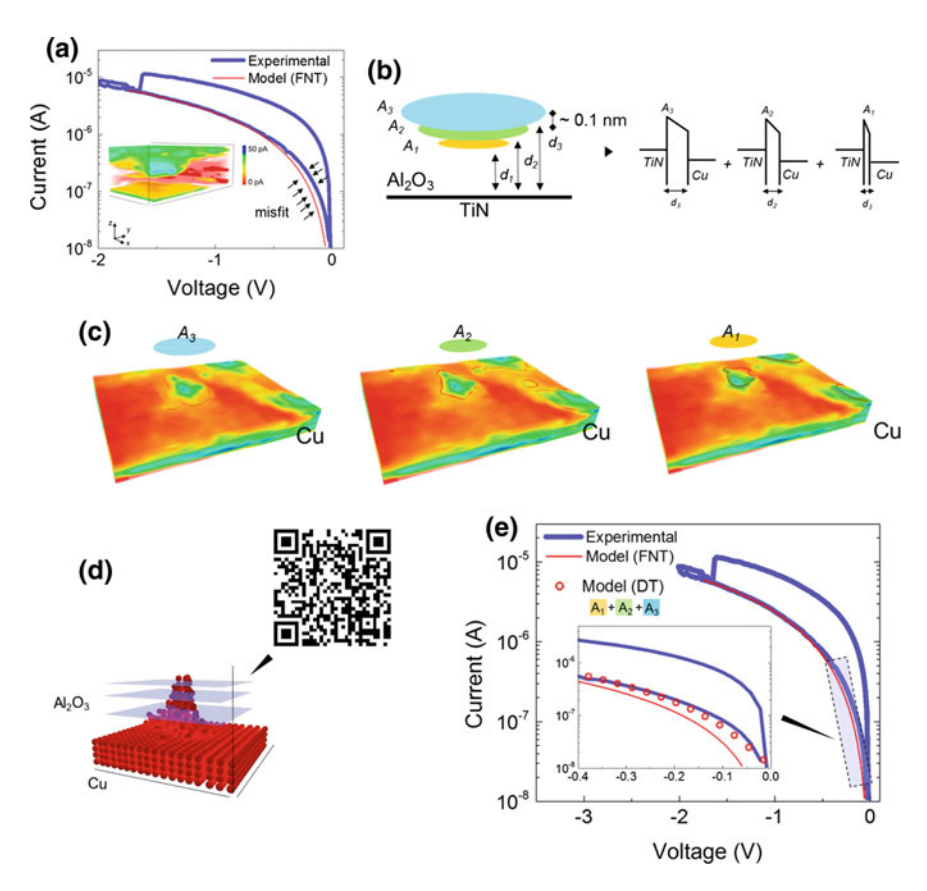


Fig. 5.11 Optimization of the tunnel junction geometry. **a** Misfit of the FNT mechanism appears in the low-bias range. **b** Approximation for the tunneling junction. We estimate the FNT-current as the sum of three overlapping planes, separated by 0.1 nm. The emission area of each plane is the corona obtained by taking away the area of the front plane e.g. $A_{3,eff} = (A_3 - A_2)$. The values of $A_{1,2,3}$ are experimentally determined from the 3D tomogram. **c** The apex of the broken filament is shown using a contour-plot function. The values for $A_{1,2,3}$ are extracted and used for the curve fitting of the static state. **d** The animated cross-section of the tomogram is available by clicking here or by scanning the QR tag. **e** The optimized geometry matches the low-bias current more accurately than the planar approximation

of an unconnected filament between the two electrodes in the case of the OFF state. A non-symmetrical geometry of the broken filament is clearly visible, (Fig. 5.4b) this suggests that a simple parallel-plate model cannot be used to fit the transport in the HRS. Based on our tomographic observation, we model the remaining CF-shape (Fig. 5.11b) as a combination of three parallel plate capacitor-rings. We estimate the FNT-current as the sum of three contributions weighted for their effective area $(A_{1,2,3})$ and oxide thicknesses $(d_{1,2,3})$ (Fig. 5.11b). Due to the exponential dependence of the FNT-current with the barrier thickness, the overlapping planes are spaced by 0.1 nm each. Using our 3D tomogram we can exactly estimate the extent of these surfaces and use them for an optimized curve fitting as shown in Fig. 5.11c. The evolution of the contour-plot of the emitting junction created by the ruptured CF can be seen using the QR tag or the hyperlink in the figure caption (Fig. 5.11d). The result using the optimized tunnel junction geometry is visible in Fig. 5.11e. The optimized geometry matches the low-bias current more accurately than a simple planar approximation. In essence, the observed misfit of the FNT model at low-bias when modeling the abrupt reset can be explained by the non-symmetrical geometry of the broken filament creating a non-planar tunnel junction, which has to be modeled according to the proper geometry. Finally, this completes the work started in Sect. 4.2.1, where by studying the tip-induced reset, we could investigate the dynamic gap formation in the HRS transition.

5.3.3 Hourglass Shaped Cu Filament

The analytical fitting of the I–Vs and the observation of the CF associated to progressive reset (Fig. 5.8d), constitute strong evidence in support of a QPC configuration for the CF in those cases. However, the reduced conductivity of the (HRS) CF, coupled with the low read-out bias ($\approx 10 \,\mathrm{mV}$), leads to very small current flowing in the CF during scalpel SPM. Thus limiting our observation capability and the image contrast in the 3D tomogram. The result is shown in Fig. 5.8d, where the CF lacks the sharp definition that we can achieve in case of the LRS. In order to overcome this limitation and obtain sufficient contrast (in the current maps), we investigate the LRS of a filament previously showing progressive reset. To this end, a CF showing progressive reset during its operation is selected for SPM tomography. The device is programmed for few tens of cycles. The I-V characteristic after reset followed a QPC conductance model (not shown). As in Sect. 5.2.1, we program the device in LRS before the scalpel C-AFM. In this case, the LRS guarantees that using a small read-out bias higher current (\approx nA) will flow in the CF. Thus leading to an improved current sensing of the C-AFM sensor and enhanced 3D observation. Figure 5.12 shows the shape of the CF in 3D. Although the wider part of the CF is still positioned at the top interface, there is no clear conical shape. Compared to the observation of Fig. 5.3 this CF presents a constriction placed almost in the middle of the Al₂O₃ layer. This can be seen by suppressing the contribution of the lowly conductive regions of

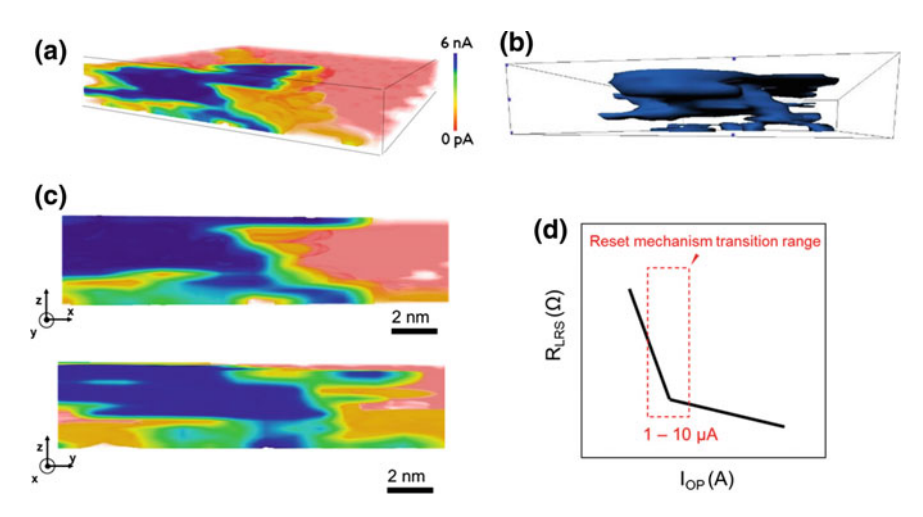


Fig. 5.12 A QPC-like filament structure. **a** Reconstructed 3D sectional view of a conductive filament (LRS) showing progressive reset during cycling. **b** All the low-current contribution is suppressed in the tomogram for the enhanced observation of the QPC constriction also shown in 2D in **c**. **d** The slope of the R_{LRS} – I_{OP} curve is used to estimate the minimum operative current required for the correct memory operation. As shown for a generic material-system the plot shows a drastic increase of the slope at low-current ($<10\,\mu\text{A}$)

the 3D tomogram in Fig. 5.12b. In other words, the LRS observation of a CF showing progressive reset indicates the presence of an atomic constriction in the filament shape, with a geometrical transition from a purely conical to an hourglass shaped CF. Combined to our previous observation of abrupt and progressive CFs, the current shape explains the failure to achieve a good analytical fitting for such CFs by any other mechanisms than OPC.

Furthermore, the existence of these two possible configurations of the Cu-filaments could explain another puzzling behavior experimentally observed i.e. the nonlinear increase of the LRS-resistance as function of the operative current (I_{OP}). When operated at low I_{OP} a drastic increase of the slope of the R_{LRS} – I_{OP} is observed (Fig. 5.12d). This phenomenon appears independently of the CBRAM material system. The level of I_{OP} that triggers the transition will depend on the switching layer (e.g. density, porosity and ionic mobility). However, in a range from 1 to $10\,\mu\text{A}$ the transition in the slope appears concurrently with a transition in the type of the reset characteristics in the I–V (from progressive to abrupt). This has important implications on the minimum operative current for the memory device which is ultimately controlled by the mobility of the cation species in the switching layer. Resulting in good low-current (<10 μ A) functionality for switching layer having a large Cu mobility, while increased switching variability, for the high current operation (>10 μ A) due to the uncontrolled Cu injection. The opposite is observed for reduced Cu mobility switching layers.

Our results indicate that the transition is the electrical fingerprint of the transition between a conical tapered and a QPC-like CF shape. In other words, the change in the slope of the R_{LRS} – I_{OP} plot (Fig. 5.12d) represents the value of current compliance at which the amount of Cu atoms injected in the electrolyte will likely induce conical tapered filaments instead of a QPC-like. The first type of CF shape will tend to break during reset and create a tunnel barrier while the second one will only undergo a size modulation at the CF constriction. This value will be specific for each material system. It has been observed in various CBRAM devices [32] and it is likely appearing in all the CBRAM switching system as it is related to the CF formation mechanisms.

5.4 Tomographic Filament Observation in VCM

In Chap. 2, resistive switching in VCM has been introduced as a reversible (soft) dielectric breakdown, associated with the generation and migration of oxygen vacancies ($V_{\ddot{O}}$) through a field-assisted thermally activated hopping [1, 34, 35]. The local valence change in the atomic lattice of the oxide causes a resistance change in a confined region (CF) that can be used to encode the bit of information. This process is based on a common property of insulators which explains why RS has been reported in a huge list of insulting material systems. As shown in the literature review on CF observation (Chap. 2), in spite of its importance, the CF observation is not only hampered by the small filament size, but also by the minimal compositional difference of the CF with the surrounding material. In this section, scalpel SPM methodologies are used to investigate the nature of resistance switching in oxide VCMs. Consistently with the rest of this work, we investigate the effect of RS in HfO₂.

In hafnia, the CF is assumed to be a highly confined sub-stoichiometric HfO_r volume located in the oxide. The lateral dimensions of the CF ($<10 \,\mathrm{nm}$) have been also inferred by means of ab initio calculations [36]. While in situ TEM has led to the observation of cation-migration (e.g. Cu or Ag ions) as responsible for the filament formation in conductive bridging memories [21] and to Magnéli phase as switching mechanism in unipolar switching [8], to date, far less has been reported for devices based on the bipolar switching mechanism. Miao et al. [37] and Park et al. [38] have reported using in situ TEM the observation of sub-10 nm conductive channels linked to the local migration of oxygen vacancies in bipolar Ta_2O_{5-x}/TaO_{2-x} structures. But TEM is still a projection technique (averaging over the TEM-lamella), and an exhaustive three-dimensional observation of the CF in scaled bipolar devices is still missing. Here we report the first three-dimensional observation of the conductive filament in oxide-based scaled bipolar VCM devices. The device under study is based on a bilayer structure Hf (10 nm)/HfO₂ (amorphous, 5 nm) sandwiched between the Ru and TiN metal electrodes (Fig. 5.13a, b). The choice of Ru is functional to the tip-induced material removal due to the extreme hardness of TiN. Ru as top electrode does not affect any electrical property of the cell since it is only used to provide an ohmic contact with the Hf (capping) layer. The bilayer approach is based on the idea that the concentration of V_o in pure HfO₂ is not sufficient to give any 'ionotronic'

(ionic + electronic) behavior. We therefore intentionally insert a 10-nm Hf metal layer in order to induce at the interface, a sub-stoichiometric HfO_x layer [39]. This interlayer increases the V_a concentration and acts as a reservoir for mobile defects (oxygen vacancies) during the device operation (Chap. 2, QPC model—Sect. 2.3.3). The electrical switching characteristic is illustrated in Fig. 5.13c. After an initial electroforming process, the device shows a bipolar resistive-switching behaviors with two stable states i.e. high-resistance (HRS) and a low-resistance (LRS). The change in resistance can be triggered as in Fig. 5.13c using ± -1 V. During cycling we limit the maximum current through the device at 50 µA in order to avoid the breakdown of the oxide and and to limit the degradation. This is achieved by connecting the (TiN) bottom electrode of the memory element to the drain of a selector transistor. The electrical operation of the device can be described through an analytical model based on conduction through a quantum point contact (QPC), in which the CF is described as a sub-stoichiometric HfO_x region where faster ion drift-diffusion occurs (Sect. 2.3.3) [28, 31]. In essence, the initial electroforming imposes the structure to the CF as in Fig. 5.13d, e and the successive transitions between LRS and HRS are determined by changes in the number of $V_{o}^{..}$ at the constriction. The I-V fitting of one of the device under investigation is reported in Fig. 5.13f.

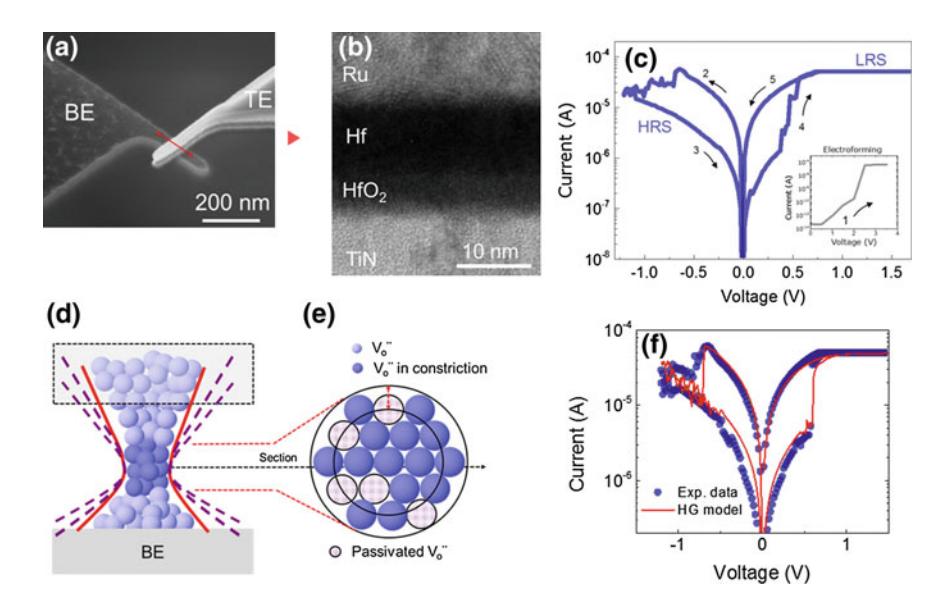


Fig. 5.13 Structure of the HfO₂/Hf memory element and resistive switching characteristic. a Scanning electron microscopy image of a 50-nm crossbar device. b High-resolution TEM image of the Ru/Hf/HfO₂/TiN structure, the switching layer appears brighter due to the relatively lower concentration of Hf metal. c Bipolar resistive switching characteristic of a 50-nm memory cell. The electroforming process is shown in the inset. d—e Schematic and cross-section representation of the conductive filament created during the electroforming and its constriction. f The memory element shows very good fitting using our hour glass model using ≈100 particle in the constriction for the LRS and ≈25 particles for the HRS

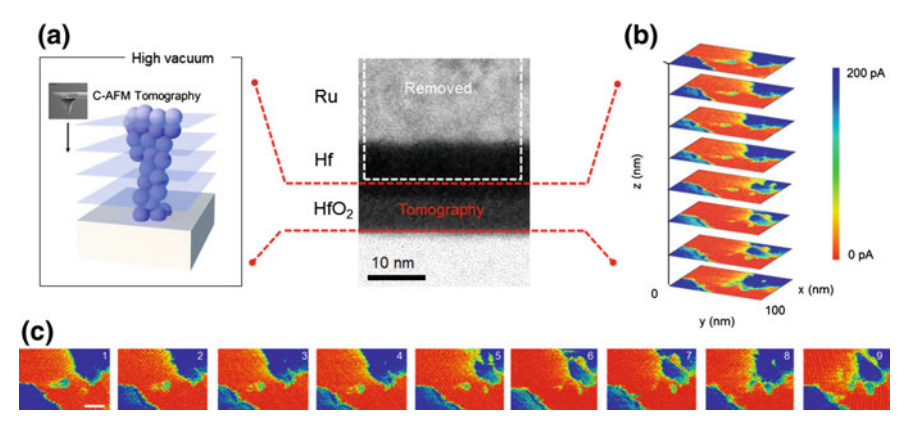


Fig. 5.14 *C-AFM tomography procedure for VCM.* a The diamond tip is used to collect several slices at different heights of the CF after the removal of the Ru and of the Hf layers. b Stacked representation of 2D C-AFM slices, prior to the 3D interpolation. Note, the average space between each slice is $0.2\,\mathrm{nm}$. The slices are aligned to correct any possible drift. c Top view of selected 2D slices throughout the device (scale bar 20 nm). The CF appears in the middle of the active area after top electrode removal. The highly conductive features on the top and bottom corners are the exposed parts of the TiN electrode, which is completely exposed during the removal of HfO₂

Due to the interaction of the CF with oxygen, the SPM tomography experiments are performed in high vacuum ($\approx 10^{-5}$ mbar) in order to minimize the possible reoxidation of the CF (Fig. 5.14a). Prior to the C-AFM tomography we electrically cycle the device as shown in Fig. 5.14b. After a few tens of cycles we set the memory element in its LRS. The C-AFM tomography starts after the removal of the top electrode. Once the Ru top electrode is removed the tip probes the Hf metal layer which still shows a uniform conduction. When the HfO₂ surface is reached (Fig. 5.14c1), the CF becomes visible as a conductive spot in the middle of the HfO2 surface which is still highly insulating (blue background in Fig. 5.14c). Note, no conductive spots are observed in the virgin (not electroformed) state of the device (not shown). Different slices are collected at constant load force (several-hundreds of nN) as in Fig. 5.14c. The bias between tip and sample is kept at $\approx 100 \,\mathrm{mV}$ positive polarity to tip. Compared to the Cu-filament case, this value is higher due to the limited conductivity of the CF. In particular the conductivity drop of the CF is concurrent with the top electrode removal indicating an undesired interaction of the CF with available oxygen also working in high vacuum. Using a removal rate of ≈ 0.2 nm/scan, the final collection constitutes 25 slices for the 5 nm thick switching layer. The acquisition is ended when the switching layer is completely removed (or too thin) and the highly conductive bottom electrode becomes visible (Fig. 5.14c9). The analysis of the consecutive images clearly indicates that the CF shrinks moving from the top to the bottom interface (Fig. 5.14c1-c9). The evolution of the 2D slices indicate the presence of a constriction in the proximity of the bottom electrode and therefore opposite to the location of the $V_0^{...}$ -reservoir (Hf/HfO₂ interface).

The area of the observed CF shrinks from $38.9\,\mathrm{nm}^2$ to $7.8\,\mathrm{nm}^2$ as shown in Fig. 5.14c3–7. According to our model the $7.8\,\mathrm{nm}^2$ constriction is the region where the spatial confinement of defects creates the QPC and the current is controlled by the corresponding current-controlling energy levels. The current observation shows that in a device of $\approx 50 \times 70\,\mathrm{nm}^2$, the filament occupies less than $7 \times 7\,\mathrm{nm}^2$ area. Similar CF-dimensions are observed consistently in other devices (programmed under the same conditions). These observations suggest that such VCM devices can be further scaled in the sub-10 nm regime [40, 41]. A 3D-reconstructured view of the analyzed volume is shown in Fig. 5.15a. A top view of the CF (surrounded by the bottom-electrode) is provided in Fig. 5.15a whereas Fig. 5.15b is a 2D zoom into the region containing the CF. The tomogram (Fig. 5.15c) emphasizes the spatial distribution of the highly conductive features by subtracting all low-current contributions. Hence this is representative for the shape of the CF which is the lower resistive path for the current inside the HfO2. The conical shape, shrinking from top to bottom electrode, becomes clear from the 3D-representation of the CF. The 3D tomogram unambigu-

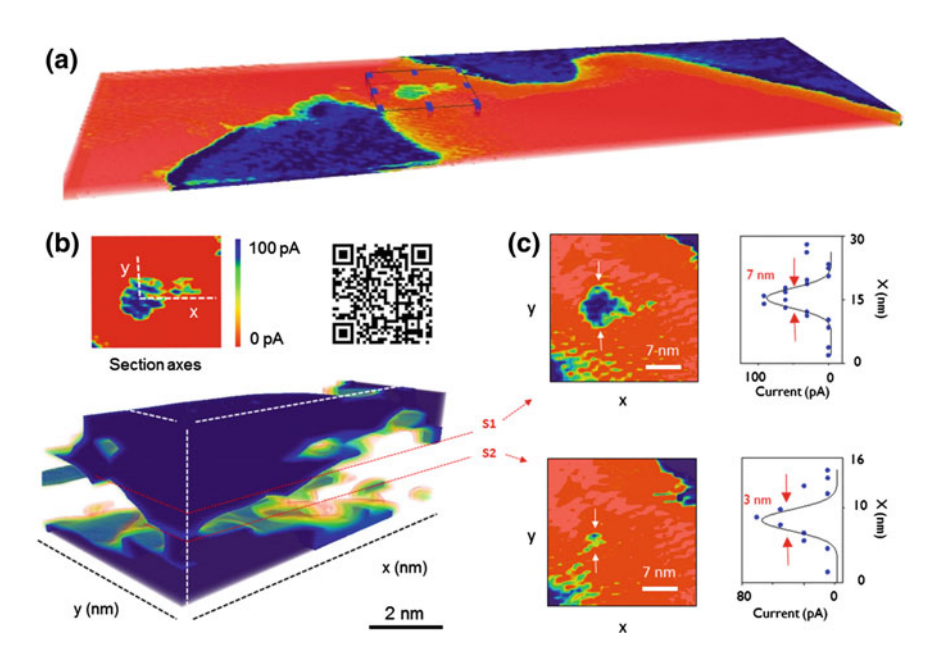


Fig. 5.15 Three-dimensional observation of the CF in oxide VCM. **a** Tomographic reconstruction of the crossbar memory cell visualized by volume rendering after top electrode removal (scan size 800×200 nm). **b** 2D zoom into the region containing the CF and observation by volume rendering and iso-surface at fixed threshold (blue shape) for the CF under investigation in 5 nm thick HfO₂ (scale bar 2 nm). The conductive filament is shown in double cross-section (axes according to inset). The low current contribution in the tomogram is suppressed to enhance the contrast of the highly conductive features. **c** 2D observation of the CF section-planes (left panels) and C-AFM spectra (right panels) to determine effective CF size. The animated cross-section of the filament top-view is available by clicking here or by scanning the QR tag

ously reveals that the CF has the narrow part close to the bottom electrode (oxygeninert electrode). The volume of the truncated cone that approximates the CF region is $\approx 200 \, \mathrm{nm}^3$. The area of the CF (top to bottom) shrinks by $\approx 60 \, \%$ in sizes as shown in Fig. 5.15c. The V_o -reservoir, deliberately induced by means of the Hf metal deposition, appears as the wider part of the CF (at the top-interface) and locally provides an exchange-layer for defects to sustain the successive CF rearrangements which is at the base of the CF's resistive changes [9, 42]. Our observation indicates that the switching mechanism in bipolar oxide-based VCM relies on the formation/cycling of a local conductive region (filament) created during the electroforming process (in the HfO₂) between the Hf and the TiN electrodes. On each subsequent memory cycle the number of V_o will be reshuffled at the constriction of the CF inducing the resistance change and flipping the bit-state. Cross-section movies of the tomogram are available using the QR tag in Fig. 5.15 or following the hyperlink in caption.

5.4.1 Filament Size Modulation in VCM

Due to the massive usage as gate dielectric in MOSFETs, HfO_2 has allowed an easy manifacturability enabling ultra scaled device integration for VCM. Govoreanu et al. [40] demonstrated a 10×10 nm device (Fig. 5.16a), and other reports have shown sub-1X nm functionality for these devices [43, 44]. Remarkably, those devices show functionality also at relatively high operative current (200 μ A as in Fig. 5.16b) leaving open the question on the CF's size at these conditions. However, the impossibility to induce low resistive filaments using a sharp AFM tip observed in Chap. 4, indicates the existence of a minimum spatial dimension required by the CF to achieve those low resistance states.

In this section, we use C-AFM tomography to tackle this open question. Figure 5.16a shows a crossbar memory element formed at the intersection between the two 20-nm-wide bottom and top electrodes. The lateral oxidation of the Hf layer contribute to the cell size reduction to ≈ 10 nm. The cell shows standard low-voltage operation (<1 V) and good functionality while using high current compliance ($200 \,\mu$ A), more details on the cell performance are available in literature [45, 46]. We program and cycle a standard device, Hf $(10 \text{ nm})/\text{HfO}_2$ $(60 \times 100 \text{ nm cell})$ sandwiched between the Ru and TiN metal electrodes. In this case using 200 µA as programming current, the cell is programmed in LRS before C-AFM tomography (Fig. 5.16b). A 2D C-AFM slice showing the CF constriction is presented in Fig. 5.16c. A 3Dtomogram of the conductivity variations within the sample is obtained by interpolation. The images indicate the presence of a conductive filament running through the oxide layer with a non-regular conical geometry. Consistently with the previous observations, the CF shows a constriction in proximity of the TiN interface (O-inert electrode). In agreement with the CF observed in the previous section (50 µA C.C.), the presence of the oxygen exchange layer (Hf) induces a widening of the conductive area of the CF at the Hf/HfO₂. The cross-section of the obtained 3D-tomogram is shown in Fig. 5.16c, d. The spatial extent of the CF, Fig. 5.16d, shows that for a device

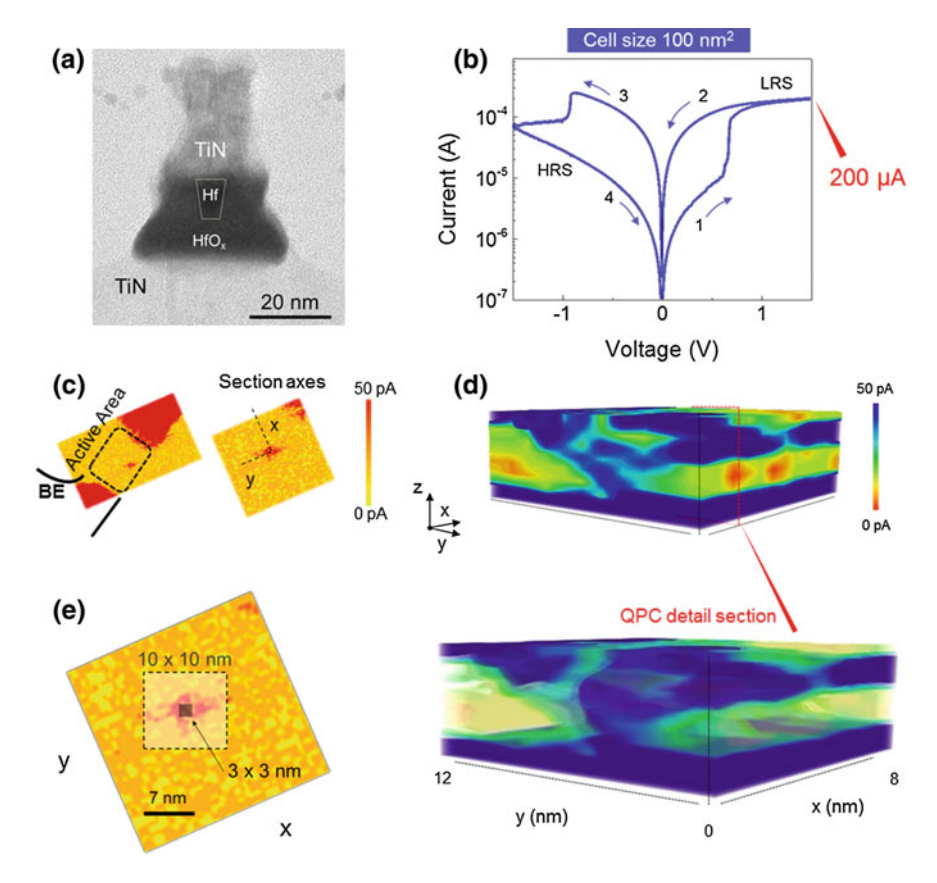


Fig. 5.16 Filament size in high current operation. a TEM image of the $10 \times 10\,\mathrm{nm}$ device proposed by Govoreanu and co-authors [reproduced from [40]]. b I–V characteristic at $200\,\mu\mathrm{A}$ current compliance of the $100\,\mathrm{nm}^2$ device. c Section-plane (C-AFM current map) showing the effective CF size in proximity of the constriction (close to the TiN electrode). d Volume rendering of the CF in the (5 nm thick HfO₂). Section and detailed observation of the QPC constriction, by low-current suppression in the 3D tomogram. e Zoom in of the section-plane holding the CF constriction. A schematic of $10 \times 10\,\mathrm{nm}$ electrode is reported, in addition a 3×3 virtual electrode is sketched to illustrate the tip-induced virtual top electrode size

of \approx 60 \times 100 nm², the filament occupies \approx 10 \times 10 nm² at the Hf/HfO₂ interface and \approx 6.2 \times 6.2 nm² area near the TiN- electrode. Due to its crucial role, the CF constriction represents the limiting factor for the required dimensions. The observed sizes of \approx 38.9 nm², demonstrate that although wider than the 50 μ A case, such constriction could easily be contained in a 10 \times 10 nm device, which explains why VCM provides device functionality at high current also in very low dimensions and suggests additional scaling capability. Despite the 200 μ A operation, the CF occupies only a small fraction the entire device area, this is schematically reported in Fig. 5.16e. Although smaller than the 10 \times 10 nm² the spot is too large to be contained in the

 $3 \times 3 \,\mathrm{nm}^2$ virtual top electrode created by the AFM tip (Fig. 5.16e). This provides a direct observation of the scaling limitation for high current RS in HfO₂ to $\approx 5 \times 5 \,\mathrm{nm}^2$ device size. Furthermore it clarifies why only the AFM tips with large contact size (e.g. tip radius) could induce lowly resistive CFs (Chap. 4).

QPC constriction and size modulation—As we did for the Cu-filaments, the dependence with the programming current of the CF volume can now be investigated also in VCM. We control the current in our device through the control-transistor and program cells at 50 and 250 μA respectively. Figure 5.17a shows their corresponding I–V reset characteristic with the programming condition in the inset. The current compliance modulation is known to induce a CF resistance modulation as observed in Fig. 5.17a [47]. We compare two current levels 50 and 250 μA . In this case, we compare the experimentally observed constriction sizes. The results in Fig. 5.17b show an increasing trend in the sizes of the CF (at its narrowest cross-section point) as function of the programming current. The higher constriction area would allow more defects determining the observed lower CF resistance achieved with high current operations

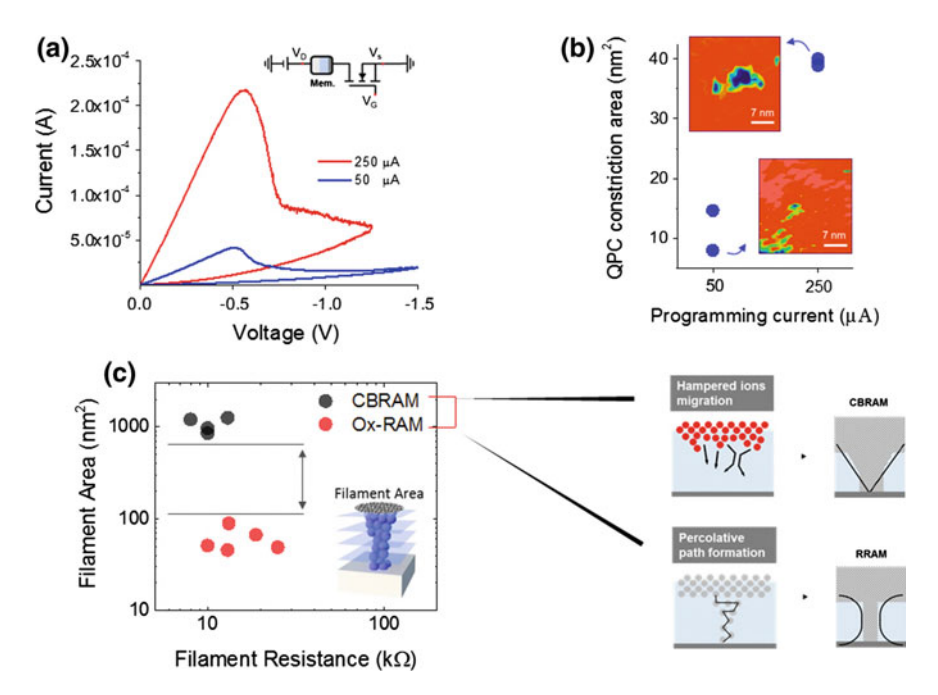


Fig. 5.17 Conductive filament dependence on the programming current. a Reset characteristic of cells programmed using different operating current, the induced CF resistance is inversely proportional to the operating current. b Dependence of the experimentally observed QPC constriction size as function of the programming current. In the inset two reference constriction points for each of the used programming conditions are shown. c Comparison between experimentally observed CFs' sizes at the top electrode interface, for cation-versus anion-based devices. In the *inset* we show the schematic of the final shape difference induced by the different switching mechanisms in CBRAM and VCM (more conical vs. more elongated)

(Fig. 5.13d, e). This supports that the CF's resistance would be determined by the number of defects and thus the size of the narrowest point of the CF. In other words, the number of defects in the CF can be related to the programming conditions, providing experimental evidences that the CF behaves as a defect modulated quantum point contact.

In the comparison between the CF observation for CBRAM and VCM, we report the unexpected difference in the spot sizes of Cu- and V_a -based filaments. The sizes of the experimentally observed CFs with comparable resistive states and induced at similar programming conditions are shown are Fig. 5.17c. The area of the filament cross-section is measured respectively at the Hf/HfO₂ and Cu/Al₂O₃ interface for VCM and CBRAM. A surprising 10x difference is observed. The unexpected result of Fig. 5.17c underlines a fundamental difference in the physics of the filament formation for cation- versus anion-based devices. It can be thought as the fingerprint of the two different filament growth mechanisms. While the Cu-filament grows as a result of the injection and migration of a foreign species into the solid electrolyte, the V_{a} -filament is the result of the formation of intrinsic defects within the oxide layer connecting the defects reservoir (i.e. oxygen scavenged interface) with the bottom electrode. The filament formation in CBRAM, combines the dielectric degradation (due to the high electric field) with the insertion of a foreign species (Cu). The poor mobility of the Cu ions in the Al₂O₃, leads to the formation of a wide-base conical shape as previously observed [6, 15]. Conversely in VCM, the CF formation arises from the generation of defects in the bulk of the oxide. This process happens according to the percolation theory [48] for dielectric-breakdown. Here, the oxygen atoms start to leave their lattice position and drift toward the anode leaving behind a local conductive path that joins the sub-stoichiometric V_a reservoir with the bottom electrode (Fig. 5.15b). Thus limiting the lateral growth of the CF in the VCM case versus the CBRAM as schematically shown in the inset of Fig. 5.17c.

5.5 Summary of the Chapter

In summary, in this chapter we have presented the direct three-dimensional observation of CFs in state-of-the-art RS devices. This has been enabled by our scalpel SPM methodology. The observation of a cone-shaped Cu-filament in the LRS of CBRAM has been important to determine the cation migration as rate limiting step in the CF formation. In addition the dependence of the CF volume with the programming conditions enabled the understanding of the resistance modulation achieved by the current compliance limitation. Afterwards, we have studied the HRS of CFs in conductive-bridging devices. Through C-AFM tomography we have been able to image on the nanoscale the morphology of erased CFs. The results show two types of reset transitions: abrupt and progressive whereby broken CFs are observed in devices showing abrupt reset, and nonbroken (highly resistive) CFs are observed in the case of progressive reset. The morphological classification is accompanied by the electrical model based on an analytical fitting of the I–V characteristics, which sup-

ports the description of erased CFs as either a tunnel-barrier or a quantum-point-contact. Our findings suggest that although driven by the same phenomenon, the final shape after the dissolution can be a fully broken CF or a constrained CF. The existence of both shapes can be explained within one dissolution theory whether the starting point (i.e. the original size of the CF) determines the final shape. In the case of oxide VCM, the CF shows a conical shape with the narrow part close to the oxygen-inert electrode (TiN). The direct observation of the CF induced at high current compliance, could clarify the remarkable functionality of $10 \times 10 \, \text{nm}^2$ devices operated at high current. In addition, the 3D visualization of a $50 \, \mu$ A filament demonstrated strong scaling potential for this technology in the sub- $10 \, \text{nm}^2$ domain. Also in this case experimental evidences of the size modulation of the filament constriction as function of the programming current provided understanding of the nature of the CF as a defects modulated quantum-point-contact.

References

- R. Waser, M. Aono, Nanoionics-based resistive switching memories. Nat. Mater. 6(11), 833– 840 (2007)
- R. Waser, R. Dittmann, G. Staikov, K. Szot, Redox-based resistive switching memories nanoionic mechanisms, prospects, and challenges. Adv. Mater. 21(25–26), 2632–2663 (2009)
- 3. I. Valov, R. Waser, J.R. Jameson, M.N. Kozicki, Electrochemical metallization memories-fundamentals, applications, prospects. Nanotechnology **22**(25), 254003 (2011)
- 4. D. Ielmini, F. Nardi, C. Cagli, Physical models of size-dependent nanofilament formation and rupture in NiO resistive switching memories. Nanotechnology **22**(25), 254022 (2011)
- X. Guo, C. Schindler, S. Menzel, R. Waser, Understanding the switching-off mechanism in Ag⁺ migration based resistively switching model systems. Appl. Phys. Lett. 91(13), 133513 (2007)
- 6. Y. Yang, P. Gao, S. Gaba, T. Chang, X. Pan, L. Wei, Observation of conducting filament growth in nanoscale resistive memories. Nat. Commun. 3, 732 (2012)
- Q. Liu, J. Sun, H. Lv, S. Long, K. Yin, N. Wan, Y. Li, L. Sun, M. Liu (2012) Real-time observation on dynamic growth/dissolution of conductive filaments in oxide-electrolyte-based ReRAM. Adv. Mater. (Deerfield Beach, Fla.), 24(14), 1844–1849 (2012)
- 8. D.-H. Kwon, K.M. Kim, J.H. Jang, J.H. Jang, J.M. Jeon, M.H. Lee, G.H. Kim, X.-S. Li, G.-S. Park, B. Lee, S. Han, M. Kim, C.S. Hwang, Atomic structure of conducting nanofilaments in TiO2 resistive switching memory. Nat. Nanotechnol. **5**(2), 148–153 (2010)
- L. Goux, A. Fantini, B. Govoreanu, G. Kar, S. Clima, Y.-Y. Chen, R. Degraeve, D.J. Wouters, G. Pourtois, M. Jurczak, Asymmetry and switching phenomenology in TiN\(Al2O3)\HfO2\Hf Systems. ECS Solid State Lett. 1(4), P63–P65 (2012)
- A. Belmonte, W. Kim, B.T. Chan, N. Heylen, A. Fantini, M. Houssa, M. Jurczak, L. Goux, A thermally stable and high-performance 90-nm. IEEE Trans. Electr. devices 60(11), 3690–3695 (2013)
- U. Celano, L. Goux, K. Opsomer, M. Iapichino, A. Belmonte, A. Franquet, I. Hoflijk, C. Detavernier, M. Jurczak, W. Vandervorst, Scanning probe microscopy as a scalpel to probe filament formation in conductive bridging memory devices. Microelectr. Eng. (in press), 120, 67–70 (2013)
- U. Celano, L. Goux, K. Opsomer, A. Belmonte, M. Iapichino, C. Detavernier, M. Jurczak, W. Vandervorst, Switching mechanism and reverse engineering of low-power Cu-based resistive switching devices. Nanoscale 5(22), 11187–11192 (2013)

 S. Menzel, S. Tappertzhofen, R. Waser, I. Valov, Switching kinetics of electrochemical metallization memory cells. Phys. Chem. Chem. Phys.: PCCP 15(18), 6945–6952 (2013)

- S.-J. Choi, G.-S. Park, K.-H. Kim, S. Cho, W.-Y. Yang, X.-S. Li, J.-H. Moon, K.-J. Lee, K. Kim, In situ observation of voltage-induced multilevel resistive switching in solid electrolyte memory. Adv. Mater. (Deerfield Beach, Fla.), 23(29), 3272–7 (2011)
- U. Celano, L. Goux, A. Belmonte, K. Opsomer, A. Franquet, A. Schulze, C. Detavernier, O. Richard, H. Bender, M. Jurczak, W. Vandervorst, Three-dimensional observation of the conductive filament in nanoscaled resistive memory devices. Nano lett. 14(5), 2401–2406 (2014)
- Y. Yang, L. Wei, Nanoscale resistive switching devices: mechanisms and modeling. Nanoscale 5(21), 10076–10092 (2013)
- Q. Liu, S. Long, H. Lv, W. Wang, J. Niu, Z. Huo, J. Chen, M. Liu, Controllable growth of nanoscale conductive filaments in solid-electrolyte-based ReRAM by using a metal nanocrystal covered bottom electrode. ACS Nano 4(10), 6162–6167 (2010)
- 18. I. Valov, R. Waser, Comment on "Dynamic Processes of Resistive Switching in Metallic Filament-Based Organic Memory Devices". pp. 8–10 (2013)
- I. Valov, R. Waser, Comment on real-time observation on dynamic growth/dissolution of conductive filaments in oxide-electrolyte- based ReRAM. Adv. Mater. (Deerfield Beach, Fla.) 25(2), 162–164 (2013)
- S. Gao, C. Song, C. Chen, F. Zeng, F. Pan, Reply to Comment on 'Dynamic Processes of Resistive Switching in Metallic Filament-Based Organic Memory Devices', pp. 6–7 (2013)
- Y. Yang, P. Gao, L. Li, X. Pan, S. Tappertzhofen, S. Choi, R. Waser, I. Valov, W.D. Lu, Electrochemical dynamics of nanoscale metallic inclusions in dielectrics. Nat. Commun. 5, 4232 (2014)
- K. Sankaran, L. Goux, S. Clima, M. Mees, J.A. Kittl, M. Jurczak, L. Altimime, G.M. Rignanese, G. Pourtois, Modeling of copper diffusion in amorphous aluminum oxide in CBRAM memory stack. ECS Trans. 45(3), 317–330 (2012)
- S. Kim, S.-J. Kim, K.M. Kim, S.R. Lee, M. Chang, E. Cho, Y.-B. Kim, C.J. Kim, U.I. Chung, I.-K. Yoo, Physical electro-thermal model of resistive switching in bi-layered resistance-change memory. Sci. Rep. 3, 1680 (2013)
- 24. U. Russo, D. Kamalanathan, D. Ielmini, A.L. Lacaita, M.N. Kozicki, Study of multilevel programming in programmable. IEEE Trans. Electr. Devices **56**(5), 1040–1047 (2009)
- S.H. Jo, W. Lu, CMOS compatible nanoscale nonvolatile resistance switching memory. Nano Lett. 8(2), 392–397 (2008)
- 26. S. Ambrogio, S. Balatti, S. Choi, D. Ielmini, Impact of the mechanical stress on switching characteristics of electrochemical resistive memory. Adv. Mater. **26**(23), 1–8 (2014)
- U. Celano, L. Goux, A. Belmonte, K. Opsomer, R. Degraeve, C. Detavernier, M. Jurczak, W. Vandervorst, Understanding the dual nature of the filament dissolution in conductive bridging devices. J. Phys. Chem. Lett. pp. 1919–1924 (2015)
- R. Degraeve, L. Ph Roussel, D.W. Goux, J. Kittl, L. Altimime, M. Jurczak, G. Groeseneken, Generic learning of TDDB applied to RRAM for improved understanding of conduction and switching mechanism through multiple filaments. IEDM Tech. Dig. IEEE Int. Electr. Devices Meet. 1, 632–635 (2010)
- V.V. Afanas'ev, F. De Stefano, M. Houssa, A. Stesmans, L. Goux, K. Opsomer, C. Detavernier, J. Kittl, M. Jurczak, Electron barrier height at CuTe1-x/Al2O3 interfaces of conducting bridge memory stacks. Thin Solid Films 533, 34–37 (2013)
- F. De Stefano, V.V. Afanas'ev, M. Houssa, A. Stesmans, K. Opsomer, M. Jurczak, L. Goux, Control of metal/oxide electron barriers in CBRAM cells by low work-function liners. Microelectr. Eng. 109, 156–159 (2013)
- R. Degraeve, A. Fantini, S. Clima, B. Govoreanu, L. Goux, Y.Y. Chen, D.J. Wouters, G.S. Ph Roussel, G. Pourtois Kar, S. Cosemans, J.A. Kittl, G. Groeseneken, M. Jurczak, L. Altimime, Dynamic 'Hour Glass' Model for SET and RESET in HfO 2 RRAM, in *Symposium on VLSI Technology (VLSIT)*, vol. 1, Honolulu, HI (2012), pp. 75–76

- A. Belmonte, R. Degraeve, A. Fantini, W. Kim, M. Houssa, M. Jurczak, L. Goux, Origin of the current discretization in deep reset states of an Al2O3/Cu-based conductive-bridging memory, and impact on state level and variability. Appl. Phys. Lett. 104(23), 233508 (2014)
- 33. U. Celano, L. Goux, A. Belmonte, A. Schulze, K. Opsomer, C. Detavernier, O. Richard, H. Bender, M. Jurczak, W. Vandervorst, Conductive-AFM tomography for 3D filament observation in resistive switching devices.in *Proceedings of the 2013 IEEE International Electron Devices Meeting (IEDM)*, pp. 21.6.1–21.6.4 (2013)
- 34. H.-S. Philip Wong, H.-Y. Lee, S. Yu, Y.-S. Chen, Y. Wu, P.-S. Chen, B. Lee, F.T. Chen, M.-J. Tsai. Metal-Oxide RRAM. Proceedings of the IEEE 100(6), 1951–1970 (June 2012)
- J.J Yang, M.D. Pickett, X. Li, D.A.A. Ohlberg, D.R. Stewart, R.S. Williams. Memristive switching mechanism for metal/oxide/metal nanodevices. Nat. Nanotechnol. 3(7), 429–433 (2008)
- 36. K. Kamiya, M. Yang, T. Nagata, S.-G. Park, B. Magyari-Köpe, T. Chikyow, K. Yamada, M. Niwa, Y. Nishi, K. Shiraishi, Generalized mechanism of the resistance switching in binary-oxide-based resistive random-access memories. Phys. Rev. B 87(15), 155201 (2013)
- F. Miao, J.P. Strachan, J.J. Yang, M.-X. Zhang, I. Goldfarb, A.C. Torrezan, P. Eschbach, R.D. Kelley, G. Medeiros-Ribeiro, R.S. Williams, Anatomy of a nanoscale conduction channel reveals the mechanism of a high-performance memristor. Adv. Mater. 53(47), 5633–5640 (2011)
- G.-S. Park, Y.B. Kim, S.Y. Park, X.S. Li, S. Heo, M.-J. Lee, M. Chang, J.H. Kwon, M. Kim, U.-I. Chung, R. Dittmann, R. Waser, K. Kim, In situ observation of filamentary conducting channels in an asymmetric TaO5-x/TaO2-x bilayer structure. Nat. Commun. 4, 2382 (2013)
- C. Chen, S. Gao, F. Zeng, G.S. Tang, S.Z. Li, C. Song, H.D. Fu, F. Pan, Migration of interfacial oxygen ions modulated resistive switching in oxide-based memory devices. J. Appl. Phys. 114(1), 014502 (2013)
- B. Govoreanu, G.S Kar, Y.-y Chen, V. Paraschiv, S. Kubicek, A. Fantini, I.P. Radu, L. Goux, S. Clima, R. Degraeve, N. Jossart, O. Richard, T. Vandeweyer, K. Seo, P. Hendrickx, G. Pourtois, H. Bender, L. Altimime, D.J. Wouters, J.A Kittl, M. Jurczak, 10x10nm 2 Hf/HfO x Crossbar resistive RAM with excellent performance, reliability and low-energy operation, in *IEDM Tech. Dig.*, pp. 31.6.1 31.6.4, Washington, DC (2011)
- 41. S. Pi, P. Lin, Q. Xia, Cross point arrays of 8 nm x 8 nm memristive devices fabricated with nanoimprint lithography. J. Vac. Sci. Technol. B: Microelectr. Nanometer Struct. **31**(6), p. 06FA02 (2013)
- 42. R. Degraeve, L.. Goux, D.J. Wouters, J.A. Kittl, L. Altimime, M. Jurczak, G. Groeseneken, Deterministic and stochastic component in RESET transient of HfSiO/FUSI gate RRAM stack. in 2011 Symposium on VLSI Technology (VLSIT), vol. 1 (2011), pp. 28–29
- 43. C. Ho, C.-l. Hsu, C.-C. Chen, J.-T. Liu, C.-S. Wu, C.-C. Huang, C. Hu, F.-l. Yang, 9nm half-pitch functional resistive memory cell with < 1 uA programming current using thermally oxidized sub-stoichiometric WO x film, in *Proceedings of the 2010 IEEE International Electron Devices Meeting (IEDM)* (2010), pp. 14–15
- 44. Z. Zhang, W. Yi, S. Member, H. Philip Wong, S. Simon Wong. Nanometer-Scale HfO x RRAM. **34**(8), 1005–1007 (2013)
- A. Fantini, L. Goux, S. Clima, R. Degraeve, A. Redolfi, C. Adelmann, G. Polimeni, Y.Y. Chen, M. Komura, A. Belmonte, D. J Wouters, M. Jurczak, Engineering of Hf 1-x Al x O y amorphous dielectrics for high-performance RRAM applications (c) (2014)
- A. Fantini, L. Goux, A. Redolfi, R. Degraeve, G. Kar, Y.Y. Chen, M. Jurczak, Lateral and vertical scaling impact on statistical performances and reliability of 10nm TiN/Hf (Al) O/Hf/TiN RRAM devices (2014), pp. 2013–2014
- 47. S. Balatti, S. Larentis, D.C. Gilmer, D. Ielmini, Multiple memory states in resistive switching devices through controlled size and orientation of the conductive filament. Adv. Mater. (Deerfield Beach, Fla.), **25**(10) (2013), pp. 1474–1478
- R. Degraeve, G. Groeseneken, R. Bellens, J.L. Ogier, M. Depas, P.J. Roussel, H.E. Maes, New insights in the relation between electron trap generation and the statistical properties of oxide breakdown. IEEE Trans. Electr. Devices 45(4), 904–911 (1998)

Chapter 6 Reliability Threats in CBRAM

6.1 Reliability Threats of Cu Filaments

For emerging devices, the reliability is one of the major obstacle in the process of optimization and commercialization. Although RS devices have already been introduced in some commercial niches, few studies have addressed the topic of the filament evolution during device operation and the related reliability issues. This is likely due to the inherently difficulties in the direct observation of the CFs in integrated cells. However, there is a lot to learn by studying how things break. This is especially true for an emerging technology such as RS memory, where the information on the failures translates in understanding of the underlying physical processes. It is clear that filamentary switching is inherently prone to variability due to the discrete nature of the defects constituting the CF. Structural modifications in the CF trigger changes in the CF resistance affecting the resistive window (RW) and the "1" – "0" read margins in the memory applications. In Chap. 4, by the characterization of the tip-induced filament rupture, we have shown the set and reset variability as originating from changes in the filament conductivity in consecutive formations. In addition, different tunnel gap thicknesses could be observed for the same CF on subsequent cycles. The latter has been recently confirmed by Lv and co-authors by means of TEM [1]. While few studies are available on the direct observation of the filament compositional changes and are generally achieved by means of TEM,[2] the electrical fluctuations induced by the filament's structural modifications have been extensively studied by random telegraph noise (RTN) analysis [3–6].

Our scalpel SPM methodology provides a privileged methodology for the analysis of the filament structure in failed devices. One can think to induce a specific type of failure in a device prior to submit it to scalpel SPM. In this chapter we have used this approach to investigate two common failure modes in CBRAM. Figure 6.1a shows

Electronic supplementary material The online version of this chapter (doi:10.1007/978-3-319-39531-9_6) contains supplementary material, which is available to authorized users.

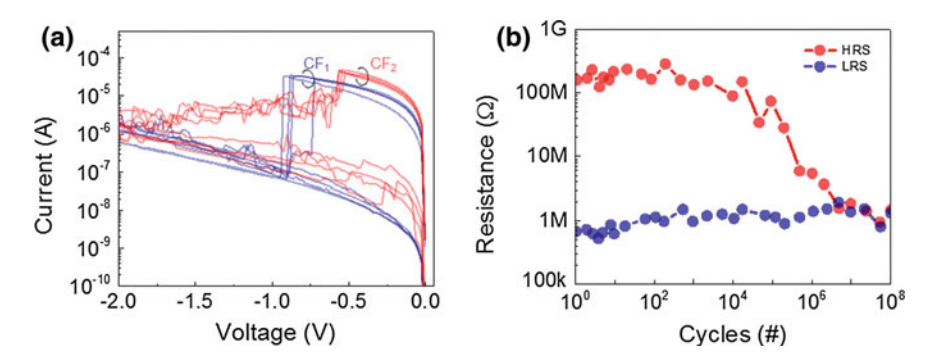


Fig. 6.1 Reliability threats in CBRAM. **a** Resistance state fluctuations observed in consecutive reset traces of CBRAM. Note, the multiple LRS and reset transitions observed suggest that different CFs are alternating. **b** Resistive window collapse on pulse endurance test, with the CF degenerating into a nonrecoverable LRS (i.e. stuck in LRS)

some reset events in CBRAM (set transitions not shown). Those are subsequent reset cycles occurring in the same device. It is worth noting that for some cycles the LRS state shows the same resistance level and reset transition (CF₁). After few cycles it evolves into another LRS resistance (CF₂) that also shows a different type of reset transition (Sect. 5.3). The appearance of different resistive states combined to the different reset transitions, suggests the existence of multiple CFs alternating throughout the device operations. Although not immediately obvious in the commonly accepted theory, we demonstrate for the first time in the following section that the existence of multiple CFs is responsible for the drift of the resistance state in such cases. As a second failure mode, the structural change of a CF responsible for the collapse of the resistive window (RW) is characterized. This type of failure is often referred to as stuck in low resistive state (stuck in LRS) Fig. 6.1b. This failure affects the endurance of the device reducing the number of possible switching cycles and therefore the device lifetime. A gradual decrease of the HRS is responsible for a gradual closure of the RW. This is a very common source of failure for both CBRAM and VCM. As for the observations in Chap. 5, all the devices in the following sections are programmed by a semiconductor parameter analyzer using the 1T1R configuration, and finally SPM tomography is used only to probe the CF in 3D.

6.2 Filament Multiplicity as Source of State Instability

From Celano, U. et al., IEEE Intern. Reliability Physics Symposium, 2015.

Due to the structural rearrangements of the atoms constituting the CF, fluctuations around the HRS and LRS values are expected from cycle-to-cycle as experimentally observed (Fig. 2.6b). We also know from Chap. 4 that larger fluctuations are expected for the HRS as compared to the LRS due to the variable tunnel gap induced in

the ruptured CF. However, any resistance state fluctuation is detrimental because it will ultimately reduce the read margins when reading the memory. As example, in Fig. 6.1a some consecutive resistive cycles are reported. The sequence of the reset characteristics presents the LRS values as clustered in two resistance levels ($CF_{1,2}$). Despite programming the CBRAM cell with the same electrical conditions, the CF shows for few cycles a stable LRS $\approx 30~\text{k}\Omega$ with abrupt reset transitions. Afterwards, the CF evolves towards a different resistance state $\approx 20~\text{k}\Omega$ (LRS) for a few more cycles and the reset transition becomes progressive. From the standpoint of the device operation this is a source of undesired variability. The changes in the LRS are reflected also in the HRS and thus on the entire RW of the memory element leading to potential corruption of the stored data.

In this case, it is hard to believe that small structural rearrangements of the atoms in the filament can account for the observed variations including those in the reset transitions. The observed variability suggests that multiple CFs might alternate in controlling the LRS/HRS states. However, it is widely accepted that the filament formation is a winner-takes-all procedure, where after the first formation all the subsequent cycles will occur at the same location. This is also supported by our results in Chap. 5. Therefore we select a device showing this specific electrical behavior (during cycling), and we use C-AFM tomography to study the morphology of the CF. The device is left in the LRS before applying the scalpel C-AFM. Figure 6.2a shows the set of C-AFM current maps, recorded in the cross-point memory element. The presence of the top electrode (TE) shields the observation of the CF. Using C-AFM tomography we remove the TE and collect C-AFM images of the conductive filament at different depths, leading to a complete sampling of the solid electrolyte volume [7]. The evolution of the current maps from the presence of the top electrode to the exposure of the bottom electrode is shown in Fig. 6.2a. The process leads to a uniform sequential removal (step-size below 1 nm) of the 5 nm Al₂O₃. The CF appears in the top-right corner of the active area (dashed white square in Fig. 6.2a) visible after the top electrode removal. Figure 6.2a1-4 show some of the slices acquired at different depths within the switching layer (Al₂O₃). Interestingly, the CF appears as constituted of two spots that are closely located. Of the two spots, the one on the left has a strong size reduction in Fig. 6.2a1-4, while the other one runs through the entire Al₂O₃. A 3D-tomogram of the sample is obtained by interpolation and shown in Fig. 6.2b. Two cross-section images are extracted from the main 3D tomogram, the lowly conductive regions are suppressed in Fig. 6.2b in order to enhance the contrast of the CFs. In Sect. 6.1 both filaments are visible and one of the two (left) is only partially formed. Section 6.2 shows the 3D cross-section of the connected filament clearly shorting the two electrodes. Though the CF in Sect. 6.2 is only fully connected, the presence of the second filament represents a potential reliability threat.

Indeed, the electrochemistry describing the filament formation does not exclude the possibility of multiple attempts of filaments-formation and the nucleation of multiple filaments has been often reported by means of TEM [8, 9]. In principle, one would expect that the CF that undergoes a complete formation (i.e. shorting the two electrodes in LRS), dominates the subsequent cycles and becomes the only one responsible for the resistive switching. As such, also the variability would be

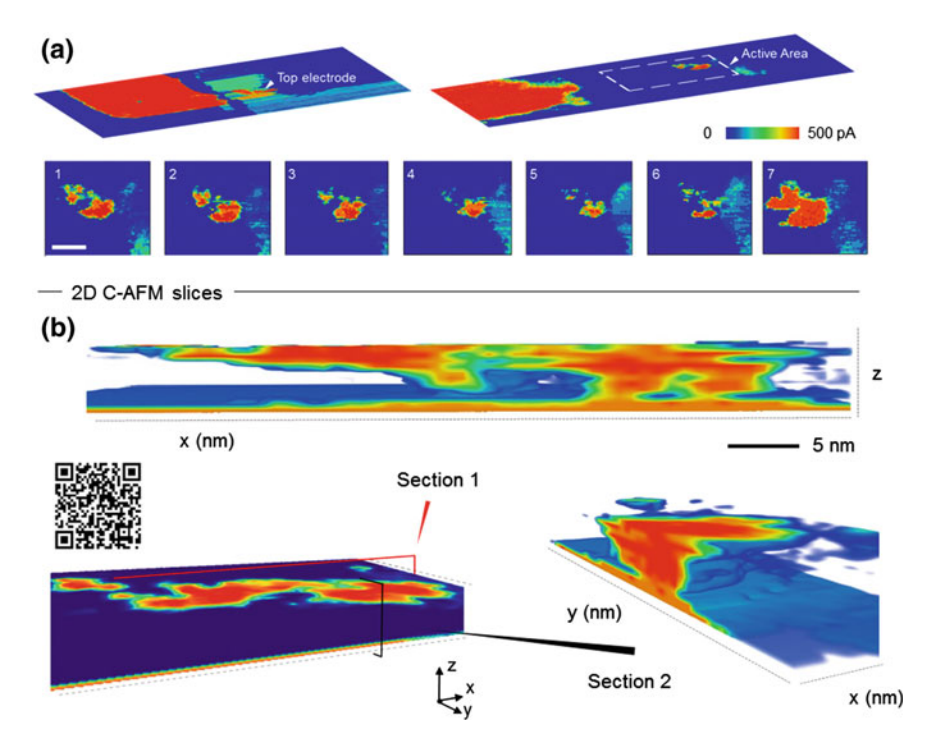


Fig. 6.2 *Multiple filaments by scalpel SPM.* **a** 2D current maps of the device under test (programmed at 100 μA C.C.). The complete evolution from the presence of the *top* electrode to the exposure of the *bottom* electrode is presented (scale bar 25 nm). **b** The 3D tomogram is interpolated and two cross-section images are extracted. Of the two spots observed after to electrode removal, only one is fully connected while a second CF is not completely formed. The animated cross-section of the tomogram is available by clicking here or by scanning the QR tag

limited. This description can be true for large (planar) structures, [8] but it is not longer verified at reduced dimensions. In fact when the solid electrolyte is only few nm thick, there is a real risk of resistance variability due to the effect schematically presented in Figure 6.3. In presence of two competing CFs, one needs to realize that the filament that was completely formed (CF₁), undergoes continuous structural rearrangements during the reset process. On each reset event the gap induced will have a certain thickness d_1 . While the partially formed CF will be separated from the bottom electrode by a gap thickness d_2 . In the next formation CF₁ will be favored for the formation only if $d_1 < d_2$. This condition is not always satisfied, especially considering millions of cycles. In fact, the reset transition is a thermal-assisted chemically activated process related to the energy dissipated in the reset i.e. it requires a formed CF and thus a current flow to occur. An originally incomplete filament (CF₂) is less sensitive to the reset process (as minimal current will flow through it). With continuous reset taking place on CF₁, CF₂ can then evolve into the favored CF for the set formation as the distance between CF₂ and the BE becomes lower than the one

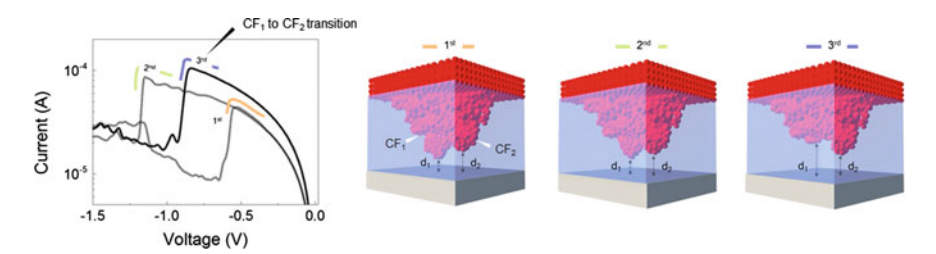


Fig. 6.3 Filament multiplicity model. Proposed model for the two-filaments instability. During the forming process, CF_1 and CF_2 attempted to grow in the Al_2O_3 . Finally, CF_1 connects and its morphology (filament's atomic structure) changes during cycles. Due to the structural changes in the CF_1 driven by the subsequent reset on the 3rd cycle CF_2 becomes the favored CF for the next formation leading to a resistance state variability associated with the potential fluctuation between the two CF_3

of (the reset) CF1. Figure 6.3 schematically show this effect over three consecutive cycles, of which the third shows a change in the LRS level. For cycles 1st and 2nd the rupture of the CF does not change the role of CF1 which is formed again on the subsequent set-step (this is also associated with a relatively similar $R_{LRS}\approx 20~k\Omega$, during the ON-state). On the 3rd cycle the reset is taking place at higher $V_{reset}\approx -1.4~V$ and it involves more power leading to a more pronounced reset of CF1. This results in a favored situation for CF2 to complete its formation on the next set-transition, that will show a new LRS value and potentially a different type of reset transition. This type of reliability threat is more pronounced in case of thin switching layer and prolonged endurance cycling. In fact, the CF formation is a self accelerated process due to the concentration of the E field lines on the CF which is more rapidly growing towards the bottom electrode. This leads to a large space between the CF connected and the others in case of a thick switching layer as also reported by TEM [8]. The space dramatically reduces for integrated devices and in combination to million of cycles the mechanism modeled in Fig. 6.3 can become relevant.

6.3 Stuck in LRS: A Cu Filament Degeneracy

Endurance failures are considered a major concern for any RS device, as they degrade the resistive window and reduce the device lifetime [2, 10]. Generally the endurance depends on many factors such as amplitude of the pulse, switching speed, read-out conditions and temperature [11]. One common type of endurance failure is the stuck in LRS often referred to as stuck-set. In this case the HRS resistance tends to decrease during the cycles until it reaches the same value of the LRS thus closing the RW (Fig. 6.1b). This is often referred as a RW collapse. In this section we provide some understanding on this failure and its physical mechanism by selecting a device stuck in LRS and using C-AFM tomography to study the morphology of the CF. To this end we select a cell and program it with 100 μ A C.C. until it does not show a stuck in LRS failure. Afterwards we use C-AFM tomography to study the morphology

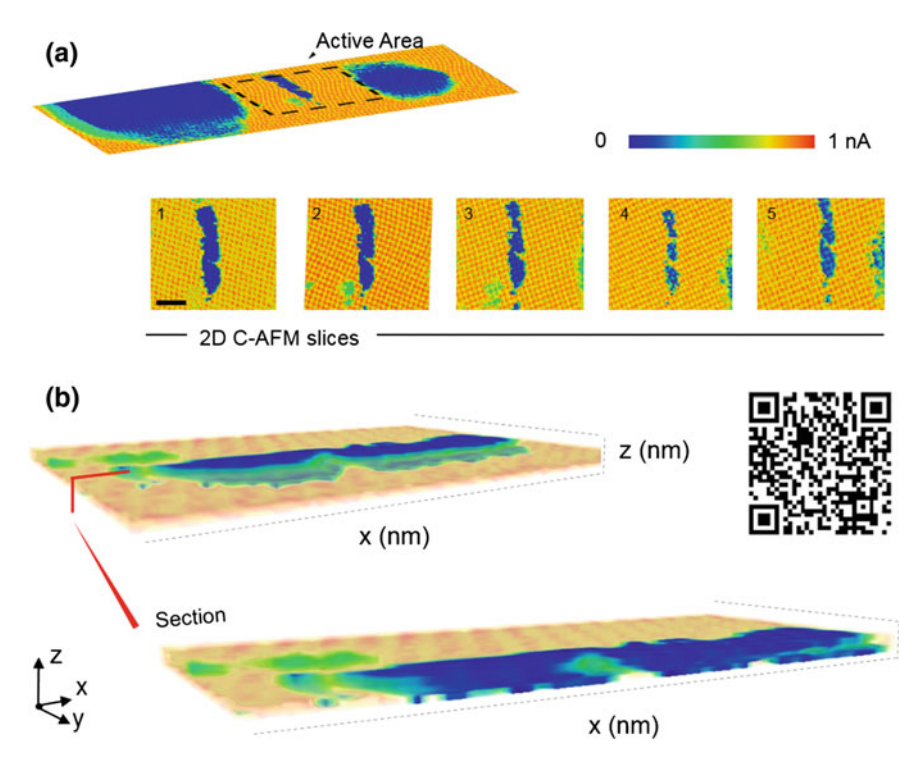


Fig. 6.4 Stuck in LRS filament observation. **a** 2D current maps of the device under test. Note after *top* electrode removal the CF appears as a large conductive platelet (scale bar 50 nm). **b** From the 3D tomogram it is possible to observe how the conductive filament degenerated into a continuous conductive wall. The latter shorts *bottom* and *top* electrodes and runs through the entire switching layer as shown in the sectional view. The animated cross-section of the tomogram is available by clicking here or by scanning the QR tag

of the CF. In our case the programming is done using DC cycles and not pulses. Figure 6.4a shows the dataset of C-AFM current maps, recorded in the cross-point memory element.

It is immediately evident that the CF is no longer a conductive spot occupying a fraction of the active electrode. The CF now appears as a long conductive platelet that runs through the entire device. This degenerated CF extends to almost the entire lateral dimension of the device (cell size $200 \times 200 \text{ nm}^2$). By observing the shape evolution of the CF within the oxide, three spots are visible in proximity of the bottom electrode (Fig. 6.4a). The 3D tomogram (Fig. 6.4b) suggests that the CF is constituted of three branches that have merged into a long and unrecoverable conductive platelet. The extension of this platelet is $\approx \! 150 \, \text{nm}$ and the three spots have an equivalent radius $\approx \! 12 \, \text{nm}$. It is clear that in this configuration the reset of the CF is impossible due to the absence of a single filament constriction or a localized point for the CF to break. In Figure 6.5 we schematically describe a possible scenario for such filament degeneration. From the previous section we know that multiple CFs formation is not

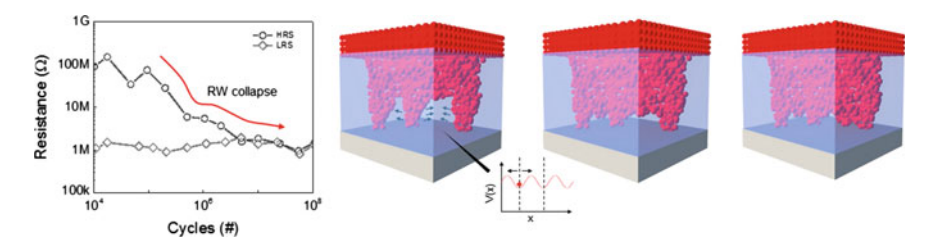


Fig. 6.5 *Stuck in LRS model.* RW collapse and schematic for the observation of Cu-platelet formation in stuck LRS device. Three original CFs join together inducing the failure. This can be related to an over injection of Cu coupled to a sideways diffusion during cycling

excluded and that during a prolonged cycling those CFs could alternate as connected CF. At the same time, the role of mechanical stress on ion migration has been often reported in CBRAM. Ambrogio et al. [12] have shown that compressive and tensile stress can appear in different regions of the solid electrolyte after filament formation. Compressive stress appears in proximity of the inert electrode, while tensile stress is observed close to the active electrode. At the same time, mechanical stress locally impacts the ion hopping resulting in a possible favored direction for the ion migration. In our case of in Fig. 6.5, the Cu platelet formation may be attributed to a thermal-activated diffusion of copper during repeated switching cycles. Due to the presence of multiple CFs, mechanical stress will be present into the electrolyte. As a possible result the ion migration will take place on a preferential direction due to local minima for Cu hopping as in the inset of Fig. 6.5. This combined to the prolonged cycling and other effects such as ions diffusion and electromigration can contribute to the size-degeneration of the CF and thus to the formation of a continuous Cu wall that does not allow any possible reset as schematically presented in Fig. 6.5.

6.4 Summary of the Chapter

In this chapter we have investigated the structural rearrangements of the CF induced by repeated cycling in CBRAM. Though the atomic structure of the CF was expected to undergo morphological changes due to the continuous movement of Cu atoms, the reality has shown a more fascinating scenario in which unexpected effects have appeared. Based on the observations of this chapter we can greatly enrich the range of physical mechanisms behind the resistance state variability and more in general of device failure in CBRAM. The observation of a multiplicity in filament branches could trigger the fluctuations in the LRS inducing the observed clustering in LRS values. This is particularly harmful at reduced dimensions of the solid electrolyte. Moreover, the presence of two/more competing CFs can explain the possibility for the same device to alternate abrupt and progressive reset transitions and potentially different HRS levels. The alternation of more filaments in a competing mechanism for the LRS formation, is identified as an undesired source of variability in memory cells leading to a serious reliability threat. The main impact of these phenomena

would be on the RW and the state stability. Similarly, for the case of stuck in LRS cell, the degeneracy of the CF due to Cu over injection is identified as a source of failure. An unrecoverable long conductive platelet is observed in the stuck in LRS device leading to the closure of the RW and the endurance failure. Also in that case the multiplicity of CF has probably been the root cause for the failure. Provided that the CF multiplicity is one of the causes of the observed variability in integrated devices, we expect that this can be reduced by aggressive scaling of the device (less room for two CFs to nucleate). Alternatively, a field-enhanced filament formation can mitigate the problem. This could be achieved for example by a cell design employing a tip-shaped electrode. However, the main conclusion is that a higher control of the resistive state can be achieved in case of a single CF operating in the device.

References

- H. Lv, X. Xiaoxin, P. Sun, H. Liu, Q. Luo, Q. Liu, W. Banerjee, H. Sun, S. Long, L. Li, M. Liu, Atomic view of filament growth in electrochemical memristive elements. Sci. Rep. 5, 13311 (2015)
- H. Lv, X. Xiaoxin, H. Liu, R. Liu, Q. Liu, W. Banerjee, H. Sun, S. Long, L. Li, M. Liu, Evolution
 of conductive filament and its impact on reliability issues in oxide-electrolyte based resistive
 random access memory. Sci. Rep. 5, 7764 (2015)
- F.M. Puglisi, L. Larcher, A. Padovani, P. Pavan, A complete statistical investigation of RTN in HfO₂-based RRAM in high resistive state. IEEE Trans. Electron Devices 62(8), 2606–2613 (2015)
- 4. D. Ielmini, F. Nardi, C. Cagli, Resistance-dependent amplitude of random telegraph-signal noise in resistive switching memories. Appl. Phys. Lett. **96**(5), 053503 (2010)
- A. Belmonte, W. Kim, B.T. Chan, N. Heylen, A. Fantini, M. Houssa, Senior Member, M. Jurczak, L. Goux, A thermally stable and high-performance 90-nm. IEEE Trans. Electron Devices 60(11), 3690–3695 (2013)
- N. Raghavan, R. Degraeve, L. Goux, A. Fantini, D.J. Wouters, G. Groeseneken, M. Jurczak, RTN insight to filamentary instability and disturb immunity in ultra-low power switching HfO x and AlO x RRAM 84(2012), 159–160 (2013)
- U. Celano, L. Goux, A. Belmonte, K. Opsomer, A. Franquet, A. Schulze, C. Detavernier, O. Richard, H. Bender, M. Jurczak, W. Vandervorst, Three-dimensional observation of the conductive filament in nanoscaled resistive memory devices. Nano Lett. 14(5), 2401–2406 (2014)
- 8. Y. Yang, P. Gao, S. Gaba, T. Chang, X. Pan, L. Wei, Observation of conducting filament growth in nanoscale resistive memories. Nat. Commun. 3, 732 (2012)
- Y. Yang, P. Gao, L. Li, X. Pan, S. Tappertzhofen, S. Choi, R. Waser, I. Valov, W.D. Lu, Electrochemical dynamics of nanoscale metallic inclusions in dielectrics. Nat. Commun. 5, 4232 (2014)
- B. Chen, Y. Lu, B. Gao, Y.H. Fu, F.F. Zhang, P. Huang, Y.S. Chen, L.F. Liu, X.Y. Liu, J.F. Kang, Y.Y. Wang, Z. Fang, H.Y. Yu, X Li, X.P. Wang, N. Singh, G.Q. Lo, D.L. Kwong, Physical mechanisms of endurance degradation in TMO-RRAM. IEDM Tech. Dig. 283–286 (2011)
- Y.Y. Chen, R. Degraeve, S. Clima, B. Govoreanu, L. Goux, A. Fantini, G.S. Kar, G. Pourtois, G. Groeseneken, D.J. Wouters, M. Jurczak, Understanding of the Endurance Failure in Scaled HfO 2 -based 1T1R RRAM through Vacancy Mobility Degradation, pp. 10–13 (2012)
- 12. S. Ambrogio, S. Balatti, S. Choi, D. Ielmini, Impact of the mechanical stress on switching characteristics of electrochemical resistive memory. Adv. Mater. 26(23), 1–8 (2014)

Chapter 7 Conclusions and Outlook

Science never solves a problem without creating ten more
—George Bernard Shaw

A broad study on the physical mechanisms of filamentary-based resistive switching has been presented. Filamentary-based resistive switches represent an intriguing emerging class of electronic devices, with potential applications in future memory and logic. Based on ions migration and solid state electrochemical reactions at the nanoscale, their study is an exiting challenge for the scientific community. Relying on a wide range of experimental results, we have clarified the formation and rupture mechanisms of Cu- and V_a -based filaments. Fundamental studies using C-AFM have been combined to the results of integrated devices in order to transfer the understanding from a purely physical to a functional-applicative framework. Finally, this PhD work has proposed a novel three-dimensional analysis methodology (scalpel SPM) that has allowed for the first time the 3D observation of the CFs in state-of-theart devices. This approach, that extends SPM for the analysis of confined volumes, employs a pioneering combination of sub-nm tip-induced material removal with contact-mode AFM techniques. A general comparison on CBRAM and VCM is combined with conclusions, challenges and potential future works in this closing chapter.

7.1 Filaments Formation and Dissolution

This dissertation has focused on the physical mechanisms and metrology of filamentary resistive switching. In order to understand how the filaments' growth and dissolution occur we have developed an experimental study using C-AFM whose outcome can be summarized as follow:

The AFM tip has been used as a virtual electrode on thin (3 nm) oxide blanket samples. Switching functionality has been successfully demonstrated on Hf/HfO₂/tipand Cu/Al₂O₃/tip-structures. This has enabled the study of RS on blanket samples constituting of two or three layers in total. Different C-AFM conductive tips were investigated in order to gain insight on the role of the tip in RS. By tuning the tip parameters (e.g. tip radius and tip resistance) we have matched the device operation with the tip-induced switching (on blanket samples). The latter has been achieved for high and low programing current (5–200 µA) by tuning either tip resistance and tip radius. The tip-induced CFs have shown cyclability up to hundreds of cycles. We have developed a dedicated evaluation method to estimate the effective electrical contact size of the C-AFM tip. Values below 10 nm² are consistently observed, thereby confirming the strong scaling potential of RS in the sub-10 nm² cell dimensions. This is attributed to the formation of filaments of reduced size and increased R_{LRS} resistance as experimentally induced and observed with C-AFM (Chap. 4). In fact, filaments with diameter of a few nanometers have been consistently formed, dissolved and observed. Moreover device data, C-AFM and analytic I-V fitting have been combined. By using the high spatial confinement of the AFM tip, conductivity and shape of the induced filaments have been experimentally related to the structural rearrangements occurring from cycle-to-cycle in the CF. On consecutive formations, the CFs presented similar sizes and different conductivity, thereby indicating the crucial role of the portion of the CF buried inside the solid electrolyte. Aiming to relate the understanding gained on blanket samples to the integrated devices, we have successfully developed a tip-induced material removal technique to access the switching layer in a MIM devices. This approach is sometimes referred to as cell de-process, and uses a diamond tip to physically erode material by scanning the AFM tip at high load force. This methodology has allowed to physically scrape material with removal rates in range 0.1–10 nm/scan and has been successfully applied to TiN, Au, Cu and Ti. These results increase the understanding required for the integration of this technology for high density storage applications.

CBRAM versus VCM—whenever possible, the list of experiments reported in this dissertation have been applied to both CBRAM and VCM enabling a direct comparison. Cu- and V_o -based filaments show scaling potential in the sub- $10\,\mathrm{nm}^2$ dimensions as their RS functionality has been demonstrated and imaged with C-AFM. After the formation of the filaments we have consistently observed spot sizes $<100\,\mathrm{nm}^2$ (Sect. 4.1.5). However, the filament resistance was generally high (\approx M Ω) and thus showing on a reduced CF stability. Cu-filaments show a better stability as compared to the V_o -based. In fact, we could observe the evolution of the CFs as function of time for CBRAM but not for VCM, whose CFs turn into poorly conductive as soon as the C-AFM tip is removed from the point contact (Fig. 4.8). Despite the differences between the standard MIM and AFM-induced operations, our observations indicate an improved stability for the CF in CBRAM. This can ultimately confer to this technology higher tolerance to a simple integration scheme as compared to the VCM devices that requires a strong oxygen passivation and care for potential etch-induced cell damages.

Leveraging the nanoscaled contact provided by the tip, we have studied the ultra-scaled reset phenomena. The analytical fitting of tip-induced I–V characteristics provided insight on the reset mechanisms (for both Hf/HfO2 and Cu/Al2O3). The formation of a tunnel gap (\approx 0.9 nm) after the reset of Cu/Al2O3/tip-structure has been consistently observed. Whereas the reset in the Hf/HfO2/tip-structure has been successfully described by the modulation of a reduced amount of defects (<20) in a quantum-point-contact. These results indicate that although both classes of RS events are based on ion hopping, in CBRAM the ions build a CF inside the empty space available in the solid electrolyte and therefore at reset the oxide still presents a tunnel barrier in correspondence of the filament withdrawal. While in VCM, a percolative path is build by a local valance change in the oxide (at forming) and this will only partially recover during reset leaving behind a defected HfO2.

Using our tip-induced material approach we have removed the top electrodes of CBRAM and VCM capacitor structures. By exposing the buried oxide in the MIM devices, we have observed highly conductive spots in the case of LRS devices while reduced conductivity is observed for the HRS in both technologies. Although this unambiguously confirmed the filamentary nature of RS and provided a link between our tip-induced experiments and CFs in capacitor structures, the analysis was still limited to a two-dimensional (2D) observation. Moreover, due to the reduced dimensions of the top electrodes in the VCM case ($5 \times 5 \,\mu\text{m}^2$), the C-AFM had to be used also for the electrical programming of the cells. The latter did not allowed the application of any current compliance during forming and cycling, making clear the need for a more controlled programming of the CFs prior to the C-AFM analysis.

7.1.1 Challenges with Tip-Induced Analysis

Although the C-AFM has demonstrated a remarkable flexibility in the analysis of RS on blanket samples, some limitations to this approach have clearly appeared.

The tip as electrode—The sharpness of the tip apex induces a strong electric field confinement coupled with a radial distribution of the field lines. The latter is responsible for an increase in the electroforming voltage required when using C-AFM. In some cases, the electroforming voltage reaches unacceptable values for the film integrity. This is due to tip-induced surface modifications that appear for the extremely high current densities involved. As a consequence, oxide thicknesses over 3 nm are generally difficult to be switched without degrading the surface morphology.

C-AFM electrical characterization limitations—The current design of commercially available tools show severe limitations for the electrical analysis. The application of pulsed signals or voltage constant stress are not allowed. Furthermore, the dynamic range of traditional sensors (Chap. 3) is limited to few μA . In some cases, more flexibility would be required for the biasing scheme of tip and sample. For example, it would be important to decouple the tip motion and sample biasing in order to achieve a stable tip-sample configuration during the electrical characteri-

zation. For certain applications it would be relevant to program a series of voltage ramps to apply in sequence. For most of these features one needs to apply custom solutions indicating some room for improvement in the present tool design.

Filament nucleation nonidealities—Since the tip acts as a movable electrode, the CF nucleates on the same tip that is used to scan the surface. Due to the extreme sensitivity of the CFs to possible adsorbed contaminants such as moisture, surface roughness and residual OH⁻ groups (acting as counter charges), the tip-induced CFs are generally unstable and their conductivity tends to decrease with time (Chap. 4). This creates a problem with the CF stability and therefore for the observation. Independently from the analysis conditions (air, nitrogen or high vacuum) we have consistently observed this effect that represents an important difference between tip-induced and CFs induced in cells with fixed electrodes.

Tip position stability—Although the modern piezo crystals employed in AFMs can guarantee \approx Å precision when held steady in point contact, small sub-nm tip displacements during the point-contact voltage ramp could be detrimental for a precise sensing. We have calibrated the electrical contact area under our measuring conditions (Chap. 3) and obtained a value in range of few nanometers squared. In other words, if one is interested to induce locally hundreds of switching cycles with the AFM tip, the tip will likely experience a slight lateral drift from the nominal point of contact. This could determine a possible loss of contact with the CF. In addition, for some AFM systems the repeated voltage ramps require a continuous tip contact withdrawal, this will certainly affect the next tip approach leading to drifts in the tip positioning. Such type of issues have to be taken into account when considering tip-induced switching stability.

7.2 Filaments 3D Observation

Aiming to characterize the CF in 3D, we have refined our tip-based material removal technique to achieve the 3D analysis of confined volumes. By applying high pressure on the cantilever sub-nm control in the material removal is successfully achieved. In essence, we collect 2D conductive profiles of the sample at different heights and we interpolate them for the 3D observation. This has extended successfully SPM into the quantitative characterization of confined volumes in $\approx\!100\,\text{nm}^3$ range. Furthermore, this method (scalpel SPM) can be applied to a fully fabricated device in a reverse engineering fashion and therefore it can be used in a large variety of applications and device geometry.

Based on scalpel SPM we could investigate for the first time in three-dimensions the CF in state-of-the-art CBRAM and VCM devices. The LRS and HRS states have been successfully investigated for devices that have been electrically programmed using the 1T1R configuration. The observation of the CF shape has been important to clarify the nature of the rate limiting processes in the CF growth. The dependence

of CF morphology with the programming current has been used to investigate the nature of the switching mechanisms and the multibit capability for each technology.

By leveraging our scalpel SPM for the single device analysis, we have investigated two major failures of CBRAM. Resistance state variability due to the filament multiplicity and the stuck in LRS have been directly investigated. We have identified the presence of multiple CFs as a major source of instability and failures. In fact, during the electroforming multiple CFs can attempt to form. This is admitted by the theory and often experimentally observed. While this effect does not represent a problem in large structures with thick switching layers, it has a severe impact on devices based on thin oxides. When more CFs attempt to form, there is a nonzero probability that different CFs will become favored for the formation over millions of cycles. This parasitic formation leads to the resistance state instabilities and degradation of the memory read margins (Chap. 6). In some cases, the degeneracy of the same effect can lead to a catastrophic failure of the device if during cycling multiple CFs cause an over injection of Cu ions and thus an unrecoverable LRS.

CBRAM versus VCM—the observation of a conical shape for the Cu-filament in LRS has been important to determine the cations migration as the rate limiting process during the filament formation. While the size dependence of the Cu-filament with the programming current has related the volume of Cu to the filament resistance (for applications such as multilevel bit storage). The observation of broken and nonbroken filaments in the HRS of CBRAM allowed us to explain the observed dual nature of the reset transition. The latter has been supported by the analytical fitting of the I–V characteristics describing the erased filament as either a tunnel-barrier or a quantum-point-contact. We were able to model broken and non-broken filaments based on Cu-volume considerations for both cases. The existence of the two filament shapes (tunnel barrier versus QPC) can now be explained within one dissolution theory whether the starting point (i.e. the original size of the CF and its volume) would determine the final shape. In fact, if few ions will constitute the CF due to a limited ion mobility in the switching layer, the tendency will be toward abrupt type of reset. While in case of fast ion mobility in the solid electrolyte the induced CFs show the QPC behavior as they will be likely constituted of more atoms. This also implies that one can think to induce one or the other reset transitions in a device by modulation of the ion mobility in the solid electrolyte.

The direct observation of the filament in the oxide-based VCM has shown a conical shape with the narrow part close to the oxygen inert electrode (TiN). This indicates that the Hf capping layer is actively providing a defect reservoir to the CF formed in the HfO2. Interestingly, although formed at $200\,\mu\text{A}$ we could observe CFs with diameter of a few nanometers. However, we have consistently observed a dependence of the CF constriction size with the programming current. The latter provides a strong experimental evidence that the CF in this material system behaves like a defects modulated quantum-point-contact.

The volume of the filaments is smaller for VCM as compared to the Cu-filaments, as result of two distinctive filament formation processes. In fact, while in CBRAM the hampered migration of Cu ions induces a wide-base conical shape for the CF, in VCM

the generation of V_o in the HfO₂ as an intrinsic defect of the oxide is preliminary to join the defects reservoir with the counter electrode therefore limiting the lateral growth of the CF. This is supported by our observations of VCM filaments induced at different programming current (Fig. 5.17). However, despite the differences in the CFs' volume, our observations indicate that both technologies can be scaled below $10\,\mathrm{nm}^2$. Indeed in both cases the limiting factor for the resistive switching is the filament's constriction, that has been consistently found smaller than $10 \times 10\,\mathrm{nm}^2$.

7.2.1 Challenges in the Three-Dimensional Observation

Scalpel SPM has enabled for the first time the direct three-dimensional observation of the CFs in scaled RS devices. However, some limitations have appeared using this approach and can be summarized as follow:

SPM tomography is destructive—Being based on the collection of multiple 2D slices of the sample at different heights, scalpel SPM is a destructive technique. After the analysis a crater of the same size of the scan area is formed. The major limitation is the impossibility to observed dynamic transitions, e.g. repeated switching events inside the same device by means of this approach.

Tip degradation due to the electrode removal—One of the main advantages of using scalpel SPM for the filament observation lies in the possibility of a controlled electrical programming which is assigned to the 1T1R configuration using a semiconductor parameter analyzer. However, after the electrical programming the top electrode has to be removed. This is generally a metal layer thick few tens of nanometers and has to be removed by the tip-induced pressure assisted mechanical material removal (similar to the rest of the slicing). To limit the tip degradation, in this phase the load force applied to the cantilever is kept moderate (few hundreds of nN) which often leads to a long time for the removal of the top electrode. In some cases this problem can be avoided by changing the top electrode material, as we did by replacing TiN with Ru in VCM (Chap. 5). However, this represents a current limitation for our scalpel SPM leading to a time consuming operation.

Limited yield in scalpel SPM—Being based on a tip-induced pressure-assisted material removal, scalpel SPM requires an accurate selection of the load force for the material removal. Since every tip-sample combination will require a slightly different amount of load force for a progressive material removal, it is very common to overestimate the load force and destroy the sample during the slicing phase. Furthermore, as the tip will apply the same pressure in each point on the scan area, in case of anisotropies such as roughness or voids in the material, the exerted pressure can be too high and thus destroy the layer during the slicing. For this reason in the current design our scalpel SPM has a poor yield often requiring multiple attempts for a successful characterization.

7.3 Outlook

To date, it can be said that the switching mechanisms in both VCM and CBRAM are fairly well understood. With the present work and many other studies also the direct observation of the conductive filament has been extensively treated. Great progresses have been achieved in the device performance (Chap. 2) and a complete 3D observation of the CFs is now available. However, there is still ample room for investigation with C-AFM in this field, as many interesting questions are still pending:

What is the smallest achievable RS device?

Concerning the switching process it would be important to explore the ultimate scaling limit of RS as physical mechanism. Not only in terms of lateral dimensions but also from the standpoint of the minimum oxide volume required for a working device. C-AFM has contributed to answer the question on lateral dimensions and could contribute also in the case of minimum oxide thickness requirements. A possible experiment could be designed by controlling the material removal on a blanket HfO_2 thin film. Using our tip-induced material removal method a staircase structure could be fabricated with sub-nm steps (Fig. 7.1a). By this design, one could locally investigate the RS as function of the oxide thickness to clarify the appearance of threshold switching (Chap. 4) or the transition of RS into tunneling current when the device sizes reach their ultimate scaling. This approach would allow to investigate devices constituted of $\approx 5-10\,\mathrm{nm}^3$ of total volume, which are currently unaccessible dimensions for the lithographic technology. Figure 7.1a shows a schematic of the aforementioned experiment.

What is the electrical interaction filament-apex and electrode?

Now that the shape and size of the CFs are known, it would be important to study the electrical interaction between the weakest part of the CFs (i.e. constriction) and the electrodes. Of particular interest would be the analysis of the narrowest part of the CF as this is the venue of important modifications when the device operates. C-AFM represents a potential solution to this type of measurement, by using a constant voltage measurements after the tip-induced CF formation. A tip-based random telegraph noise (RTN) study could be considered to understand better the types of interactions that occur in the CF during formation, read-out and reset. By placing the tip directly on top of the CF and then in its close proximity RTN signals could potentially reveal more about the electrical fingerprint of the CF. The same type of study could be applied in a pre-electroformed stage to understand the defects generation on at the nanoscale using the C-AFM tip to identify the types of traps actively contributing in the CF formation. C-AFM can effectively enhance the analysis by limiting any foreground noise generally presents in larger cells. Figure 7.1b shows a schematic of the aforementioned experiment.

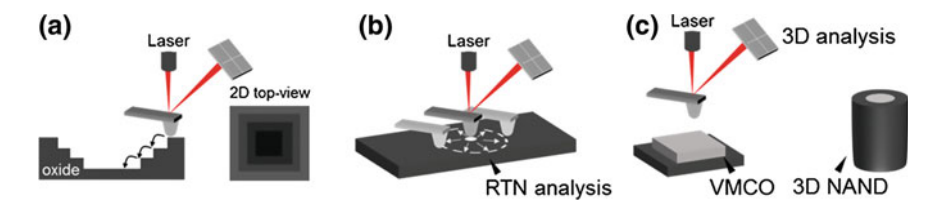


Fig. 7.1 Future works. **a** C-AFM in combination with the controlled material removal could allow the sampling of virtual devices below $10\,\mathrm{nm}^3$, to understand the ultimate scaling potential of RS. **b** The study of RTN during and after filament formation with C-AFM could allow a deep understanding of the interactions between the CF-apex and the electrodes. **c** Two potential applications of scalpel SPM for memory devices in the field of VMCO and 3D NAND

What happens in a stuck-in-HRS failure event?

As previously introduced commercial applications require a full understanding of failures and of the device reliability. It is generally accepted that the stuck in LRS failure is due to the hard breakdown of the switching layer. While less is known abut the opposite type of failure. It would be possible by scalpel SPM to study in 3D the CFs of stuck in HRS devices for CBRAM and VCMs.

Where else scalpel SPM would be applicable?

The possibilities enabled by scalpel SPM are manifold as it can be applied in the fundamental studies on material characterization up to reverse engineering. Remaining in the field of solid state memory, two immediate applications which can follow this PhD work are for the vacancies modulated conductive oxide VCM (VMCO) and for 3D NAND as in Fig. 7.1c. VMCO is an alternative to filamentary based RS and it is based on the area-scalable resistive switching (though to be) triggered by the collective motion of V_o is in certain material systems. To date, there is no direct observation of the switching mechanisms and scalpel SPM could be applied for (1) the direct observation of the areal switching effect. (2) The 3D analysis of the conductive oxide would clarify if VMCO is based on bulk or surface effects. And (3) relate the programming conditions to the change in the conductivity of the conductive oxide. The other potential test bench of scalpel SPM is 3D NAND, this is the replacement of the planar Flash technology. It relies on a vertical channel transistor, created with a gate-last fabrication approach. The latter introduces a lot of defects and nonidealities in the conductive properties of the vertical channel. The conduction properties inside the channel could be investigated more in detail using scalpel SPM. In particular by studying the transport into the channel in 3D while changing the bias to the vertical gate would provide a deep understanding on the conduction during the programming operations and thus direct the future device engineering.

7.3 Outlook 159

7.3.1 Improving Scalpel SPM

The present implementation of SPM tomography is based on the usage of a commercial SPM-system by means of a single in-house fabricated diamond tip. The latter is currently used for the material removal as well as for the probing. This imposes severe limitations to our current approach:

- To limit the tip wear during scalpel one must limit the load forces which leads to slow removal rates and long analysis times.
- Being confined to one single (diamond) tip prevent the usage of functionalized tips limiting other applications, such as magnetic coatings for magnetic force microscopy (MFM) to study magnetic memory or spin-based devices.
- Physical contact between tip and sample is required to remove material implying
 that we are restricted to contact-based AFM modes. Non-contact or intermittent
 modes e.g. tapping or peak-force are not possible although they would allow MFM,
 PFTUNA or KPFM, thus broadening the range of observable material properties.

These limitations could be overcome through the design of a dedicated scalpel SPM system. Three potential future designs are proposed in Fig. 7.2. A dual head AFM system with one tip for material removal and one tip for sensing (Fig. 7.2a). The decoupling between the scalpel and sensing function could dramatically improve the tomographic performance, reduce the measurement time and increase the range of applications of our technique. Compared to the existing SPM tomography, the novelty in this new design is the use of a movable stage operating with nm-scale precision for the sample movement thus allowing an alternation between the eroding and the sensing AFM scans (Fig. 7.1a). The first tip removes the material using our current

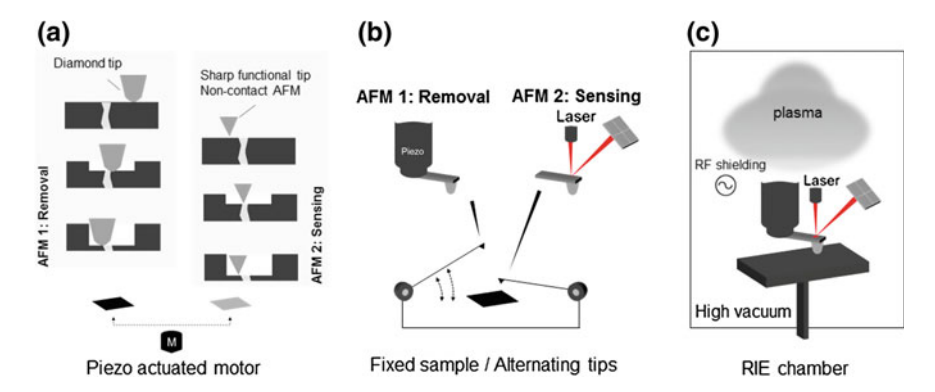


Fig. 7.2 Scalpel SPM three possible future designs. **a** Dual tip approach based on a movable stage, to alternatively position the sample under a removal tip (diamond) and a sensing tip. **b** Dual tip approach based on a fixed stage and two movable AFM heads. The two tips are alternated onto the sample surface for a coordinated removal and sensing. **c** Using a dry etching chamber, a compact AFM system could be use for probing at different stage of the etching process to achieve a 3D tomography using a dry etch for the material removal

approach, while the second tip could use any desired AFM modes. This combination allows to probe the sample faster at ever increasing depths (Fig. 7.1a). The technical challenge is that the stage that moves the sample between the two AFM heads has to provide a motion precision in the order of nanometers over centimeters distances. This could be accomplished by a combination of accurate motor-driven positioning and corrective software algorithms (drift correction algorithm) leading to an accurate sample positioning between the two phases. Note, that by using a two head approach, the acquired AFM profiles of the sensing tip can provide a wide range of material properties e.g. resistance, conductivity, hardness, adhesion, magnetic and surface potential. Another possibility to enable the same result is reported in Fig. 7.2b. Here the sample is maintained in a fixed position while two AFM heads are alternatively placed onto the analysis area. The latter can be achieved by positioning the AFM heads on two rotational joints which can be automated to alternatively be raised and lowered on the same scan area. In this configuration the AFM dedicated to the material removal could be implemented by an ultra-flat piezo-actuated scanner that allows only contact AFM but reduces the overall design complexity. The second AFM head could be based on a standard 4-quadrant photodiode design. Alternatively, another possibility is to achieve the nm-precise material removal without the tip-induced approach, in this case multiple scenarios are possible and some have been already explored (diamond blades or wet etching). Here we report an original solution still unexplored, represented by the combination of an AFM into a dry etch chamber Fig. 7.2c. Both plasma and reactive ion etching have demonstrated to be selective, uniform and operating with reduced etch rate (below 10 nm). The AFM scans could be alternated by dry etch in order to achieve the slice-and-view method. One can even imagine to use a RF biasing scheme on the tip to create directional electric fields and achieve a tip isolation during bombardment to avoid tip degradation due to the ion bombardment. Each of the three proposals allows the 3D mapping of the samples in an elegant slice-and-view solution. The 3D data analysis of confined volumes (below 100 nm³) is widely accepted as one of the main area of development for semiconductor R&D in the coming 10 years. As such the implementation of an automated scalpel SPM system will have a strong impact on the semiconductors industry and potentially in many more fields.

Appendix A Cellulose Nanopaper Memory

A.1 Cellulose for Memory Applications

Cellulose nanofibers are mainly produced from the plants, and therefore the high availability of cellulose in nature makes the cost of this material remarkably inexpensive. The applications for nanopaper go from roll-to-roll fabrication up to production of flexible electronic for displays, solar cells, OLED, flexible and wearable electronics [3, 4]. Paper-based electronics is an emerging and interesting new research area. In this appendix we describe the fabrication of a memory device based on the CBRAM operative principles using cellulose. The paper-based memory candidate requires remarkable performances and simple fabrication process. Due to its simple fabrication, the CBRAM architecture can be used also for the paper-based memory devices. We believe that CNF is an attractive material for the following major reasons: (1) it is abundantly available in nature and therefore low cost. (2) It is biodegradable because it is extracted from plants. (3) It shows attractive properties such as foldability, transparency and flexibility. (4) It shows excellent prospects of scalability as we demonstrate with resistive switching using a single cellulose nanofiber. In this appendix, we first demonstrate, the usage of cellulose nanofibers as a functional material for nonvolatile Si-based resistive switching devices. Next, we fabricate a cost effective and environmental friendly memory device starting from a transparent CNF sheet. The memory device shows high resistance ON/OFF ratio $(>10^6)$, good retention and multilevel capability. Finally, by means of Peak Force TUNA (PF-TUNA) we investigate at the nanoscale the mechanical and electrical properties of single cellulose nanofibers. We fabricate the MIM structure constituted of Ag/Cellulose nanopaper/Pt as in Fig. A.1a. We deposited 100 nm Pt film with 5 nm Ti adhesion layer on a Si-substrate to serve as bottom electrode. The nanopaper is deposited by dropcasting technique to act as switching layer of thickness 50 nm [5]. Finally 100-nm thick Ag top electrodes are deposited and patterned by means of a metal mask. Figure A.1b shows the surface of the nanopaper layer before top electrode deposition. Inside the nanopaper, tiny nanofibrils smaller than 4nm combine into bundles 15–20 nm of nanofibers [1]. These cellulose bundles composed of longer

molecules, are laterally stabilized by hydrogen bonds forming crystalline domains [6]. This inner structure provides to the CNF paper good mechanical strength, not flexibility, heat transfer properties and low thermal expansion coefficient [6]. The fibers-like structure of the nanopaper can be seen in the atomic force microscopy image (Fig. A.1c). The elastic modulus is reported in Fig. A.1d where the bright regions represent stiffer areas in the whole sample surface. Figure A.1a presents the current-voltage (I–V) curves for a $100 \times 100 \,\mu\text{m}^2$ cell measured in air at room temperature. The measurement is conducted by a dc voltage sweep mode where the bias is applied to the top electrode (Ag) while the bottom electrode (Pt) is grounded. During the operation the internal current compliance of the semiconductor parameter analyzer is kept at 1 mA. All devices show clear bipolar switching memory characteristics, associated with the memristive hysteresis. Pristine Ag/CNF/Pt-cell shows an initial low resistance state, which suggests an in diffusion of Ag during deposition. A sudden decrease in current is observed during the negative sweep indicating the recovery of the high resistive state (HRS). Afterwards the device can be cycled between HRS and low resistive state (LRS) as shown in Fig. A.1a. The increase in current during positive sweep indicates that the resistance changes into LRS. The LRS is kept until the negative voltage is applied. During the negative voltage sweep, the resistance state goes back into high resistive state (HRS) at \approx -0.2 V. To evaluate the nonvolatility, the retention property is characterized under a readout voltage of 0, 1 V. A significant OFF/ON ratio as large as $\approx 10^4$, with stable retention is reported for our Ag/CNF/Pt devices as shown in Fig. A.1b. In Fig. A.1c we report the endurance for 60 continuous cycles (Fig. A.2).

Next we take advantage of the mechanical properties of the cellulose nanopaper to replace the Si-substrate in our devices. Thus the nanopaper has a twofold use: first, it is used as a transparent substrate. Second, it is used as a solid electrolyte for the nonvolatile resistive switching. Figure A.3a shows the 30 μ m thick nanopaper used as substrate. The surface morphology of the CNF-sheet shows similar properties as compared to the material deposited by drop-casting technique (inset Fig. A.3a). The root mean square (RMS) of the surface roughness is \approx 20 nm for a 10 μ m² which ensures the use as substrate. The device structure of the memory cell, is presented in the inset of Fig. A.3c. Noteworthy on the volume basis, 99.3% of our device is

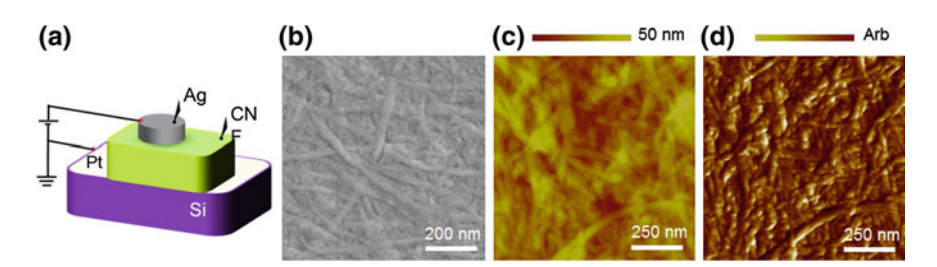


Fig. A.1 A cellulose-based CBRAM. **a** Schematic of the device structure. Cellulose nanopaper is used as switching layer. **b** SEM image of the cellulose nanopaper after deposition. **c** AFM topography and **d** elastic modulus of the cellulose nanopaper after deposition

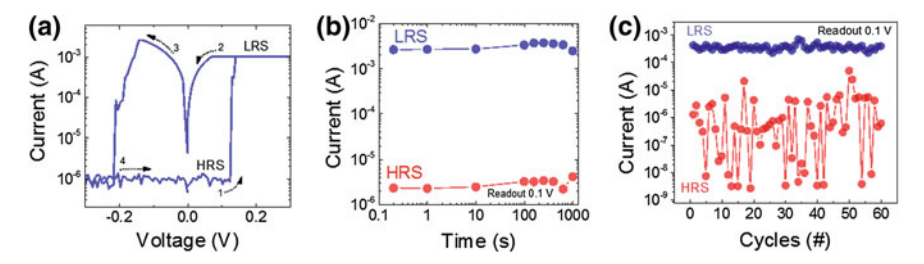


Fig. A.2 Cellulose-memory electrical characterization. a Typical I–V curves for a $100 \times 100 \, \mu m^2$ Ag/CNF/Pt device. The bias is applied in voltage sweep mode. 1 mA current compliance is imposed to the device for positive sweep to prevent the electrical breakdown of the cell. b Retention characteristic for HRS and LRS under readout voltage of 0.1 V. In the *inset* endurance characteristic of 60 consecutive cycles

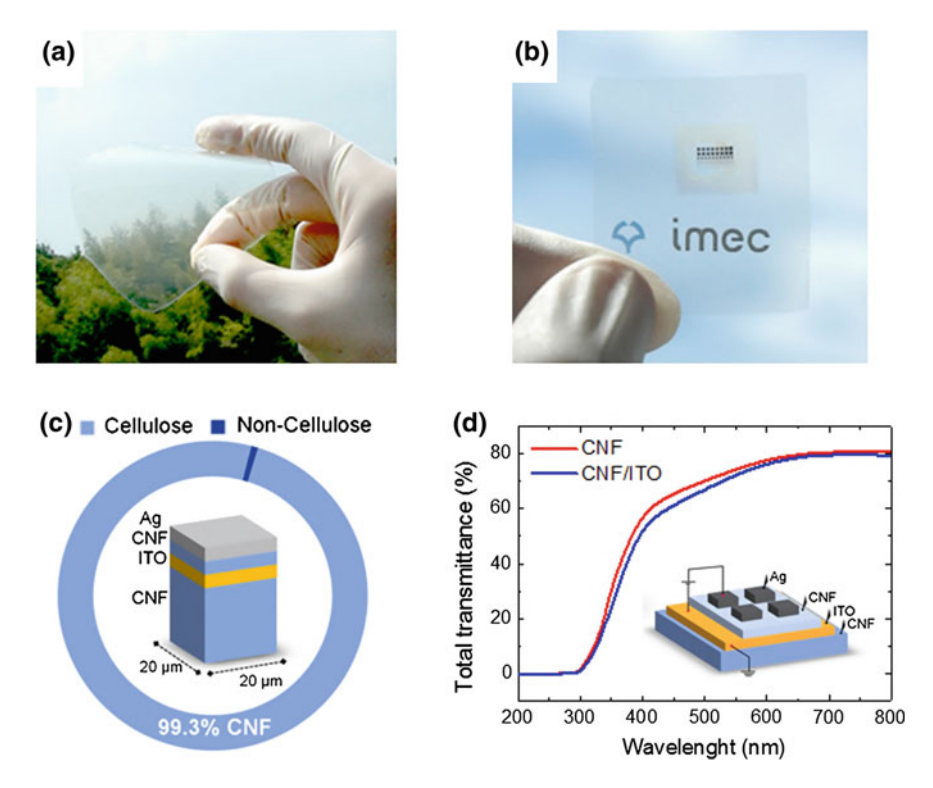


Fig. A.3 Cellulose-on-cellulose memory. a Specimen of CNF paper, used as substrate with a thickness of $\approx 30\,\mu$ m. In the inset the AFM image of the surface. b Optical image of device structure after fabrication. c Volume calculation of cellulose content in our device. d Total light transmittance of CNF substrate before (red line) and after (blue line) ITO/CNF deposition. In the inset device structure of CNF-based memory cell

composed of CNF. Conductive 100 nm-thick indium tin oxide (ITO), is deposited on CNF substrate as bottom electrode. A second layer of CNF ≈100 nm is deposited onto the ITO and used as switching layer. Finally, 100-nm thick Ag top electrodes are deposited and patterned by mean of metal mask. The optical image of the final Ag/CNF/ITO-cell is shown in Fig. A.3b. In Fig. A.3d we compare the optical transparency of the nanopaper before and after ITO/CNF deposition. In Fig. A.3d the total transmittance of the nanopaper is measured in 200-800 nm wavelength range. The transmittance of the device within the visible range is >60%, and the influence of ITO and CNF on transmittance is rather small. The measured value is $\approx 80\%$ at a wavelength of 590 nm [1]. Figure A.4a presents the current-voltage (I–V) curves for a $100 \times 100 \,\mu\text{m}^2$ cell measured in air at room temperature. The measurement is conducted by a dc voltage sweep mode whereby the bias is applied to the top electrode (Ag) while the bottom electrode (ITO) is grounded. Contrary to the Si-based device, pristine Ag/CNF/ITO-cell shows an initial high resistance state. As commonly observed for RRAM devices, the initial sweep requires a relatively higher voltage than cycles, e.g. ≈1, 5V (black line Fig. A.4a). The sudden increase in current during positive sweep indicates that the resistance changes into a low resistive state (LRS). LRS is kept until the negative voltage is applied. During the negative voltage sweep, the resistance state goes back into high resistive state (HRS) at ≈ -0.5 V. To evaluate the nonvolatility of the Ag/CNF/ITO-cell, the retention property is characterized under a readout voltage of 0.1 V. High resistance ON/OFF ratio (>10⁶) and good retention are shown in Fig. A.4b. Both HRS and LRS present no clear changes for more than 10⁴ s. The wider resistive window observed as compared to the Si-based device is the result of the thicker CNF layer in combination with the ITO which may partially act as an extension of the switching layer. In order to take full advantage of the wide open resistance window, we investigate multilevel resistive switching in our CNF-based devices. The capability of storing multilevel resistance states in a single memory cell is one of the most important requirements for next generation nonvolatile memory because it can dramatically enhance the memory density. It is known for RRAM devices that the different current compliance levels during the cycling operations can be utilized in order to achieve clearly distinguishable resistance states in LRS. Figure A.4c shows the resistance data using three different current compliances (50 µA, 500 µA, 1 mA). The result shows very distinctive three-level resistance states, each associated to different programming conditions. Retention characteristics for each state are recorded at 0, 1 V readout voltage and presented in Fig. A.4d. All resistance states are stably maintained for 10³ s without degradation. The flexible operation of CNF-based memories is treated elsewhere [5]. Thus CNFs device shows robust nonvolatile resistive switching effects. We suggest a switching model based on an electric-field driven and thermally activated hopping of Ag ions responsible for a redox-induced Ag metallic filament formation and rupture. In case of CNF we consider that the structure of the cellulose nanofibers has a major role in the cation migration. In particular, the presence of water and the fiber-like composition are believed to enhance the ionic transport properties of the mobile species during the device operations [7]. The latter has an impact in the low forming voltage observed (below 2 V) and on the wide OFF/ON ratio reported. Finally, we investigate

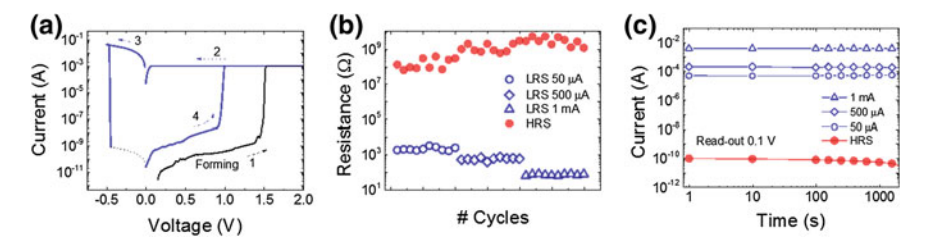


Fig. A.4 Cellulose-on-cellulose electrical characterization. **a** Typical I–V curves for a $100 \times 100 \, \mu m^2$ Ag/CNF/ITO device. The bias is applied in voltage sweep mode. 1 mA current compliance is imposed to the device for positive sweep (black and blue) to prevent the electrical breakdown of the cell. **b** Multilevel capability demonstrated for different current compliance (50, $500 \, \mu A$, 1 mA). **d** Retention characteristics for multilevel states under readout voltage of 0, 1 V. **c** Retention characteristic for HRS and LRS under readout voltage of 0, 1 V

the ultimate scaling of resistive switching using cellulose. We deposited cellulose nanopaper on a Si-substrate previously coated with Ag (Fig. A.5a). We have used a low concentration of cellulose to achieve the deposition of individual bundles of cellulose. The fibers are 50-80 nm in diameter and can reach several micrometers in length (Fig. A.5b). The fibers can easily be localized thanks to their characteristic mechanical and electrical properties. Their elastic modulus is lower than the surrounding material (Ag) and electrically they behave like insulators as shown in Fig. A.5d, e. The conductive tip of the AFM is exploited in order to create an ultra-scaled AFMtip/cellulose/Ag-cell (inset Fig. A.5f). The conductive AFM-tip is grounded and the bias is applied to the Ag electrode. In this configuration the resistance of the tip is the only element providing a limitation to the current flowing during cycling [8]. Highly resistive tips are used in order to achieve a current compliance of few µA. We observe a reproducible resistive switching locally induced in the cellulose fiber. The tip/cellulose/Ag-cell can be repeatedly cycled over 20 cycles (Fig. A.5f) with low operative current ($<10\,\mu\text{A}$). Nevertheless, due to the dissipation of heat and to the high current density we also observe a structural degradation of the cellulose after tip-induced cycling.

In summary, this appendix has reported on resistive switching using cellulose nanofibers. We have designed CNF-based memories using the CBRAM architecture. Our Ag/CNF/Pt-device achieves good nonvolatile properties with ON/OFF ratio $(>10^3)$, stable retention and long endurance. Next we have introduced a 99.3 % CNF-based memory devices, using cellulose as substrate and switching layer. Our paper memories show remarkable nonvolatile memory performance, such as high resistance ON/OFF ratio $(>10^6)$, long retention, and multilevel capability in Ag/CNF/ITO cell. Finally, we demonstrate the scaling capability of this material system inducing resistive switching on a single bundles of cellulose nanofiber. The properties of the CNF layer may be further engineered by tuning its composition and morphology in order to enhance the performances of the devices as reported elsewhere [5]. Furthermore

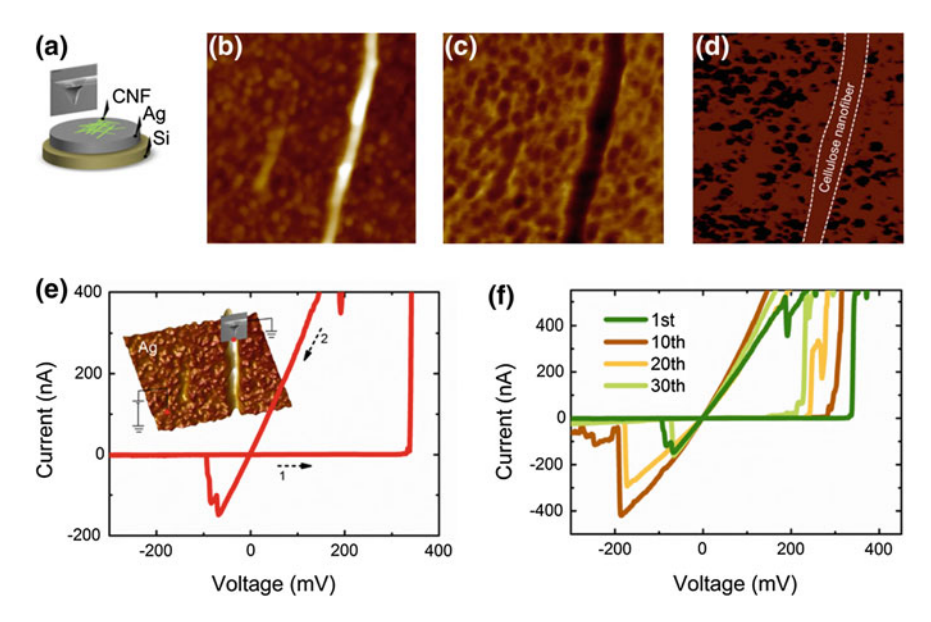


Fig. A.5 Single fiber switching. a Schematic of the sample structure used for the local cycling of single-fiber. Single cellulose bundles can be located with AFM. b Topography of a $2 \times 2 \,\mu m$ scan. The zoom in topography (c), the elastic modulus (d) and the (e) electrical properties of the surface reveal the presence of cellulose fiber which can be used for the tip-induce switching. f The I–V curves for tip/CNF/Ag-cell is presented in air and at room temperature. The bias is applied to the Ag electrode and the current is limited by the high resistance of the tip

these highly desirable properties can be combined with fully transparent and foldable substrate, which paves the way to flexible, wearable, and environmental friendly electronics. Therefore, after its glorious past, cellulose-based paper is most probably expected to continuously revolutionize our life also in future.

References

- M. Nogi, H. Yano, Transparent nanocomposites based on cellulose produced by bacteria offer potential innovation in the electronics device industry. Adv. Mater. 20(10), 1849–1852 (2008)
- M. Nogi, S. Iwamoto, A.N. Nakagaito, H. Yano, Optically transparent nanofiber paper. Adv. Mater. 21(16), 1595–1598 (2009)
- 3. M. Nogi, N. Komoda, K. Otsuka, K. Suganuma, Foldable nanopaper antennas for origami electronics. Nanoscale **5**(10), 4395–4399 (2013)
- D. Gaspar, S.N. Fernandes, A.G. de Oliveira, J.G. Fernandes, P Grey, R.V. Pontes, L. Pereira, R. Martins, M.H. Godinho, E. Fortunato. Nanocrystalline cellulose applied simultaneously as the gate dielectric and the substrate in flexible field effect transistors. Nanotechnology 25(9), 094008 (2014)

- K. Nagashima, H. Koga, U. Celano, F. Zhuge, M. Kanai, S. Rahong, G. Meng, Y. He, J. De Boeck, M. Jurczak, W. Vandervorst, T. Kitaoka, M. Nogi, T. Yanagida, Cellulose nanofiber paper as an ultra flexible nonvolatile memory. Sci. Rep. 4, 5532 (2014)
- F.J. Schmied, C. Teichert, L. Kappel, U. Hirn, W. Bauer, R. Schennach, What holds paper together: nanometre scale exploration of bonding between paper fibres. Sci. Rep. 3, 2432 (2013)
- 7. T. Tsuruoka, K. Terabe, T. Hasegawa, I. Valov, R. Waser, M. Aono, Effects of moisture on the switching characteristics of oxide-based. gapless-type atomic switches. Adv. Funct. Mater. **22**(1), 70–77 (2011)
- 8. U. Celano, L. Goux, K. Opsomer, A. Belmonte, M. Iapichino, C. Detavernier, M. Jurczak, W. Vandervorst, Switching mechanism and reverse engineering of low-power Cu-based resistive switching devices. Nanoscale **5**(22), 11187–1192 (2013)



Umberto Celano received his B.Eng. in Electronic Engineering and a M.Sc. degree in Nanoelectronics with honors from the University of Rome "Sapienza", Italy in 2009 and 2011 respectively. He holds a Ph.D. degree in Physics from the KU Leuven, Belgium.

In 2010, he joined imec in Belgium for his M.Sc. thesis, working on the chemical and electrical analysis of high-k dielectrics for sub-30 nm transistors node. One year later, he started a Ph.D. at KU Leuven performing his research at imec on ionic devices for non-volatile memory. In 2013, Umberto visited Osaka University in Japan, where he collaborated on the design of nanocellulose-based devices. His dissertation, reported in this book, has been awarded by the faculty of Science of KU Leuven with an honorable mention. Umberto is the recipient of the Rogen A. Haken Best Paper Award at IEDM (2013) and has authored or co-authored 50+ papers in international journals and conference proceedings. As a service for the profession he works with the metrology working-group in the International Technology Roadmap for Semiconductors (ITRS) and he is a member of the early carrier editorial board of Nano Letters.

Currently, Umberto is a Researcher in the material and component analysis group of imec. His research interests include nanometer scale issues in materials, emerging nanoelectronics and physical characterization. His goal is to explore methods and novel metrology techniques that enable the understanding of the physics in nanomaterials and nanoelectronics devices.

Invited Talks and Awards

 Celano, U. and Vandervorst, W., "Scanning probe tomography toward the threedimensional characterization of confined volumes" Nanoitaly, Rome (IT), 2015.

- Celano, U. and Vandervorst, W., "Scanning probe tomography for the 3Dobservation of conduction paths in advanced memory devices" Material Research Society spring meeting, San Francisco (CA), 2015.
- 3. Celano, U. and Vandervorst, W., "Metrology and characterization of emerging nonvolatile memory"
 - Nanoforum, Rome (IT), 2015.
- 4. Celano, U. and Vandervorst, W., "Scanning probe tomography for advanced material characterization"
 - IEEE International Integrated Reliability Workshop, South Leaf Lake (CA), 2014.
- 5. Celano, U., Best Paper Award, "Physical mechanism in ionic devices as studied by nanoscopic observation and manipulation"
 International Nanotechnology Conference 10, Gaithersburg (MD), 2014.
- 6. Celano, U., imec Excellence Award Recognition of high quality/impact publications (3 winners on 250 imec PhDs), Leuven (BE), 2014.
- 7. Celano, U., Goux, L., Belmonte, A., Opsomer, K., Franquet, A., Schulze, A., Detavernier, C., Richard, O., Bender, H., Jurczak, M., Vandervorst, W., Roger A. Haken Best Student Paper Award
 - "Conductive-AFM tomography for 3D filament observation in resistive switching devices", IEEE International Electron Devices Meeting (IEDM), Washington (DC), 2013.

Journal Papers

- 8. Celano, U., Nagashima, K., Koga, H., Nogi, M., Suganuma, K., Zhuge, F., Meng, G., He, Y., De Boeck, J., Jurczak, M., Vandervorst, W., Yanagida, T., "Ecofriendly and Biocompatible Nanocellulose based Resistive Switching Memory", *submitted* vol. n/a p. n/a, 2016.
- 9. Celano, U., Giammaria, G., Goux, L., Belmonte, A., Jurczak, M., Vandervorst, W., "Nanoscopic structural rearrangements of the Cu-filament in conductive-bridge memories", Nanoscale (*DOI:10.1039/C5NR08735J*) vol. n/a p. n/a, 2016.
- Celano, U., Goux, L., Fantini, A., Degraeve, R., Richard, O., Bender, H., Jurczak, M., Vandervorst, W., "Imaging in the three-dimension the conductive channel in filamentary-based oxide resistive switching memory", *Nano Lett.* vol. 15 p. 7970, 2015.
- 11. Celano, U., Hantschel, T., Giammaria, G., Chintala, R., Conard, T., Bender, H., Vandervorst, W., "Evaluation of the electrical contact area in contact-mode scanning probe microscopy", *J. Appl. Phys.* vol. 117 p. 214305, 2015.

12. Celano, U., Goux, L., Belmonte, A., Opsomer, K., Degraeve, R., Detavernier, C., Jurczak, M., Vandervorst, W., "Understanding the dual nature of the filament dissolution in conductive bridging devices", *J. Phys. Chem. Lett.* vol. 6 p. 1919, 2015.

- Celano, U., Goux, L., Belmonte, A., Opsomer, K., Franquet, A., Schulze, A., Detavernier, C., Richard, O., Bender, H., Jurczak, M., Vandervorst, W., "Threedimensional observation of the conductive filament in nanoscaled resistive memory devices", *Nano Lett.* vol. 14 p. 2401, 2014.
- Celano, U., Goux, L.; Opsomer, K.; Iapichino, M.; Belmonte, A.; Franquet, A.; Hoflijk, I.; Detavernier, C.; Jurczak, M.; Vandervorst, W., "Scanning probe microscopy as a scalpel to probe filament formation in conductive bridging memory devices", *Microelectron. Eng.* vol. 120 p. 67, 2014.
- Celano, U., Goux, L., Opsomer, K., Belmonte, A., Iapichino, M., Detavernier, C., Jurczak, M., and Vandervorst, W., "Switching mechanism and reverse engineering of low-power Cu-based resistive switching devices", *Nanoscale* vol. 5 p. 11187, 2014.
- Celano, U., Chintala, R., C., Adelmann, C., Richard, O., Vandervorst, W., "The unexpected effects of crystallization on Ta₂O₅ as studied by HRTEM and C-AFM", *Microelectron. Eng.* vol. 109 p. 318, 2013.
- 17. Celano, U., Chen, Y., Y., Wouters, D. J., Groeseneken, G., Jurczak, M., and Vandervorst, W., "Filament observation in metal-oxide resistive switching devices", *Appl. Phys. Lett.* vol. 102 p. 121602, 2013.
- 18. Belmonte, A., Celano, U., Redolfi, A., Fantini, A., Muller, R., Vandervorst, W., Houssa, M., Jurczak, M., Goux, L., "Analysis of the Excellent Memory Disturb Characteristics of a Hourglass-Shaped Filament", *IEEE Trans. Electron Dev.* vol. 6 p. 62, 2015.
- Belmonte, A., Celano, U., Degraeve, R., Fantini, A., Redolfi, A., Vandervorst, W., Houssa, M., Jurczak, M., Goux, L., "Operating-current dependence of the Cumobility requirements in oxide-based Conductive-Bridging-Memory Systems", IEEE Electron Device Lett. vol. 36 p. 775, 2015.
- 20. Hou, Y., Celano, U., Liu, L., Goux, L., Fantini, A., Degraeve, R., Zhang, L., Kang, J., Jurczak, M., Vandervorst, W., "Sub-10 nm low current resistive switching behavior in hafnium oxide stack", *Appl. Phys. Lett.* vol. n/a p. n/a, 2016.
- 21. Nagashima, K., Koga, H., Celano, U., Zhuge, F., Kanai, M., Rahong, S., Meng, G., He, Y., De Boeck, J., Jurczak, M., Vandervorst, W., Kitaoka, T., Nogi, M., Yanagida, T., "Cellulose nanofiber paper as an ultra flexible nonvolatile memory", *Sci. Rep.* vol. 4 p. 5532, 2014.
- Clima, S., Sankaran, K., Chen, Y. Y., Fantini, A., Celano, U., Belmonte, A., Zhang, L., Goux, L., Govoreanu, B., Degraeve, R., Wouters, D., J., Jurczak, M., Vandervorst, W., De Gendt, S., Pourtois, G., "RRAMs based on anionic and cationic switching: a short overview", *Phys. Status Solidi Rapid Res. Lett.* vol. 11 p. 501, 2014.
- 23. Nagashima, K., Yanagida, T., Kanai, M., Celano, U., Rahong, S., Meng, G., Zhuge, F., He, Y., Ho Park, B., Kawai, T., "Carrier type dependence on spatial

asymmetry of unipolar resistive switching of metal oxides", *Appl. Phys. Lett.* vol. 103 p. 173506, 2013.

Hantschel, T., Schulze, a., Celano, U., Moussa, A., Arstila, K., Eyben, P., Majeed, B., Tezcan, D. S., Werner, T., Vandervorst, W., "TiN scanning probes for electrical profiling of nanoelectronics device structures", *Microelectron. Eng.* vol. 97 p. 255, 2012.

Conference Proceedings

- 25. Celano, U., Goux, L., Belmonte, A., Opsomer, A., Detavernier, C., Jurczak, M., Vandervorst, W., "Conductive filaments multiplicity as a variability factor in CBRAM.", in *IEEE International Reliability Physics Symposium IRPS*, 2015.
- Celano, U., Goux, L., Belmonte, A., Giammaria, G., Opsomer, A., Detavernier, Richard, O., Bender, H., Irrera, F., C., Jurczak, M., Vandervorst, W., "Progressive vs. Abrupt reset behavior in conductive bridging devices: a C-AFM tomography study.", in *IEEE International Electron Devices Meeting - IEDM*, p.14.1.1– 14.1.4, 2014.
- 27. Celano, U. and Vandervorst, W., "Scanning probe tomography for advanced material characterization.", in *IEEE Integrated Reliability Workshop Final Report IIRW*, p. 1–5, 2014.
- 28. Celano, U., Goux, L., Belmonte, A., Opsomer, K., Franquet, A., Schulze, A., Detavernier, C., Richard, O., Bender, H., Jurczak, M., Vandervorst, W., "Conductive-AFM tomography for 3D filament observation in resistive switching devices.", in *IEEE International Electron Devices Meeting IEDM*, p. 21.6.1–21.6.4, 2013.
- 29. Celano, U., Conard, T., Hantschel, T., Vandervorst, W., "Probing the metal gate high-k interactions by backside XPS and C-AFM.", in *Material Research Society Proceedings MRS*, 2011.
- 30. Belmonte, A., Fantini, A., Degraeve, R., Celano, U., Vandervorst, W., Redolfi, A., Houssa, M., Jurczak, M., Goux, L., "Fast and Stable sub-10 μA Pulse Operation in W/SiO₂/Ta/Cu 90 nm 1T1R CBRAM devices.", in *IEEE International Memory Workshop IMW*, 2015.
- 31. Goux, L., Kim, W., Opsomer, K., Belmonte, A., Kar, G., De Stefano, F., Afanas'ev, V.V., Celano, U., Houssa, M., Devulder, W., Detavernier, C., Muller, R., Vandervorst, W., Jurczak, M., "Optimization of W/Al₂O₃/Cu(-Te) material stack for high-performance conductive-bridging memory cells.", in *Electrochemical Society Transactions ECS*, p. 175, 2015.
- 32. Hantschel, T., Schulze, A., Celano, U., Moussa, A., Arstila, K., Eyben, P., Majeed, B., Sabuncuoglu Tezcan, D., Werner, T., Vandervorst, W., "TiN scanning probes for electrical profiling of nanoelectronics device structures.", in *Microand Nanoengineering Conference Proceedings*, 2011.

Book Chapters

33. Celano, U. and Vandervorst, W., "Scalpel SPM for three-dimensional characterization of confined volumes.", in Conductive Atomic Force Microscopy, applications in Nanomaterials (monography), *Wiley-VCH*, in preparation, 2016.

Conference Contributions

- 34. Celano, U., Capogreco, E., Lisoni, J., G., Arreghini, A., Kunert, B., Guo, W., Van den bosch, G., Van Houdt, J., De Meyer, K., Furnemont, A., Vandervorst, W., "Direct three-dimensional observation of the conduction in poly-Si and In_{1-x}Ga_xAs 3D NAND vertical channels.", in *Symposium on VLSI Technology VLSIT*, 2016.
- 35. Celano, U. and Vandervorst, W., "Scalpel SPM: a slice-and-view approach for tomography based on scanning probe microscopy.", in *Material Research Society spring meeting MRS*, 2016.
- 36. Celano, U., Y., Hou, L., Goux, L., Fantini, A., Degraeve, R., Richard, O., Bender, H., Jurczak, M., Vandervorst, W., "Tomographic filament observation and scaling projection of RRAM in 3 × 3 nm dimensions.", in *Material Research Society spring meeting MRS*, 2016.
- 37. Celano, U., Mirabelli, L., Goux, L., Opsomer, K., Devoulder, W., Crupi, F., Detavernier, C., Jurczak, M., Vandervorst, W., "Tuning the switching behavior of conductive-bridge memory by the Cu content modulation in the cation-supplier alloys.", in *Materials for Advanced Metallization MAM*, 2016.
- 38. Celano, U. and Vandervorst, W., "Scanning probe tomography toward the three-dimensional characterization of confined volumes.", in *Nanoitaly*, 2015.
- 39. Celano, U., Goux, L., Belmonte, A., Opsomer, A., Detavernier, C., Jurczak, M., Vandervorst, W., "Conductive filaments multiplicity as a variability factor in CBRAM.", in *IEEE International Reliability Physics Symposium IRPS*, 2015.
- 40. Celano, U. and Vandervorst, W., "Scanning probe tomography for the 3D-observation of conduction paths in advanced memory devices.", in *Material Research Society spring meeting MRS*, 2015.
- Celano, U., Goux, L., Belmonte, A., Giammaria, G., Opsomer, K., Detavernier, C., Richard, O., Bender, H., Irrera, F., Jurczak, M., Vandervorst, W., "Progressive vs. Abrupt reset behavior in Conductive Bridging devices: a C-AFM tomography study.", in *International Electron Devices Meeting - IEDM*, 2014
- 42. Celano, U., Goux, L.; Opsomer, K.; Detavernier, C.; Jurczak, M., Vandervorst, W., "Low-current conductive filament instability in conductive-bridging memories for non-volatile multilevel cells.", in *Semiconductor on Insulator Specialists Conference SISC*, 2014.
- 43. Celano, U. and Vandervorst, W., "Scanning probe tomography for advanced material characterization.", in *International Integrated Reliability Workshop IIRW*, 2014.

44. Celano, U. and Vandervorst, W., "Metrology and physical characterization of emerging nonvolatile memory.", in *Nanoforum*, 2014.

- 45. Celano, U., Nagashima, K., Koga, H., Nogi, M., Suganuma, K., De Boeck, J., Jurczak, M., Vandervorst, W., "Cellulose nanofibers for resistive switching: toward a paper-based electronics.", in *European Material Research Society spring E-MRS*, 2014.
- 46. Celano, U. and Vandervorst, W., "Physical mechanism in ionic devices as studied by nanoscopic observation and manipulation.", in *The Tenth International Nanotechnology Conference INC10*, 2014.
- 47. Celano, U., Goux, L., Belmonte, A., Schulze, A., Opsomer, K., Detavernier, C., Richard, O., Bender, H., Jurczak, M., Vandervorst, W., "Conductive-AFM tomography for 3D filament observation in resistive switching devices.", in *International Electron Devices Meeting IEDM*, 2013.
- 48. Celano, U., Chintala, R., Hoflijk, I., Moussa, A., Vanhaeren, D., Mannarino, M., Nazir, A., Eyben, P., Vandervorst, W., "Damage-free contact mode current sensing SPM: benchmarking PFTUNA vs. C-AFM.", in *SPM Dutch user meeting SPMDUM*, 2013.
- 49. Celano, U., Chintala, R., Adelmann, C., Richard, O., Vandervorst, W., "The unexpected effects of crystallization on Ta₂O₅ as studied by HRTEM and C-AFM.", in 18th Conference of Insulting Films on Semiconductors INFOS, 2013.
- 50. Celano, U., Goux, L., Opsomer, K., Iapichino, M., Franquet, A., Hoflijk, I., Jurczak, M., Vandervorst, W., "Scanning probe microscopy as a scalpel to probe filament formation in RRAM devices.", in *Materials for Advanced Metallization MAM*, 2013.
- 51. Celano, U., Goux, L., Opsomer, K., Belmonte, A., Jurczak, M. and Vandervorst, W., "Instability of conductive filaments in conductive bridging memory devices.", in *Nonvolatile memory workshop NVMW*, 2013.
- 52. Celano, U., Goux, L., Opsomer, K., Conard, T., Franquet, A., Jurczak, M., Vandervorst, W., "Cu alloys for conductive bridging memories as studied by C-AFM.", in *European Material Research Society fall meeting- E-MRS*, 2012.
- 53. Celano, U., Chen, Y., Y., Wouters, D., Jurczak, M., Vandervorst, W., "De-process and physical characterization of HfO₂ based resistive memory as studied by C-AFM.", in *Electrochemical Society fall Meeting ECS*, 2012.
- 54. Celano, U., Conard, T., Opsomer, K., Goux, L., Jurczak, M., Vandervorst, W., "Cu migration in conducting bridging memories as studied by C-AFM.", in *Material Research Society spring meeting MRS*, 2012.
- 55. Celano, U., Conard, T., Hantschel, T., Vandervorst, W., "Probing the metal gate high-k interactions by backside XPS and C-AFM.", in *Material Research Society spring meeting MRS*, 2011.
- 56. Mannarino, M., Celano, U., Anh Khoa, A., L., Chintala, R., Paredis, K., Vandervorst, W., "A 3D electrical characterization of single stacking faults in InP by conductive-AFM.", in *Material research Society fall meeting MRS*, 2015.

57. Eyben, P., Celano, U., Chintala, R., Nazir, A., Paredis, K., Vandervorst, W., "Electrical AFM at IMEC: from dopant profiling in organic and inorganic semi-conductors to analysis of resistive switching mechanisms at the nm-scale.", in *Benelux SPM user meeting - BLSPM*, 2014.

- 58. Belmonte, A., Fantini, A., Degraeve, R., Celano, U., Vandervorst, W., Redolfi, A., Houssa, M., Jurczak, M., Goux, L., "Fast and Stable sub-10 μA Pulse Operation in W/SiO₂/Ta/Cu 90 nm 1T1R CBRAM devices.", in *IEEE International Memory Workshop IMW*, 2015.
- 59. Goux, L., Kim, W., Opsomer, K., Belmonte, A., Kar, G., De Stefano, F., Afanas'ev, V.V., Celano, U., Houssa, M., Devulder, W., Detavernier, C., Muller, R., Vandervorst, W., Jurczak, M., "Optimization of W/Al₂O₃/Cu(-Te) material stack for high-performance conductive-bridging memory cells.", in *Electrochemical Society fall meeting ECS*, 2013.
- Hantschel, T., Schulze, A., Celano, U., Moussa, A., Arstila, K., Eyben, P., Majeed, B., Sabuncuoglu Tezcan, D., Werner, T., Vandervorst, W., "TiN scanning probes for electrical profiling of nanoelectronics device structures.", in *Microand Nanoengineering Conference MNE*, 2011.
- 61. Schulze, A., Hantschel, T., Eyben, P., Dathe, A., Nazir, A., Mody, J., Celano, U., Ke, X. and Vandervorst, W., "Electrical characterization of carbon nanotube based interconnects.", in *Benelux SPM User meeting BNLSPM*, 2011.